Understanding the Nucleation and Growth Mechanism of Metal Nanoparticles and Fluorescent Metal Quantum Clusters and their Applications

Thesis Submitted to AcSIR For the Award of
the Degree of
DOCTOR OF PHILOSOPHY
In Biological Sciences

By
Puneet Khandelwal
Registration Number:10BB11A26053

Under the guidance of
Dr. Pankaj Poddar

Physical and Materials Chemistry Division
CSIR-National Chemical Laboratory
Dr. Homi Bhabha Road
Pune-411008.

Dedicated to my Parents

Acknowledgements

There are so many people, whose support, encouragement and inspiration are very much necessary to accomplish any major achievements in life, especially, if it involves the elements of fulfilling one's cherished dreams. I take this opportunity to acknowledge and extend my sincere gratitude towards all these people who have been involved, directly or indirectly, to make the research work described in this thesis possible.

First, I would like to express my deepest gratitude to my research supervisor Dr. Pankaj Poddar, for giving me an opportunity to pursue my Ph.D. research with him. It has been a great privilege to work under his guidance for the past five years. His innovative thinking and highly spirited attitude have inspired me to conduct and complete my doctoral research quite efficiently. He has not only grafted my scientific skills and knowledge but also moulded me into a better human being. His constant encouragement helped me to push beyond my limits. His guidance always challenged me intellectually and provided a perfect ambience that I needed to grow as a researcher. I am really grateful to him for his critical comments and tremendous efforts in preparing this dissertation. I thank him for his endless support filled with patience and enthusiasm during my whole tenure of Ph.D.

I would also like to thank my doctoral advisory committee members, Dr. Sarika Maitra Bhattacharyya, Dr. Guruswamy Kumaraswamy and Dr. Amol Arvindrao Kulkarni for their constructive and innovative suggestion. I owe a great deal of appreciation and gratitude to my external expert Dr. Partha Hazra. I warmly thank him for his precious advice, analysis, criticism and discussions on my work.

I extend my sincere thanks to the present (Dr. Ashwini Kumar Nangia) and former directors (Dr. Vijaymohanan, Dr. Sourav Pal), present (Dr. P.A. Joy) and former (Dr. Anil Kumar) head of physical and materials chemistry division, for their kind help and encouragement during the course of this work. I am grateful to DBT, New Delhi for fellowship support. I thank all the nonteaching staff of CSIR-NCL for their assistance on various occasions.

I also would like to thank my collaborators Dr. Samit Chattopadhyay from NCCS, Pune (his student Aftab Alam) and Dr. Subashchandrabose Chinnathambi (his student Nalini V. Gorantala) for their help and support in my studies.

I take an opportunity to thank my seniors Adhish bhaiya, Umesh bhaiya, Imran bhaiya, Richa di, Dheeraj bhaiya, Raja bhaiya, Chandu bhaiya, Guptaji, Subhadeep bhaiya, Subhadi, my fellow labmates Mousumi, Padhye, Anupam, Gayatri, Sameer, Monika and Shubhra. Although many have moved away from NCL, I will never forget the experiences we've shared and hope to stay in touch. I thank Subhadi, Guptaji, Mousumi, Padhye for interesting discussions on a cup of tea. These friends have been there for me when the challenges of PhD seemed too great to overcome. I also thank project trainees Srijeet, Vasudev, Amie, Parul, Sandhya, Subhi, Arvind, Lakshya, because of them I learned a lot.

A special thanks to my roommates Jugal, Rajendra, Bhanu for the stimulating discussions, sleepless nights, discussions on Sunday morning tea, best food, many trips and for all the support at various critical time points and fun we had in the last five years. I also thank to my friends in NCL Vikas, Ashish, Kavita, Yachi, Suman, Zinoy, Kedar, Manoj, Prabhu, Pravin for their help and support at the time of PhD in NCL. I extend my thanks to M.Sc. friends Vishal, Rahul, Putta, Damuka, Rajesh, Subhadeep for their help and support at several time points in my PhD and with them I have enjoyed a lot.

I would like to express the deepest gratitude to my Mummy and Papa who provided support, encouragement and interest in my thesis work. Thank you for believing in me and allowing me to pursue my ambition. Thanks for listening to my problems and providing perspective. I would also like to thank my brother Ankur and sister Priya for their constant help and support and being with me in my hard times and listening to my tantrums.

I could not have completed my research without the support of all these wonderful people!

Last but by no means least I thank Lord Ganesha for making my life so special.

Puneet Khandelwal……

Contents

Preface

Metal nanoparticles and quantum clusters are excellent systems due to their tunable electronic and optical properties including optical absorption, scattering, electrical/thermal conductivity, luminescence, non-linear optical properties (two photon absorption, two photon fluorescence, and second/third harmonic generation), surface enhancement of electric field, and ultrafast dynamics (relaxation kinetics, electron-phonon coupling, and radiative emission). These excellent properties have resulted into their wide rending applications. To list a few— (1) sensing of ions (heavy metal ions, anions), biomolecules (proteins, DNA, miRNA, and enzymes), (2) they act as catalysts, (3) they are used in diagnosis and therapy due to their optical signature and due to ease of surface functionalization etc. Apart from that, these systems had a long history of being excellent model systems for studying various nucleation and growth processes including the nanoparticles synthesis.

In **chapter 1**, I discuss about the history of metal nanoparticles and metal quantum clusters; and the evolution of various theories to understand the properties of these systems. I also discuss the nucleation and growth mechanisms of metal nanoparticles and provide an overview of various theories. Various parameters which affect the nucleation and growth of these nanoparticles are also discussed in this chapter. I also review the properties shown by these metal clusters including optical, catalytic, and magnetic properties. Later, I discussed the applications, especially for metal clusters, including sensing and bio-imaging. Finally, I discussed outline of thesis.

Chapter 2 addresses the synthesis of antibiotic capped gold nanoparticles and gold quantum clusters and their applications as antibacterial agents, sensing of mercury ions and the imaging of bacterial cells. Here, I show the use of an antibiotic—cefradine as reducing as well as capping agent. My work is to understand the interplay of precursor molar ratio

($HAuCl_4$/cefradine), temperature, and pH of the reaction on the assembly of gold atoms is also presented in this chapter. I show that how to my surprise, at pH 6, I observed the synthesis of relatively higher fraction of smaller particles (with diameter < 2 nm) which could be isolated by simple centrifugation method. The as-obtained supernatant contains Au_8 clusters (validated from MALDI analysis) and shows strong blue luminescence. The blue luminescent gold clusters were applied for mercury ion sensing as well as their imaging in bacterial cells. These antibiotic protected gold nanoparticles and clusters were also used as an antibacterial agent.

In **chapter 3**, I discuss my work on the synthesis of curcumin capped gold quantum clusters, where curcumin acts as a weak reducing as well as capping agent. Curcumin is a very well-known therapeutically important molecule and has potential applications in various diseases. But, the water insolubility of curcumin, which leads to the poor bioavailability, poor oral absorption, rapid metabolism and rapid excretion, hindered its biological applications. Therefore, curcumin was allowed to conjugate with gold clusters *in situ* to enhance its water dispersibility which may also modify its activity. Later, in this chapter, I show the results of the anticancer properties of the curcumin-conjugated gold clusters and show that these clusters preserves the anticancer activity of curcumin with low cytotoxicity to normal cells than curcumin alone.

Chapter 4 describes the synthesis of curcumin-conjugated silver clusters to visualize their interaction with human Tau protein. Tau protein fibrillation was found to be one of the major reasons behind onset of Alzheimer's disease. Motivation comes from the earlier research which shows that curcumin has potential anti-Alzheimer's applications. Also, the silver nanoparticles of certain size, shape and surface functionality are well known to cross the blood brain barrier (BBB), which can access to the Tau proteins present in the brain and can inhibit the Tau fibrillation. In this chapter, I show the use of curcumin-conjugated silver

clusters for the inhibition of Tau fibrillation. Results show that curcumin-conjugated silver clusters were able to efficiently inhibit the Tau fibrillation process than curcumin-conjugated silver nanoparticles, GSH-conjugated silver clusters and curcumin alone.

Finally, **chapter 5** will describe the conclusion of the overall work presented in this thesis. The future direction of this thesis also presented in this chapter.

List of abbreviations

1.	Gold nanoparticles	Au-NPs
2.	Gold quantum clusters	Au-QCs
3.	Cefradine	CFD
4.	Silver nanoparticles	Ag-NPs
5.	Silver quantum clusters	Ag-QCs
6.	Blood brain barrier	BBB
7.	Glutathione	GSH
8.	Propidium iodide	PI
9.	X-ray diffraction	XRD
10.	Transmission electron microscope	TEM
11.	Inductively coupled plasma optical emission spectrometry	ICP-OES
12.	Ultraviolet visible spectroscopy	UV-vis
13.	Cyclic voltammetry	CV
14.	X-ray photoelectron spectroscopy	XPS
15.	Atomic force microscopy	AFM
16.	Mass assisted laser desorption ionization mass spectrometry	MALDI-MS
17.	Electrospray ionisation mass spectrometry	ESI-MS
18.	Fourier transform infrared spectroscopy	FTIR
19.	Photoluminescence	PL
20.	Density functional theory	DFT
21.	X-ray computed tomography	CT
22.	Positron emission tomography	PET
23.	Sodium dodecyl sulfate polyacrylamide gel electrophoresis	SDS-PAGE

24.	Circular dichroism	CD
25.	2',7'-dichlorodihydrofluorescein diacetate	H2DCFDA
26.	Room temperature	RT
27.	Luria-Bertani medium	LB medium
28.	Fluorescence-activated cell sorting	FACS
29.	Dulbeccòs modified Eagles medium	DMEM
30.	3-(4, 5-dimethylthiazol-2-yl)-2,5- diphenyltetrazolium bromide	MTT
31.	Alzheimer's disease	AD
32.	β-amyloid	Aβ
33.	Isopropyl β-D-1-thiogalactopyranoside	IPTG
34.	Dithiothreitol	DTT
35.	2-(N-morpholino)ethanesulfonic acid	MES
36.	Phosphate-buffered saline	PBS
37.	N,N-bis(2-hydroxyethyl)-2-aminoethanesulfonic acid	BES
38.	Thioflavin S	ThS
39.	Dimethyl sulfoxide	DMSO
40.	Dynamic light scattering	DLS

Chapter I

Introduction

This chapter provides an introduction to the metal NPs and metal QCs including a brief history of research in these systems, and the overview of the existing theories to understand their properties. We also discuss about the nucleation and growth mechanism and the factors or parameters by which these processes affects. At the end of the chapter, we give the introduction of various properties of QCs, their synthesis methods, and also a present a vast and updated overview of applications covering various fields.

1.1 History of metal colloids

Bulk coinage metals (Au, Ag, Cu) are very well known since an ancient time due to their high electrical conductivity and beautiful surface luster which was extensively used for conducting wires, ornamentals, colored glass windows etc. Metal colloids, especially gold colloids, have a long history starting from the 4th century B.C. when the colloidal gold was used to make ruby glass and for coloring ceramics. The famous example is "Lycurgus Cup" which shows different colors depending on whether or not light is passing through it. It looks ruby-red in transmitted light while greenish in reflected light due to the presence of gold colloids (Figure 1).

Figure 1. *Lycurgus cup appears (a) ruby-red in transmitted light, and (b) greenish in reflected light. Present location: British Museum, Room 41, London, UK. © Trustees of the British Museum.*

The use of Bhasmas, an Ayurvedic metallic preparation, is well documented in the Ayurveda since 7th century AD usually recommended for the treatment of many disease condition. Now, it is shown that Bhasma contains metal nanoparticles.[1] The colloidal gold which was known as soluble gold or drinkable gold, considered for medicinal importance. In Ayurveda, until the Middle Ages (16th century) to cure several diseases including tumors, rheumatoid arthritis and syphilis.[2] In 17th century, a colorant of glass, which became popular

as “Purple of Cassius”, was the hetero-coagulation of gold particles and tin dioxide. It was also reported in 1718 that boiling with starch solution, enhances the stability of gold sol.[3] The explanation of different colors by gold sol was also given in 1818 that pink or purple solutions contain gold in the finest degree of subdivision, whereas yellow solutions were found when the fine particles were aggregated.[4]

The first scientific research on colloidal gold dates back to Faraday’s time. In 1857, in a basement laboratory of Royal Institution, London, Faraday reported the synthesis of deep red colored gold colloid in two-phase reaction medium by the reduction of aqueous solution of chloroauric acid using phosphorous in diethyl ether.[5] While most colloids last for a few months or even a year, Faraday's gold colloids are still optically active even after 160 years and displayed in Faraday’s original laboratory on the Lower Ground Floor of the Royal Institution in the Faraday Museum. Faraday’s work laid down the foundation for later colloid science.

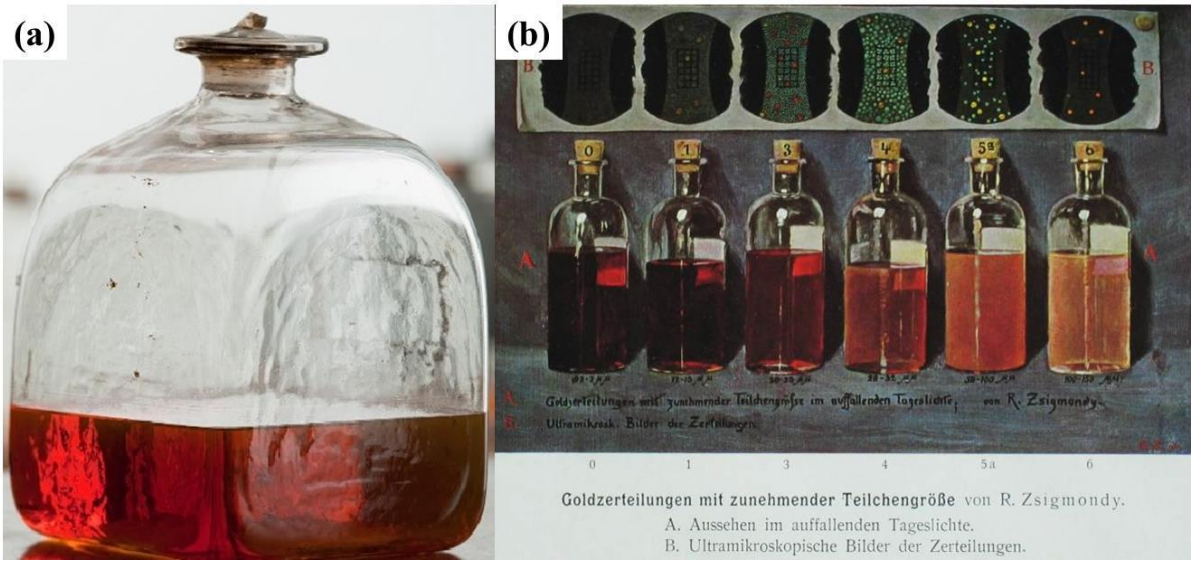

Figure 2. *Gold colloid samples prepared by (a) Michael Faraday, and (b) R. A. Zsigmondy.*

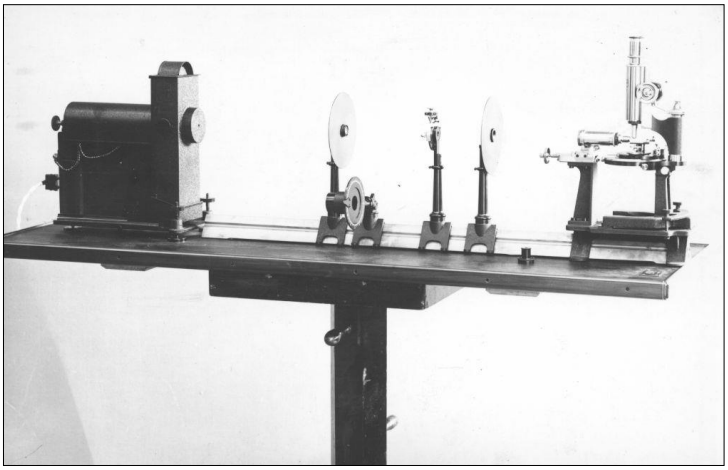

Figure 3. *An ultra-microscope invented by Henry Siedentopf and Richard A. Zsigmondy in 1903 in which light of an arc lamp was projected through a slit aperture to observe gold particles.*[6] *© 2006-2016 Vibrant Software Corp.*

The term "colloid" (from the French, *colle*) was coined shortly thereafter by Graham, in 1861.[7] Then, in 1898, Richard Adolf Zsigmondy developed a method for synthesis of gold colloids in liquid which became quite popular and this method involves the reduction the chloroauric acid by formaldehyde (Figure 2b).[8] In 1903, the ultra-microscope was also invented by Henry Siedentopf and Richard A. Zsigmondy to observe the gold particles (Figure 3).[6]

Richard A. Zsigmondy also awarded by the Nobel Prize in Chemistry in 1925 for his contribution to understand the behavior of colloids.[8] Before the discovery of TEM, the sizes of colloidal particles were primarily determined by Ultramicroscopy. In 1918, Paul Scherrer reported that the size of colloidal particles could be estimated by X-ray diffraction.[9] Later, this method became popular and widely used till now. Meanwhile, Theodor Svedberg who was a Nobel Prize winner in chemistry in 1926, used ultracentrifugation to measure particle sizes using Stokes' law of sedimentation in 1940s; this method is also used to date.[10]

After the invention of TEM by Max Knoll and Ernst August Friedrich Ruska (Nobel Prize in Physics in 1986 shared by Ruska with Gerd Binnig and Heinrich Rohrer for invention of STM) in 1933 and commercialization after world war II, in 1949, Turkevich et al. reported

the first TEM image of gold nanoparticles synthesized by the reduction of chloroauric acid by citric acid— known as Turkevich method.[11] Turkevich et al. also performed thorough study on the nucleation and growth processes in the synthesis of colloidal gold from 1951 to 1964.[12–15] Then onwards, a tremendous advancement was observed in the field of nanomaterial's research and their applications. In past two decades, almost all the branches of natural science are hugely impacted by the nanoscience and nanotechnology.

Parallelly, in 1965, L. Naldini and F. Cariati reported the work on the synthesis of copper, silver and gold clusters synthesized using triphenylphosphine ligands. They reported the synthesis of gold clusters made up of ≤ 5 gold atoms.[16] Later, in 1967, the same group also reported the stabilization of Au_6 clusters with the ligand 1,2 Bis (diphenylphosphino)ethane with various different anions. The authors used conductivity measurements, infrared spectra and exchange reactions to identify the presence of gold clusters.[17] At the same time, people were also interested in calculations of electronic properties of metal clusters but it was not possible until a breakthrough research reported by Hohenberg and Walter Kohn in 1964, which is now known as "Density Functional Theory (DFT)". They reported that there is no need to determine the positions of every electron in the system; instead, knowing the average density of electrons at all points in space is enough to uniquely determine the total energy. Other available methods at that time required wave functions, which depend on the positions of every electron in the system and are far more complicated functions than the density.[18] In 1965, W. Kohn with Lu Sham described a procedure for deriving the electron density and energy, based on solving a set of self-consistent equations which include, in an approximate way, exchange and correlation effects equations for a corresponding system of non-interacting electrons, which is much easier to

manage.[19] These contributions in chemistry lead to the Nobel Prize to W. Kohn in 1998. In 1967, Robbins et al. reported the production of small sodium clusters up to eight atoms in the gas phase using an isentropic flow of high pressure vapor through a small orifice (Figure 4).[20]

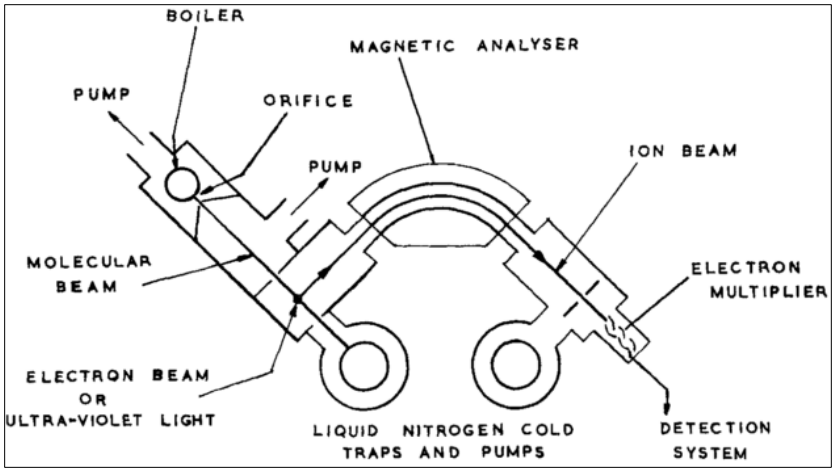

Figure 4. *Schematic representation of apparatus used for the production of sodium clusters by Robbins et al. Reproduced from ref. 20 with permission.*

In 1969, McPartlin et al. reported the synthesis of $Au_{11}(PPh_3)_7(SCN)_3$, in which metal-metal bonds are postulated between the central gold atom and its ten neighbors.[21] Later, there were series of reports published by many groups in 1970s on the 'first' synthesis of several types of metal-clusters composed of cobalt, manganese, copper, osmium, ruthenium, rhodium, niobium, tantalum, platinum etc.[22–29] In 1970s, L. Naldini and F. Cariati group again reported the series of works on the synthesis of several types of gold cluster species, such as $Au_{11}L_7X_3$, $Au_9L_8X_3$ (L = tris-para substituted phenylphosphine), $[AuPAr_3]_6^{2+}$ (PAr_3 = tris-p-tolylphosphin), $Au_8(PPh_3)_8$ (PPh_3 = triphenylphosphine) and reported the X-ray crystal structure of most of them.[30–33] In 1981, Echt et al. reported the first experimental observation of synthesis of magic numbered noble gas (Xe) clusters abundantly.[34] The observed numbers (n = 13, 55, and 147) coincide with the number of spheres required for complete shell icosahedra (Figure 5). Subsequently, in 1983, He, Ar and Kr clusters were also reported with magic numbers.[35,36]

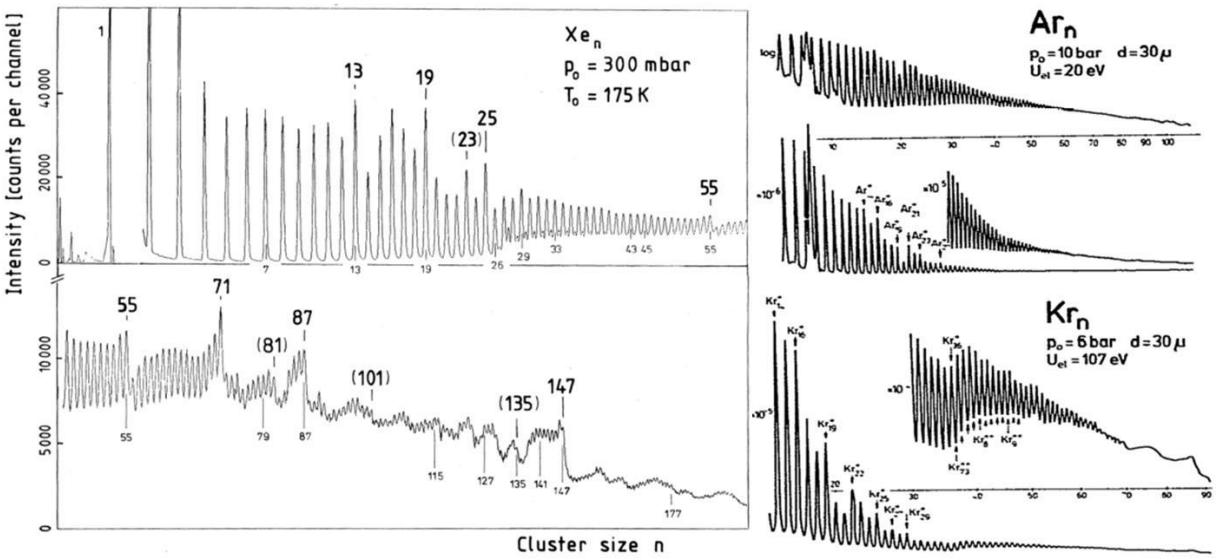

Figure 5. *(Right side) Mass spectrum of xenon clusters. Brackets are used for numbers with less pronounced effects. Numbers below the curve indicate predictions or distinguished sphere packings. (Left side) The mass spectra of Ar and Kr clusters. Reproduced from ref. 34 and 35 with permission.*

In 1975, M. Cini was probably the first to replace the ion cores of metal clusters by a uniform positive Jellium background in his theoretical calculations and used density functional formalism given by Kohn and Sham (previously described).[37] Thereafter, a series of reports appeared on the use of modified approaches and approximations by several groups such as Martins et al. which reported the theoretical approach to study the structural and electronic properties of simple metal clusters with a model based on the density functional formalism.[38] The vibrational spherical model, which they reported, takes into account the electron relaxation effects and the lattice structure through the introduction of pseudopotentials. Results for the ionization potential and electron affinity, binding and surface energies and lattice relaxation are presented for bcc and icosahedral Na clusters having up to 350 atoms.[39] In 1982, D. M. Wood and N. W. Ashcroft, reported the quantum confinement

effect in the optical properties of metal clusters and used the Jellium model ($\sim E_f/N^{1/3}$) for justification of energy gap in small metal clusters, rather than Kubo gap ($\sim E_f/N$).[40]

Then, the subsequent work reported by Knight et al. in 1984, became popular due to their systematic study for the synthesis of sodium clusters made up of ~ 100 atoms, and their observation of abundance of few cluster population with the number of atoms (N) = 8, 20, 40, 58, and 92 (Figure 6).[41,42] In order to understand this behavior, they also proposed the application of a one-electron shell model in which independent delocalized atomic 3s electrons are bound in a spherically symmetric potential well.

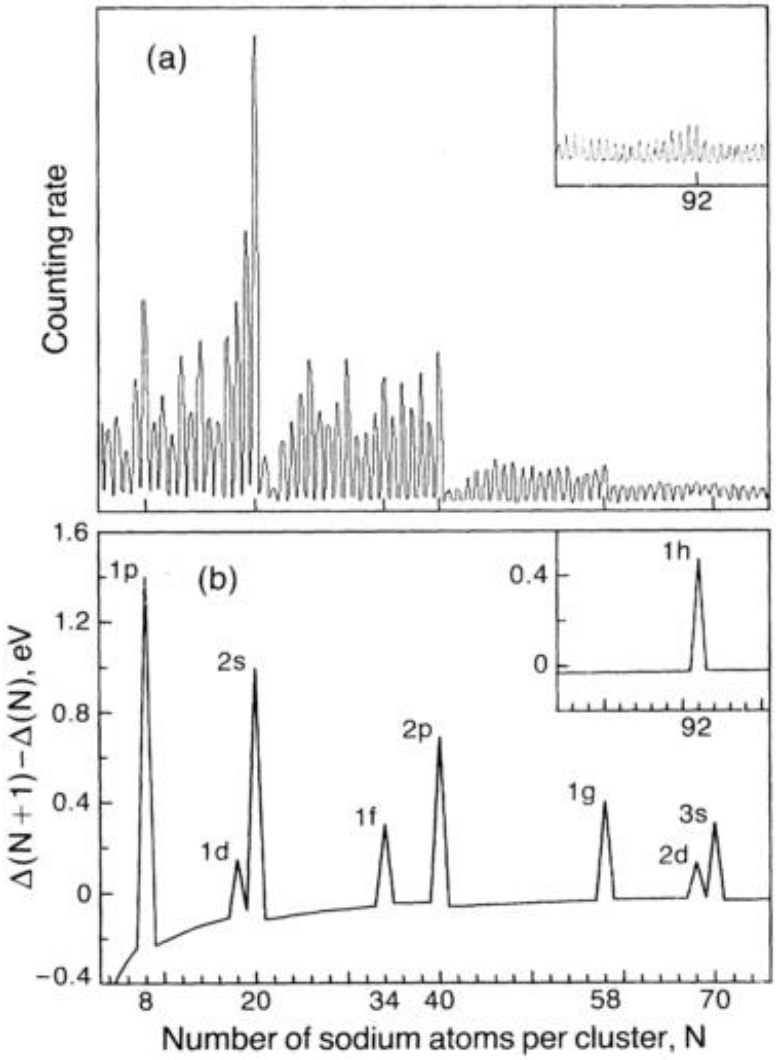

Figure 6*. (a) Mass spectrum of sodium clusters, N =4-75. (b) The calculated change in the electronic energy difference, Δ(N+1) - Δ(N) vs N. The labels of the peaks correspond to the closed-shell orbitals. Reproduced from ref. 41 with permission.*

One another modification in the Jellium model was to use self-consistent calculations in order to calculate the electronic structures of small metal clusters reported by D.E. Beck and W. Ekardt in 1984.[43] Ekardt reported the electronic structure, dynamic polarizability, and work functions of small metal clusters using self-consistent calculations within the framework of the local-density approximation applied to the spherical Jellium model.[44–46] He has also reported the theoretical analysis of photoemission from small metal clusters. The method used is the time-dependent local-density approximation (TDLDA) applied to the self-consistent spherical Jellium background model.[47]

1.2 Theories for metals

The properties of bulk metals completely change when transformed to nano-size. Unlike the bulk, the nanoscale metals show various colors from red to violet, mainly due to be the collective oscillations of conduction band electrons, known as surface plasmon resonance (SPR).[48] The nano-scale metals can be divided in three main categories according to their size regimes such as: (a) large NPs ($R > \lambda$), optical responses of these NPs simply depend on their size and free electron density. The dielectric function of these NPs is almost similar to the bulk and can be quantitatively described by Mie theory; (b) small NPs, when the size of NPs approaches the electron mean free path (~ 50 nm for Au and Ag), the dielectric function and refractive indices become strongly size dependent, however, the Mie theory still can provide the adequate description, if applied properly; (c) MQCs, when the size of NPs reaches the Fermi wavelength of an electron (ie. de Broglie's wavelength of an electron at Fermi energy ~ 0.5 nm for both Au and Ag), the optical, electronic, and chemical properties differs drastically from other two regimes.[49] These metal clusters are made up of few to few tens of metal atoms

and turns as a connecting link between molecules or atoms to nanoparticles or even to the bulk.

1.2.1 Drude model

In 1900, Paul Drude proposed the "Drude model" to explain the electrical and thermal conductivities of metals. This model was the modification of kinetic theory of gases, which assumes that (a) the interaction of electrons with other particles was neglected between the successive collisions, (b) electron-electron scattering was neglected, (c) the valence electrons were considered as free electrons which are delocalized and do not belong to any metal atom in the bulk metal.[50]

1.2.2 Mie theory

Over the years many theories were given to understand the coloration of colloidal metals including the theories given by Felix Ehrenhaft and J. C. Maxwell-Garnett. According to F. Ehrenhaft, the colors could be due to optical resonance while Maxwell (in 1904) demonstrated that the colors of the colloidal metals can be satisfactorily explained by the theory developed by L. Lorenz for optically inhomogeneous media. The theory gives a well-defined absorption curve which can be determined from the optical constants of the colloidal metals, accordingly, the patterns of these absorption curves were quite different than the pattern of absorption curves of solid metals, and they not at all do with the resonance in the sense described by F. Ehrenhaft. However, this explanation given by Maxwell did not fit well for many other cases.[51]

Later, in 1908, using Maxwell's electromagnetic theory, Gustav Adolf Feodor Wilhelm Ludwig Mie provided a theoretical treatment of plasmon resonance absorption of gold colloids. The sharp absorption bands depend on the particle size and explain the change

in color that occurs as the size of the colloid nanoparticles is increased from 20 to 1600 nm. The Mie solution to Maxwell's equations (also known as the Lorenz–Mie solution, the Lorenz–Mie–Debye solution or Mie scattering) describes the scattering of an electromagnetic plane wave by a homogeneous dielectric sphere. The term "Mie theory" used for this collection of solutions and methods; it does not refer to an independent physical theory.[51]

1.2.3 Kubo criterion

In 1962, Ryogo Kubo reported quantitatively the electronic structure of very small metal clusters based on the recognition that the quasi-continuous electron energy states of bulk metals become discrete on the few-atom scale. The energy-level spacing between adjacent levels for an N-atom particle is on the order of E_f/N, where E_f is the Fermi energy of the bulk metal. The relative difference between the energy-level spacing and thermal energy has become a criterion for distinguishing metallic from nonmetallic behavior which is known as "Kubo criterion".[52] If the energy-level spacings are smaller than k_BT, thermal energy can create mobile electron-hole pairs in the metals, and current can flow (Figure 7). However, if energy-level spacings are much larger than the available thermal energy, the free electrons in the metal clusters are confined to discrete energy levels.[52,53] Thus, the metal clusters are often considered to be nonmetallic, even though they may exhibit free-electron scaling behavior. Although Kubo predicted some properties of the metal-cluster electronic structure, the quantitative correlation of electronic structures with the number of metal atoms was not elucidated until early 1980s.

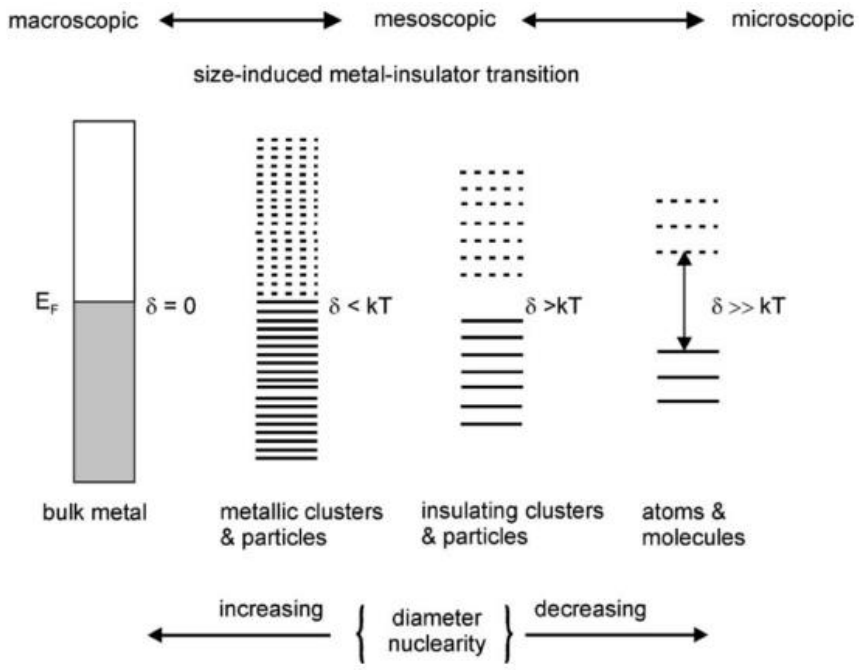

Figure 7. *Evolution of the band gap and the density of states as the number of atoms in a system increases (from right to left). δ is the so-called Kubo gap. Reproduced from ref. 53 with permission.*

1.2.4 Jellium model

The term jellium was coined by Conyers Herring, alluding to the "positive jelly" background, and the typical metallic behavior it displays. As discussed in the previous section, jellium which is also known as the uniform electron gas (UEG) or homogeneous electron gas (HEG), is a quantum mechanical model consist of interacting electrons and a positive background charge. Both the electron density and the positive charge background density are homogeneous and equal in magnitude in an infinite system. While, at the jellium surface, a sharp change was observed in the surface (step function) of the positive background charge and the electron density "spills out" slightly from the background, which results in a dipole layer at the surface (Figure 8).[54,55]

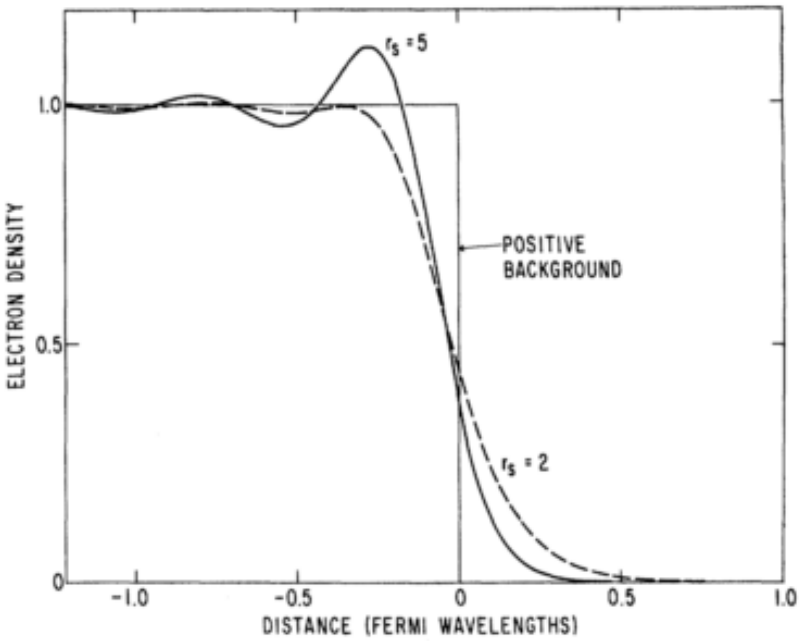

Figure 8. *Self-consistent charge density near metal surface (uniform positive background model or jellium model). Reproduced from ref. 55 with permission.*

1.3 Theories of nucleation and growth

The synthesis of nanocrystals is basically the precipitation of solid phase from solution. Therefore, a good knowledge about the parameters that affect the precipitation process, can be very helpful for synthesis of nanocrystals with various desired morphologies. There is a specific solubility of a particular solute in a solvent, so, the addition of excess amount of solute leads to the precipitation and formation of nanocrystals. The excess amount of solute can be added either direct addition or by the addition of reactant which ultimately increases the concentration of solute. The nucleation process can be of three types: (a) homogenous, (b) heterogeneous, and (c) secondary nucleation. The homogenous nucleation occurs in the absence of solid phase where only the solute molecules combine to produce the nuclei. The thermodynamics is a main driving force behind the homogenous nucleation because the supersaturated solution is not energetically stable. The overall free energy (ΔG) is the sum of the energy created due to the formation of (a) new volume (ΔG_v), and (b) new surface (ΔG_s). For a spherical particle,

$$\Delta G = \Delta Gv + \Delta Gs = -\frac{4}{V}\pi r^3 \kappa_B T \, In(S) + 4\pi r^2 \gamma \quad (1)$$

where, v is the molecular volume of the precipitate, r is the radius of nuclei, κ_B is Boltzmann constant, S is saturation ratio, and γ is surface free energy per unit surface area. Since, ΔG_s is always positive and ΔG_v is always negative, there should be a maximum free energy at which nuclei will pass through to form a stable nucleus which can be obtained by differentiating ΔG with respect to r and setting to zero which gives critical free energy (ΔG_{crit}). When S>1, ΔG is positive minimum at a critical size r*. This ΔG acts as activation energy for nucleation. The nuclei larger than its critical size decrease its ΔG for growth and form stable nuclei that grow to form particles. The particles with the radius (r) larger than the critical radius (r*), for a given value of S, tend to grow further while the particles with the radius smaller than the critical radius tends to dissolve (Figure 9).[56]

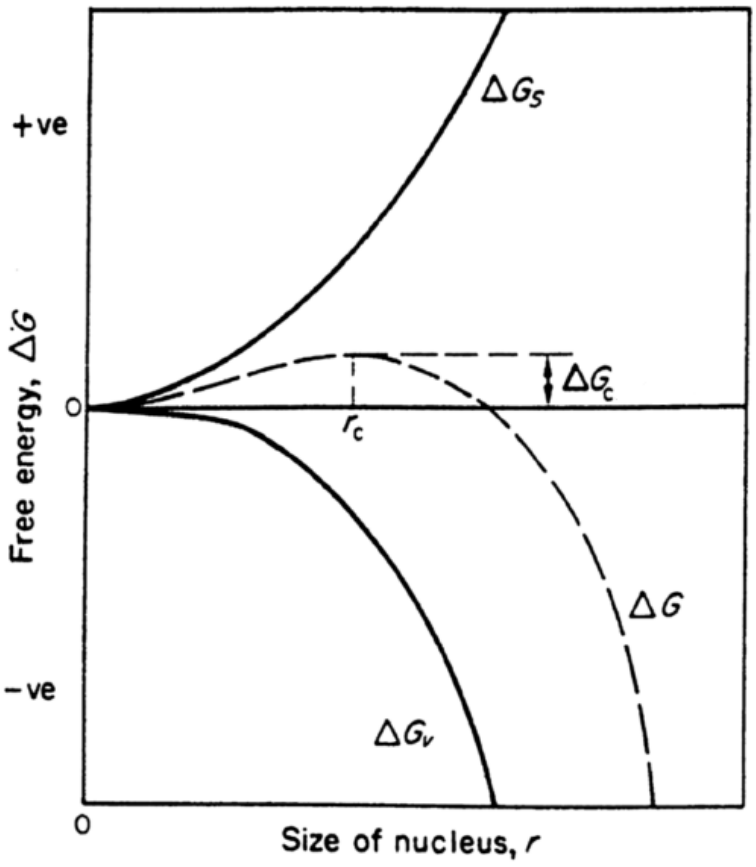

Figure 9. *The representation of overall free energy as a function of particle size (r) at the time of growth. Reproduced from ref. 56 with permission.*

When the concentration of monomers reached below the critical level, the nucleation stops and the nuclei grow by molecular addition until the equilibrium between the precipitated species is reached. The uniformity in size distribution happens with a process known as self-sharpening growth in which the smaller particle has higher tendency to grow than larger ones. It is due to the free energy driving force which is higher for smaller particles than larger particles. It is possible to get nearly monodisperse population if the reaction quickly stopped or supplying the reactant solution which keep the saturated condition. On the other hand, if the reactant concentration drops due to the particle growth then the Ostwald ripening or defocusing may occur. In this situation, the larger particles continue to grow whereas smaller particles get smaller in size and finally dissolve. The reason behind this is that the saturation ratio (S) decreases which lead to the increment in critical nuclei size, therefore, any particle smaller than this new r, get dissolves. If the reaction stops at this stage then the particles will have broad size distribution. Once the reaction goes in this stage, it is very difficult to get the monodisperse population unless the reaction is allowed for such a long time that nuclei are completely diminished. In that case, the size of the particles may be very large and can be extended to macron size. In addition to the growth by molecular addition, the particles may grow by aggregation with other particles and known as secondary growth. In the next section, the different mechanisms given for synthesis of NPs with various shapes are highlighted.

1.4 The mechanisms of particle shape control

Different mechanisms were given which involves in the control the shape of nanoparticles such as selective adsorption and growth, under potential deposition, oriented attachment, and self-assembly.

1.4.1 Selective adsorption and under potential deposition

According to Wulff's rule, growth rate of nanoparticles depend on the minimization of the surface free energy. Particles with higher surface energy grow faster to reduce surface area resulting in spherical nanoparticles, but, the shape of nanoparticles will be decided by their slow growth rate. Therefore, selective binding/adsorption of the surfactant/additives is the effective strategy to reduce the surface tension which results in the desirable shape of NPs. Basically, particles with ionic/coordination bonds/polar/hydrophobic facets form electronic charges which allows the adsorption of oppositely charged surfactant molecules. However, the adsorption also depends on the concentration and nature of surfactant.

The deposition of metal cations at various types of substrates such as metal and metal oxides with more positive potentials also leads to the shape modulation of nanoparticles during growth process. The change in the amount and type of cations promotes the preferential growth in one dimension and forms high index anisotropic nanoparticles.

1.4.2 Aggregation and agglomeration

Aggregation is a common and complex phenomenon of nanoparticles colloids which leads to undefined shape of nanoparticles. It occurs mainly due to high surface free energy of nanoparticles. The Brownian motion of particles and net inter-particle weak (van der Waal's force) attractive force are required for aggregation phenomenon to occur which can be avoided by coating with capping agent or change in the surface charge of nanoparticles.

Agglomeration is the formation of concrete body of aggregated NPs with addition of molecules onto the surface by chemical bonds such as hydrogen bonding which is much higher in strength than van der Waal's force. Agglomeration leads to the synthesis of usually micron size spherical shaped particles.

1.4.3 Coalescence and orientation attachment

As it is clear from the name itself, in the coalescence, the particles get attach together without any specific orientation whereas, orientation attachment is related to the spontaneous self-organization of adjacent particles at their high energy facets to minimize the surface energy.[57] These self-organized particles share common crystallographic planes. There are two intermediate steps involves in OA: (a) collision of aligned NPs in suspension, and (b) realignment of misaligned NPs until they find a perfect lattice match (Figure 10).[58]

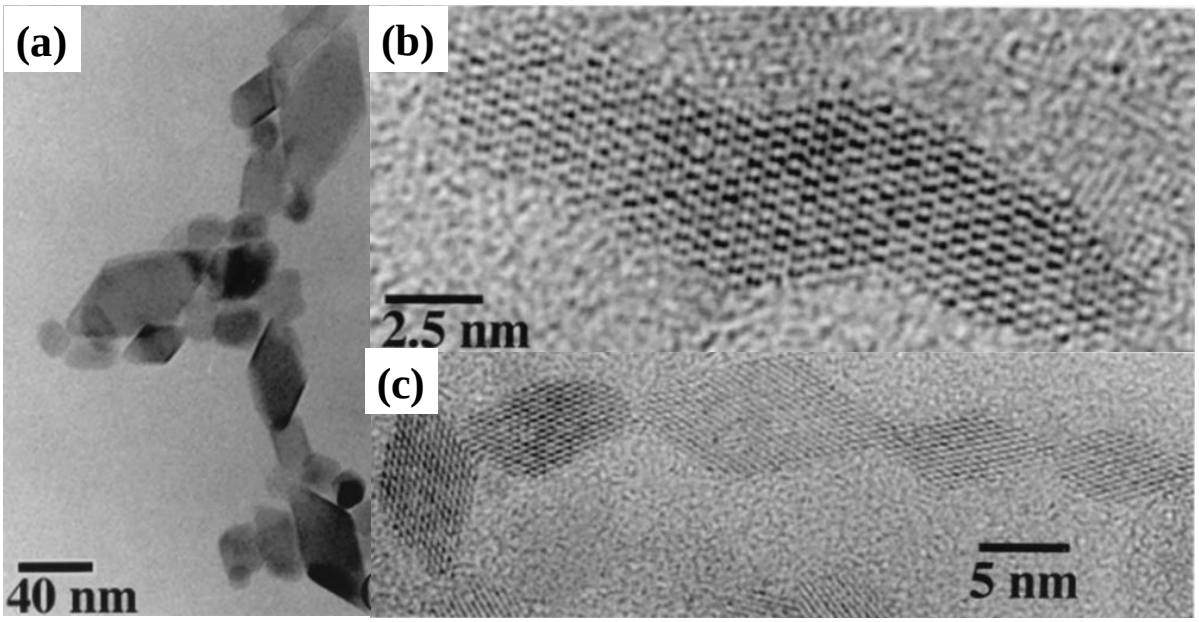

Figure 10. *The TEM images of titania grown by (a) coalescence, and (b, c) oriented attachment growth. Reproduced from ref. 58 with permission.*

1.4.4 Self-assembly

Self-assembly can be of two types: (a) static, and (b) dynamic. Static self-assembly is most common and generally occur in the case of atomic/ionic/molecular/colloidal crystal systems. This process may be with a global or local equilibrium and does not involve energy dissipation. The self-assembly process mainly involves either non-covalent or weak covalent interactions (electrostatic/van der Waal's/hydrophobic interaction/hydrogen bond/co-

ordination bond etc.). However, it also depends on many other factors. For example, in the case of self-assembly on 2D substrate, monodispersity, shape, and surface adsorption features of preformed NPs, type of substrates and reaction condition are also major determining factors. The major difference between the OA and self-assembly is that OA is an uncontrollable process which depends on reaction process and condition while self-assembly is a controllable process and depends on the ligands and bonds between particles.[57]

1.4.5 Ostwald ripening

Ostwald ripening is proposed by Ostwald in 1900 and also known as coarsening process. The local concentration of solute at the surface of larger particles is lower than the concentration of solute at the surface of smaller particles which leads to the flow of solute ions from smaller particles to larger ones. This process leads to the growth of large particles to larger ones at the expanse of smaller ones until the equilibrium state of bulk solution.[59] Therefore, this process is considered diffusion controlled, but generally produces quasi-spherical particles, which is considered as more thermodynamically stable morphology (Figure 11).[57]

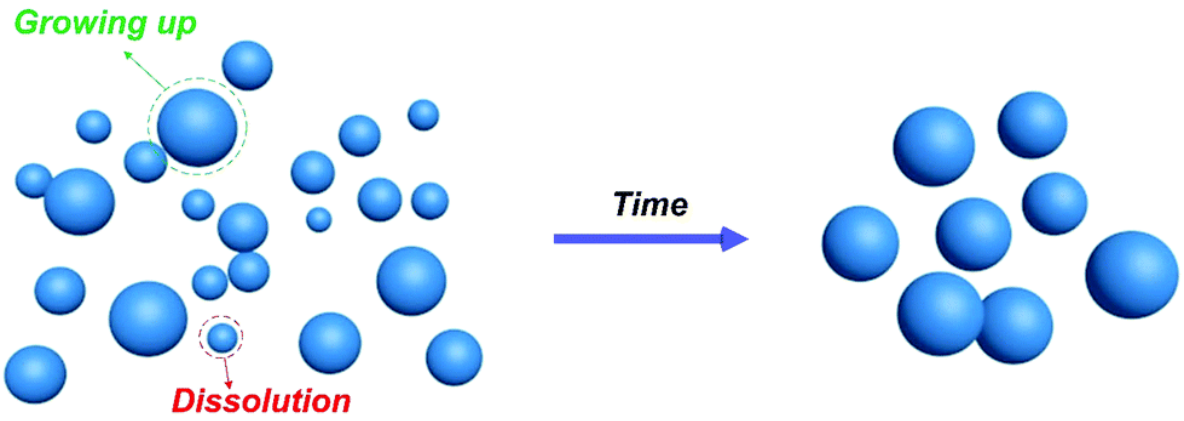

Figure 11. *Schematic representation of Ostwald ripening process. Reproduced from ref. 59 with permission.*

1.5 Conventional factors on shape control

1.5.1 Supersaturation

Supersaturation occurs in a solution when the dissolved precursor amount is higher than the solvent could able to dissolve in normal circumstances. In the case of high concentration of precursor monomers, the growth of generated nuclei mostly driven by kinetic control which leads to the synthesis anisotropic nanoparticles. Therefore, supersaturation strongly influences the nucleation and growth which, itself, can be altered by concentration of precursor monomers, coordination of solvent, chelation effect.[59]

1.5.2 The concentration of precursor monomers and additives

The ratio of concentration of precursor monomer and additives (such as reductant concentration) directly controls the depleting rate of precursor monomers for the formation of nanoparticles.[59] The high concentration of reductant leads to the rapid growth of seeds which produces a thermodynamically unstable structure while the low concentration of reductant favors the synthesis of thermodynamically stable structure.

1.5.3 pH effect

The pH of the reaction plays a very important role in the nucleation and growth. The change in pH of a reaction leads to the modulation of chemical species as well as the coordination bonding with ions, which, in-turn; changes the initial nucleation rate for shape control. The change in pH does not only affect the nucleation and growth processes but also affect the suspension stability of preformed nanoparticles.[59] The change in the pH of a preformed nanoparticle suspension, changes the surface properties of preformed NPs as well as the chemical state of surfactants which leads to the different adsorption mode and different adsorption amount on the surface of preformed NPs. As a result, selective growth or aggregation/agglomeration and self-assembly favor the shape evolution of NPs.[59]

1.5.4 Solvent

The functional groups present in different solvents provide different kind of interaction between the precursor molecules which results in the alteration of nucleation and growth process; as well as the final morphology of nanoparticles.[59] Therefore, the change in the proportion of different solvents in the reaction may leads to the shape control of nanoparticles. The selective adsorption of solvent molecules on the surface of preformed nanoparticles also involves in the mono-dispersity as well as the shape of NPs. For example, the minor change in the solvent structure of polyol process (ethylene glycol, diethylene glycol, triethylene glycol, tetraethylene glycol) leads to the synthesis of various shape of nanoparticles.[59]

1.5.5 Temperature

Temperature is a reaction parameter which controls the reaction rate thermodynamically. Increase in the reaction temperature leads to the energetic movement of molecules and ions in the reaction suspension which leads to the increase in the supersaturation rate as well as reduction rate of precursor monomers.[59] This results in the enhancement of nucleation and growth rate and the synthesis of quasi-spherical nanoparticles more preferably. Therefore, in order to synthesize the anisotropic nanoparticles, the reaction temperature should be properly monitored to modulate the nucleation and growth process under kinetic control, not in thermodynamic control.[59]

Increase in the temperature also affects the suspension of preformed NPs and leads to the aggregation/oriented attachment/ions diffusion/phase transition etc. due to minimize the free energy of the reaction system.

1.5.6 Seeds/template

Seeds/templates are usually used as an efficient mediator for shape control of nanoparticles because their surface provides an existed site for depleting monomers to grow further in the bulk solution.[59] This is mainly because the activation energy barrier for addition of precursor monomers on to the surface of seeds/templates is very low than the formation of new nuclei from the homogenous bulk solution. The main difference between the seed and template mediated growth of nanoparticles is that the various shapes of nanoparticles can be obtained in seed mediated growth while in the template mediated growth, there is more uniformity in the shape as well as the final shape of nanoparticles is highly dependent on the shape of template.

Furthermore, the size of the seeds should be very small because the final shape of nanoparticles is barely affected the already formed shape of seeds if the size of the initial seeds is over the critical size. Moreover, the seed amount, pH, temperature, concentration of precursor monomers, surfactants etc. are significant factors for final shape of nanoparticles.

1.5.7 Surfactant or additives

Nanoparticles have tendency to aggregate into larger particles with irregular and undesirable morphologies during growth in bulk solution to minimize their high free energy at the nanoscale. Therefore, surfactants/additives can adsorb on to some facets of the growing nanoparticles dynamically to reduce their surface energy and allow the controllable growth of specific facets for desirable morphology of nanoparticles. Like this, they also prevent the particles to aggregate in solution.[59] The surfactants/additives have functional/coordinating groups which act as capping/stabilizing agent to adsorb on to the surface of growing NPs. Thus the adsorption ability and stability of these functional groups (-OH, -SH, -NH_2, -R) should be well considered for selection of capping agent.

The common polymers which have been used are: polyvinyl pyrrolidone (PVP), polyacryl amide (PAA), PAH, polyethyleneimine (PEI), polyvinyl alcohol (PVA), polyethylene glycol (PEG) etc. and the small molecules: cetyl trimethyl ammonium bromide (CTAB), CTAC, trioctyl phosphine oxide (TOPO), octadecyl amine (ODA), trioctyl phosphine (TOP), sodium dodecyl sulphate (SDS), oleic acid, and oleylamine.[59] However, it is not limited to polymer/small molecules, halides ($Cl^-/Br^-/I^-$) are also commonly used controlling agents which selectively adsorb on to the specific facets of growing NPs and help in modulation of shape of nanoparticles. Besides the use of single capping agent, a mixture of different surfactants may be more useful in controlling the nucleation and growth of nanoparticles due to their synergistic interaction of multiple functional groups with different metal ions and different facets of nanoparticles.[59]

1.6 Properties

The properties of gold nanoparticles fascinated the scientists long back since Faraday's time. They show different properties according to their size from optical absorption to photoluminescence, nonlinear properties and ultrafast dynamics. Each of them is described as below:

1.6.1 Optical absorption

Gold nanospheres are known for their absorption ~520 nm due to localized surface plasmon resonance and can be understood well theoretically by classical electrodynamics such as Maxwell equations. However, when the particle size reduces further to ~2 nm, the absorption features ~520 nm get diminished. In this small size regime, these particles behave as molecular species and show strong quantum confinement which leads to discretization of energy states. The energy gap between the energy states depends on the number of metal

atoms in the clusters. However, the picture related to energy gap distribution and quantum confinement was not clear until the crystal structure was studied. The first crystal structure of $Au_{25}(SR)_{18}$ was reported in 2008, by Zhu et al. in which the correlation between the structure and optical properties was described. They have observed 3 different absorptions: a, c, and b which were found due to the HOMO to LUMO intra-band transition, HOMO – orbitals (d-band) to LUMO inter-band transition, and mixed type transition, respectively (Figure 12).[60]

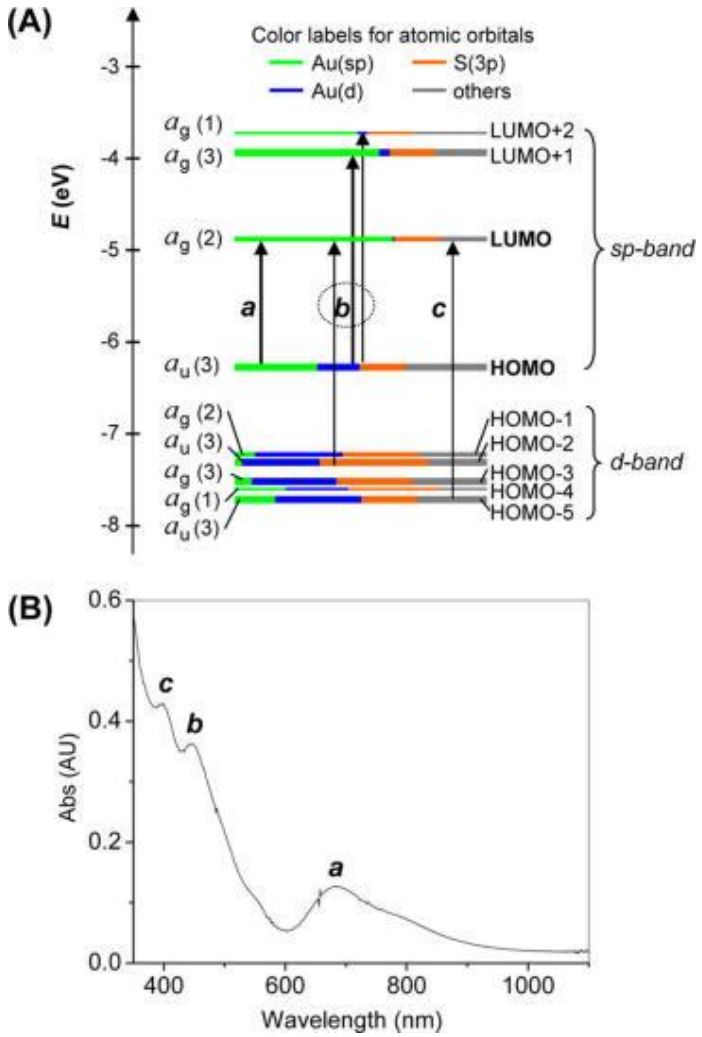

Figure 12. *(a) Kohn-Sham orbital level diagram for Au_{25} clusters. (b) Peak assignment of absorption spectrum of Au_{25} clusters. Reproduced from ref. 60 with permission.*

1.6.2 Photoluminescence

The broad range photoluminescence from visible to NIR in metal clusters make them very useful for various biological applications.[61–63] In the earlier studies, most of the thiol protected metal clusters were reported to give photoluminescence with very low quantum yield (QY) < 1%.[64,65] Recently, people have tried various ways to improve the photoluminescence such as: (a) capping with different ligands, (b) doping with other metal ions, and (c) exploiting other phenomenon such as aggregation induced emission.[66,67] Increase in the positivity of charge state of cluster or their oxidation shown to enhance the QY. Zhou et al. showed that doping with silver ions enhances the QY of gold clusters.[68] However, there are many issues related to the photoluminescence property of gold clusters which have to be addressed such as (i) the exact reason of luminescence in gold clusters (from core or surface states), (ii) how the luminescence can be further increased?, and (iii) how does the interaction between metal kernel and staple motifs affect the luminescence?

1.6.3 Non-linear optical properties

Recently, researchers started to explore the non-linear optical properties of clusters which mainly include the two photon absorption (TPA), two photon fluorescence (TPF), and second/third harmonic generation (SHG/THG), made them a promising candidate for high resolution multiphoton imaging, and optical limiting applications.[69–71] Ramakrishna et al. first time reported the TPA effect in $Au_{25}(SR)_{18}$ clusters in 2008. They have reported an emission around 830 nm upon excitation with 1290 nm and a cross section of 2700 GM. Moreover, the cross section of TPA increases with the cluster size from 1.1 to 4.0 nm, but the cross section per gold atom decreases dramatically (Figure 13).[72]

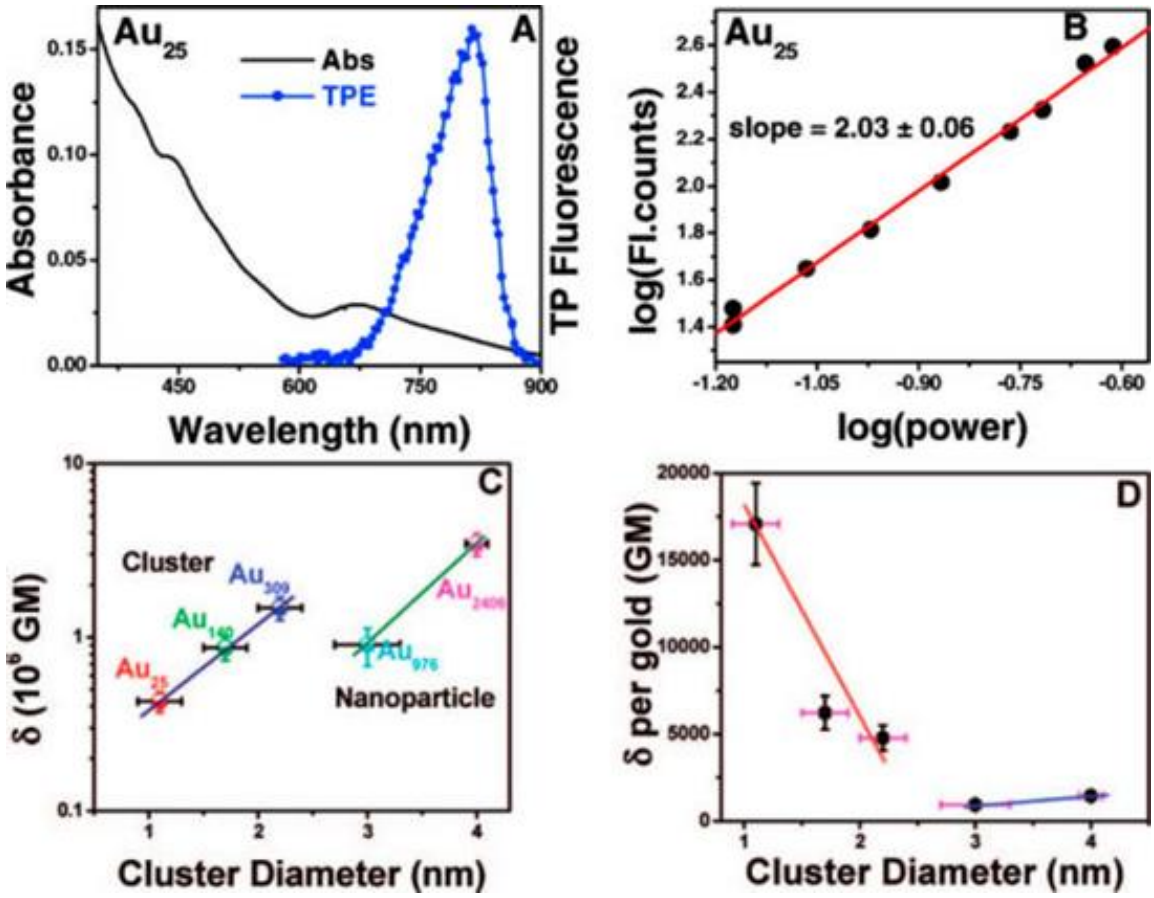

Figure 13. *(A) TPF from Au_{25}. (B) Power dependence suggests TPF. (C) TPA cross sections for different-sized gold clusters. (D) TPA cross section per gold atom as a function of cluster size. Reproduced from ref. 72 with permission.*

Knoppe et al reported the SHG and THG for Au_{25} and Au_{38} clusters, and observed that Au_{38} clusters show stronger SHG/THG in comparison to Au_{25}. The reason behind this observation was found to be the centro-symmetricity of Au_{25} clusters which leads to decrease in the SHG/THG properties.[73–75]

1.6.4 Ultrafast dynamics

The study of ultrafast electron dynamics which includes relaxation kinetics, electron-phonon coupling, and radiative emission, is of great importance to understand the atomic structure of

gold clusters as well as proper execution of their applications in various fields. The understanding of ultrafast electron dynamics can also be used to differentiate the molecular and metallic behavior to analyze their pump-power dependence because gold nanoparticles shows strong power-dependent electron-phonon coupling, whereas gold clusters exhibit laser power independent electron dynamics.[76,77] There were many reports appeared on the understanding of ultrafast electron dynamics of the atomically precise metal clusters using femtosecond time-resolved fluorescence up-conversion, transient absorption, and other techniques.[76,78–81] Devadas et al. studied the ultrafast fluorescence dynamics of gold clusters and observed that ultrafast fluorescence in visible region occurs from the metal core while the long lived luminescence in NIR region appears from surface staple states (Figure 14).[82]

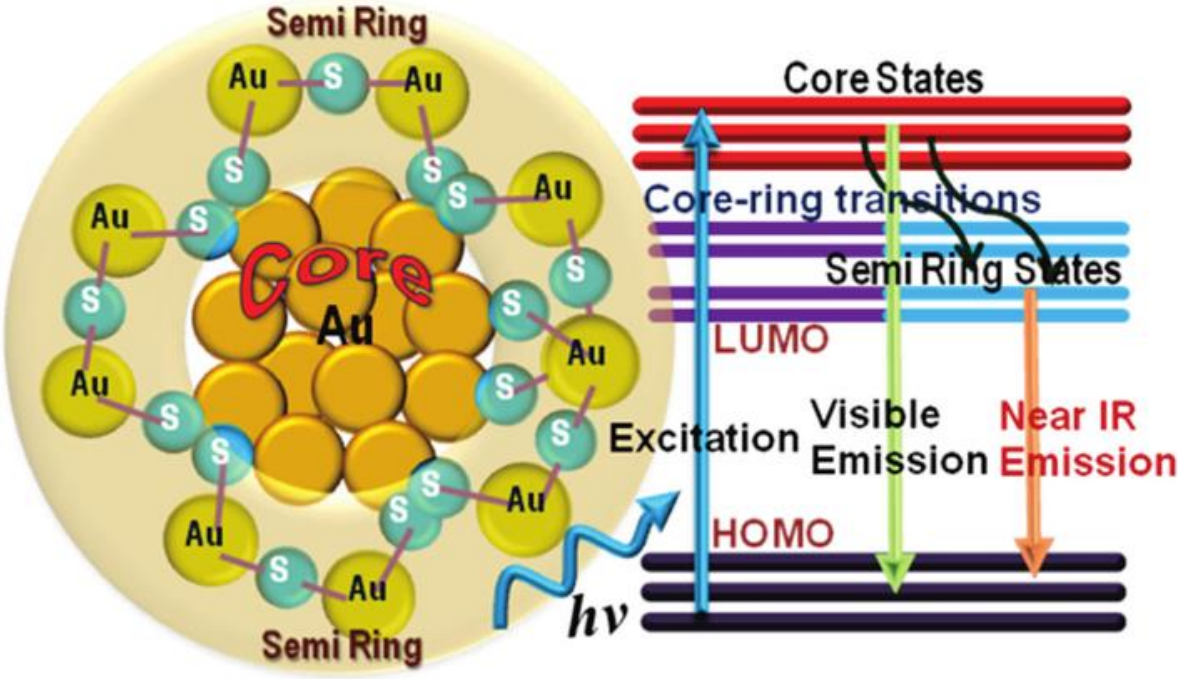

Figure 14. *Schematic showing the relaxation pathways in $Au_{25}L_{18}$ clusters showing the gold core states and semi-ring states. Reproduced from ref. 82 with permission.*

1.6.5 Catalytic properties

Gold is known to be chemically inert, therefore, not used for catalytic application for a long time. Later, the discovery of catalytic property of nano-gold leads to a huge excitement in the field of catalysis.[6,83,84] Atomically precise gold clusters $Au_x(SR)_y$, especially $Au_{25}(SR)_{18}$, have been heavily used to study their catalytic properties mainly due to their well-established synthesis methods and fully characterized formula and structure.[64,85,86] These gold thiolate clusters are used for several kinds of catalytic reactions including catalytic oxidation, hydrogenation, C-C coupling reactions, electron transfer catalysis, electro-catalysis, photo-catalysis, photo-electrochemical water splitting, and photovoltaics.[87–97]

1.6.6 Magnetic properties

Although the conduction band electrons exhibit weak paramagnetism (Pauli paramagnetism) but due to sum of conduction electron Landau diamagnetism and Au^+-core diamagnetism (exceeds Pauli paramagnetism), the bulk gold show overall diamagnetic character.[6] However, there are reports which show the ferromagnetic property of nanoscale gold at very low temperature, but the topic of magnetism in gold is still in debate.[98–101]

However, a significant amount of work done on $Au_{25}(SR)_{18}$ clusters demonstrate that these clusters show paramagnetic property only in neutral charged state.[102–104] Whereas anionic $Au_{25}(SR)_{18}^-$ clusters synthesized upon reduction of the neutral charged clusters, do not show paramagnetic property (Figure 15).[102] In another report by McCoy et al., the $Au_{102}(pMBA)_{44}$ cluster shows paramagnetic property after chemical oxidation and used for heating in an oscillating magnetic field component of a radio-frequency field.[105] The paramagnetic property of these clusters can be utilized in magnetic resonance imaging and other fields in near future.

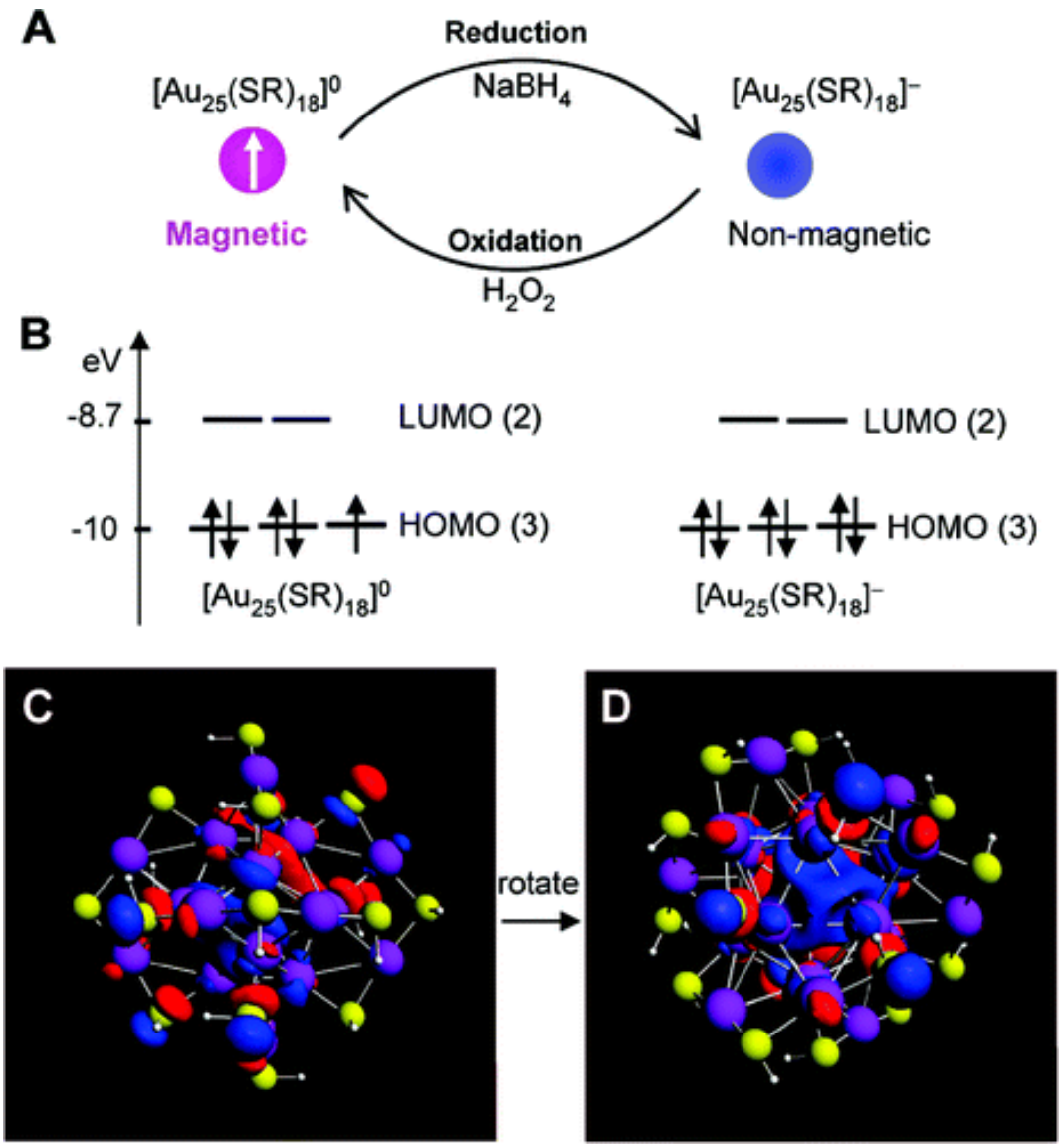

Figure 15. *(A) The reversible conversion between the neutral and anionic $Au_{25}(SR)_{18}$ clusters. (B) Kohn−Sham orbital energy-level diagrams for both of the clusters obtained from DFT calculations. (C−D) Kohn−Sham HOMO and its rotated view for $[Au_{25}(SH)_{18}]^0$. Color code: purple, Au; yellow, S; white, H. Reproduced from ref. 102 with permission.*

1.7 Synthesis of metal clusters

The metal cluster synthesis is a crucial and very sensitive process which is affected by many reaction parameters such as reactant's molar ratio, nature of reducing as well as capping agent, pH, and temperature of the reaction, stirring speed etc.[106–109] The selection of capping

agent may hugely change the photoluminescence of the synthesized metal clusters.[110,111] Sometimes, capping agent itself, acts as reducing agent as well.[112,113] There is a list of capping agents available used for the synthesis of highly fluorescent clusters including from protein molecules to peptides, amino acids, nucleic acid (DNA/RNA), polymers, thiolates, glycans etc.[107,108,110,114–129] Two well-known approaches: (a) top-down, and (b) bottom-up can be used to synthesize the metal clusters. Top-down approach involves the methods such as chemical etching of metal nanoparticles using organic molecules and polymers while bottom approach involves the methods such as chemical reduction, photo-reduction, and microwave.[130–136]

1.7.1 Chemical route synthesis

Initially, thiol containing ligands such as *n*-alkyl thiolates were most often used because of their well-known chemistry of the formation of Au-S bonds.[137–143] The separate reducing agents such as sodium borohydride ($NaBH_4$) were necessary for the synthesis of Au NCs. Later, alkyl thiols were replaced by glutathione (an anti-oxidant) to improve the stabilization of gold clusters in water, as alkyl thiolates are very poorly soluble in water. Glutathione is a tripeptide, consisting of the amino acids l-cysteine, l-glutamic acid and glycine, which have high aqueous solubility and the prepared gold clusters also found to have high aqueous dispersibility. But the photoluminescence quantum yield was very less for the clusters prepared by this route.[64,65,144,145] Later, it was observed that when GSH, itself, was used as reducing as well as capping agent, then, the quantum yield increased.[146]

In addition to thiol, polymers such as poly-amidoamines (PAMAM) dendrimers, polyethyleneimine (PEI), polyethylene glycol (PEG) were used to synthesize highly fluorescent metal clusters. Zheng et al. reported for the first time, the use of second and fourth generation OH-terminated PAMAM (G2-OH and G4-OH) dendrimers for the synthesis of

luminescent silver and gold clusters with high fluorescence quantum yield.[147,148] Later, the same group reported the different size of gold quantum clusters with wide range of fluorescence from UV to NIR, using the same approach.[149] In contrast, Lee et al. reported that the luminescence in these clusters may arise only from PAMAM dendrimers in absence of gold clusters.[150] Later, Tran et al. described the modified procedure in order to solve the debate and observed some specific spectral features specially in the case of gold clusters, which were absent for PAMAM dendrimers.[151] PAMAM dendrimers were also reported by Prof. Inouye group to synthesize the blue luminescent Pt clusters with ~ 18% quantum yield.[152] Qu et al. reported the PEI conjugated blue luminescent silver clusters.[153] Due to the cationic nature of PEI, these clusters were best suited in their use for the sensing of halide ions, metal ions, pH, temperature, organic molecules (folic acid, aspirin) etc.[123,154,155] Thiolated PEG, and block copolymers were also used to synthesize water dispersible highly fluorescent Au clusters.[156,157]

Peptides and proteins were used heavily for the synthesis of highly fluorescent water dispersible metal clusters. Because protein molecules are biocompatible in nature and often highly water-soluble, therefore they provide scaffolds for the nucleation and growth of metal clusters. The bovine serum albumin (BSA) was the first and most commonly used protein molecule for the synthesis of red luminescent gold clusters.[127,130,158–166] The synthesis reaction needed a high pH (> 10) and higher molar ratio of protein molecules to gold ions. Later, various protein molecules have been used for the successful synthesis of water dispersible highly luminescent metal clusters such as lysozyme, pepsin, trypsin, transferrin family proteins, urease, insulin, horse radish peroxidase (HRP), DNase I, ribonuclease A (RNase A) etc.[108–110,124,167–181] The reaction pH is a very crucial factor in the synthesis of Au cluster

which can change the size, reducing strength, fluorescence, capping capability etc. A very good example of the pH effect is the synthesis of gold clusters using pepsin protein molecules. According the pH, the size of the clusters were varied from Au_5 (Au_8), Au_{13}, Au_{25} at pH 9, pH 1, pH 12, with the fluorescence from blue to green and red, respectively.[109] The most interesting observation of protein stabilized metal clusters is that most of them retains their protein activity even after synthesis of cluster. For instance, HRP-Au NCs retains peroxidase activity while insulin stabilized gold clusters retains its activity of regulating the blood glucose.[181,182]

1.7.2 Microwave assisted synthesis

Microwave irradiation (MWI) is one of the most promising techniques for the preparation of nanomaterials since no high temperatures or high pressures are needed. The main advantage of MWI over conventional heating is rapid and uniform. Due to the difference between the dielectric constants of the solvent and the reactant, selective dielectric heating can provide significant enhancement in the transfer of energy directly to the reactants, which generally causes an instantaneous internal temperature rise. Therefore, both nucleation and growth can be controlled easily to produce nano-products with the desired shape or size.[130]

Chen et al. in 2010 reported for the first time the synthesis of lysozyme protected gold clusters and studied their antimicrobial property.[170] Subsequently, the synthesis of BSA and DHLA capped gold clusters were reported using microwave irradiation approach and found the reduced reaction time and increase quantum yield by approx. 5 folds.[131,183] Subsequently, Helmbrecht et al. performed the X–ray absorption studies on microwave assisted synthesized Au clusters to understand the structure–property relationships of these clusters.[132]

1.7.3 Photoreduction

Zhang et al. were first to report the synthesis of water-soluble fluorescent copper, silver and gold clusters using photoreduction in the presence of poly (methacrylic acid) functionalized with pentaerythritol tetrakis 3-mercaptopropionate.[184] This process didn't use any reducing agent therefore, it has reported to be clean, non-toxic and less time consuming. Later, the same group reported the effect of polymer structures on the fluorescence of gold clusters prepared by photoreduction. According to them, the polymers with higher electron-donating abilities and steric hindrance effect increase the fluorescence of gold clusters.[185]

1.7.4 Chemical etching

This approach was used to synthesize highly fluorescent metal clusters from metal nanoparticles using organic ligands (mostly thiol containing) which dissociate the large metal nanoparticles into smaller ones, usually, at high pH values >10. Whetten group reported for the first time, the controlled etching of gold nanoparticles with ~1.1 nm core, heated in neat dodecane-thiol solution under inert atmosphere, for the formation of smaller Au clusters.[186] Subsequently, numerous ligands from precursors, simple molecules to polymers were reported for the synthesis of gold clusters which mainly includes Au precursor ($HAuCl_4$), 11-mercaptoundecanoic acid (11-MUA), dopamine, glutathione (GSH), tris(2-carboxyethyl)phosphine (TCEP), hyperbranched polyethylenimine (*M*n = 1800 g/mol), biomolecules (amino acids, peptides, proteins, and DNA) etc.[187–195] In addition, hydroxyl radical induced etching was also reported for the first time to synthesize oligomeric Au^{I}-thiolate complexes from glutathione-capped gold nanoparticles.[196] This process was reported to be highly efficient and can be applied for the removal of gold from scrap electronics. A unique hetero-phase ligand exchange induced etching process was also reported to transform gold nanoparticles into organic-soluble fluorescent gold clusters.[197]

Cathcart et al. reported a novel etching approach of cyclic reduction in oxidative condition for the synthesis of silver clusters.[198] Likewise, synthesis of silver clusters (as well as gold clusters) was also reported by Prof. Pradeep's group by an interfacial etching reaction conducted at an aqueous/organic interface.[199,200] Prof. Xie's group also reported the synthesis of Ag clusters (as well as Au/Pt/Cu clusters) using electrostatically induced reversible phase transfer etching process.[201,202] Later, small molecule such as dihydrolipoic acid (DHLA) was used as etching agents for the synthesis of water dispersible silver clusters.[203] Similarly, synthesis of yellow emitting Pt clusters was also reported using glutathione mediated etching process of Pt nanoparticles.[204]

1.7.5 Hydrothermal method

The hydrothermal method is an environmental friendly process, provides uniform heating in solution which leads to the easy control of the size and morphology of the crystal just by temperature and time regulation. Liu et al. reported this new approach for the first time to synthesize fluorescent Ag-NCs in the presence of poly(methacrylic acid sodium salt) (PMAA).[205]

1.7.6 Sono-chemical method

Sono-chemical method is another approach reported to synthesize the fluorescent silver clusters.[206–208] During ultra-sonication, a localized hot spot with temperature ~5000 K and pressure of hundreds of bars can be generated which leads to the production of highly reactive species including $HO_2^{\bullet}$, $H^{\bullet}$, $OH^{\bullet}$ etc.[208]

1.8 Applications

The unique optical, electrical, and physiochemical properties of metal clusters made them interesting for application in various fields from sensing of heavy metal ions, inorganic

anions, small molecules, proteins, DNA, RNA to antibacterial, anticancer, biological imaging and labelling. In this section, we have summarized each of them.

1.8.1 Heavy metal ion sensing

Due to the high toxicity of heavy metal ions, their detection at nano-molar levels is highly essential in biological as well as environmental samples. Metal clusters are evolving as prominent candidates for the sensing applications due to their long-lived high luminescence. Xie et al. were probably the first to report the gold clusters based mercury ion sensor which was label-free, highly-sensitive (able to sense ~0.5 nM) and selective to the mercury ions in aqueous medium.[209] Subsequently, Lin et al. reported the ultrasensitive detection of mercury and methyl mercury (a highly toxic product of microbial biomethylation of mercury) at a level of 3 pM and 4 nM, respectively.[210] Later, series of reports published on the validation of using gold clusters for sensitive and selective sensing, and imaging of mercury ions in aqueous as well as real biological and environmental samples.[112,131,169,202,211–216] In parallel, silver and gold-silver bimetallic clusters were also reported for the highly sensitive and selective sensing of mercury ions in aqueous as well as environmental samples.[205,217–223] In addition to sensing of mercury ions, there are many other studies reported the sensing of other heavy toxic metal ions such as Fe^{3+}, Cd^{2+}, Pb^{2+}, Cu^{2+}, Cr^{3+}, Cr^{6+}, As^{3+}, Sn^{4+}, Ag^{+}, Al^{3+} etc.[113,130,133,163,212,224–233]

1.8.2 Inorganic anion sensing

In addition to heavy metal ions, it has become essential to detect the few very toxic anions at trace amounts in environmental samples. The highly toxic cyanide (CN^{-}) anion has become one of the most concerning anion which halts the cellular respiration by inhibiting the activity of cytochrome c oxidase in mitochondria. Liu et al. reported the gold cluster based fluorescence sensor for highly sensitive and selective detection of cyanide anions in real

aqueous environmental samples up to the concentration as low as 200 nM, which is approximately 14 times lower than the maximum level (2.7 μM) of cyanide permitted by WHO in drinking water.[234]

On the other hand, sulfide (S^{2-}) ions found to be widely distributed in natural as well as waste water and considered as an environmental monitoring agent. Therefore, it is necessary to detect the presence of sulfide ions at the maximum sensitivity as well as selectivity. Chen et al. made the DNA templated Au/Ag clusters for highly sensitive and selective sensing of sulfide ions up to the concentration of 0.83 nM in hot spring and seawater samples.[235] Subsequently, there were many other reports which further validated the use of gold and silver quantum clusters for sulfide ion sensing at nano-molar level.[206,236] In the similar way, other anions such as halides and phosphate ions were also detected at high sensitivity using silver clusters.[153,237]

Nitrite (NO_2^-) is another anion of high medicinal concern because of its huge adverse health effects, especially on infants and children. Nitrite ions heavily used as preservatives and fertilizing agents for food and therefore, widely distributed and enhance the chances of its contamination in our daily diet. Liu et al. reported the gold clusters based sensor for highly sensitive and selective sensing of nitrite ions.[238] Subsequently, Zhang et al. designed a Boolean NAND logic gate for the detection of nitrite ions based on fluorescent BSA conjugated gold clusters.[239] Afterwards, several reports were published on the sensing of nitrite ions including the chemiluminescence strategy to enhance the detection limit by gold clusters.[240–243]

1.8.3 Small biomolecules sensing

The design of small biomolecules (such as glucose, glutathione) detection system is of prime importance in order to enhance the sensitivity and reliability of the present systems for diagnosis. Glucose is one of the biomolecule of which, the detection and estimation at high sensitivity is very important, especially for diabetics. Hussain et al. reported the glucose sensing at high sensitivity and selectivity using L-cysteine functionalized gold clusters.[244] Later, people have also designed glucose sensors based on silver and copper clusters.[245–248] However, there is still a requirement to improve these sensors further in the terms of their validity in real biological samples. In order to address this problem, Wang et al. developed a ratio-metric fluorescent probe based on gold clusters and alizarin red-boronic acid, for monitoring glucose level in mice brain microdialysate.[249] Fluorescent gold clusters were also used to developed photoelectrochemical sensors for detection of glucose.[250]

Glutathione is a another important low molecular weight biomolecule which acts as an antioxidant to fight with oxidative stress as well as maintain the redox homeostasis in the cells. Therefore, the detection of glutathione at high sensitivity and selectivity, is considered as an essential factor in several diseases and therapy.[251] Tian et al. developed gold cluster based sensing probes for the sensing of glutathione in living cells with the detection limit as low as 7 nM.[252] Subsequently, Chen et al. designed the lysozyme functionalized gold cluster based sensor for the detection of glutathione in a single drop of blood with detection limit ~ 20 nM.[108] Likewise, there are other biomolecules such as folic acid, dopamine etc. which have to be essentially detected in trace amounts because the minute change in their amount may drastically affect the human health. Folic acid, one of the water soluble vitamin B, has a huge impact because of its involvement in fertility, heart disease, dementia, cancer, age related muscular degeneration, malaria etc. It is also essential for DNA and hemoglobin

biosynthesis. The lack of folic acid in pregnant women may increase the chances of neural tube defects. Considering all these facts, it is important to detect the trace amount of folic acid very precisely. Zhang et al. developed the polyethylenimine capped silver clusters for the detection of folic acid up to the concentration of 0.1 nM and validated the test in the real samples.[123] Gold clusters were also explored for the sensing of folic acid in order to generalize the use of metal clusters for the detection of folic acid.[253,254]

Dopamine is a very important neurotransmitter which plays a vital role in the functioning of cardiovascular system, nervous system, and renal systems. The deficiency of dopamine may lead to several neurodegenerative disorders such as Alzheimer's, Parkinson's, schizophrenia etc. that makes essential to detect it at very small concentrations with high precision. Li et al. reported the electro-generated chemiluminescence of gold clusters for the detection of dopamine.[255] Further, Tao et al. designed the fluorescence as well as colorimetric based sensor using gold clusters which can detect the dopamine at the concentration as low as 10 nM and validated the test in cellular samples as well.[256] Afterwards, in order to validate, many groups worked on the use of gold as well as silver clusters for the sensing of dopamine in real samples in the presence of other molecules.[207,257–259]

Similarly, urea is a byproduct of protein metabolism and can be a marker for evaluating the toxins and function of kidney and liver which makes the detection of urea highly important. Nair et al. developed the urease conjugated gold cluster based sensor for the selective detection of urea.[175] Likewise, bilirubin is a yellow compound and a product in intermediate step of catabolic pathway for heme degradation. The altered level of bilirubin may induce the chances of jaundice which generates the necessity to detect the bilirubin concentration very precisely in blood serum. Santosh et al. developed the human serum

albumin functionalized gold clusters based fluorometric as well as colorimetric sensing probe for the detection of free bilirubin in blood serum.[260] Cholesterol is also of biological interest due to its importance for nerve and brain cells. Its excess concentration may lead to the atherosclerosis and low concentration associated with the hypocholesterolemia. Gold clusters based sensor was developed by chang et al., able to detect the cholesterol very precisely with a detection limit of 1.4 μM.[261]

1.8.4 Nucleotide and nucleic acid sensing

Guanosine 5′-triphosphate (GTP) is a nucleotide anion which plays an important role in several biological processes such as RNA and protein synthesis. However, there are very few reports published on the sensing of GTP and involve complicated synthesis and separation step. Zhao et al. developed the copper clusters based sensors for highly sensitive and selective detection of GTP.[262] Moreover, detection of DNA is also very important due to their application in wide range of fields such as molecular diagnosis, pathogenics, genetics, anti-bioterrorism etc. Lan et al. reported the oligonucleotide (5′-CCAGATACTCACCGG-3′) stabilized silver clusters as sensing probe for a gene of fumarylacetoacetate hydrolase (FAH) with a limit of detection of 14 nM.[263] Wang et al. also reported the oligonucleotide (5′-AAAAATGGGGCAAATA-3′) functionalized silver clusters combined with MWCNTs for the detection of genes for respiratory syncytial virus (RSV) with a detection limit of 24 nM. The MWCNTs were used to enhance the signal to noise ratio due to their fluorescence quenching ability.[264] Further, super-sandwich model was proposed in order to enhance the sensitivity and selectivity of DNA functionalized silver clusters for target DNA detection.[265] Moreover, Enkin et al. and others reported the parallel multiplexed analysis of two genes (such as the Werner Syndrome gene and the HIV, human immunodeficiency virus gene) by

implementing two different-sized silver clusters-modified sensing modules.[266–268] Gold clusters were also reported as an alternate approach for the ratio-metric fluorescent sensing of nucleic acids.[269] Further, Guo et al. extended the application of DNA conjugated silver clusters to identify the single nucleotide mutation in the case of sickle cell anemia and validated the approach by identifying more general types of single-nucleotide mismatches.[270]

MicroRNAs (miRNA) play key roles in several biological regulatory processes mainly involves developmental and metabolic processes. Therefore, the miRNA levels can be used as a marker for several cellular processes and disease diagnosis. Thus, there is a need to develop sensing mechanism which should detect very small amount of miRNA with the high precision. Yang et al. developed DNA conjugated silver clusters based sensors for the detection miRNA.[271] In order to highly enhance the detection limit, Liu et al. developed a new approach namely target-assisted isothermal exponential amplification (TAIEA) coupled with fluorescent DNA-scaffolded silver clusters which enhanced the sensitivity of detection to two atto-molar.[272] Subsequently, TAIEA approach was also coupled with multiplexing to detect the presence of multiple miRNAs.[273] Later, another approach based on electrochemical property was used simultaneously with two amplification strategies namely target-assisted polymerization nicking reaction (TAPNR) and hybridization chain reaction (HCR) in order to achieve sub-femtomolar detection of miRNA-199a.[274]

1.8.5 Amino acid, peptide, proteins determination

Amino acids play a vital role in many cellular processes and critical bioactivities which makes the necessary technical basis for the identification of them at high sensitivity. Wang et al. reported the BSA-capped gold clusters based ratio metric fluorescence sensing probe for the identification of amino acids.[275] Later, integrated logic gate approach was used based on

bimetallic (Au/Ag) clusters for the sensing of histidine and cysteine.[276] Gold clusters in conjugation with CdTe QDs were also explored for the sensing of L-cysteine amino acid with a limit of detection 192 nM.[277]

Proteins are one of the most important classes of bio-macromolecules which play several key roles in many cellular processes. Therefore, the precise detection of their concentration is of prime importance for several body tests, and diagnosis. Glutathione-S-transferase (GST) is a kind of protein used for tagging by recombinant proteins for their easy purification. Therefore, gold clusters based sensing probes developed for the detection of GST from cell lysates with maximum achieved limit of detection about 1.5 nM.[278,279] Likewise, metal cluster based sensing probes were developed for detection of several proteins and their activity including insulin, human α-thrombin, esterase, alkaline phosphatase, hypoxia-inducible factors, phospholipase C, acetyl-cholinesterase, lysozyme, trypsin, inorganic pyro-phosphatase etc.[68,176,280–287]

1.8.6 Bacterial cells detection

The detection of bacterial cells is of high importance due to their involvement in various diseases and industrial production of many molecules. Metal clusters are found to be very helpful in this perspective also.[288] Chan et al. designed mannose-capped gold clusters based sensing probes for uropathogenic *E. coli* with the limit of detection as low as ~2 X 10^6 cells/mL.[129] The same group also developed the lysozyme conjugated gold clusters based affinity mass spectrometry for distinguishing various pathogenic bacterial cells.[289] Liu et al also developed the lysozyme conjugated gold clusters based fluorescence enhancement sensor for the detection of *E. coli* with high sensitivity (LOD ~2 X 10^4 CFU/mL).[290]

1.8.7 Cancer cell detection

The highly specific and sensitive detection of cancer cells is of great importance for the early stage detection of cancer for effective diagnosis as well as for the detection of cancer metastasis. Yin et al. developed a label-free and "turn-on" fluorescence aptamer strategy for cancer cells detection based on the strategy of aptamer recognition-induced hybridization and fluorescence enhancement effect of DNA-Ag clusters in proximity of guanine-rich DNA sequences (Figure 16).[291]

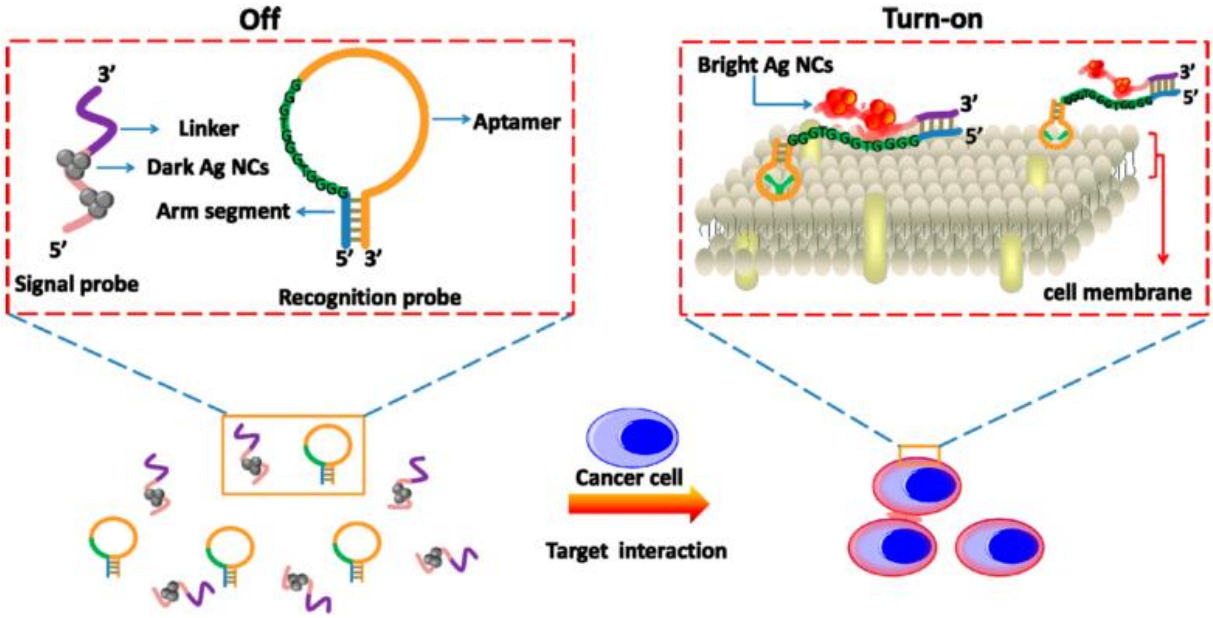

Figure 16. *Schematic representation of the label-free and turn-on aptamer strategy for cancer cell detection based on DNA-silver cluster fluorescence upon recognition-induced hybridization. Reproduced from ref. 291 with permission.*

1.8.8 Biological imaging and therapeutic applications

Metal clusters have emerged out to be highly potential candidate for biological imaging and therapeutic applications due to their low cytotoxicity, small size, easy functionalization, high aqueous dispersibility and stability, high fluorescence quantum yield, large stokes shift, wide range of luminescence, photostability etc.[111,292] Among metal clusters, gold and silver clusters

were highly explored for biological imaging and diagnosis.[63,121,293–309] However, the initial work was done for *in vitro* cellular imaging. Dickson's group in 2007 reported the *in vitro* intracellular synthesis of peptide conjugated silver clusters and simultaneously imaging of these cells.[310] Later, they have developed DNA encapsulated silver clusters for live cell surface labelling.[311]

Lin et al. developed the nuclear localizing peptide conjugated blue luminescent gold clusters for nucleus targeting and intracellular imaging.[312] Further, Wu et al. explored the possibility of using NIR emitting gold clusters for tumor imaging *in vivo.* They have reported that the reason behind the high accumulation of gold clusters at tumor site was due to enhanced permeability and retention (EPR) effects.[313] Wang et al. observed that dihydrolipoic acid conjugated gold clusters were highly biocompatible and used as marker for *in vitro* and *in vivo* tracking of endothelial cells.[314] Simultaneously, red, green, and blue light emitting gold clusters were also developed for anticancer gene theranostics.[315] Inouye group reported the PAMAM dendrimer encapsulated blue and green luminescent platinum clusters for cellular imaging.[115,152] The blue luminescent copper clusters were also reported for their use as specific cell imaging probe.[316]

Shang et al. and others reported the fluorescence life time imaging (FLIM) application of DHLA capped and PEGylated gold clusters due to their long life time (> 100 ns), which is longer than the auto-fluorescence from live cells.[317,318] The mechanistic aspects of fluorescent gold cluster internalization by live HeLa cells were also studied and it was found that uptake of gold clusters is energy-dependent and involves clathrin-mediated endocytosis and micropinocytosis pathways.[319] Later, Wang et al. used both, fluorescent correlation spectroscopy (FCS) and FLIM to track the dynamics of Herceptin^{TM} conjugated gold clusters.

This approach is able to probe at single particle sensitivity to reveal the diffusion and entry into the nucleus in live cell conditions in order to enhance the $HER2^+$ breast cancer therapy.[320] Two photon fluorescence imaging property was also reported in the case of gold clusters, facilitating deep tissue penetration while minimizing background fluorescence and scattering issues.[156,321]

In a study by Chen et al., the BSA conjugated gold clusters were functionalized with methionine (tumor targeting ability) and MPA (NIR emitting dye). Also, the doxorubicin anticancer drug was further conjugated with methionine to synthesize multifunctional gold clusters. Results suggested that gold clusters were able to show the tumor therapy and imaging *in vivo*.[61] *In situ* bio-synthesized gold, silver and platinum clusters were also reported for their application in the selective tumor theranostics. These clusters can be synthesized only by cancerous cells, not by normal cells.[188,322–325]

Gold clusters were also used for 'fluorescence imaging guided' photodynamic therapy for the treatment of cancer. For this purpose, usually gold clusters attached with photosensitizers such as chlorin e6 (Ce6) and protoporphyrin IX.[326,327] However, Vankayala et al. reported that in absence of photosensitizers also, gold clusters were able to sensitize formation of singlet oxygen ($^1O_2$) for the destruction of cancer cells upon NIR light photoexcitation.[62]

Gold clusters, which can rapidly excrete from the body, are in high demand for *in vivo* theranostics applications.[328] Glutathione-capped gold clusters were found to show a much longer tumor retention time, faster normal tissue clearance, and efficient renal clearance property than other capping agents such as BSA-functionalized gold clusters (Figure 17).[329,330] These gold clusters can also act as effective radio-sensitizer and leads to the strong

enhancement of radiotherapy. These gold clusters show ultrahigh tumor uptake, targeting specificity via enhanced ERR effect, and efficient renal clearance which made them ideal radiotherapy sensitizers.[331–333]

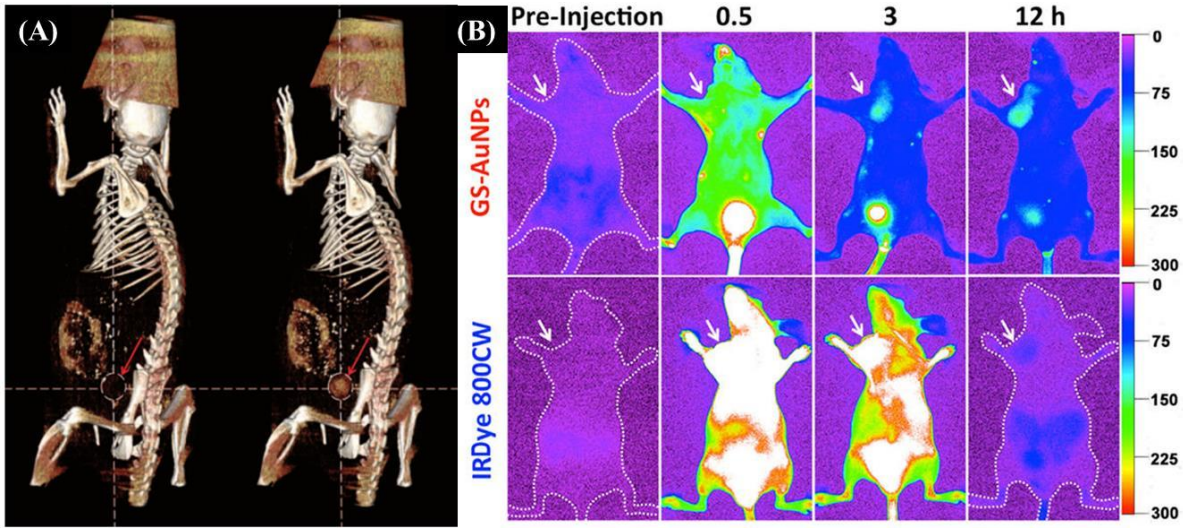

Figure 17. *(A) CT images of a live mouse (left) before and (right) 30 min after IV injection of glutathione-capped gold clusters. Reproduced from ref. 329 with permission. (B) Representative in vivo NIR fluorescence images of MCF-7 tumor-bearing mice iv-injected with GS-Au-NPs and IRDye 800CW collected 0.5, 3, and 12 h p.i. The tumor areas are indicated with arrows. Reproduced from ref. 333 with permission.*

Metal clusters were also used in combination with other nanomaterials or heavy metal ions to impart various properties in single system. Wang et al. reported the GO conjugated transferrin protein functionalized gold clusters in order to image cancer cells and small animals, where GO shows super fluorescence quenching property which leads to negligible background fluorescence.[172] In order to provide dual imaging (fluorescence/magnetic resonance) property, the gold clusters were functionalized with Gd^{3+} ions and magnetic iron oxide nanoparticles.[334,335] Fluorescence imaging coupled with CT imaging was also reported in the case of gold clusters conjugated with either mesoporous silica nanoparticles or calcium

phosphate nanoparticles.[336–338] Gold clusters doped with ^{64}Cu was used as dual imaging probe (positron emission tomography/computed tomography) for breast cancer and metastasis.[339,340]

1.8.9 Antibacterial applications

Due to the emergence of antibiotic resistance worldwide, the need for development of new therapeutics has come into the demand. The advancement in the understanding leads to the development of metal clusters based therapeutics for antibacterial applications which mainly includes the surface functionalization with antimicrobial peptides and proteins, DNA, polymers, antibiotics, high silver content etc. Chen et al. developed the lysozyme functionalized gold clusters which shown potent antibacterial activity especially against antibiotic resistant strains including pan-drug-resistant *Acinetobacter baumannii* and vancomycin-resistant *Enterococcus faecalis*.[170] Silver clusters protected with several ligands including glutathione, dihydro-lipoic acid, thiol-terminated phosphorylcholine, PEI, and DNA protected silver clusters were also proven to be good antibacterial agents probably due to their high content of silver ions.[341–348] Antibiotics protected gold as well as silver clusters also reported to show the enhanced antibacterial property.[112,349] Recently, photodynamic inactivation approach was also reported using BSA-PS protected Au clusters in order to inactivate methicillin-sensitive and methicillin-resistant *Staphylococcus aureus*.[350]

1.8.10 Metal cluster based thermometers and pH meters

Nanoscale thermometers find huge applications in various fields starting from nanoelectronics, nanophotonics, and nano-biomedicines based on their capability to sense the changes in the temperature at submicron scale. The temperature sensing probe was designed based on the change in the fluorescence of copper clusters as the temperature of the surrounding environment changes.[351,352] The same sensing strategy was also reported in the

case of gold clusters.[305] Similarly, pH of the system plays very crucial role especially in the case of many biological processes such as ATP synthesis which is truly a proton gradient dependent phenomenon. Therefore, nanomaterials with pH sensitive optical properties become highly important. For this purpose, gold, silver and copper clusters were reported to show the pH-sensitive fluorescence properties.[154,158,353,354]

1.9 About the present understanding

1.9.1 What is known?

After a scientific research of more than 150 years on gold colloids, there are numerous methods developed to control the size and shape of nanoparticles with a high precision. With the help of modern instruments, a very good understanding has developed about the nucleation and growth mechanisms; and structure of nanoparticles. Also, a very good knowledge about the surface functionalization by various ligands and their modification has been developed which leads to the development of huge applications of gold nanomaterials in diverse fields from nano-electronics to nano-medicines.

1.9.2 What is not known?

Although the chemistry of gold colloids has been studied since 150 years ago but still there are some questions remaining which have to be answered such as:

(a) The understanding about the interface between the inorganic core and the organic ligands: There is still poor understanding about the binding of organic ligands on the surface of inorganic particles. The high end TEM instruments cannot able to visualize the organic ligands on the nanoparticles surface. Also, it is assumed that the top 1-2 layers of nanoparticles surface shows amorphous nature which makes it difficult to visualize very precisely by TEM. Scanning tunneling microscopy provides better alternate to perform the

atomic scale imaging but again it suffered by imaging of only the top layer of capping agents, not the underneath inorganic layer. There are some other techniques such as IR and NMR, but all those have their own pros and cons.

(b) About the structure of nanoparticles: It is still not known exactly that at what size, the structure of gold nanoparticle will freeze to FCC structure. It is very well studied that for clusters which are made up of few atoms to few tens of atoms, the structure change drastically from tetrahedral to icosahedral, bi-icosahedral, decahedral and then FCC.

(c) It is unclear that with the same size of nuclei, how the different shapes of anisotropic nanoparticles form. Why is the shape of nanoparticles affected by different ligands and ions, not their core FCC structure. It is also not very clear that why particular ligand get adsorb to particular facets (e.g., {111} or {110}) of the nanoparticles, not to any other facets. Whether the particle stabilized by ligand or the ions or both and if both, then how much percentage contribution will be there and how they contribute to the stability. These all the questions are still unclear and there is a need to get better, in-depth understanding about these issues.

1.10 Thesis outline

Metal nanoparticles and quantum clusters are of prime interest due to their wide applications including sensing of heavy metal ions, anions, biomolecules, proteins, DNA, miRNA, and enzyme activity to catalysis, diagnosis and therapy. These huge applications of metal nanoparticle and quantum clusters would have been possible due to their various electronic and optical properties including optical absorption, conductivity, luminescence, non-linear optical properties (two photon absorption, two photon fluorescence, and second/third harmonic generation), and ultrafast dynamics (relaxation kinetics, electron-phonon coupling, and radiative emission). Not only due to the applications, they are also important due to a

long history, and model systems for studying the nucleation and growth process for nanoparticles synthesis.

Chapter 2 addressed the synthesis of antibiotic capped gold nanoparticles and gold quantum clusters for antibacterial properties, sensing of mercury ions and their imaging in bacterial cells. We have used antibiotic (cefradine) molecules itself, as reducing as well as capping agent. The effect of precursor molar ratio ($HAuCl_4$/cefradine), temperature, and pH of the reaction were also studied on the nucleation and growth of nanoparticles. Surprisingly, at pH 6, we have observed higher fraction of small particles (< 2 nm) population which we have isolated by centrifugation. The as-obtained supernatant contains Au_8 clusters, validated from MALDI analysis, shows strong blue luminescence. The blue luminescent Au clusters were applied for mercury ion sensing as well as their imaging in bacterial cells. These antibiotic protected gold nanoparticles and clusters were also used as an antibacterial agent.

In **chapter 3**, we have synthesized curcumin-capped Au-QCs, where curcumin itself, act as reducing as well as capping agent. Curcumin is very well known therapeutically important molecule and has potential application in various diseases. But, the water insolubility of curcumin, which leads to the poor bioavailability, poor oral absorption, rapid metabolism and rapid excretion, hindered its biological applications. Therefore, curcumin was allowed to conjugate with gold clusters *in situ* to enhance its water dispersibility. Later, the curcumin-conjugated gold clusters were studied for their anticancer property and shown enhanced anticancer activity and low cytotoxicity than curcumin and GSH-conjugated gold clusters alone.

Chapter 4 described the synthesis of curcumin-conjugated silver clusters to visualize their interaction with human Tau protein. Tau protein fibrillation was found to be major

reason for Alzheimer's disease. Curcumin is known to show the potential anti-Alzheimer's applications, therefore, we have used curcumin-conjugated silver clusters for inhibition of Tau fibrillation. Silver nanoparticles are well known to cross the blood brain barrier (BBB), which can access to the Tau proteins present in the brain and can inhibit the Tau fibrillation. Results show that curcumin-conjugated silver clusters were able to efficiently inhibit the Tau fibrillation process than curcumin-conjugated silver nanoparticles, GSH-conjugated silver clusters and curcumin alone.

Finally, **chapter 5** described the conclusion of the overall work presented in this thesis. The future direction of this thesis also presented in this chapter.

1.11 References

1 Dilipkumar Pal, C. K. Sahu, A. Haldar, D. Pal, C. K. Sahu and A. Haldar, *J. Adv. Pharm. Technol. Res.*, 2014, **5**, 4–12.

2 D. H. Brown and W. E. Smith, *Chem. Soc. Rev.*, 1980, **9**, 217.

3 E. A. Hawser, *J. Chem. Educ.*, 1952, **29**, 456–458.

4 M. C. M. Daniel and D. Astruc, *Chem. Rev.*, 2004, **104**, 293–346.

5 M. Faraday, *Philos. Trans. R. Soc. London*, 1857, **147**, 145–181.

6 R. Jin, C. Zeng, M. Zhou and Y. Chen, *Chem. Rev.*, 2016, **116**, 10346–10413.

7 T. Graham, *Philos. Trans. R. Soc. London*, 1861, **151**, 183–224.

8 R. Zsigmondy, *Nobelprize.org. Nobel Media AB 2014*, 1926, **1**, Nobelprize.org. Nobel Media AB 2014.

9 A. L. Patterson, *Phys. Rev.*, 1939, **56**, 978–982.

10 US1648369 A, 1927, 1,648,369.

11 J. Turkevich and J. Hillier, *Anal. Chem.*, 1949, **21**, 475–485.

12 J. Turkevich, P. C. Stevenson and J. Hillier, *Discuss. Faraday Soc.*, 1951, **11**, 55.

13 J. Turkevich, P. C. Stevenson and J. Hillier, *J. Phys. Chem.*, 1953, **57**, 670–673.

14 J. Turkevich, G. Garton and P. . Stevenson, *J. Colloid Sci.*, 1954, **9**, 26–35.

15 Y. Chiang and J. Turkevich, *J. Colloid Sci.*, 1963, **18**, 772–783.

16 L. Malatesta, L. Naldini, G. Simonetta and F. Cariati, *Chem. Commun. (London)*, 1965, **1**, 212–213.

17 F. Cariati, L. Naldini, G. Simonetta and L. Malatesta, *Inorganica Chim. Acta*, 1967, **1**, 315–318.

18 P. Hohenberg and W. Kohn, *Phys. Rev.*, 1964, **136**, B864–B871.

19 W. Kohn and L. J. Sham, *Phys. Rev.*, 1965, **140**, A1133–A1138.

20 E. J. Robbins, R. E. Leckenby and P. Willis, *Adv. Phys.*, 1967, **16**, 739–744.

21 M. McPartlin, R. Mason and L. Malatesta, *J. Chem. Soc. D*, 1969, 334–334.

22 R. C. Elder, F. A. Cotton and R. A. Schunn, *J. Am. Chem. Soc.*, 1967, **89**, 3645–3646.

23 L. E. McCandlish, E. C. Bissell, D. Coucouvanis, J. P. Fackler and K. Knox, *J. Am. Chem. Soc.*, 1968, **90**, 7357–7359.

24 C. H. Wei and L. F. Dahl, *J. Am. Chem. Soc.*, 1968, **90**, 3960–3969.

25 C. O. Quicksall and T. G. Spiro, *Inorg. Chem.*, 1968, **7**, 2365–2369.

26 N. S. Voronovich and D. V. Korol'kov, *J. Struct. Chem.*, 1971, **12**, 458–464.

27 J. G. Converse and R. E. McCarley, *Inorg. Chem.*, 1970, **9**, 1361–1366.

28 V. G. Albano and P. L. Bellon, *J. Organomet. Chem.*, 1969, **19**, 405–415.

29 R. G. Vranka, L. F. Dahl, P. Chini and J. Chatt, *J. Am. Chem. Soc.*, 1969, **91**, 1574–1576.

30 F. Cariati and L. Naldini, *Inorganica Chim. Acta*, 1971, **5**, 172–174.

31 P. L. Bellon, F. Cariati, M. Manassero, L. Naldini and M. Sansoni, *J. Chem. Soc. D Chem. Commun.*, 1971, 1423.

32 P. L. Bellon, M. Manassero, L. Naldini and M. Sansoni, *J. Chem. Soc. Chem. Commun.*, 1972, 1035.

33 M. Manassero, L. Naldini and M. Sansoni, *J. Chem. Soc. Chem. Commun.*, 1979, 385.

34 O. Echt, K. Sattler and E. Recknagel, *Phys. Rev. Lett.*, 1981, **47**, 1121–1124.

35 P. W. Stephens and J. G. King, *Phys. Rev. Lett.*, 1983, **51**, 1538–1541.

36 A. Ding and J. Hesslich, *Chem. Phys. Lett.*, 1983, **94**, 54–57.

37 M. CINI, *J. Catal.*, 1975, **37**, 187–190.

38 R. Car and J. L. Martins, *Surf. Sci.*, 1981, **106**, 280–286.

39 J. L. Martins, R. Car and J. Buttet, *Surf. Sci.*, 1981, **106**, 265–271.

40 N. W. Ashcroft and D. M. Wood, *Phys. Rev. B*, 1982, **25**, 6255–6274.

41 W. D. Knight, K. Clemenger, W. A. de Heer, W. A. Saunders, M. Y. Chou and M. L. Cohen, *Phys. Rev. Lett.*, 1984, **52**, 2141–2143.

42 W. D. Knight, K. Clemenger, W. A. de Heer and W. A. Saunders, *Phys. Rev. B*, 1985, **31**, 2539–2540.

43 D. E. Beck, *Solid State Commun.*, 1984, **49**, 381–385.

44 W. Ekardt, *Berichte der Bunsengesellschaft für Phys. Chemie*, 1984, **88**, 289–291.

45 W. Ekardt, *Phys. Rev. Lett.*, 1984, **52**, 1925–1928.

46 W. Ekardt, *Phys. Rev. B*, 1984, **29**, 1558–1564.

47 W. Ekardt, *Solid State Commun.*, 1985, **54**, 83–86.

48 S. Eustis and M. A. el-Sayed, *Chem. Soc. Rev.*, 2006, **35**, 209–217.

49 J. Zheng, P. R. Nicovich and R. M. Dickson, *Annu. Rev. Phys. Chem.*, 2007, **58**, 409–431.

50 A. March, *Ann. Phys.*, 1916, **354**, 710–724.

51 G. Mie, *Ann. Phys.*, 1908, **330**, 377–445.

52 R. Kubo, *J. Phys. Soc. Japan*, 1962, **17**, 975–986.

53 E. Roduner, *Chem. Soc. Rev.*, 2006, **35**, 583–92.

54 M. Koskinen, P. O. Lipas and M. Manninen, *Zeitschrift für Phys. D Atoms, Mol. Clust.*, 1995, **35**, 285–297.

55 N. Lang and W. Kohn, *Phys. Rev. B*, 1970, **1**, 4555–4568.

56 A. Perrin, O. M. Musa and J. W. Steed, *Chem. Soc. Rev.*, 2013, **42**, 1996.

57 N. T. K. Thanh, N. Maclean and S. Mahiddine, *Chem. Rev.*, 2014, **114**, 7610–7630.

58 R. L. Penn and J. F. Banfield, *Geochim. Cosmochim. Acta*, 1999, **63**, 1549–1557.

59 Z. Wu, S. Yang and W. Wu, *Nanoscale*, 2016, **8**, 1237–1259.

60 R. Jin, *Nanoscale*, 2010, **2**, 343–362.

61 H. Chen, B. Li, X. Ren, S. Li, Y. Ma, S. Cui and Y. Gu, *Biomaterials*, 2012, **33**, 8461–8476.

62 R. Vankayala, C.-L. Kuo, K. Nuthalapati, C.-S. Chiang and K. C. Hwang, *Adv. Funct. Mater.*, 2015, **25**, 5934–5945.

63 H. Chen, B. Li, C. Wang, X. Zhang, Z. Cheng, X. Dai, R. Zhu and Y. Gu, *Nanotechnology*, 2013, **24**, 55704.

64 Y. Negishi, K. Nobusada and T. Tsukuda, *J. Am. Chem. Soc.*, 2005, **127**, 5261–5270.

65 Y. Negishi, Y. Takasugi, S. Sato, H. Yao, K. Kimura and T. Tsukuda, *J. Am. Chem. Soc.*, 2004, **126**, 6518–6519.

66 N. Goswami, Q. Yao, Z. Luo, J. Li, T. Chen and J. Xie, *J. Phys. Chem. Lett.*, 2016, **7**, 962–975.

67 X. Dou, X. Yuan, Y. Yu, Z. Luo, Q. Yao, D. T. Leong and J. Xie, *Nanoscale*, 2014, **6**, 157–161.

68 Q. Zhou, Y. Lin, M. Xu, Z. Gao, H. Yang and D. Tang, *Anal. Chem.*, 2016, **88**, 8886–8892.

69 S. H. Yau, N. Abeyasinghe, M. Orr, L. Upton, O. Varnavski, J. H. Werner, H.-C. Yeh, J. Sharma, A. P. Shreve, J. S. Martinez and T. Goodson, *Nanoscale*, 2012, **4**, 4247–54.

70 Ž. Sanader, M. Krstić, I. Russier-Antoine, F. Bertorelle, P. Dugourd, P.-F. Brevet, R. Antoine and V. Bonačić-Koutecký, *Phys. Chem. Chem. Phys.*, 2016, **18**, 12404–12408.

71 L. Polavarapu, M. Manna and Q.-H. Xu, *Nanoscale*, 2011, **3**, 429–434.

72 G. Ramakrishna, O. Varnavski, J. Kim, D. Lee and T. Goodson, *J. Am. Chem. Soc.*, 2008, **130**, 5032–5033.

73 S. Knoppe, M. Vanbel, S. van Cleuvenbergen, L. Vanpraet, T. Bürgi and T. Verbiest, *J. Phys. Chem. C*, 2015, **119**, 6221–6226.

74 I. Dolamic, S. Knoppe, A. Dass and T. Bürgi, *Nat. Commun.*, 2012, **3**, 798.

75 S. Knoppe, A. Dass and T. Bürgi, *Nanoscale*, 2012, **4**, 4211.

76 G. V Hartland, *Chem. Rev.*, 2011, **111**, 3858–3887.

77 S. H. Yau, O. Varnavski, J. D. Gilbertson, B. Chandler, G. Ramakrishna and T. Goodson, *J. Phys. Chem. C*, 2010, **114**, 15979–15985.

78 M. S. Devadas, V. D. Thanthirige, S. Bairu, E. Sinn and G. Ramakrishna, *J. Phys.*

Chem. C, 2013, **117**, 23155–23161.

79 M. Zhou, S. Vdović, S. Long, M. Zhu, L. Yan, Y. Wang, Y. Niu, X. Wang, Q. Guo, R. Jin and A. Xia, *J. Phys. Chem. A*, 2013, **117**, 10294–10303.

80 C. Yi, H. Zheng, L. M. Tvedte, C. J. Ackerson and K. L. Knappenberger, *J. Phys. Chem. C*, 2015, **119**, 6307–6313.

81 J. Koivisto, X. Chen, S. Donnini, T. Lahtinen, H. Häkkinen, G. Groenhof and M. Pettersson, *J. Phys. Chem. C*, 2016, **120**, 10041–10050.

82 M. S. Devadas, J. Kim, E. Sinn, D. Lee, T. G. Iii and G. Ramakrishna, *J. Phys. Chem. C*, 2010, **114**, 22417–22423.

83 M. Haruta, *Chem. Rec.*, 2003, **3**, 75–87.

84 G. Li and R. Jin, *Acc. Chem. Res.*, 2013, **46**, 1749–1758.

85 M. Zhu, E. Lanni, N. Garg, M. E. Bier and R. Jin, *J. Am. Chem. Soc.*, 2008, **130**, 1138–1139.

86 M. Zhu, C. M. Aikens, F. J. Hollander, G. C. Schatz and R. Jin, *J. Am. Chem. Soc.*, 2008, **130**, 5883–5885.

87 X. Nie, H. Qian, Q. Ge, H. Xu and R. Jin, *ACS Nano*, 2012, **6**, 6014–6022.

88 G. Li and R. Jin, *J. Am. Chem. Soc.*, 2014, **136**, 11347–11354.

89 G. Li, D. Jiang, C. Liu, C. Yu and R. Jin, *J. Catal.*, 2013, **306**, 177–183.

90 H. Chong, P. Li, S. Wang, F. Fu, J. Xiang, M. Zhu and Y. Li, *Sci. Rep.*, 2013, **3**, 3214.

91 D. R. Kauffman, D. Alfonso, C. Matranga, H. Qian and R. Jin, *J. Am. Chem. Soc.*, 2012, **134**, 10237–10243.

92 N. Sakai and T. Tatsuma, *Adv. Mater.*, 2010, **22**, 3185–3188.

93 C. Yu, G. Li, S. Kumar, H. Kawasaki and R. Jin, *J. Phys. Chem. Lett.*, 2013, **4**, 2847–2852.

94 Y. Negishi, M. Mizuno, M. Hirayama, M. Omatoi, T. Takayama, A. Iwase and A. Kudo, *Nanoscale*, 2013, **5**, 7188–7192.

95 Y. S. Chen, H. Choi and P. V. Kamat, *J. Am. Chem. Soc.*, 2013, **135**, 8822–8825.

96 M. A. Abbas, T.-Y. Y. Kim, S. U. Lee, Y. S. Kang and J. H. Bang, *J. Am. Chem. Soc.*, 2016, **138**, 390–401.

97 A. Kogo, N. Sakai and T. Tatsuma, *Electrochem. commun.*, 2010, **12**, 996–999.

98 P. Crespo, R. Litrán, T. C. Rojas, M. Multigner, J. M. de la Fuente, J. C. Sánchez-López, M. A. García, A. Hernando, S. Penadés and A. Fernández, *Phys. Rev. Lett.*, 2004, **93**, 87204.

99 G. L. Nealon, B. Donnio, R. Greget, J. Kappler, E. Terazzi and J.-L. Gallani, *Nanoscale*, 2012, **4**, 5244.

100 V. Tuboltsev, A. Savin, A. Pirojenko and J. Räisänen, *ACS Nano*, 2013, **7**, 6691–6699.

101 Z. Wu, J. Chen and R. Jin, *Adv. Funct. Mater.*, 2011, **21**, 177–183.

102 M. Zhu, C. M. Aikens, M. P. Hendrich, R. Gupta, H. Qian, G. C. Schatz and R. Jin, *J.*

Am. Chem. Soc., 2009, **131**, 2490–2492.

103 T. Dainese, S. Antonello, J. A. Gasc?n, F. Pan, N. V Perera, M. Ruzzi, A. Venzo, A. Zoleo, K. Rissanen and F. Maran, *ACS Nano*, 2014, **8**, 3904–3912.

104 M. De Nardi, S. Antonello, D. Jiang, F. Pan, K. Rissanen, M. Ruzzi, A. Venzo, A. Zoleo and F. Maran, *ACS Nano*, 2014, **8**, 8505–8512.

105 R. S. McCoy, S. Choi, G. Collins, B. J. Ackerson and C. J. Ackerson, *ACS Nano*, 2013, **7**, 2610–2616.

106 L. G. AbdulHalim, Z. Hooshmand, M. R. Parida, S. M. Aly, D. Le, X. Zhang, T. S. Rahman, M. Pelton, Y. Losovyj, P. A. Dowben, O. M. Bakr, O. F. Mohammed and K. Katsiev, *Inorg. Chem.*, 2016, acs.inorgchem.6b02067.

107 C. C. Wang, C. C. Wang, L. Xu, H. Cheng, Q. Lin and C. Zhang, *Nanoscale*, 2014, **6**, 1775–1781.

108 T.-H. Chen and W.-L. Tseng, *Small*, 2012, **8**, 1–8.

109 H. Kawasaki, K. Hamaguchi, I. Osaka and R. Arakawa, *Adv. Funct. Mater.*, 2011, **21**, 3508–3515.

110 Y. Xu, J. Sherwood, Y. Qin, D. Crowley, M. Bonizzoni and Y. Bao, *Nanoscale*, 2014, **6**, 1515–24.

111 L. Zhang and E. Wang, *Nano Today*, 2014, **9**, 132–157.

112 P. Khandelwal, D. K. Singh, S. Sadhu and P. Poddar, *Nanoscale*, 2015, **7**, 19985–20002.

113 P. Khandelwal, D. K. Singh, S. Sadhu and P. Poddar, *Chempluschem*, 2014, **79**, 134–142.

114 P. Maity, S. Yamazoe and T. Tsukuda, *ACS Catal.*, 2013, **3**, 182–185.

115 S. Tanaka, K. Aoki, A. Muratsugu, H. Ishitobi, T. Jin and Y. Inouye, *Opt. Mater. Express*, 2013, **3**, 3437–3439.

116 R. C. Triulzi, M. Micic, J. Orbulescu, S. Giordani, B. Mueller and R. M. Leblanc, *Analyst*, 2008, **133**, 667–72.

117 Y.-G. Kim, S.-K. Oh and R. M. Crooks, *Chem. Mater.*, 2004, **16**, 167–172.

118 G. Liu, Y. Shao, K. Ma, Q. Cui, F. Wu and S. Xu, *Gold Bull.*, 2012, **45**, 69–74.

119 G.-M. Han, Z.-Z. Jia, Y.-J. Zhu, J.-J. Jiao, D.-M. Kong and X.-Z. Feng, *Anal. Chem.*, 2016, **88**, 10800–10804.

120 J. T. Petty, S. P. Story, J.-C. Hsiang and R. M. Dickson, *J. Phys. Chem. Lett.*, 2013, **4**, 1148–1155.

121 J. Qiao, X. Mu, L. Qi, J. Deng and L. Mao, *Chem. Commun.*, 2013, **49**, 8030.

122 Z. Zhou, C. Zhang, Q. Qian, J. Ma, P. Huang, X. Zhang, L. Pan, G. Gao, H. Fu, S. Fu, H. Song, X. Zhi, J. Ni and D. Cui, *J. Nanobiotechnology*, 2013, **11**, 17.

123 J. R. Zhang, Z. L. Wang, F. Qu, H. Q. Luo and N. B. Li, *J. Agric. Food Chem.*, 2014, **62**, 6592–6599.

124 X. Le Guével, N. Daum and M. Schneider, *Nanotechnology*, 2011, **22**, 275103.

125 B. A. Russell, B. Jachimska, I. Kralka, P. A. Mulheran and Y. Chen, *J. Mater. Chem. B*, 2016, **4**, 6876–6882.

126 D. An, J. Su, J. K. Weber, X. Gao, R. Zhou and J. Li, *J. Am. Chem. Soc.*, 2015, **137**, 8412–8418.

127 J. Xie, Y. Zheng and J. Y. Ying, *J. Am. Chem. Soc.*, 2009, **131**, 888–889.

128 C. Shen, X. Xia, S. Hu, M. Yang and J. Wang, *Anal. Chem.*, 2015, **87**, 693–698.

129 P. H. Chan, B. Ghosh, H. Z. Lai, H. L. Peng, K. K. T. Mong and Y. C. Chen, *PLoS One*, 2013, **8**, 1–7.

130 Y. Yue, T.-Y. Liu, H.-W. Li, Z. Liu and Y. Wu, *Nanoscale*, 2012, **4**, 2251–4.

131 L. Shang, L. Yang, F. Stockmar, R. Popescu, V. Trouillet, M. Bruns, D. Gerthsen and G. U. Nienhaus, *Nanoscale*, 2012, **4**, 4155.

132 C. Helmbrecht, D. Lützenkirchen-Hecht and W. Frank, *Nanoscale*, 2015, **7**, 4978–4983.

133 J. A. Annie Ho, H.-C. C. Chang and W.-T. T. Su, *Anal. Chem.*, 2012, **84**, 3246–3253.

134 Y. Negishi and T. Tsukuda, *J. Am. Chem. Soc.*, 2003, **125**, 4046–4047.

135 T. Imaoka, H. Kitazawa, W. Chun, S. Omura, K. Albrecht and K. Yamamoto, *J. Am. Chem. Soc.*, 2013, **135**, 13089–13095.

136 K. G. Stamplecoskie, Y.-S. Chen and P. V. Kamat, *J. Phys. Chem. C*, 2013, **118**, 1370–1376.

137 M. M. Alvarez, J. T. Khoury, T. G. Schaaff, M. N. Shafigullin, I. Vezmar and R. L. Whetten, *J. Phys. Chem. B*, 1997, **5647**, 3706–3712.

138 T. G. Schaaff, M. N. Shafigullin, J. T. Khoury, I. Vezmar, R. L. Whetten, W. G. Cullen, P. N. First, C. Gutiérrez-Wing, J. Ascensio, M. J. Jose-Yacamán, C. Gutierrez-Wing, J. Ascensio and M. J. Jose-Yacaman, *J. Phys. Chem. B*, 1997, **101**, 7885–7891.

139 R. S. Ingram, M. J. Hostetler, R. W. Murray, T. G. Schaaff, J. T. Khoury, R. L. Whetten, T. P. Bigioni, D. K. Guthrie, P. N. First, C. Hill and N. Carolina, *J. Am. Chem. Soc.*, 1997, **7863**, 9279–9280.

140 M. M. Alvarez, J. T. Khoury, T. G. Schaaff, M. Shafigullin, I. Vezmar and R. L. Whetten, *Chem. Phys. Lett.*, 1997, **266**, 91–98.

141 T. G. Schaaff, M. N. Shafigullin, J. T. Khoury, I. Vezmar and R. L. Whetten, *J. Phys. Chem. B*, 2001, **105**, 8785–8796.

142 T. P. Bigioni, R. L. Whetten and Ö. Dag, *J. Phys. Chem. B*, 2000, **104**, 6983–6986.

143 L. Chen, C. Wang, Z. Yuan and H. Chang, *Anal. Chem.*, 2015, **87**, 216–229.

144 T. G. Schaaff and R. L. Whetten, *J. Phys. Chem. B*, 2000, **104**, 2630–2641.

145 T. Gregory Schaaff, G. Knight, M. N. Shafigullin, R. F. Borkman and R. L. Whetten, *J. Phys. Chem. B*, 1998, **102**, 10645–10646.

146 L. V Nair, R. V Nair and R. S. Jayasree, *Dalt. Trans.*, 2016, **45**, 11286–11291.

147 J. Zheng and R. M. Dickson, *J. Am. Chem. Soc.*, 2002, **124**, 13982–13983.

148 J. Zheng, J. T. Petty and R. M. Dickson, *J. Am. Chem. Soc.*, 2003, **125**, 7780–7781.

149 J. Zheng, C. Zhang and R. M. Dickson, *Phys. Rev. Lett.*, 2004, **93**, 0774021–0774024.

150 W. I. Lee, Y. Bae and A. J. Bard, *J. Am. Chem. Soc.*, 2004, **126**, 8358–8359.

151 M. L. Tran, A. V. Zvyagin and T. Plakhotnik, *Chem. Commun.*, 2006, 2400.

152 S.-I. Tanaka, J. Miyazaki, D. K. Tiwari, T. Jin and Y. Inouye, *Angew. Chemie Int. Ed.*, 2011, **50**, 431–435.

153 F. Qu, N. B. Li and H. Q. Luo, *Anal. Chem.*, 2012, **84**, 10373–10379.

154 F. Qu, N. B. Li and H. Q. Luo, *Langmuir*, 2013, **29**, 1199–1205.

155 J.-L. Zhu, Y. Liu, X.-Y. Liu, H.-J. Liu and Y. Chen, *RSC Adv.*, 2015, **5**, 8146–8151.

156 E. Oh, F. K. Fatemi, M. Currie, J. B. Delehanty, T. Pons, A. Fragola, S. Lévêque-Fort, R. Goswami, K. Susumu, A. L. Huston and I. L. Medintz, *Part. Part. Syst. Charact.*, 2013, **30**, 453–466.

157 N. N. M. Adnan, S. Ahmad, R. P. Kuchel and C. Boyer, *Mater. Chem. Front.*, 2017.

158 H. Xiong, W. Wang, J. Liang, W. Wen, X. Zhang and S. Wang, *Sensors Actuators, B Chem.*, 2017, **239**, 988–992.

159 N. Fernández-Iglesias and J. Bettmer, *Nanoscale*, 2014, **6**, 716–721.

160 M. Zhang, Y. Dang, T. Liu, H.-W. Li, Y. Wu, Q. Li, K. Wang and B. Zou, *J. Phys. Chem. C*, 2013.

161 X. Wen, P. Yu, Y. Toh, A. Hsu, Y. Lee and J. Tang, *J. Phys. Chem. C*, 2012, **116**, 19032–19038.

162 H.-W. Li, K. Ai and Y. Wu, *Chem. Commun. (Camb).*, 2011, **47**, 9852–4.

163 H.-W. W. Li, Y. Yue, T. Y. Liu, D. Li and Y. Wu, *J. Phys. Chem. C*, 2013, **117**, 16159–16165.

164 X. Le Guével, B. Hötzer, G. Jung, K. Hollemeyer, V. Trouillet, M. Schneider, X. Le Guével, B. Hötzer, G. Jung, K. Hollemeyer, V. Trouillet and M. Schneider, *J. Phys. Chem. C*, 2011, **115**, 10955–10963.

165 Y. Yu, J. Geng, E. Y. X. Ong, V. Chellappan and Y. N. Tan, *Adv. Healthc. Mater.*, 2016, **5**, 2528–2535.

166 X. Chen and G. A. Baker, *Analyst*, 2013, **138**, 7299.

167 T. Zhou, Y. Huang, W. Li, Z. Cai, F. Luo, C. J. Yang and X. Chen, *Nanoscale*, 2012, **4**, 5312.

168 C.-J. Yu, T.-H. Chen, J.-Y. Jiang and W.-L. Tseng, *Nanoscale*, 2014, **6**, 9618–9624.

169 H. Wei, Z. Wang, L. Yang, S. Tian, C. Hou and Y. Lu, *Analyst*, 2010, **135**, 1406.

170 W.-Y. W.-J. Chen, J. Lin, W.-Y. W.-J. Chen, L. Luo, E. Wei-Guang Diau and Y. Chen, *Nanomedicine*, 2010, **5**, 755–764.

171 R. Ghosh, A. K. Sahoo, S. S. Ghosh, A. Paul and A. Chattopadhyay, *ACS Appl. Mater. Interfaces*, 2014, **6**, 3822–3828.

172 Y. Wang, J. Chen and X. Yan, *Anal. Chem.*, 2013, **85**, 2529–2535.

173 P. L. Xavier, K. Chaudhari, P. K. Verma, S. K. Pal and T. Pradeep, *Nanoscale*, 2010, **2**, 2769–2776.

174 P. Pomastowski, M. Sprynskyy, P. Žuvela, K. Rafińska, M. Milanowski, J. J. Liu, M. Yi and B. Buszewski, *J. Am. Chem. Soc.*, 2016, **138**, 7899–7909.

175 L. V Nair, D. S. Philips, R. S. Jayasree and A. Ajayaghosh, *Small*, 2013, **9**, 2673–7.

176 C. Liu, H. Wu, Y. Hsiao, C. Lai, C. Shih, Y.-K. Peng, K.-C. Tang, H.-W. Chang, Y.-C. Chien, J.-K. Hsiao, J.-T. Cheng and P.-T. Chou, *Angew. Chemie Int. Ed.*, 2011, **50**, 7056–7060.

177 H. H. Wu, Y. Liu, M. Li, Y. Chong, M. Y. Zeng, Y. M. Lo and J.-J. J. Yin, *Nanoscale*, 2015, **7**, 4505–4513.

178 H. K. Awasaki, K. Y. Oshimura, K. H. Amaguchi and R. A. Rakawa, *Japan Soc. Anal. Chem.*, 2011, **27**, 591–596.

179 A. L. West, M. H. Griep, D. P. Cole and S. P. Karna, *Anal. Chem.*, 2014, **86**, 7377–7382.

180 Y. Kong, J. Chen, F. Gao, R. Brydson, B. Johnson, G. Heath, Y. Zhang, L. Wu and D. Zhou, *Nanoscale*, 2013, **5**, 1009–1017.

181 F. Wen, Y. Dong, L. Feng, S. Wang, S. Zhang and X. Zhang, *Anal. Chem.*, 2011, **83**, 1193–1196.

182 X. Wu, Y. Zhang, T. Han, H. Wu, S. Guo and J. Zhang, *RSC Adv.*, 2014, **4**, 3299.

183 L. Yan, Y. Cai, B. Zheng, H. Yuan, Y. Guo, D. Xiao and M. M. F. Choi, *J. Mater. Chem.*, 2012, **22**, 1000.

184 H. Zhang, X. Huang, L. Li, G. Zhang, I. Hussain, Z. Li and B. Tan, *Chem. Commun.*, 2012, **48**, 567.

185 L. Li, Z. Li, H. Zhang, S. Zhang, I. Majeed and B. Tan, *Nanoscale*, 2013, **5**, 1986–92.

186 T. G. Schaaff and R. L. Whetten, *J. Phys. Chem. B*, 1999, **103**, 9394–9396.

187 C.-C. Huang, H.-Y. Liao, Y.-C. Shiang, Z.-H. Lin, Z. Yang and H.-T. Chang, *J. Mater. Chem.*, 2009, **19**, 755–759.

188 S. Chattoraj and K. Bhattacharyya, *J. Phys. Chem. C*, 2014, **118**, 22339–22346.

189 Y. Shichibu, Y. Negishi, H. Tsunoyama, M. Kanehara, T. Teranishi and T. Tsukuda, *Small*, 2007, **3**, 835–839.

190 M. A. Habeeb Muhammed, S. Ramesh, S. S. Sinha, S. K. Pal and T. Pradeep, *Nano Res.*, 2008, **1**, 333–340.

191 H. Duan and S. Nie, *J. Am. Chem. Soc.*, 2007, **129**, 2412–2413.

192 R. Zhou, M. Shi, X. Chen, M. Wang and H. Chen, *Chem. - A Eur. J.*, 2009, **15**, 4944–4951.

193 H. C. Lee, T. H. Chen, W. L. Tseng and C. H. Lin, *2012 7th IEEE Int. Conf. Nano/Micro Eng. Mol. Syst. NEMS 2012*, 2012, 665–668.

194 T. Shu, J. Wang, L. Su and X. Zhang, *Anal. Chem.*, 2016, **88**, 11193–11198.

195 C. J. Lin, T. Yang, C. Lee, S. H. Huang, R. A. Sperling, M. Zanella, J. K. Li, J.-L. Shen, H.-H. Wang, H.-I. Yeh, W. J. Parak and W. H. Chang, *ACS Nano*, 2009, **3**, 395–401.

196 T.-H. Chen, C.-C. Nieh, Y.-C. Shih, C.-Y. Ke and W.-L. Tseng, *RSC Adv.*, 2015, **5**, 45158–45164.

197 W. Guo, J. Yuan, E. Wang, J. Yuanab and E. Wang, *Chem. Commun.*, 2012, **48**, 3076–8.

198 N. Cathcart, P. Mistry, C. Makra, B. Pietrobon, N. Coombs, M. Jelokhani-Niaraki and V. Kitaev, *Langmuir*, 2009, **25**, 5840–6.

199 T. Udaya Bhaskara Rao and T. Pradeep, *Angew. Chemie - Int. Ed.*, 2010, **49**, 3925–3929.

200 M. A. H. Muhammed, P. K. Verma, S. K. Pal, R. C. A. Kumar, S. Paul, R. V. Omkumar and P. Thalappil, *Chem. - A Eur. J.*, 2009, **15**, 10110–10120.

201 X. Yuan, Z. Luo, Q. Zhang, X. Zhang, Y. Zheng, J. Y. Lee and J. Xie, *ACS Nano*, 2011, **5**, 8800–8808.

202 X. Yuan, T. J. Yeow, Q. Zhang, J. Y. Lee and J. Xie, *Nanoscale*, 2012, **4**, 1968–71.

203 C. Zhang, X. Sun, J. Li and Y. Liu, *Nanoscale*, 2013, **5**, 6261.

204 X. Le Guével, V. Trouillet, C. Spies, G. Jung and M. Schneider, *J. Phys. Chem. C*, 2012, **116**, 6047–6051.

205 J. Liu, X. Ren, X. Meng, Z. Fang and F. Tang, *Nanoscale*, 2013, **5**, 10022.

206 T. Zhou, M. Rong, Z. Cai, C. J. Yang and X. Chen, *Nanoscale*, 2012, **4**, 4103–6.

207 T. Liu, L. Zhang, H. Song, Z. Wang and Y. Lv, *Luminescence*, 2013, **28**, 530–535.

208 H. Xu and K. S. Suslick, *ACS Nano*, 2010, **4**, 3209–3214.

209 J. Xie, Y. Zheng and J. Y. Ying, *Chem. Commun.*, 2010, **46**, 961–963.

210 Y. Lin and W. Tseng, *Anal. Chem.*, 2010, **82**, 9194–9200.

211 H.-C. Chang, Y. Chang, N. Fan and J. A. Ho, *ACS Appl. Mater. Interfaces*, 2014, **6**, 18824–18831.

212 P. Huang, S. Li, N. Gao and F. Wu, *Analyst*, 2015, **140**, 7313–21.

213 J. Zang, C. Li, K. Zhou, H. Dong, B. Chen, F. Wang and G. Zhao, *Anal. Chem.*, 2016, **88**, 10275–10283.

214 Y. Zhang, M. Yan, J. Jiang, P. Gao, G. Zhang, M. M. F. Choi, C. Dong and S. Shuang, *Sensors Actuators B Chem.*, 2016, **235**, 386–393.

215 B. Paramanik, S. Bhattacharyya and A. Patra, *Chem. - A Eur. J.*, 2013, **19**, 5980–5987.

216 K.-Y. Pu, Z. Luo, K. Li, J. Xie and B. Liu, *J. Phys. Chem. C*, 2011, **115**, 13069–13075.

217 B. Adhikari and A. Banerjee, *Chem. Mater.*, 2010, **22**, 4364–4371.

218 J. Yin, X. He, X. Jia, K. Wang and F. Xu, *Analyst*, 2013, **138**, 2350–6.

219 D. Lu, C. Zhang, L. Fan, H. Wu, S. Shuang and C. Dong, *Anal. Methods*, 2013, **5**, 5522.

220 N. Zhang, Y. Si, Z. Sun, L. Chen, R. Li, Y. Qiao and H. Wang, *Anal. Chem.*, 2014, **86**, 11714–11721.

221 S. Roy, A. Baral and A. Banerjee, *ACS Appl. Mater. Interfaces*, 2014, **6**, 4050–4056.

222 Y. Zhong, C. Deng, Y. He, Y. Ge and G. Song, *Anal. Methods*, 2015, **7**, 1558–1562.

223 N. Xia, J. Yang and Z. Wu, *Nanoscale*, 2015, **7**, 10013–10020.

224 Z. Yuan, M. Peng, Y. He and E. S. Yeung, *Chem. Commun.*, 2011, **47**, 11981.

225 Z. Lin, F. Luo, T. Dong, L. Zheng, Y. Wang, Y. Chi and G. Chen, *Analyst*, 2012, **137**, 2394.

226 T. Zhou, L. Lin, M. Rong, Y. Jiang and X. Chen, *Anal. Chem.*, 2013, **85**, 9839–9844.

227 J. Sun, J. Zhang and Y. Jin, *J. Mater. Chem. C*, 2013, **1**, 138–143.

228 D. Li, B. Li and S. I. Yang, *Anal. Methods*, 2015, **7**, 2278–2282.

229 M. Zhang and B.-C. Ye, *Analyst*, 2011, **136**, 5139–42.

230 X. Yang, L. Yang, Y. Dou and S. Zhu, *J. Mater. Chem. C*, 2013, **1**, 6748.

231 J. Sun, Y. Yue, P. Wang, H. He and Y. Jin, *J. Mater. Chem. C*, 2013, **1**, 908.

232 Z. Yuan, N. Cai, Y. Du, Y. He and E. S. Yeung, *Anal. Chem.*, 2014, **86**, 419–426.

233 X. Fang, Q. Zhao, H. Cao, J. Liu, M. Guan and J. Kong, *Analyst*, 2015, **140**, 7823–7826.

234 Y. Liu, K. Ai, X. Cheng, L. Huo and L. Lu, *Adv. Funct. Mater.*, 2010, **20**, 951–956.

235 W. Chen, G. Lan and H. Chang, *Anal. Chem.*, 2011, **83**, 9450–9455.

236 L. Wang, G. Chen, G. Zeng, J. Liang, H. Dong, M. Yan, Z. Li, Z. Guo, W. Tao and L. Peng, *New J. Chem.*, 2015, **39**, 9306–9312.

237 C. Dai, C.-X. Yang and X.-P. Yan, *Anal. Chem.*, 2015, **87**, 11455–11459.

238 H. Liu, G. Yang, E. S. Abdel-Halim and J.-J. Zhu, *Talanta*, 2013, **104**, 135–139.

239 J. Zhang, C. Chen, X. Xu, X. Wang and X. Yang, *Chem. Commun.*, 2013, **49**, 2691.

240 Q. Yue, L. Sun, T. Shen, X. Gu, S. Zhang and J. Liu, *J. Fluoresc.*, 2013, **23**, 1313–1318.

241 B. Unnikrishnan, S.-C. Wei, W.-J. Chiu, J. Cang, P.-H. Hsu and C.-C. Huang, *Analyst*, 2014, **139**, 2221–8.

242 W.-Y. Chen, C. Huang, L. Chen and H. Chang, *Nanoscale*, 2014, **6**, 11078–11083.

243 Y. Sui, M. Deng, S. Xu and F. Chen, *RSC Adv.*, 2015, **5**, 13495–13501.

244 A. M. P. Hussain, S. N. Sarangi, J. A. Kesarwani and S. N. Sahu, *Biosens. Bioelectron.*, 2011, **29**, 60–65.

245 T. Wen, F. Qu, N. B. Li and H. Q. Luo, *Anal. Chim. Acta*, 2012, **749**, 56–62.

246 L. Hu, Y. Yuan, L. Zhang, J. Zhao, S. Majeed and G. Xu, *Anal. Chim. Acta*, 2013, **762**, 83–86.

247 Y. Ling, N. Zhang, F. Qu, T. Wen, Z. F. Gao, N. B. Li and H. Q. Luo, *Spectrochim. Acta Part A Mol. Biomol. Spectrosc.*, 2014, **118**, 315–320.

248 X. Xia, Y. Long and J. Wang, *Anal. Chim. Acta*, 2013, **772**, 81–86.

249 L. L. Wang, J. Qiao, H. H. Liu, J. Hao, L. Qi, X. P. Zhou, D. Li, Z. X. Nie and L. Q. Mao, *Anal. Chem.*, 2014, **86**, 9758–9764.

250 J. Zhang, L. Tu, S. Zhao, G. Liu, Y. Wang, Y. Wang and Z. Yue, *Biosens. Bioelectron.*, 2015, **67**, 296–302.

251 X. Zhang, F. Wu, P. Liu, N. Gu and Z. Chen, *Small*, 2014, **10**, 5170–5177.

252 D. Tian, Z. Qian, Y. Xia and C. Zhu, *Langmuir*, 2012, **28**, 3945–3951.

253 B. Hemmateenejad, F. Shakerizadeh-shirazi and F. Samari, *Sensors Actuators B. Chem.*, 2014, **199**, 42–46.

254 X. Yan, H. Li, B. Cao, Z. Ding and X. Su, *Microchim. Acta*, 2015, **182**, 1281–1288.

255 L. Li, H. Liu, Y. Shen, J. Zhang and J.-J. Zhu, *Anal. Chem.*, 2011, **83**, 661–665.

256 Y. Tao, Y. Lin, J. Ren and X. Qu, *Biosens. Bioelectron.*, 2013, **42**, 41–46.

257 B. Aswathy and G. Sony, *Microchem. J.*, 2014, **116**, 151–156.

258 Y. Teng, X. Jia, J. Li and E. Wang, *Anal. Chem.*, 2015, **87**, 4897–4902.

259 R. Ban, E. S. Abdel-Halim, J. Zhang and J.-J. Zhu, *Analyst*, 2015, **140**, 1046–1053.

260 M. Santhosh, S. R. Chinnadayyala, A. Kakoti and P. Goswami, *Biosens. Bioelectron.*, 2014, **59**, 370–376.

261 H.-C. Chang and J.-A. A. Ho, *Anal. Chem.*, 2015, **87**, 10362–10367.

262 X. J. Zhao and C. Z. Huang, *New J. Chem.*, 2014, **38**, 3673.

263 G. Lan, W. Chen and H. Chang, *Biosens. Bioelectron.*, 2011, **26**, 2431–2435.

264 W. Wang, L. Zhan, Y. Q. Du, F. Leng, Y. Chang, M. X. Gao and C. Z. Huang, *Anal. Methods*, 2013, **5**, 5555.

265 G. Wang, Y. Zhu, L. Chen, L. Wang and X. Zhang, *Analyst*, 2014, **139**, 165–169.

266 N. Enkin, F. Wang, E. Sharon, H. B. Albada and I. Willner, *ACS Nano*, 2014, **8**, 11666–11673.

267 Y. Zhang, C. Zhu, L. Zhang, C. Tan, J. Yang, B. Chen, L. Wang and H. Zhang, *Small*, 2015, **11**, 1385–1389.

268 W. Yang, J. Tian, L. Wang, S. Fu, H. Huang, Y. Zhao and S. Zhao, *Analyst*, 2016, **141**, 2998–3003.

269 Z.-Y. Li, Y.-T. Wu and W.-L. Tseng, *ACS Appl. Mater. Interfaces*, 2015, **7**, 23708–23716.

270 W. Guo, J. Yuan, Q. Dong and E. Wang, *J. Am. Chem. Soc.*, 2010, **132**, 932–934.

271 S. W. Yang and T. Vosch, *Anal. Chem.*, 2011, **83**, 6935–6939.

272 Y. Liu, M. Zhang, B. Yin and B. Ye, *Anal. Chem.*, 2012, **84**, 5165–5169.

273 M. Zhang, Y. Q. Liu, C. Y. Yu, B. C. Yin and B. C. Ye, *Analyst*, 2013, **138**, 4812.

274 C. Yang, K. Shi, B. Dou, Y. Xiang, Y. Chai and R. Yuan, *ACS Appl. Mater. Interfaces*, 2015, **7**, 1188–1193.

275 M. Wang, Q. Mei, K. Zhang and Z. Zhang, *Analyst*, 2012, **137**, 1618–1623.

276 J. Sun, F. Yang, D. Zhao, C. Chen and X. Yang, *ACS Appl. Mater. Interfaces*, 2015, **7**, 6860–6866.

277 B. Paramanik, S. Kundu, G. De and A. Patra, *J. Mater. Chem. C*, 2016, **4**, 486–496.

278 C.-T. Chen, W.-J. Chen, C.-Z. Liu, L.-Y. Chang and Y.-C. Chen, *Chem. Commun.*, 2009, 7515.

279 L. Qin, X. He, L. Chen and Y. Zhang, *ACS Appl. Mater. Interfaces*, 2015, **7**, 5965–5971.

280 X. Ren, Z. Chen, X. Meng, D. Chen and F. Tang, *Chem. Commun.*, 2012, **48**, 9504.

281 J. Li, X. Zhong, H. Zhang, X. C. Le and J. Zhu, *Anal. Chem.*, 2012, **84**, 5170–5174.

282 Y. Chen, H. Zhou, Y. Wang, W. Li, J. Chen, Q. Lin and C. Yu, *Chem. Commun.*, 2013, **49**, 9821.

283 T. Zhao, Q. Chen, C. Zeng, Y. Lan, J. Cai, J. Liu and J. Gao, *J. Mater. Chem. B*, 2013, **1**, 4678–4683.

284 W.-Y. Chen, L. Chen, C. Ou, C. Huang, S. Wei and H. Chang, *Anal. Chem.*, 2013, **85**, 8834–8840.

285 H. Li, Y. Guo, L. Xiao and B. Chen, *Analyst*, 2014, **139**, 285–289.

286 X. Liu, R. Hu, Z. Gao and N. Shao, *Langmuir*, 2015, **31**, 5859–5867.

287 C.-X. Zhuo, L.-H. Wang, J.-J. Feng and Y.-D. Zhang, *Sensors*, 2016, **16**, 1477.

288 H. Xiong, H. Zheng, W. Wang, J. Liang, W. Wen, X. Zhang and S. Wang, *Biosens. Bioelectron.*, 2016, **86**, 164–168.

289 P. H. Chan, S. Y. Wong, S. H. Lin and Y. C. Chen, *Rapid Commun. Mass Spectrom.*, 2013, **27**, 2143–2148.

290 J. Liu, L. Lu, S. Xu and L. Wang, *Talanta*, 2015, **134**, 54–59.

291 J. Yin, X. He, K. Wang, F. Xu, J. Shangguan, D. He and H. Shi, *Anal. Chem.*, 2013, **85**, 12011–12019.

292 L. Shang and G. U. Nienhaus, *Biophys. Rev.*, 2012, **4**, 313–322.

293 X. Le Guével, C. Spies, N. Daum, G. Jung and M. Schneider, *Nano Res.*, 2012, **5**, 379–387.

294 P. Bian, J. Zhou, Y. Liu and Z. Ma, *Nanoscale*, 2013, **5**, 6161.

295 V. Venkatesh, A. Shukla, S. Sivakumar and S. Verma, *ACS Appl. Mater. Interfaces*, 2014, **6**, 2185–2191.

296 A. Fu and E. Zhang, *Int. J. Nanomedicine*, 2015, **10**, 2115.

297 J. Yang, N. Xia, X. Wang, X. Liu, A. Xu, Z. Wu and Z. Luo, *Nanoscale*, 2015, **7**, 18464–18470.

298 F. Zhou, B. Feng, H. Yu, D. Wang, T. Wang, J. Liu, Q. Meng, S. Wang, P. Zhang, Z. Zhang and Y. Li, *Theranostics*, 2016, **6**, 679–687.

299 J. Li, Y. Dai, S. Wang, C. Han and K. Xu, *Sensors Actuators B Chem.*, 2016, **232**, 1–8.

300 A. K. Sahoo, U. Goswami, D. Dutta, S. Banerjee, A. Chattopadhyay and S. S. Ghosh, *ACS Biomater. Sci. Eng.*, 2016, **2**, 1395–1402.

301 H. Li, H. Huang, A.-J. Wang, H. Feng, J.-J. Feng and Z. Qian, *Sensors Actuators B Chem.*, 2016, 6–11.

302 D. Dutta, A. K. Sahoo, A. Chattopadhyay and S. S. Ghosh, *J. Mater. Chem. B*, 2016, **4**, 793–800.

303 A. Ghoshal, U. Goswami, A. Raza, A. Chattopadhyay and S. S. Ghosh, *RSC Adv.*, 2016, **6**, 85763–85772.

304 D. Chen, B. Li, S. Cai, P. Wang, S. Peng, Y. Sheng, Y. He, Y. Gu and H. Chen, *Biomaterials*, 2016, **100**, 1–16.

305 L. Tian, W. Zhao, L. Li, Y. Tong, G. Peng and Y. Li, *Sensors Actuators B Chem.*, 2017, **240**, 114–124.

306 J.-Y. Zhao, R. Cui, Z.-L. Zhang, M. Zhang, Z.-X. Xie and D.-W. Pang, *Nanoscale*, 2014, **6**, 13126–13134.

307 R. Mukherji, A. Samanta, R. Illathvalappil, S. Chowdhury, A. Prabhune and R. N. Devi, *ACS Appl. Mater. Interfaces*, 2013, **5**, 13076–13081.

308 A. Yahia-Ammar, D. Sierra, F. Mérola, N. Hildebrandt and X. Le Guével, *ACS Nano*, 2016, **10**, 2591–2599.

309 S. Chandirasekar, C. Chandrasekaran, T. Muthukumarasamyvel, G. Sudhandiran and N. Rajendiran, *ACS Appl. Mater. Interfaces*, 2015, **7**, 1422–1430.

310 J. Yu, S. A. Patel and R. M. Dickson, *Angew. Chemie - Int. Ed.*, 2007, **46**, 2028–2030.

311 J. Yu, S. Choi, C. I. Richards, Y. Antoku and R. M. Dickson, *Photochem. Photobiol.*, 2008, **84**, 1435–1439.

312 S. Lin, N. Chen, S. Sum, L. Lo and C.-S. Yang, *Chem. Commun.*, 2008, 4762.

313 X. Wu, X. He, K. Wang, C. Xie, B. Zhou and Z. Qing, *Nanoscale*, 2010, **2**, 2244–2249.

314 H. H. Wang, C.-A. J. A. J. Lin, C. H. Lee, Y. C. Lin, Y. M. Tseng, C.-L. L. C. T. Hsieh, C. H. Chen, C. H. Tsai, C.-L. L. C. T. Hsieh, J. L. Shen, W. H. Chan, W. H. Chang and H.-I. I. Yeh, *ACS Nano*, 2011, **5**, 4337–4344.

315 A. K. Sahoo, S. Banerjee, S. S. Ghosh and A. Chattopadhyay, *ACS Appl. Mater. Interfaces*, 2014, **6**, 712–724.

316 N. K. Das, S. Ghosh, A. Priya, S. Datta and S. Mukherjee, *J. Phys. Chem. C*, 2015, **119**, 24657–24664.

317 L. Shang, N. Azadfar, F. Stockmar, W. Send, V. Trouillet, M. Bruns, D. Gerthsen and G. U. Nienhaus, *Small*, 2011, **7**, 2614–2620.

318 J. Zhang, Y. Fu, C. V Conroy, Z. Tang, G. Li, R. Y. Zhao and G. Wang, *J. Phys. Chem. C*, 2012, **116**, 26561–26569.

319 L. Yang, L. Shang and G. U. Nienhaus, *Nanoscale*, 2013, **5**, 1537.

320 Y. Wang, J. Chen and J. Irudayaraj, *ACS Nano*, 2011, **5**, 9718–9725.

321 R. Khandelia, S. Bhandari, U. N. Pan, S. S. Ghosh and A. Chattopadhyay, *Small*, 2015, **11**, 4075–4081.

322 J. Wang, G. Zhang, Q. Li, H. Jiang, C. Liu, C. Amatore and X. Wang, *Sci. Rep.*, 2013, **3**, 1–6.

323 S. Gao, D. Chen, Q. Li, J. Ye, H. Jiang, C. Amatore and X. Wang, *Sci. Rep.*, 2014, **4**, 1–6.

324 D. Chen, C. Zhao, J. Ye, Q. Li, X. Liu, M. Su, H. Jiang, C. Amatore, M. Selke and X. Wang, *ACS Appl. Mater. Interfaces*, 2015, **7**, 18163–18169.

325 A. L. West, N. M. Schaeublin, M. H. Griep, E. Gardner, D. P. Cole, A. M. Fakner, S. M. Hussain, S. P. Karna, E. I. Maurer-Gardner, D. P. Cole, A. M. Fakner, S. M. Hussain and S. P. Karna, *ACS Appl. Mater. Interfaces*, 2016, **8**, 21221–21227.

326 P. Huang, J. Lin, S. Wang, Z. Zhou, Z. Li, Z. Wang, C. Zhang, X. Yue, G. Niu, M. Yang, D. Cui and X. Chen, *Biomaterials*, 2013, **34**, 4643–4654.

327 L. V. Nair, S. S. Nazeer, R. S. Jayasree and A. Ajayaghosh, *ACS Nano*, 2015, **9**, 5825–5832.

328 X. D. Zhang, J. Chen, J. Yang, J. Y. Wang, X. Shen, S. S. Song, H. Wang, H. He, X. J. Wang, S. J. Fan, Y. M. Sun and M. L. Guo, *J. Mater. Chem. B*, 2015, **3**, 4735–4741.

329 C. Zhou, M. Long, Y. Qin, X. Sun and J. Zheng, *Angew. Chemie - Int. Ed.*, 2011, **50**, 3168–3172.

330 X. Zhang, D. Wu, X. Shen, P. Liu, F.-Y. Fan and S. Fan, *Biomaterials*, 2012, **33**,

4628–4638.

331 X. D. Zhang, Z. Luo, J. Chen, X. Shen, S. Song, Y. Sun, S. Fan, F. Fan, D. T. Leong and J. Xie, *Adv. Mater.*, 2014, **26**, 4565–4568.

332 X.-D. Zhang, Z. Luo, J. Chen, S. Song, X. Yuan, X. Shen, H. Wang, Y. Sun, K. Gao, L. Zhang, S. Fan, D. T. Leong, M. Guo and J. Xie, *Sci. Rep.*, 2015, **5**, 8669.

333 J. B. Liu, M. X. Yu, C. Zhou, S. Y. Yang, X. H. Ning and J. Zheng, *J. Am. Chem. Soc.*, 2013, **135**, 4978–4981.

334 G. Liang, D. Ye, X. Zhang, F. Dong, H. Chen, S. Zhang, J. Li, X. Shen and J. Kong, *J. Mater. Chem. B*, 2013, **1**, 3545–3552.

335 C. Wang, Y. Yao and Q. Song, *J. Mater. Chem. C*, 2015, **3**, 5910–5917.

336 X. Wu, L. Li, L. Zhang, T. Wang, C. Wang and Z. Su, *J. Mater. Chem. B*, 2015, **3**, 2421–2425.

337 L. Li, L. Zhang, T. Wang, X. Wu, H. Ren, C. Wang and Z. Su, *Small*, 2015, **11**, 3162–3173.

338 J. G. Croissant, D. Zhang, S. Alsaiari, J. Lu, L. Deng, F. Tamanoi, A. M. AlMalik, J. I. Zink and N. M. Khashab, *J. Control. Release*, 2016, **229**, 183–191.

339 Y. Zhao, L. Detering, D. Sultan, M. L. Cooper, M. You, S. Cho, S. L. Meier, H. Luehmann, G. Sun, M. Rettig, F. Dehdashti, K. L. Wooley, J. F. DiPersio and Y. Liu, *ACS Nano*, 2016, **10**, 5959–5970.

340 F. Chen, S. Goel, R. Hernandez, S. A. Graves, S. Shi, R. J. Nickles and W. Cai, *Small*,

2016, **12**, 2775–2782.

341 X. Yuan, M. I. Setyawati, A. S. Tan, C. N. Ong, D. T. Leong and J. Xie, *NPG Asia Mater.*, 2013, **5**, e39.

342 I. Chakraborty, T. Udayabhaskararao, G. K. Deepesh and T. Pradeep, *J. Mater. Chem. B*, 2013, **1**, 4059.

343 X. Yuan, M. I. Setyawati, D. T. Leong and J. Xie, *Nano Res.*, 2014, **7**, 301–307.

344 Y. Liu, L. Wang, C. Bu, G. Wang, Y. Zhang, S. Fang and W. Shi, *J. Nanomater.*, 2015, **2015**, 1–8.

345 S. K. Mishra, S. Raveendran, J. M. F. Ferreira and S. Kannan, *Langmuir*, 2016, **32**, 10305–10316.

346 S. Javani, R. Lorca, A. Latorre, C. Flors, A. L. Cortajarena and Á. Somoza, *ACS Appl. Mater. Interfaces*, 2016, **8**, 10147–10154.

347 A. Sangsuwan, H. Kawasaki, Y. Matsumura and Y. Iwasaki, *Bioconjug. Chem.*, 2016, **27**, 2527–2533.

348 D. Xu, Q. Wang, T. Yang, J. Cao, Q. Lin, Z. Yuan and L. Li, *Int. J. Environ. Res. Public Health*, 2016, **13**, 334.

349 K. Zheng, M. I. Setyawati, T.-P. P. Lim, D. T. Leong and J. Xie, *ACS Nano*, 2016, **10**, 7934–7942.

350 B. Khlebtsov, E. Tuchina, V. Tuchin and N. Khlebtsov, *RSC Adv.*, 2015, **5**, 61639–61649.

351 H. Huang, H. Li, A. Wang, S. Zhong, K. Fang and J. Feng, *Analyst*, 2014, **139**, 6536–6541.

352 S. Ghosh, N. K. Das, U. Anand and S. Mukherjee, *J. Phys. Chem. Lett.*, 2015, **6**, 1293–1298.

353 Y.-T. Wu, C. Shanmugam, W.-B. Tseng, M.-M. Hiseh and W.-L. Tseng, *Nanoscale*, 2016, **8**, 11210–11216.

354 G. Zhang, T. Xu, H. Du, Y. Qiao, X. Guo, L. Shi, Y. Zhang, S. Shuang, C. Dong and H. Ma, *J. Mater. Chem. C*, 2016, **4**, 3540–3545.

Chapter II

Study of the nucleation and growth of antibiotic-labeled Au-NPs and Au_8 QCs for Hg^{2+} ion sensing, cellular imaging and antibacterial applications

In this chapter, a detailed experimental study supported by DFT calculations is performed to understand the mechanism behind the synthesis of cefradine (CFD- an antibiotic) labeled gold nanoparticles (Au-NPs) by employing CFD both as mild reducing and capping agent. The analysis of the effect of growth conditions reveals that lower concentration of $HAuCl_4$, higher temperature, and larger pH leads to the formation of a larger population of smaller isotropic particles. Surprisingly, at pH 6, a large population of small particles with small population of large particles was observed. The MALDI-TOF mass spectrometric results of supernatant of pH 6 reaction indicate the formation of $[Au_8(CFD)_2S_6]$ QCs which shows the fluorescence at ca. 432 nm with a Stokes shift of ca. 95 nm. These Au_8 QCs were applied for sensing of Hg^{2+} ions and they offer good selectivity and a high sensitivity with a detection limit of ca. 2 nM which is lower than the detection requirement of 10 nM by the U.S. EPA and 30 nM by WHO for drinking water. We have also applied the sensing probe to detect the Hg^{2+} ions in the bacterial cells. Further, we investigated the antibacterial property of as-synthesized Au-NPs using MIC, growth curve and cell survival assay. The SEM study shows the degradation and blabbing of bacterial cell-wall upon exposure with Au-NPs which was further supported by fluorescence microscopic results. We believe that the bacterial cytotoxicity is due to the direct contact of the Au-NPs with bacterial cells.

Reproduced by permission of The Royal Society of Chemistry.[1]

(http://pubs.rsc.org/en/Content/ArticleLanding/2015/NR/C5NR05619E#!divAbstract)

2.1 Introduction

It is fascinating as well as challenging to explore the effect of reaction conditions (monomer concentration, temperature and pH of the reaction) on the nucleation and growth mechanism behind the formation of nano-crystallites in the solution phase; starting from monomers (atoms/molecules/ions). The role of reduction potential of reducing agents and relative binding affinities of capping agents to different lattice facets, in the formation and stabilization of larger (tens of nm or larger) and sub-nm metal clusters (which are otherwise not stable), is also interesting. These fundamental studies are non-trivial even for much simpler model system such as the gold nanoparticles (Au-NPs) synthesized by the reduction of Au^{3+} ions.[2–4] It is already well researched that, among the metal NPs, Au-NPs are more fascinating because of their low toxicity,[5–8] size and shape dependent optical properties at the nanoscale[6,9–15] which make them interesting for applications in many fields such as biosensor,[10,16–18] drug delivery,[19–22] and catalysis.[23] Interestingly, these properties become even more fascinating when the size decreases to an extent, when it becomes comparable to the Fermi wavelength of an electron (ca. 0.5 nm for Au).[24,25] The particles in this small size regime are called as quantum clusters (QCs) which are made up of few atoms to few tens of atoms and exhibit size-dependent fluorescence.[26–29] The fluorescence of these Au-QCs generally follows a simple relation $E_{Fermi}/n^{1/3}$, known as Jellium model.[30] The electronic properties of Au-NPs as well as Au-QCs heavily depend on the surface modification with suitable functional molecules, which provide additional tunability and functionality.[12,31–34]

In a typical noble metal NP synthesis, the use of strong reducing agents (e.g. $NaBH_4$, citric acid etc.) result into the formation of highly monodispersed particles. While

using the strong reducing agents, the monomer concentration instantaneously drops below the saturation limit and that stops further nucleation events, therefore, it is difficult to experimentally probe and follow the growth events (*in situ*) using the conventional photon correlation techniques based on scattering as the nucleation and growth of Au-NPs using stronger reducing agents usually ends in a fraction of second. In contrast, the antibiotic-mediated synthesis method gives an edge over the conventional methods as recently reported by our group.[9,11] Due to the fact that beta lactam antibiotic molecules are weaker reducing agents, (1) we get poly-dispersed particles, as fresh nuclei keep forming while the existing particles grow further (2) we observe the formation of stable quantum clusters by tuning the reaction parameters, and (3) due to the slow kinetics, it is easy to follow the reaction pathways to some extent by doing a time dependent study of the particle evolution using light scattering, absorption spectroscopy or electron microscopy techiques.[9–11,35] Recently, our group used an *in situ*, real-time, static/dynamic light scattering and absorption spectroscopy measurements in combination with electron microscopy imaging, to track the time evolution of seeds and noticed the simultaneous growth of two different populations of Au-NPs (quite different in sizes). We have noticed that the smaller particles (diameter < 2 nm) could grow and coexist simultaneously with larger particles (diameter > 40 nm) and the larger particles were the results of aggregation of smaller clusters to form isotropic/anisotropic nanocrystallites.[11] We also reported the effect of concentration of monomers and the reaction temperature on the nucleation and growth mechanism.[9] In another study, our group has also shown the synthesis of antibiotic (cefadroxil, CFX) labeled blue emissive Au-QCs and their application in the sensing of Sn^{4+} ions.[10]

In the present chapter, we have used cefradine, as a model system, to study the nucleation and growth of antibiotic-labeled Au-NPs and blue luminescent Au_8 quantum clusters for Hg^{2+} ion sensing, cellular imaging and antibacterial applications. Cefradine is a *β*-lactam antibiotic, effective against a wide range of Gram-positive and a limited range of Gram-negative bacteria.[36] This is relatively resistant to *β*-lactamases[37] and has a tendency to interact with metal ions. In comparison to cefadroxil (CFX), cefradine (CFD) does not have –OH group at the 4^{th} position of phenyl ring. The use of antibiotic molecules as reducing and surface capping agents for the synthesis of Au-NPs and blue luminescent Au-QCs may add few key advantages. The luminescent nature of the Au-QCs may be useful for imaging and sensing applications.[10,38] The capping of antibiotic molecules onto the nanoparticles may synergistically enhance the antibacterial properties of these particles.[35,39–42] Therefore, first, the interaction of the luminescent Au-QCs with various heavy and toxic metal ions is investigated for sensing applications. It is found that Au-QCs can be used to sense as low as ca. 2 nM concentration of mercury ions in pH 7 buffer with high selectivity over various metal ions based on a mechanism involving particle aggregation-induced fluorescence quenching, possibly due to screening of charges of Au-QCs after binding selectively with cations. Mercury is one of the serious environment pollutant and most hazardous heavy metal ion which ultimately accumulates in the human body via food chain and possesses the serious health issues related to immune, nervous and digestive systems and affects the lungs, kidneys, skin and eyes.[43] It also affects the development of the child in utero and early in life. The maximum permitted level of mercury in drinking water by WHO and the U.S. Environmental Protection Agency (EPA) has set at 30 and 10 nM, respectively.[44] In view of these facts, it is very essential to detect

the presence of Hg^{2+} ions in environment at very low concentrations especially at nano-molar range. We have also demonstrated the use of the Hg^{2+} ion-sensing probe for detection of the Hg^{2+} ions in the bacterial cells.

The interaction of the metal ions and nanoparticles with biological entities is another very interesting issue for researchers. In an earlier investigation, while probing the effect of Co^{2+} ions on marine bacterium, our group observed that the bacterial cells exhibit co-operative, self-organized and structured colonies under the stress of Co^{2+} ions which triggers a redox process mediated by the biomolecules that results in to the formation of Co_3O_4 NPs and the microbial cells also undergo tremendous change in their nanomechanical behavior such as cellular adhesion, elasticity, and plasticity as probed by in situ AFM investigation.[45] In contrast to the interaction of cells with ions, the study of interaction of stable nanoparticles with certain microbes also comes with novel results.[46–48] Recently, our group reported the novel process of biomilling where the large particles such as ZnO nanorods can be milled to much smaller quasi-spherical nanoparticles upon interaction with yeast *S. cerevisae*.[48]

In this chapter, we discuss the Au-NPs capped with antibiotic molecules so it becomes very interesting to study the fate of the antimicrobial activity of the antibiotic molecules in the proximity to the Au-NPs surfaces. According to a recent reports, there are conflicting observations about the antibacterial activity of Au-NPs.[49] Au-NPs are generally considered as non-bactericidal or weakly-bactericidal. In view of these facts, we have performed detailed investigations of the antibacterial properties of CFD labeled Au-NPs against *E. coli*, a Gram-negative rod shaped model bacterium to contribute towards the understanding about the antibacterial activity of antibiotic capped Au-NPs.

2.2 Experimental Details

2.2.1 Materials

All the chemicals were of analytical grade and used *as-received* without any further purification unless otherwise described. The reagents $HAuCl_4.3H_2O$ (≥ 49.0% Au basis), dibasic sodium phosphate (> 99%), monobasic sodium phosphate (> 99%), CH_3COOK (> 99%), sodium acetate (≥ 99 %), acetic acid (> 99.7%), $Ni(NO_3)_2.6H_2O$ and fluorescein diacetate (FDA) were purchased from Sigma-Aldrich. Cefradine was purchased from Fluka and $(NH_4)_2Ce(NO_3)$ (99.9%), $Mg(NO_3)_2{\cdot}6H_2O$, $Al(NO_3)_3{\cdot}9H_2O$, $Zn(NO_3)_2.6H_2O$ (96 – 103%), $LiNO_3$, propidium iodide (PI) and 2′,7′-dichlorofluorescein (DCF) were purchased from Loba chemie. The reagents $Pb(NO_3)_2$, $Hg(NO_3)_2.H_2O$, $NaNO_3$, $Cu(NO_3)_2.3H_2O$, KNO_3, $Ba(NO_3)_2$ (> 99%), and $MgCl_2$ were purchased from Merck; and $Cr(NO_3)_3.9H_2O$ (98–101%), $Cd(NO_3)_2.4H_2O$, $Cr(NO_3)_3.9H_2O$, $Fe(NO_3)_2.9H_2O$, KCl, and NaCl were purchased from Thomas baker. $AgNO_3$ was purchased from RFCL limited. $CaCl_2$ was purchased from BDH chemicals. Luria-Bertani (LB) and agar powder were purchased from Himedia. All glassware were washed with aquaregia (HCl: HNO_3 = 3:1) carefully and rinsed with double distilled water before using them for synthesis.

2.2.2 Synthesis of CFD labeled Au-NPs

The CFD labeled Au-NPs were synthesized by the addition of CFD molecules in aqueous medium (final concentration of CFD molecules in the mixture was 5×10^{-4} M) in $HAuCl_4$ solution (final concentration in mixture was varied from 10^{-4} M to 10^{-3} M) followed by continuous stirring for 2 h at 27 ^{o}C. We have also studied the effect of varying the reaction temperature (10 ^{o}C to 50 ^{o}C) and pH (4 to 8) on Au-NPs size and morphology in the presence of both CFD and $HAuCl_4$ at a final concentration of 5×10^{-4} M. In the synthesis of

CFD labeled Au-NPs, CFD itself provides the sequestration site for Au^{3+} ions and acts as both mild reducing and capping/stabilizing agent, without further use of any other reducing agents or templates.

2.2.3 Isolation of Au-QCs

During the course of the reaction performed at pH 6, the simultaneous production of Au-NPs and Au-QCs in the reduction of $HAuCl_4$ with CFD occurred and the color of the solution changed from an original light-yellow to a final dark-brown. Probably, the Au-QCs have been generated by the modulated reduction of $HAuCl_4$ by CFD at pH 6. Relatively larger particles were removed at the end of reaction through centrifugation at 15000 rpm for 15 min, providing a light-brown supernatant containing the Au-QCs.

2.2.4 Effect of pH and ionic strength on the fluorescence of Au-QCs

We have investigated the effect of pH on the fluorescence of Au-QCs by varying the pH of the medium from pH 4, pH 7, and pH 10 using buffer solutions. The effect of ionic strength of various salts like NaCl, KCl, $MgCl_2$, and $CaCl_2$ on the fluorescence of Au-QCs was also investigated by addition of these salts in a concentration range from 0.01 M to 0.2 M. An aliquot of Au-QCs suspension was added to pH 7 buffer containing various concentrations of NaCl/KCl/$MgCl_2$/$CaCl_2$ salts. The mixture was shaken vigorously and left for 5 min. The fluorescence emission spectra were then recorded at the excitation of 337 nm.

2.2.5 Fluorescence based detection of Hg^{2+} ions using fluorescent Au-QCs

Herein, we have developed the fluorescence quenching based sensor for Hg^{2+} ions. We have investigated the effect of adding various metal ions (100 μM, all metal ions were taken as nitrate salts and the reaction pH were maintained at pH 7 using phosphate buffer)

on the fluorescence of CFD labeled Au-QCs. An aliquot of Au-QCs suspension (10 μL) was added to 1 mL pH 7 buffer containing various concentrations of Hg^{2+} ions. The solution was mixed thoroughly and left to react at room temperature for 5 min. The fluorescence emission spectra were then recorded at the excitation of 337 nm.

2.2.6 Fluorescence microscopic imaging based detection of Hg^{2+} ions in bacterial cells using Au-QCs as Hg^{2+} ion sensing probe

The *E. coli* cell suspension with $O.D._{600}$ (optical density measured at 600 nm) ca. 0.1 was treated with Au-QCs at the final concentration of 20 μg/mL for 2 h. The Au-QCs were first dialyzed with benzoylated dialysis tube with MWCO ca. 2 kDa to ensure the removal ionic impurities and unbound antibiotic molecules. We have also performed the MIC test of dialyzed Au-QCs to ensure the concentration of Au-QCs used should not be itself toxic to the bacterial cells. After 2 h incubation, the cells were pelleted-out by centrifugation at 10,000 g for 10 min at 4 ^{o}C, washed twice with PBS buffer and re-suspended in PBS buffer. An aliquot from of the bacterial cells were taken from the above cells suspended in PBS buffer and incubated for 5 min with Hg^{2+} ions, followed by washing with PBS buffer. Finally, the cells with and without Hg^{2+} treatments were drop-casted onto the two separate glass slides and covered with coverslip by nail polish for fluorescence microscopic examination.

2.2.7 Antibacterial study of Au-NPs

The Au-NPs synthesized at pH values of 4, 5 and 6 were dialyzed against double-distilled water for 24 h and named as pH 4 Au-NPs, pH 5 Au-NPs, and pH 6 Au-NPs, respectively. The water was replaced and changed at least two times during the dialysis process, before using the dialyzed Au-NPs for bacterial cytotoxicity determination to ensure the removal

of ionic impurities and unbound antibiotic**.** For this purpose, *E. coli* culture (NCIM 2064) was sourced from National Collection of Industrial Microorganisms (NCIM), CSIR-National Chemical Laboratory, Pune, India and was stored as agar slant at 4 ^{o}C (not exceeding 2 weeks). For every experiment, a loop-full of bacterial culture was taken and inoculated in fresh LB medium and grown at standard culture condition of 37 ^{o}C at 180 rpm shaking speed.

2.2.8 Minimum inhibitory concentration (MIC) determination

The MIC value corresponds to the concentration of compound at which the bacterial growth is inhibited by as much as 90% compared with the control. We determined the MIC value using microbroth dilution method. For this purpose, overnight grown culture of *E. coli* cells was added into fresh LB medium to give a concentration of $O.D._{600}$ ca. 0.1. This culture was equally distributed in 9 different culture tubes. Eight culture tubes were added with various amounts of Au-NPs (pH4/ pH5/ pH6, on the basis of antibiotic concentration used for reaction and assumed that all the antibiotic molecules consumed at the time of Au-NPs synthesis)/ CFD in such a way that final concentration will be 64, 32, 16, 8, 4, 2, 1, 0.5 μg/mL. The culture tubes without NPs and without inoculum were used as positive and negative control, respectively. The cultures were then grown at 37 ^{o}C, 180 rpm for 18 h and the optical density at 600 nm was measured. The experiment was done in triplicates.

2.2.9 Reduction in cell-growth

For this purpose, overnight grown culture of *E. coli* cells were used as seed culture. This seed culture was added into fresh LB medium to give a concentration of $O.D._{600}$ ca. 0.1. This culture was equally distributed in five different culture tubes. Then, the CFD labeled Au-NPs (synthesized at pH 4, pH 5, pH 6), and CFD were added into four different culture

tubes at the final concentration of 64 μg/mL. The culture without nanoparticles was used as positive control. The cultures were then grown at 37 ^{o}C, 180 rpm for 18 h. The culture was withdrawn from each culture tube at every 2 h and O.D.$_{600}$ was measured. The experiment was done in triplicates.

2.2.10 Cell survival assay

The cell survival assay was performed using colony count method. For this, the *E. coli* cell suspension (in PBS) with O.D.$_{600}$ ca. 0.1 was incubated with Au-NPs (synthesized at pH 4, 5 and 6) and CFD at the final concentration of 64 μg/mL for 24 h at 180 rpm and 37 ^{o}C temperature. The cells suspended in PBS buffer were used as control. 100 μl aliquots were taken out from each sample at 0 h and 24 h; and diluted to 10^{-3} dilution, plated on the petri plate and incubated at 37 ^{o}C for 18 h to visualize the colonies. The digital images of the plates were captured. The experiment was performed in triplicates.

2.2.11 Sample preparation for SEM imaging

The *E. coli* cell suspension with O.D.$_{600}$ ca. 0.1 was treated with Au-NPs (synthesized at pH 4, 5 and 6) and CFD at the final concentration 64 μg/mL for 4 h. Following that, the cells were pelleted-out by centrifugation at 10,000 g for 10 min at 4 ^{o}C, washed twice with PBS buffer and resuspended in 2% glutaraldehyde solution and incubated for 20 min. Then, these cells were again washed twice with PBS buffer (pH=7.4, 0.01M) by centrifugation at 10,000 g for 10 min at 4 °C and were drop-casted on to the Si wafer and coated with gold for SEM imaging.

2.2.12 Sample preparation for fluorescence microscopy

The *E. coli* cell suspension with O.D.$_{600}$ ca. 0.1 was treated with Au-NPs (synthesized at pH 4, 5 and 6) and CFD at the final concentration 64 μg/mL for 24 h. The *E. coli* cell

suspension in PBS buffer was treated as control. After 24 h incubation, the cells were pelleted-out by centrifugation at 10,000 g for 10 min at 4 ^{o}C, washed twice with PBS buffer and resuspended in PBS buffer. The propidium iodide (PI) dye was added at the final concentration of ca. 10 μM, incubated for 20 min in dark and washed with PBS buffer. Finally, the cells were drop-casted onto the glass slide and covered with coverslip by nail polish.

2.2.13 ROS determination

The *E. coli* suspension with O.D.$_{600}$ ca. 0.1 was treated Au-NPs (concentration 64 μg/mL) for 6 h. After incubation period of 6 h, the cells were pelletized by centrifugation at 10,000 g for 10 min at 4 °C, washed twice with PBS buffer and re-suspended in PBS buffer. DCF dye was added to above bacterial suspension at a final concentration of 5 μM and incubated for 1 h, at mild shaking. DCF dye is a non-fluorescent dye and gets converted to fluorescent dye in the presence of ROS; it determines the presence of intracellular ROS. The presence of fluorescent DCF dye was measured at an emission wavelength of 525 nm upon exciting the sample at an excitation wavelength 488 nm. The ROS concentration is considered directly proportional to the fluorescence intensity of the DCF dye. The experiment was performed in triplicates.

2.3 Characterization techniques

Absorbance spectra were recorded using a Jasco UV-vis-NIR dual beam spectrometer (Model V570) operated at a resolution of 2 nm. Excitation and emission spectra were recorded using a Cary Eclipse photoluminescence spectrophotometer from Varian equipped with Xenon flash lamp. Time-resolved fluorescence measurements were performed on a time correlated single photon counting (TCSPC) spectrometer (Horiba

Jobin Yvon IBH, UK). The detailed description of the instrument can be found elsewhere.[50] TEM images of CFD labeled Au-NPs were recorded using Tecnai G-2 T20 transmission electron microscope (TEM) working at accelerating voltage of 200 kV. HR-TEM measurements on the CFD labeled Au-QCs were performed using a Tecnai F30 HR-TEM from FEI Inc., equipped with field emission source operating at 300 kV with S-TWIN objective lens and Cs value of 1.2 mm. The point resolution of the microscope was 0.24 nm. The sample was drop-casted on a carbon coated copper grid and air-dried for imaging. The cyclic voltammetry measurements were performed using CH Instruments Potentiostats. The CFD solution concentration was kept constant to 1mM and the lithium perchlorate (100 mM) was used as an electrolyte. The counter, working and reference electrodes were Pt foil, Pt wire and Ag/AgCl electrodes. Powder XRD patterns were recorded using a PANalytical X'Pert PRO instrument and the iron-filtered Cu-Kα radiation (λ = 1.54 Å) in the 2θ range of 10–80° with a step size of 0.02°on drop-coated samples on glass substrate. FTIR spectra were obtained using a Perkin-Elmer Spectrum One instrument. The spectrometer operated in the % transmission mode at a resolution of 2 cm^{-1}. Raman spectroscopy measurements were recorded at room temperature on an HR 800 Raman spectrophotometer (Jobin Yvon, Horiba, France) using monochromatic radiation emitted by a He-Ne laser (633 nm), operating at 20 mW. The experiment was repeated several times to verify the consistency of the recorded spectra. The samples for the Raman studies were prepared simply by drop-casting the liquid onto the glass slide. X-ray photoelectron spectroscopy (XPS) analysis was done on a VG Micro Tech ESCA 3000 instrument at a pressure of < $1x10^{-9}$ Torr with the overall resolution of 1 eV. The spectra were recorded with unmonochromatic Mg Kα radiation at pass energy of

50 eV and an electron take off angle of 60^{o}. The sample was drop casted on a clean Si wafer, and air-dried for analysis. Mass spectra were collected by using MALDI TOF/TOF Instrument (AB SCIEX TOF/TOF^{TM} 5800 System). As-synthesized Au-QCs suspension was mixed with DHB (in methanol) in 1:1 ratio by volume. Then, 0.5 µL of this solution was deposited on a MALDI target plate and air-dried. The plate was inserted into the instrument and irradiated by a Nd: YAG laser. Scanning electron microscopic study has been performed using FEI Quanta 200 environmental SEM to evaluate the morphological changes in the bacterial cells in presence and absence of Au-NPs. A PALS Zeta Potential Analyzer Ver 3.54 (Brookhaven Instrument Corps.) was used to determine the electrophoretic mobilities. Mobilities were converted to zeta potential (ζ) using the Smolochowski model. The fluorescence microscopic images were taken by Carl Zeiss inverted fluorescence microscope model Axio Observer.Z1.

2.3.1. DFT computational method

All the theoretical calculations were performed using Gaussian 09 programming package.[51] The geometrical optimization of CFD and its various possible conjugations with Au^{3+} ions were calculated in gas phase as well as bulk solvation using Density Functional Theory (DFT) with B3LYP hybrid functional, which is found to be very useful in predicting molecular properties.[52–55] In the present study, Lanl2dz basis set[56] was employed for the heavy Au atom as recent reports indicated its good performance[57–59] and 6-311++g(d, p) basis set for C, H, N, O and S atoms containing molecules in all the calculations. Since experimentally all the synthesis were performed in aqueous environment, so having the condition quite close to the experiment, polarizable continuum model (PCM)[60] was also taken into account for the bulk solvent effects in all the calculation.

2.4 Results and Discussion

2.4.1 Study of growth kinetics of CFD labeled NPs

In order to visualize the effect of variation in the $HAuCl_4$/CFD concentration, temperature and pH on the morphology of the particles, we performed a detailed UV-vis-NIR spectroscopic and TEM study as follows:

2.4.1.1 Effect of $HAuCl_4$/CFD concentration on the morphology of the Au-NPs

As indicated earlier, CFD labeled Au-NPs have been synthesized by the addition of CFD aqueous solution (final concentration in the mixture was 5×10^{-4} M) in $HAuCl_4$ aqueous solution (final concentration in the mixture was varied from 10^{-4} M to 10^{-3} M) and incubated for 2 h at 25 ^{o}C followed by UV-vis-NIR spectroscopic analysis (figure 1a). When $HAuCl_4$ concentration in the mixture was 10^{-4} M, a single peak was observed in the visible region ca. 550 nm that corresponds to the transverse component of surface plasmon resonance (TSPR). The TSPR peak indicates the formation of isotropic NPs in the suspension. The broadness of the TSPR peak and long tail part extending into NIR region also indicate the presence of polydispersed particles. When the final concentration of $HAuCl_4$ was increased to 3×10^{-4} M, the NIR absorption get enhanced along with a relative increase in the TSPR peak and an appearance of shoulder at ca. 720 nm due to longitudinal component of surface plasmon resonance (LSPR).

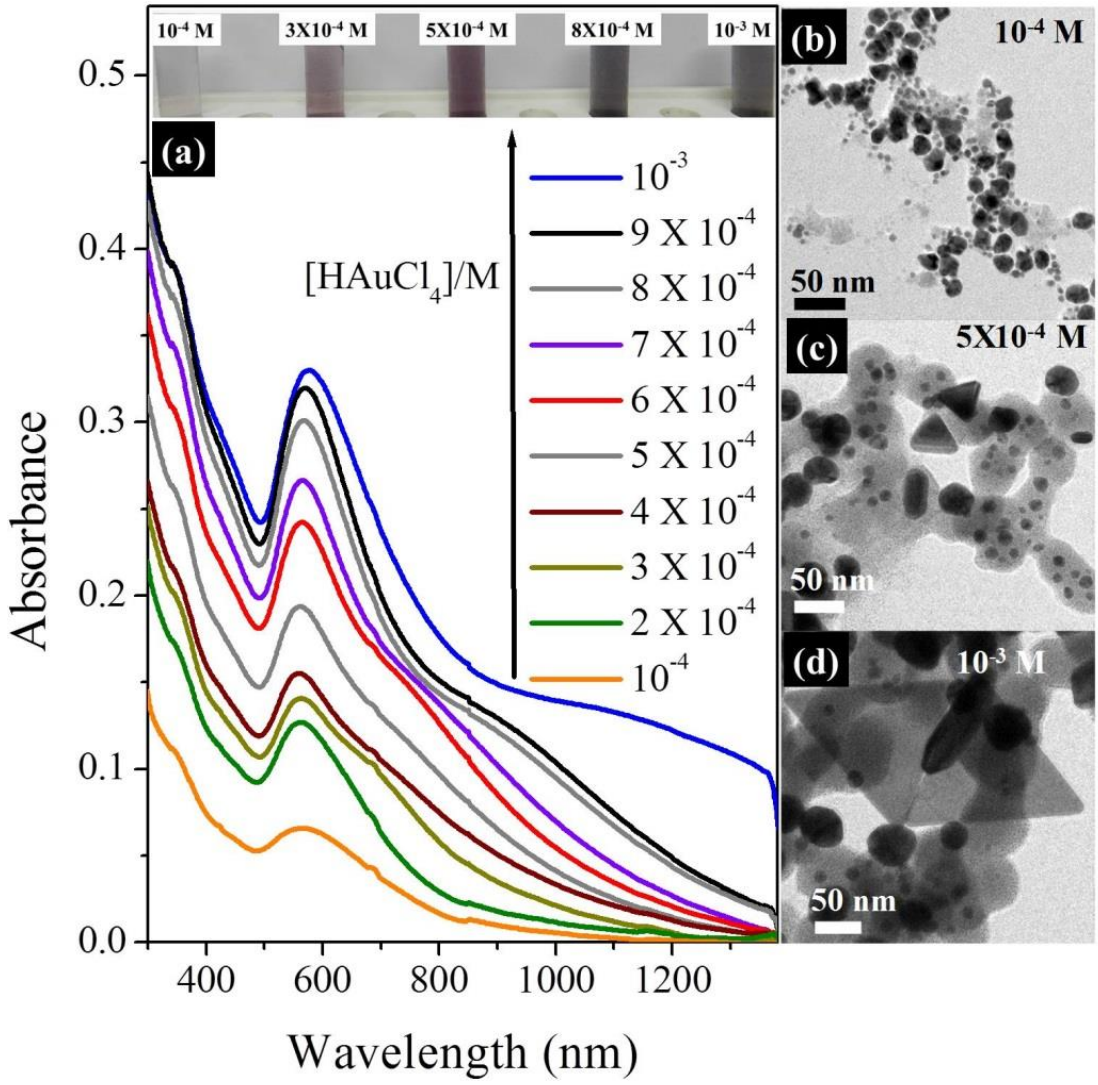

Figure 1. *(a) The UV-vis-NIR spectra for the CFD labeled Au-NPs synthesized at various final concentrations of $HAuCl_4$ (10^{-4} M to 10^{-3} M) while keeping the CFD final concentration same to 5×10^{-4} M. The absorbance values for various curves are shifted with respect to each other for the sake of clarity. TEM images of CFD labeled Au-NPs synthesized at various final concentrations of $HAuCl_4$ (b) 10^{-4} M, (c) 5×10^{-4} M, and (d) 10^{-3} M while keeping the CFD final concentration same to 5×10^{-4} M. The polydispersity of the nanoparticles is due to inherently slow reaction kinetics as the antibiotic molecules are considered weak reducing agents.*

This feature indicates the presence of anisotropic Au-NPs (along with isotropic NPs) with an increasing fraction.[9] Interestingly, when the final concentration of $HAuCl_4$ in the mixture was further increased to 8×10^{-4} M and 10^{-3} M, the LSPR peak (and overall absorption in the NIR region) became more prominent with continuous shift towards higher wavelength at ca. 870 nm and 1100 nm, respectively, (figure 1a) which is symptomatic of an increment in the edge length of anisotropic nanoparticles.[61]

The influence of $HAuCl_4$/CFD concentration on the morphology of as-synthesized CFD labeled Au-NPs has also been studied by TEM and the results were consistent with UV-vis spectroscopic results. The TEM images in the figures 1b, c, and d correspond to the formation of CFD labeled Au-NPs when the final concentration of $HAuCl_4$ in the mixture was 10^{-4} M, 5×10^{-4} M, and 10^{-3} M, respectively (for CFD concentration 5×10^{-4} M). For the $HAuCl_4$ concentration of 10^{-4} M, a clear observation of bimodal distribution of isotropic (quasi-spherical) NPs with an average size ca. 13 nm was noticed. When the $HAuCl_4$ concentration was increased to 5×10^{-4} M, a small population of triangular shaped Au-NPs (edge length ca. 40 nm), with a large population of quasi-spherical NPs formed. Upon increase in the concentration to 10^{-3} M, a larger population of triangular shaped particles (edge length ca. 150 nm) was synthesized. As we discussed earlier, the polydispersity of the Au-NPs is due to the fact that antibiotic molecules are weak reducing agents in comparison to citric acid and $NaBH_4$ etc, which leads to relatively slow growth kinetics that, in turn, allows the low energy surface facets to expose and bind with chloride ions. For each Au^{3+} ion, there would be four times increment in the Cl^- ions in the solution. Retardation of growth along the <111> direction due to preferential chemisorption of Cl^- ions on the (111) lattice planes could be the conceivable reason behind the formation of

anisotropic nanostructures.[62] Further, to study the effect of variation of temperature and pH, on the synthesis of Au-NPs by CFD, equimolar (5×10^{-4} M) concentration of both CFD and $HAuCl_4$ in final solution was used as a default concentration. The results are discussed in the sections below.

2.4.1.2 Effect of reaction temperature on the morphology of the Au-NPs

The effect of temperature on the synthesis of CFD labeled Au-NPs was also studied by mixing the pre-thermalized (at the specific temperature mentioned here) solutions of CFD and $HAuCl_4$ (final concentration of both in the mixture was 5×10^{-4} M) at a temperature range from 10 ^{o}C to 50 ^{o}C and corresponding UV-vis-NIR spectra have been shown in figure 2a. When the reaction temperature was 10 ^{o}C, in addition to the TSPR peak, we found a broad absorption even beyond 1200 nm, which indicated the growth of relatively large anisotropic nanostructures. However, for the growth at higher temperatures (ca. 20 ^{o}C and 30 ^{o}C), the NIR absorption got reduced and the relative peak intensity of TSPR got enhanced. The TSPR peak also showed blue-shift, indicating the reduction in the particle size.[61] Interestingly, when the reaction was carried out at further higher temperatures (40 ^{o}C and 50 ^{o}C), the LSPR peak disappeared suggesting the formation of isotropic Au-NPs only (figure 2a).

Figures 2 b and c compare the TEM images of CFD labeled Au-NPs synthesized at 50 ^{o}C and 10 ^{o}C, respectively. At 50 ^{o}C, the growth of nearly isotropic NPs was observed with an average size ca. 15 nm (figure 2b). At 10 ^{o}C, a sharp change in the particle morphology can be easily noticed with a larger fraction of triangular shaped NPs (edge length ca. 120 nm). These results were consistent with UV-vis-NIR absorption spectroscopy.

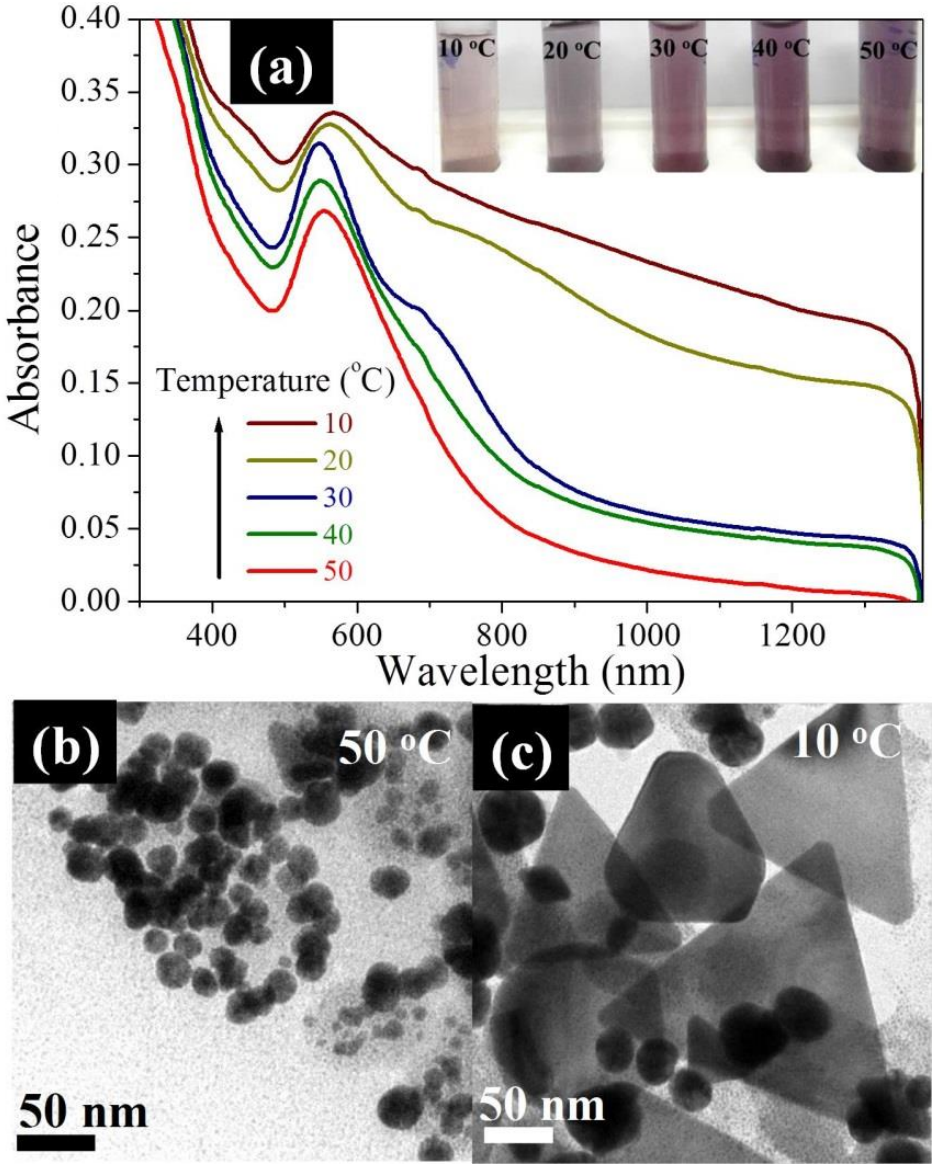

Figure 2. *(a) UV-vis-NIR spectra of CFD labeled Au-NPs synthesized at various temperatures (at final concentration of 5 × 10^{-4} M for both $HAuCl_4$ and CFD). The absorbance values for various curves are shifted with respect to each other for the sake of clarity. TEM images of CFD labeled Au-NPs synthesized at (b) 50 ^{O}C, and (c) 10 ^{O}C of reaction temperature when the final concentration of both CFD and $HAuCl_4$ was 5×10^{-4} M.*

The synthesis of gold nanotriangles is a relatively slow process and can occur at low temperature where the rate of reduction of metal ions become low and possibly

facilitates the oriented growth of nuclei and thus promotes the formation of anisotropic NPs.[63–65] Increase in the temperature of the reaction results in an increase in the rate of reduction of gold ions which leads to an enhanced nucleation rate and the consumption of most of the chloroaurate ions in the formation of nuclei, results in the stalled secondary reduction process on the surface of the preformed nuclei.[61] As a result, a much higher population of spherical NPs in comparison with triangular ones was obtained which shows that a simple variation in the reaction temperature enables the synthesis and tailoring of the size of the triangular NPs.

2.4.1.3 Effect of reaction pH on the morphology of the Au-NPs

The pH effect on the synthesis of Au-NPs has also been investigated by mixing the CFD and $HAuCl_4$ solutions at final concentration of 5×10^{-4} M from pH range 4 to 8. The drastic changes have been observed, when the reaction was performed at different pH environments. A comparison of the UV-vis-NIR spectra indicated that, as the pH of reaction was increased from 4 to 5, the TSPR peak is blue-shifted from ca. 566 nm to ca. 532 nm and the color of the suspension changes from purple to intense red, indicating a decrease in the average size of quasi-spherical Au-NPs. Interestingly, at pH 6, the color of suspension completely changed to brown and SPR peak almost disappeared with just a broad absorption peak visible at ca. 360 nm, indicating the dominant synthesis of gold particles with size below 2 nm[26] (in addition to some big particles). At pH 7 and 8, the solution became colorless and showed the maximum absorption at ca. 357 nm and ca. 351 nm, respectively. This might be the sign of the presence of gold - antibiotic complexes in the solution (figure 3a).[66,67]

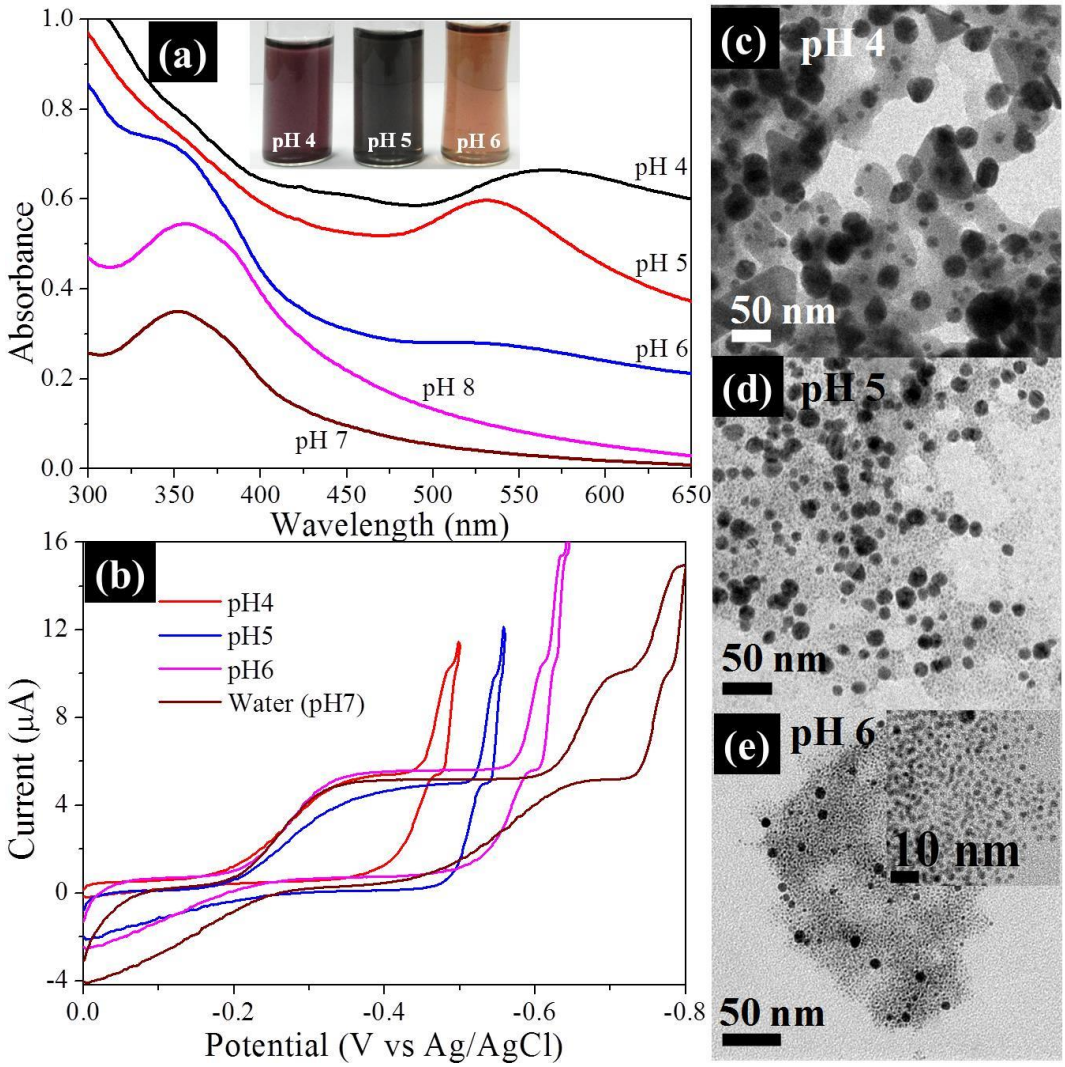

Figure 3. *(a) UV-vis-NIR spectra of CFD labeled Au-NPs synthesized at various pH values. Inset shows the color change at different pH values (at final concentration of 5 × 10^{-4} M for both $HAuCl_4$ and CFD). The absorbance values for various curves are shifted with respect to each other for the sake of clarity. (b) Cyclic voltammetry curves of antibiotic (CFD) in different pH environments showing the shift in reduction potential according to the pH of the environment. TEM images of CFD labeled Au-NPs synthesized at (c) pH 4, (d) pH 5 and (e) pH 6 when final concentration of both CFD and $HAuCl_4$ was 5×10^{-4} M.*

To validate the absorption spectroscopy results, TEM analysis of the CFD labeled Au-NPs synthesized at pH 4, 5 and 6 was performed and presented in figures 3c, d and e. TEM images corresponding to pH 7 and 8 have not been shown (as we were unable to find Au-NPs in these samples). Figure 3c shows the presence of both isotropic and anisotropic population of Au-NPs with an average size ca. 20 nm. At pH 5, a larger fraction of the NPs seems to be isotropic in nature with an average size ca. 12 nm. In agreement with the results of UV-vis-NIR absorption, at pH 6, an average particle size was decreased to ca. 1 nm, along with relatively smaller population of bigger NPs with an average size ca. 6 nm. We have also measured the hydrodynamic diameter of the as synthesized particles at different pH to further have an idea about particle distribution in the suspension and the results were well correlated with the UV-vis and TEM results. The analysis of pH 4 suspension (Figure 4) shows that a large population of particles from 19 - 50 nm with a small population of particles or their aggregates with a size around 200 nm was present. Some aggregates were very large even a size around 5 micron.

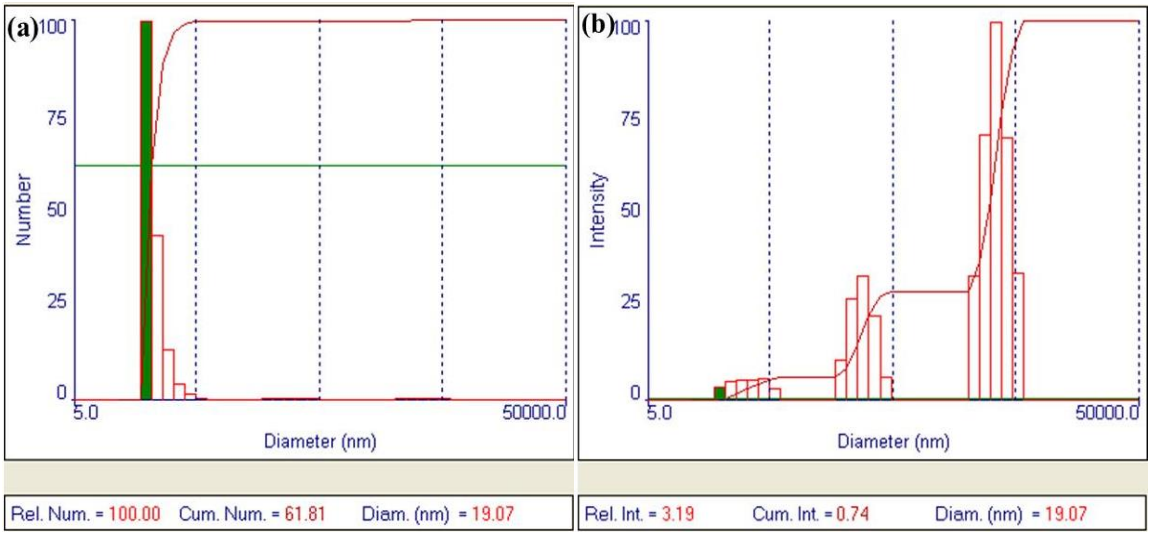

Figure 4. *Dynamic light scattering measurements (a) particle numbers and (b) intensity of scattering light, of gold nanoparticle suspension synthesized at pH 4. The study shows the presence of a large population of ca. 19 - 50 nm particles with a small population of big nanoparticles and large aggregates.*

Whereas at pH 5, a large population of ca. 9 - 13 nm particles with a small population of big nanoparticles and/or their small aggregates (ca. 50 nm) were observed (Figure 5). Figure 6 shows the presence of a large population of ca. 3 - 4 nm particles with a small population of big nanoparticles and/or their small aggregates (ca. 18 nm). Therefore, it can be concluded that the suspension synthesized at pH 4 was highly unstable (starts to settle down within 1.5 h) compared to the particle suspension synthesized at pH 5 and pH 6 (did not settle after storage for even 2 days at room temperature, figure 7). Therefore, pH of the reaction medium is an extremely crucial factor in the synthesis of Au-NPs. It is anticipated that the reduction from Au^{3+} to Au^{0} for synthesis of nanoparticles, would depend on the reduction potential of CFD molecules which itself depends on the pH of the reaction medium.

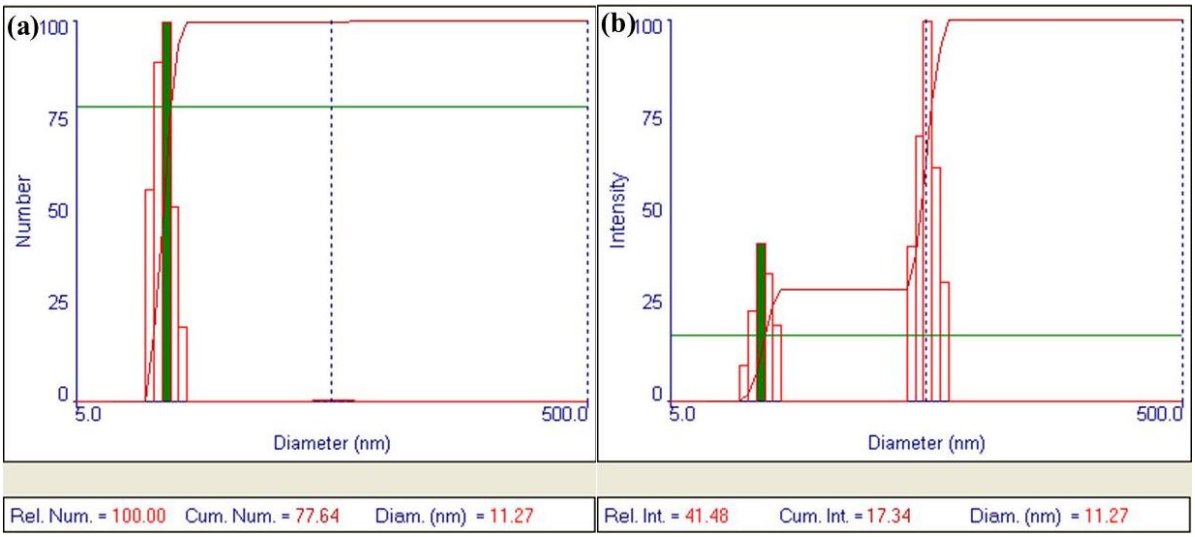

Figure 5. *Dynamic light scattering measurements (a) particle numbers and (b) intensity of scattering light, of gold nanoparticle suspension synthesized at pH 5. The study shows the presence of a large population of ca. 9 - 13 nm particles with a small population of big nanoparticles and small aggregates (ca. 50 nm).*

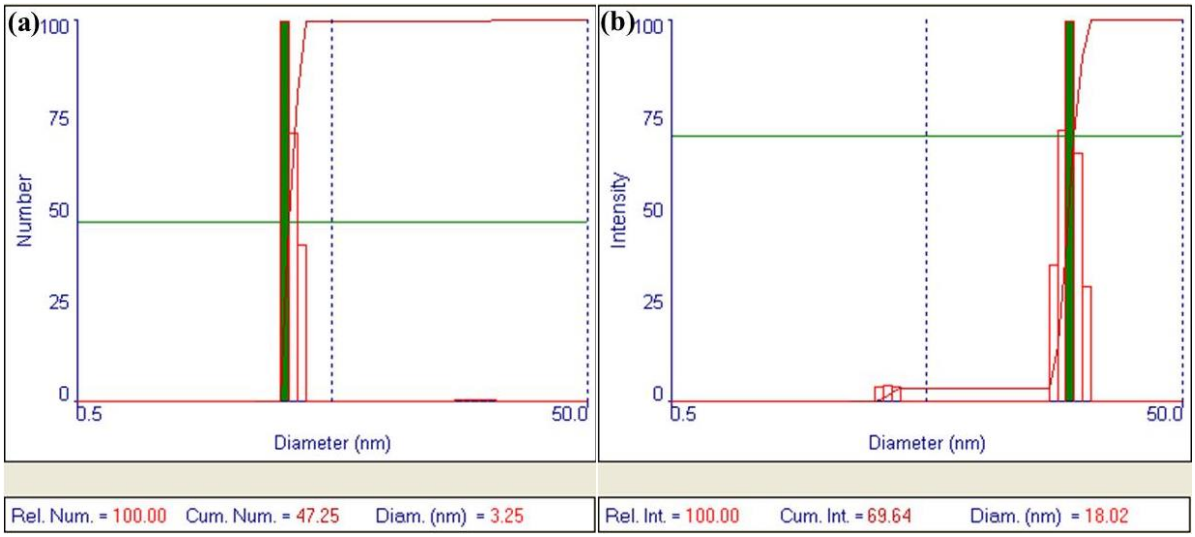

Figure 6. *Dynamic light scattering measurements (a) particle numbers and (b) intensity of scattering light, of gold nanoparticle suspension synthesized at pH 6. The study shows the presence of a large population of ca. 3 - 4 nm particles with a small population of big nanoparticles and small aggregates (ca. 18 nm).*

It is evident from the cyclic voltammetry study that upon increase in the pH from 4 to 7, the reduction potential of CFD has increased from ca. 0.45 V, 0.53 V, 0.58 V to 0.63 V, respectively (figure 3b). Therefore, in summary, the ability of synthesis of Au-NPs using CFD molecule depends on the pH of reaction mixture to the great extant and will decrease upon increase in the pH from 4 to 7.

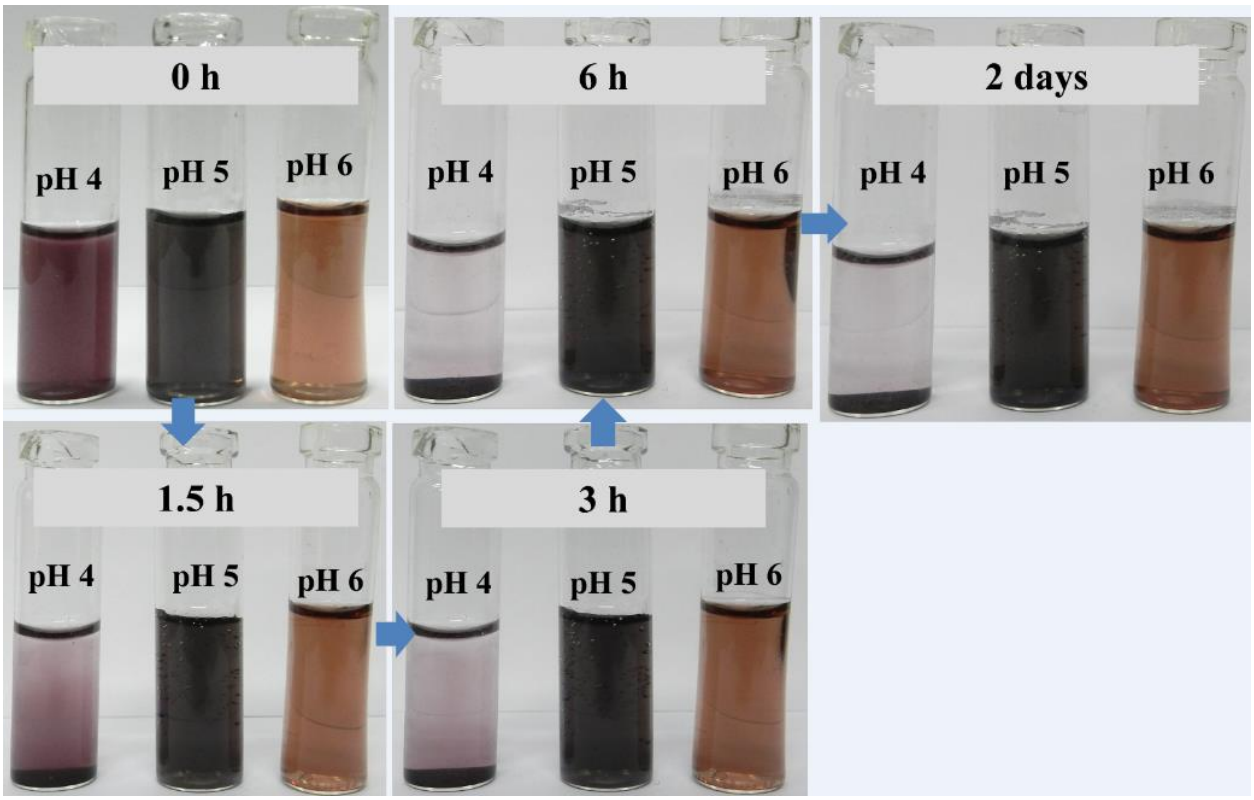

Figure 7. *Photographs of reaction suspension synthesized at pH 4, pH 5 and pH 6 at different time period showing the stability of the suspensions.*

The change in the crystalline structure of the synthesized CFD labeled Au-NPs at different concentration of $HAuCl_4$, temperature and pH of the reaction (where the final concentration of both the constituents (CFD and $HAuCl_4$) was 5×10^{-4} M and reaction temperature was 27 ^{o}C), was studied through PXRD and presented in figure 8a, b and c, respectively. The XRD pattern revealed the relative dominance of (111) plane when the Au-NPs synthesized at higher $HAuCl_4$ concentrations, decrease in the temperature and decrease in pH of the reaction indicating the increase in the synthesis of anisotropic nanostructures.

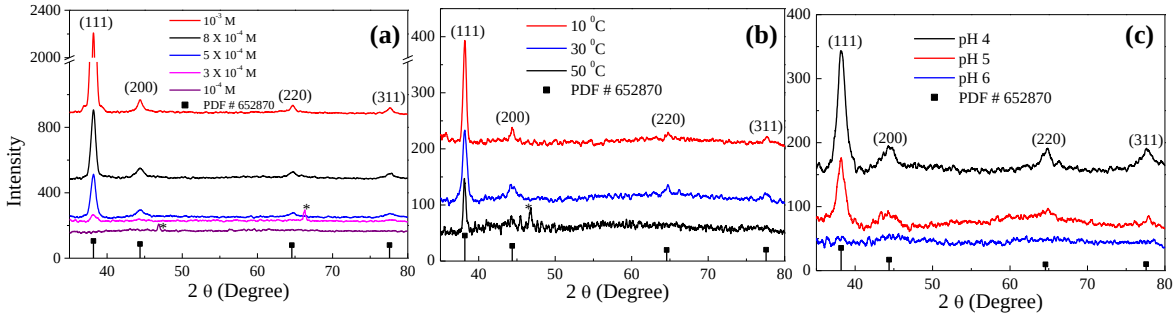

Figure 8. *Powder X-ray diffraction pattern of CFD labeled Au-NPs synthesized at (a) different concentrations of $HAuCl_4$, (b) different temperatures at final concentration of 5 × 10^{-4} M for both CFD and $HAuCl_4$, and (c) different reaction pH at final concentration of 5 × 10^{-4} M for both CFD and $HAuCl_4$. The data is compared with the standard data file # 652870.*

Moreover, FTIR, Raman and XPS studies have been performed to analyze the functional group(s) responsible for binding of CFD to Au-NPs surface. FTIR and Raman spectroscopic results (figures 9 and 10, respectively) indicate the possible involvement of $–NH_2$ and >C=O groups in the binding of CFD to Au-NPs surface. Whereas XPS results in figure 11 indicate that amine and carbonyl group of (probably, *β*-lactam ring) CFD molecule simultaneously plays important role in binding to Au-NPs surface. We also used DFT calculations to investigate the interactions between Au^{3+} ions and CFD molecule where the special emphasis was put on the analysis of geometrical configurations, electronic structures and electron transfers between CFD and Au^{3+} ions complexes during the interaction.

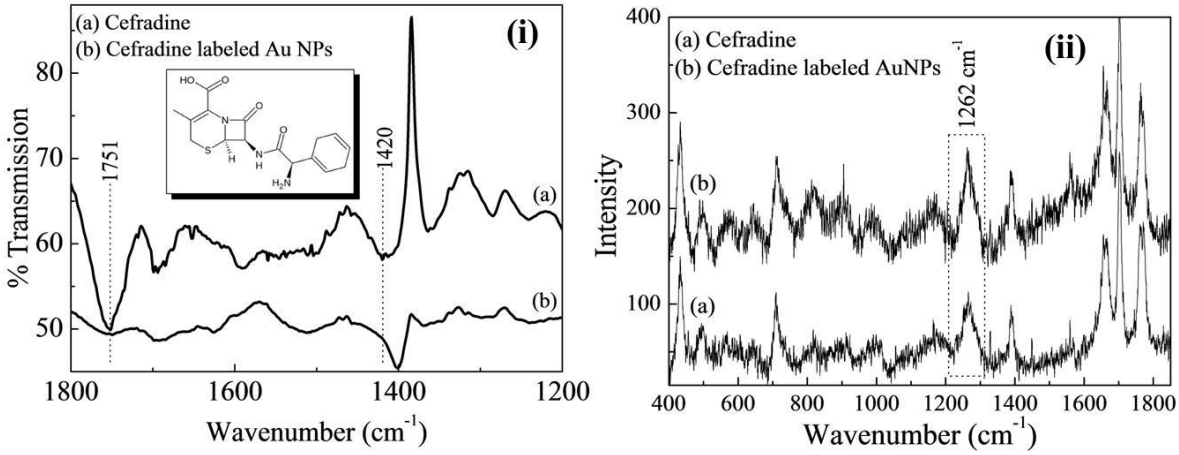

Figure 9. *(i) FTIR spectra and (ii) Raman spectra of (a) 5 × 10^{-4} M CFD aqueous solution and (b) CFD labeled Au-NPs synthesized at final concentration of 5 × 10^{-4} M for both CFD and $HAuCl_4$.*

2.4.2 Calculation of optimized geometries of CFD and its conjugation with Au^{3+} ions using density functional theory

The initial geometries of Au^{3+} ions and CFD complexes were optimized by placing Au^{3+} ions near the possible active sites of CFD molecule. The active sites of CFD molecules are sulfur, carbonyl and amine groups and their corresponding numbering (from 1 to 5) was presented in figures 12 a to f. Due to the electron rich moieties in these groups, the tendency to form the anchoring bonds with Au^{3+} ions in the complexes increases. Further, Au^{3+} can also play the role as a proton acceptor and form nonconventional hydrogen bonds with hydroxide (Au···H–O) as shown in figure 12b. These two factors could also be responsible for the stability of the complexes of CFD with Au^{3+} ions. The interaction between CFD and Au^{3+} ions is either monodentate or bidentate, where, in the latter case, it usually involves non-conventional hydrogen bonding.

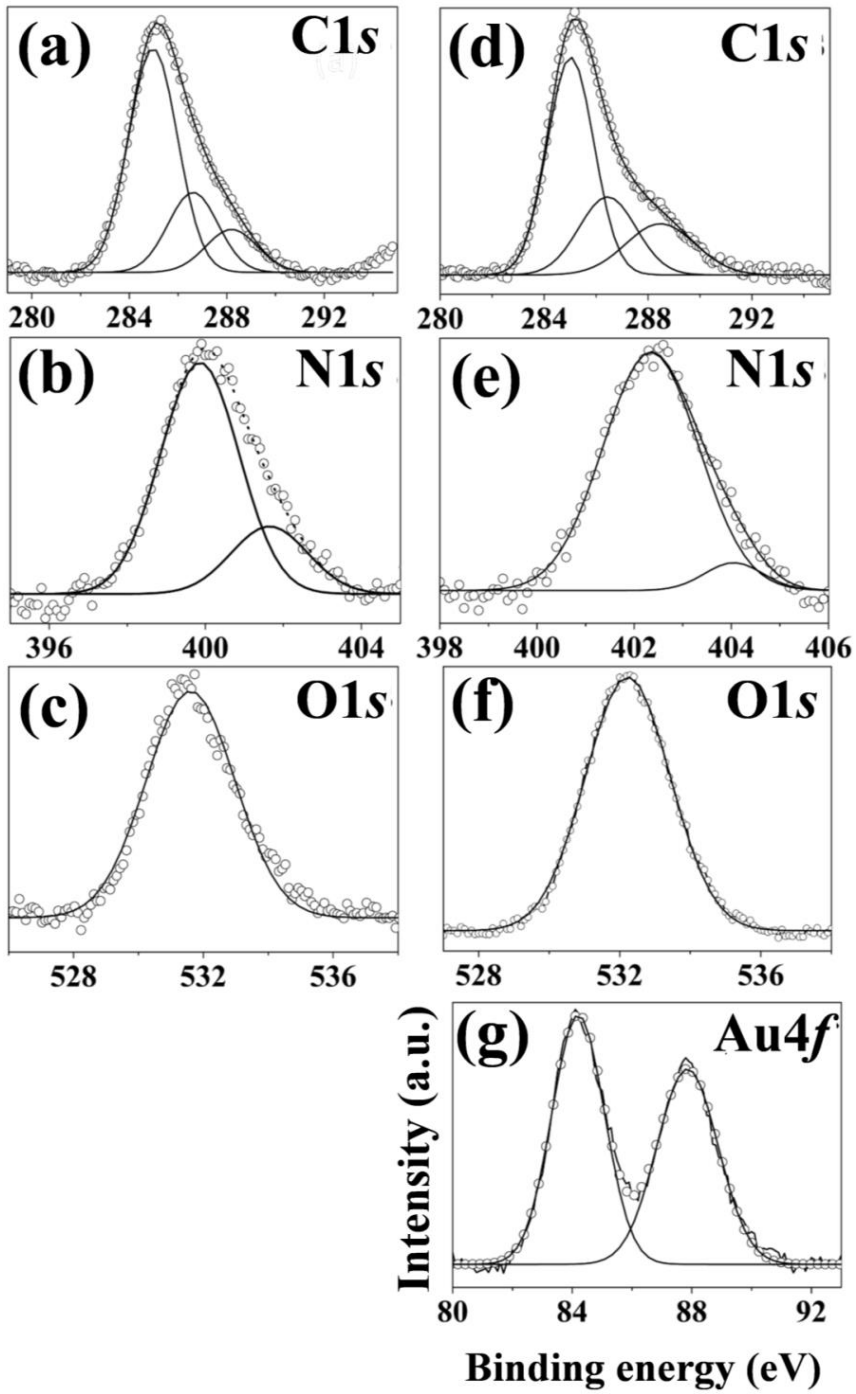

Figure 11. *X-ray photoelectron spectroscopy data for 5 × 10^{-4} M CFD (panels, a-d) and CFD labeled Au-NPs synthesized at final concentration of 5 × 10^{-4} M for both $HAuCl_4$ and CFD (panels, e-i).*

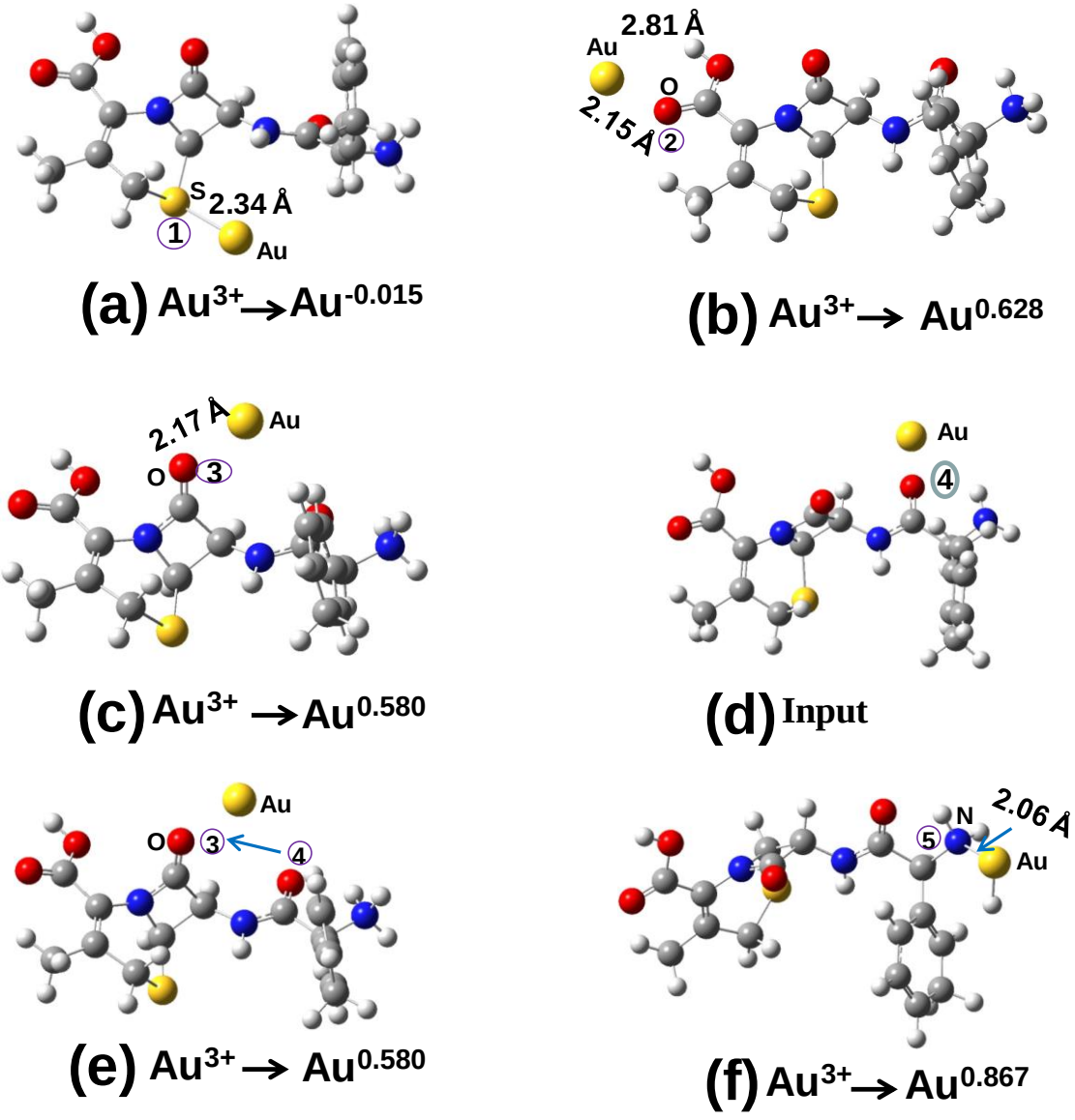

Figure 12. *Optimized interactions of CFD monomers with single Au^{3+} ion in aqueous environment using PCM approach (a) CFD + 1 Au_1, (b) CFD + 1 Au_2, (c) CFD + 1 Au_3, (d) input geometry of CFD + 1 Au_4, (e) output geometry of CFD + 1 Au_4 (f) CFD + 1 Au_5. [Gray, white, red, blue and yellow colors indicate the carbon, hydrogen, oxygen, nitrogen, and sulfur atoms, respectively. However, Au^{3+} is mentioned in different figures separately].*

For this study, we started our calculations by first checking the binding of Au^{3+} ions with sulfur group of CFD (figure 12a i.e. CFD + 1Au_1). Our calculations yield Au-S anchoring bonds with bond length of 2.34 Å, which is very close to the sum of the covalent radii 2.36 Å of S (1.02 Å) and Au (1.34 Å).[68] The result is in good agreement with a previously calculated value of 2.45 Å.[69] Thus, one may expect a stronger covalent contribution to the sulfur bonding. The reduction in charge of Au^{3+} to $Au^{-0.015}$ was also taking place upon formation of Au-S anchoring bonds as shown in Table S1 and figure 12 a. Further, we checked the possibility of binding of Au^{3+} ions with carbonyl group of CFD molecule. There are three possibilities of adding the Au^{3+} ions with carbonyl group of CFD molecule that is denoted by CFD + 1Au_2, CFD + 1Au_3 and CFD + 1Au_4 and displayed in figure 12 b, c, and d, respectively. In the CFD + 1Au_2 and CFD + 1Au_3 complex, the Au-O bond lengths were 2.15 and 2.17 Å and charge reduction down to $Au^{+0.628}$ and $Au^{+0.580}$, respectively. The input geometry of CFD+1Au_4 complex got completely changed to CFD+1Au_3 structure after optimization (see figure 12d to 12e). These results clearly suggest that among the three Au-O bond formations, the CFD+1Au_3, which belongs to β-lactam ring, shows the stronger interactions and reduction property.

The interaction of the Au^{3+} ions with amine group of CFD (see figure 12f i.e. CFD+1Au_5) was also calculated which yields Au-N bond length of 2.02 Å which is very close to the sum of the covalent radii of nitrogen (0.75 Å) and Au (1.35 Å)[69] indicating a stronger bond. The interaction of two CFD molecules with one Au^{3+} ion was also considered and the same trend (discussed above) of bond formation and reduction in Au^{3+} ions were obtained and shown in figures 13 a, b, and c, respectively.

Table S1: Total electronic energies (E), binding energies (BE) and input - output charges for complexes of CFD with Au^{3+} ions

	E (a.u.)	BE (eV)	Charge (Au) (Input)	Charge (Au) (Output)
CFD	-1484.7883	-----	-----	-----
Dimer1	-2969.5810	00.12	-----	-----
Dimer2	-2969.5868	00.28	-----	-----
Dimer3	-2969.6007	00.66	-----	-----
CFD+1Au_1	-1619.7409	52.78	+3	-0.015
CFD+1Au_2	-1619.7168	52.12	+3	+0.628
CFD+1Au_3	-1619.7170	52.14	+3	+0.580
CFD+1Au_5	-1619.6252	49.63	+3	+0.867
2CFD+1Au_1	-3104.5413	53.11	+3	-0.926
2CFD+1Au_3	-3104.5836	54.26	+3	-0.008
2CFD+1Au_4	-3104.3397	47.62	+3	+0.015
CFD+2Au_1	-1754.4480	98.87	+6	+1.158
CFD+2Au_2	-1754.4380	98.60	+6	+1.719
CFD+2Au_4	-1754.4470	98.84	+6	+1.687
CFD+3Au_1	-1888.9979	140.69	+9	+3.566
CFD+3Au_5	-1888.9941	140.59	+9	+3.477

E (Au^{3+}) = -133.0130 a.u.

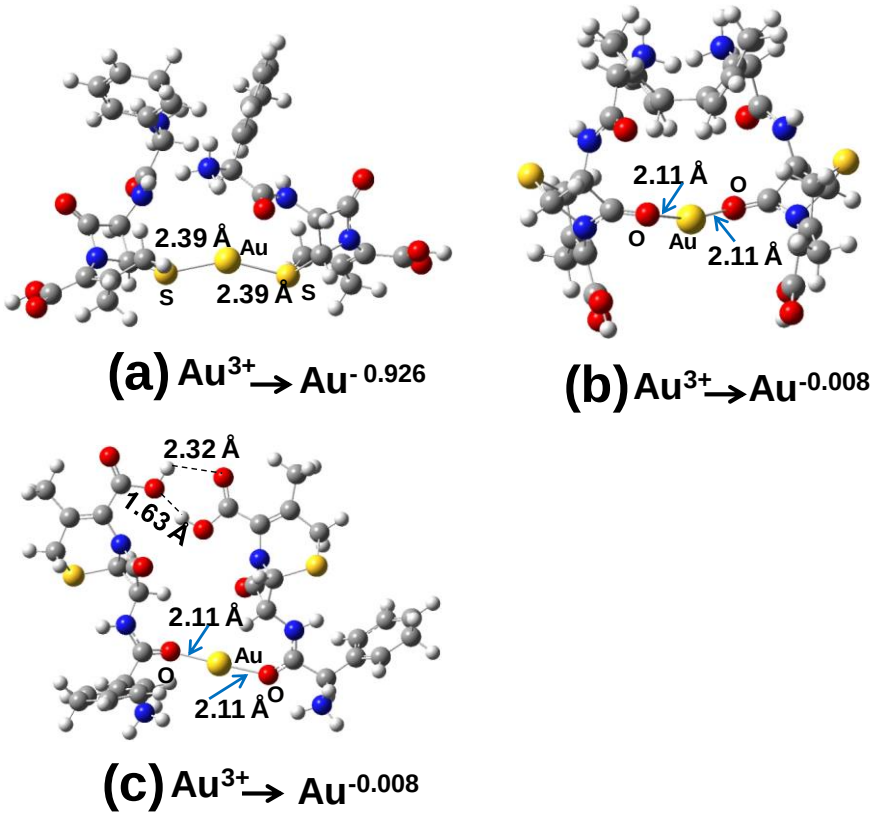

Figure 13. *Optimized interactions of dimers of CFD with single Au^{3+} ion in different possible geometrical forms in aqueous environment using PCM approach (a) 2 CFD + 1 Au_1, (b) 2 CFD + 1 Au_3, (c) 2 CFD + 1 Au_4. [Gray, white, red, blue and yellow colors indicate carbon, hydrogen, oxygen, nitrogen, and sulfur atoms, respectively and the position of Au^{3+} ions is indicated separately in the figure.]*

Apart from studying interaction of one Au^{3+} ion with CFD, we also calculated the interaction of two and three Au^{3+} ions with CFD molecule, simultaneously, especially at sulfur and amine groups as shown in figures 14a to 5c. However, earlier DFT calculations have shown that the DFT results obtained by taking a single metal atom are sufficient to describe the experimental results.[70–72] In the case of CFD + 2Au_1 and CFD + 3Au_1

complex (figure 14a and b), the Au-S anchoring bonds are calculated to be 2.39 Å and 2.37 Å and the corresponding average Au-Au distances are found to be 3.06 Å and 3.30 Å, respectively. In the case of CFD + 3Au_5 complex (figure 14c), the bidentate interaction was taking place where the Au-N and Au-O anchoring bonds were calculated to be 2.07 and 2.08 Å, respectively and the average Au-Au distance was found to be 3.51 Å. The average charge reduction of Au^{3+} ions in different complexes were also presented in Table S1, which clearly indicates the reduction of Au^{3+} to Au^{0} state. Thus, on the basis of strong Au-S, Au-N and Au-O bond, calculated binding energies and reduction in charges of Au^{3+} ions, one may easily conclude that the sulfur plays a dominant role in reduction / binding to Au-NPs surfaces, however, the amine and carbonyl groups (β-lactam ring) also play role in stabilizing the NPs.

The electrostatic potential surface has been mapped and shown in figures 14d, and 14e for CFD and its complex with Au^{3+} ions *i.e.* CFD+ 1 Au_1, respectively (for detailed see supporting information). Such surfaces depict the size, shape, charge density, and site of chemical reactivity of the molecules. The different values of the electrostatic potential at the surface are represented by different colors; red represents regions of most negative electrostatic potential, blue represents regions of most positive electrostatic potential, and green represents regions of zero potential. Potential increases in the order red < orange < yellow < green < blue. In figures 14d, and 14e, the electrostatic potential at different points on the electron density isosurface is shown by coloring the isosurface with contours. In the case of CFD, the O atom of β-lactam ring shows most negative electrostatic potential (red color). However, in the case of CFD+1Au_1 complex the significant amount of charge was transferred as shown in figure 14e.

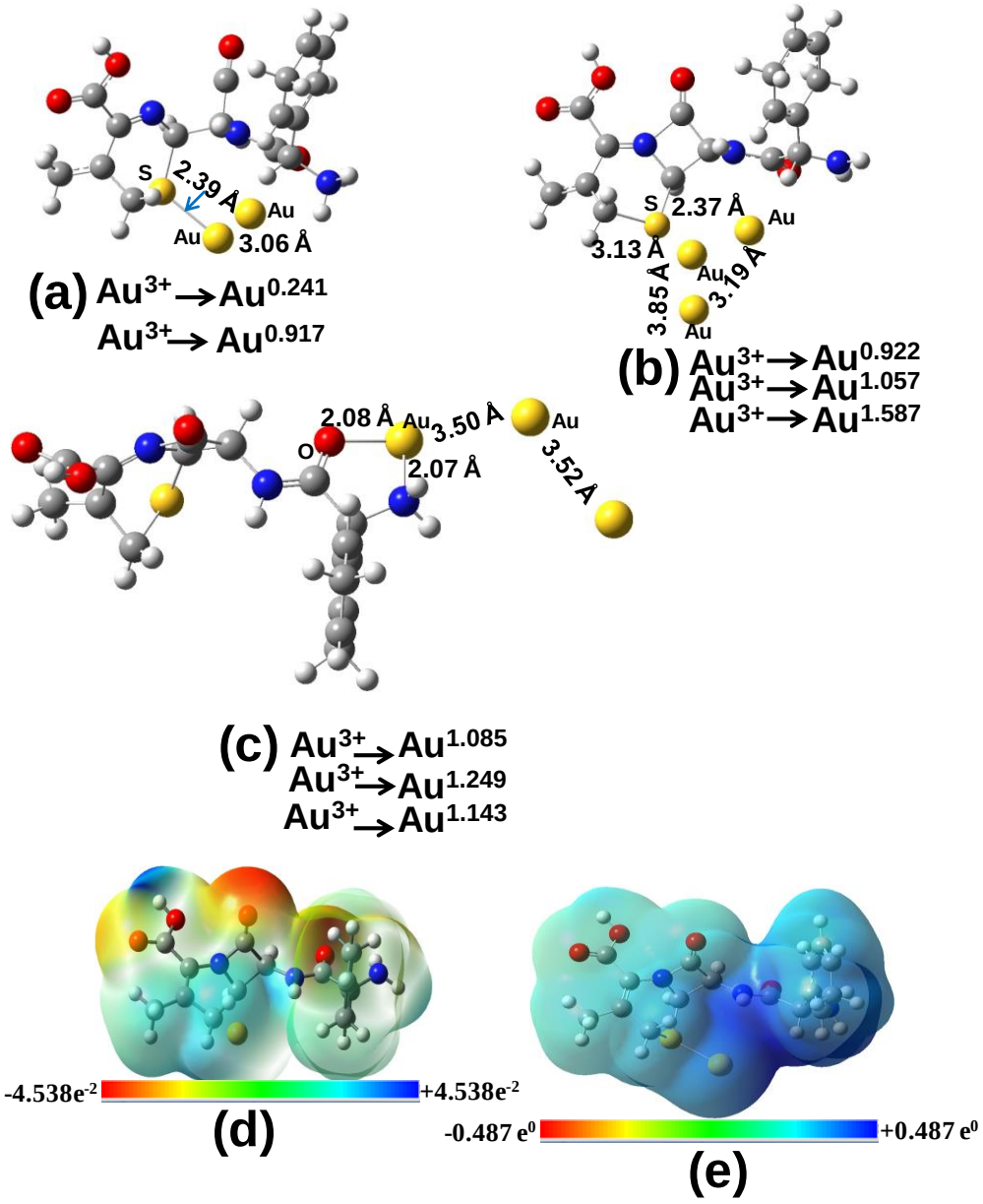

Figure 14. *Optimized interactions of CFD with two and three Au^{3+} ions in aqueous environment using PCM approach (a) CFD + 2 Au_1, (b) CFD + 3 Au_1, (c) CFD + 3 Au_5. Electron density from total SCF density (isoval=0.0004; {mapped with electrostatic potential from total SCF density}) (d) CFD, (e) CFD + 1 Au_1. [The colors of the atoms are discussed in figure 13].*

The time dependent Density Functional Theory (TD-DFT) excited state calculations of the lowest singlet-singlet and singlet-triplet excitations of CFD + 1Au_1 complexes performed in water using PCM method. The calculated values of corresponding most probable electronic transitions having larger vertical excitation and oscillator strength were presented in figure 15 and 16. The TD - DFT calculation of CFD + 1Au_1 complex in aqueous environment gives rise to the most prominent absorption bands at 511 nm with oscillator strength (f = 0.778) due to HOMO → LUMO + 1 transitions. In HOMO orbital of CFD + 1Au_1 system, the electron densities are mainly concentrated on the β-lactam ring moiety; while in LUMO + 1 orbital's the electron densities were shifted towards the Au (see figure 16). Our TD - DFT calculations clearly indicate the evidence of electron transfer from CFD to the Au center and essentially indicate that Au^{3+} ions are reduced to ca. Au^{0} as a consequence of complexation.

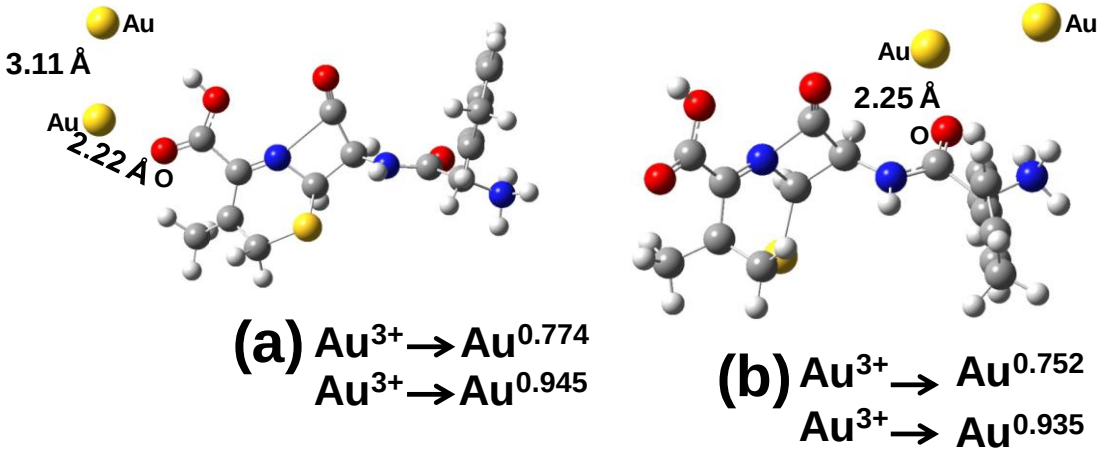

Figure 15. *Optimized interactions of CFD monomer with Au^{3+} ions in aqueous environment using PCM approach (a) CFD + 2 Au_2, (b) CFD + 2 Au_4. [Gray, white, red, blue and yellow colors indicate carbon, hydrogen, oxygen, nitrogen, and sulphur atoms, respectively and the position of Au^{3+} ions is indicated separately in the figure.]*

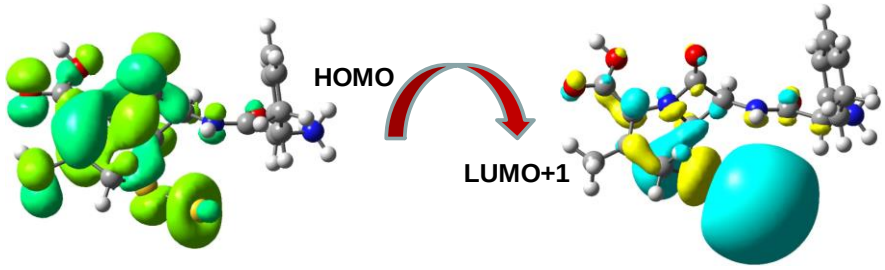

Figure 16. *Highest occupied molecular orbital (HOMO) and lowest unoccupied molecular orbital (LUMO) level frontier orbital contour of CFD+1Au_1, complex using PCM having water environment which show the HOMO→LUMO + 1 electronic transition, an isosurface value of 0.02 e/Å^3 was used for orbital.*

2.4.3 UV-vis spectroscopic and photoluminescence study of CFD labeled Au-QCs

As mentioned earlier, the gold particle suspension synthesized at pH 6, was centrifuged at 15,000 rpm for 10 min to assure the absence of big nanoparticles in the brown colored supernatant. UV-vis spectrum of supernatant shows a continuous absorption in the UV range starting from ca. 470 nm as shown in figure 17a_2 (green curve), in addition, the complete absence of SPR absorption peak at ca. 520 nm, confirms the presence of Au-QCs with the size < 2 nm. It is important to mention that the UV-vis spectrum of Au-QCs was quite different than the UV-vis spectrum of CFD aqueous solution, with a broad absorption peak at ca. 350 nm in Au-QCs spectrum (compare curves (a_1) and (a_2) in figure 17a) which may be due to the ligand to metal ion charge transfer in CFD-Au ion complexes.[66,67]

Photoluminescence properties of Au-QCs have also studied. Usually, the emission peak position of fluorescent Au-QCs depends on the size of the Au-QCs core. According to the spherical Jellium model, Au-QCs with larger core size emit at longer wavelengths [e.g., UV (Au_5), blue (Au_8), green (Au_{13}), and red (Au_{25}) emission].[73,74]

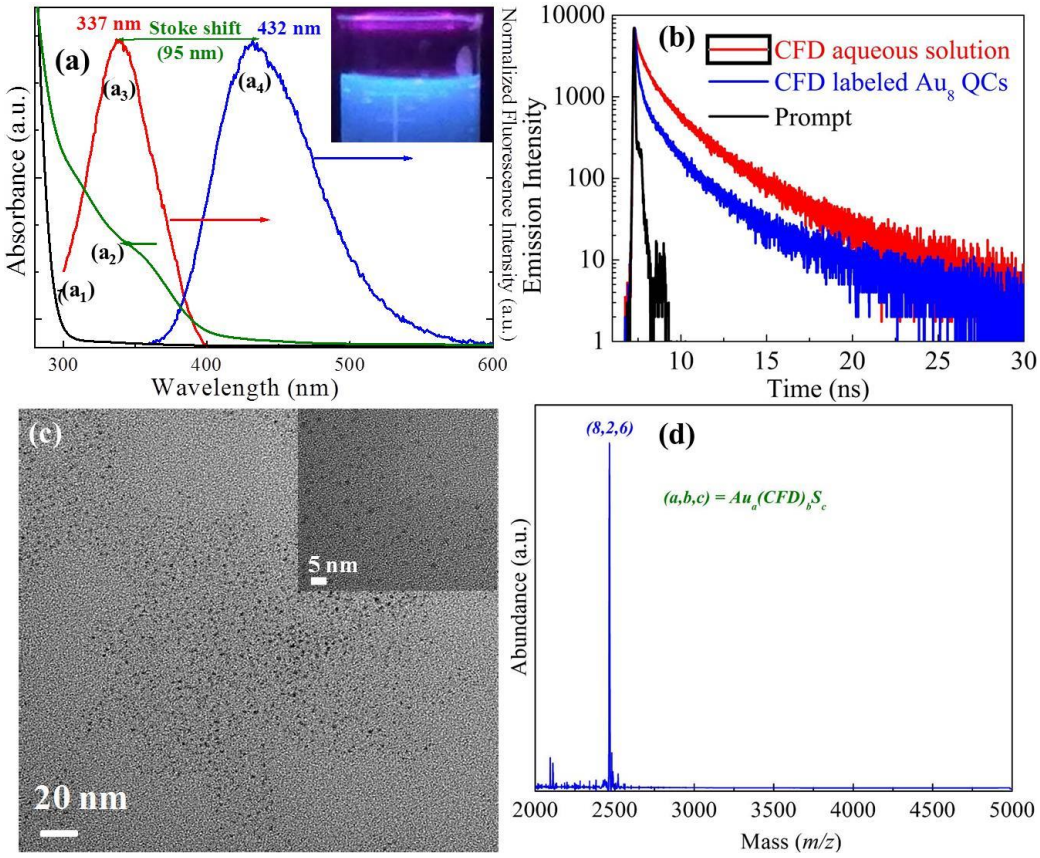

Figure 17. *(a) Absorbance spectra of (a_1) CFD aqueous solution and (a_2) CFD labeled Au-QCs; fluorescence (a_3) excitation spectrum and (a_4) emission spectrum of CFD labeled Au-QCs. Inset shows blue emissive CFD labeled Au-QCs suspension which confirms the formation of quantum clusters. (b) Fluorescence decay of the CFD aqueous solution and Au_8 QCs collected at ca. 432 nm (excited at 337 nm). (c) HR-TEM image of CFD labeled Au_8 QCs and its magnified view (inset). (d) Positive ion linear mode MALDI-TOF mass spectrum for CFD labeled Au_8 QCs. The mass spectrum was baseline corrected by using the Data Explorer software.*

Here, the Au-QCs suspension exhibits the blue luminescence with an excitation and emission maxima at ca. 337 nm and ca. 432 nm (figure 17a_3, a_4), respectively, with Stokes

shift of ca. 95 nm and quantum efficiency ca. 0.9%. This blue emission wavelength is close to the reported values for Au_8 QCs blue emission at λ_{em} = 450 nm from PAMAM[26] and BSA[75] encapsulated Au_8 QCs, λ_{em} = 455 nm from lysozyme type VI stabilized Au_8 QCs[76] and λ_{em} = 465 nm from Au_8 QCs[77] synthesized by etching of mercaptosuccinic acid capped Au-NPs, which shows that the CFD labelled Au clusters were Au_8 QCs. Although, the fluorescence of Au-QCs was less intense, but, it is slightly red shifted by around 4 nm with respect to the fluorescence of CFD alone (figure 18), and more intense than the CFD-Au-NPs and pH 6 reaction suspension which support the synthesis of Au-QCs. To differentiate the Au-QCs component from CFD fluorescence, the fluorescence lifetime decay study has performed on both samples and presented in the next section.

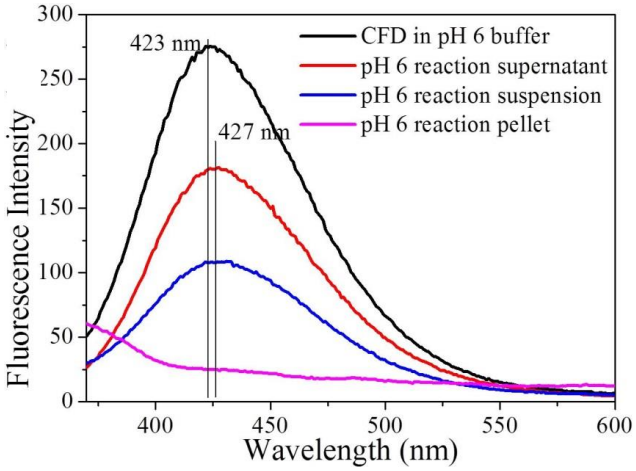

Figure 18. *Fluorescence spectra of CFD in pH 6 buffer (black color), pH 6 reaction supernatant (red color), pH 6 reaction suspension (blue color), and pH 6 reaction pellet (magenta color) showing that with respect to CFD alone, fluorescence signal has red shifted by ca. 4 nm in case of Au-QCs. It can also be seen that the fluorescence is very strong for Au-QCs (supernatant), in comparison to the mixture of Au-NPs and Au-QCs (reaction suspension), and Au-NPs alone (pellet).*

The effect of pH and salt concentration on the photoluminescence of Au-QCs has also studies, and presented in figure 19 and 20, respectively. Upon increase in the pH from 4 to 7, the fluorescence of Au-QCs has not changed but upon further increases in the pH to 10 leads to the enhancement of the fluorescence of Au-QCs almost around two times. However, upon addition of various concentrations (10mM to 200 mM) of salts (NaCl, KCl, $MgCl_2$, and $CaCl_2$) did not affect the fluorescence of Au-QCs meaningfully.

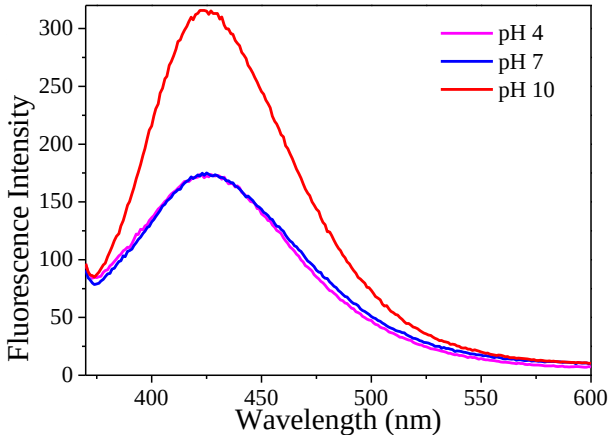

Figure 19. *Fluorescence spectra of Au-QCs as a function of change in the pH of the medium.*

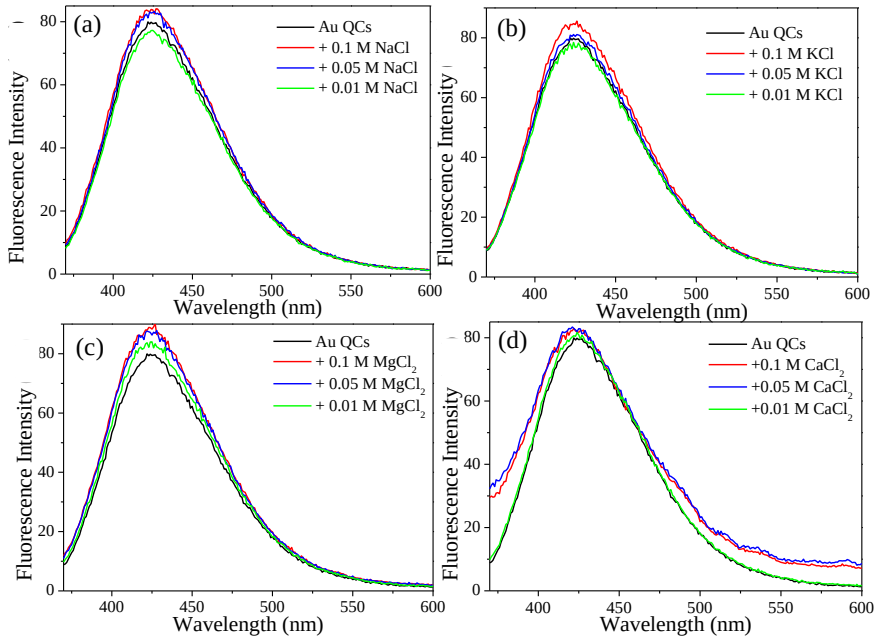

Figure 20. *Fluorescence spectra of Au-QCs in presence of (a) NaCl, (b) KCl, (c) $MgCl_2$, and (d) $CaCl_2$ salts at a concentration ranging from 0.01 M to 0.2 M. The decrease in the fluorescence in case of $CaCl_2$ may be due to the insolubility of $CaCl_2$ in pH 7 buffer.*

2.4.4 Time resolved fluorescence study

The time resolved fluorescence measurements of CFD aqueous solution and CFD labeled Au_8 QCs have been performed and compared in figure 17b. The fluorescence decay time analysis for both CFD aqueous solution and CFD labeled Au_8 QCs reveals a tri-exponential decay profile. The lifetime components for CFD aqueous solution were 0.94 ns (26.4%), 3.44 ns (67%) and 0.12 ns (6.6%) while for CFD labeled Au_8 QCs, the values were 1.21 ns (6.7%), 4.82 ns (0.8%) and 0.097 ns (92.5%). The average decay time for CFD alone was 2.56 ns whereas this value has been decreased to 0.2 ns for CFD labeled Au_8 QCs (Table 1). From the above data, it is clear that the lifetime of Au_8 QCs is markedly different from CFD aqueous solution alone. Generally, it has been observed that Au-QCs exhibit a large component of a few tens of picoseconds and several small components of nanosecond[78] which were consistent with lifetime decay results for CFD labeled Au_8 QCs.

Table 1. *Time resolved fluorescence decay study of CFD aqueous solution and CFD labeled Au_8 QCs.*

Sample	$\bar{N}_1$	$\bar{N}_2$	$\bar{N}_3$	τ_1 (ns)	τ_2 (ns)	τ_3 (ns)	$\langle\tau\rangle$ (ns)	χ^2
CFD aqueous solution	0.028	0.071	0.007	0.94	3.44	0.12	2.56	1.08
CFD labeled Au_8 QCs	0.009	0.001	0.124	1.21	4.82	0.097	0.2	1.07

2.4.5 HR-TEM and MALDI-TOF mass spectroscopic study of CFD labeled Au-QCs

The HR-TEM results also support the formation of Au-QCs (figures 17c and inset) with the size ca. 0.5 nm (the corresponding population distribution histogram is presented in

figure 21a). Figure 21b presents mass spectrum of CFD, which shows substantial difference in comparison with Au-QCs mass spectrum. The figure 17d shows the positive ion linear mode mass spectrum for as-synthesized Au-QCs, using low laser power to suppress the fragmentation. Interestingly, the mass spectrum contains very limited peaks with only one major peak that can be easily distinguished from other peaks. The figure 17d shows one major peak in the mass spectrum at the position of 2466.6 Da (this value is very close to the reported value ca. 2256.4 Da for the mass of Au_8 cluster)[79] assigned to $[Au_8(CFD)_2S_6]$ clusters (following Yang *et al.* peak assignment for gold clusters stabilized with penicillamine,[80] see Table 2).

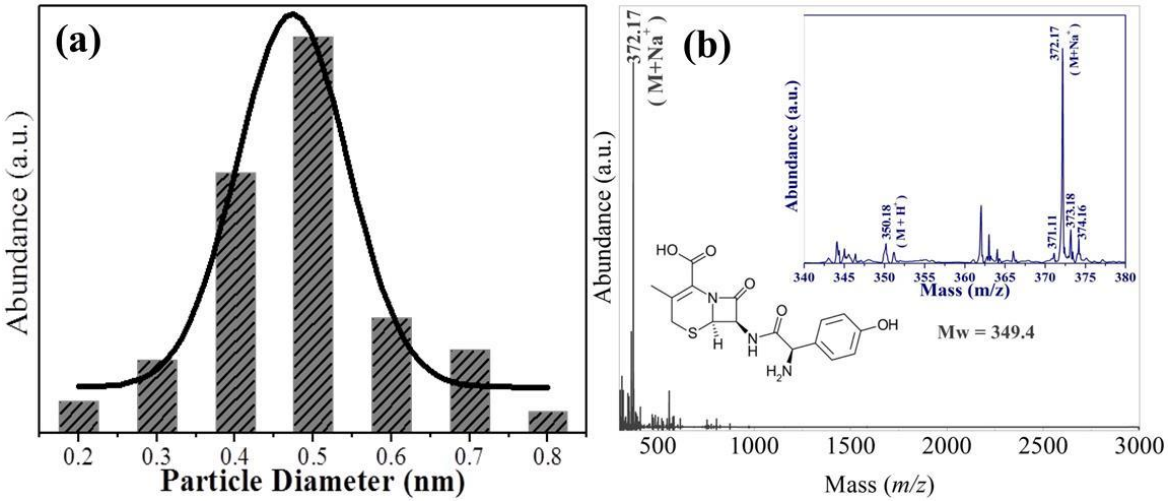

Figure 21. (a) *The population distribution histogram showing the particle size distribution in the Au-QCs sample. The average size of the particles was found ca. 0.5 nm.* ***(b)*** *Positive ion mass spectrum for CFD aqueous solution. Inset shows the expanded view.*

Table 2. Summary of Mass assignments for observed mass peak. Most probable mass composition is shown in bold and highlighted.

Experimental	*a*	*b*	*c*	Calculated mass	Molecular formula

mass					$\{Au_a(CFD)_bS_c\}$
2466.6	5	3	13	2449.9	$[Au_5(CFD)_3S_{13}]$
	5	4	2	2446.6	$[Au_5(CFD)_4S_2]$
	5	4	3	2478.6	$[Au_5(CFD)_4S_3]$
	5	5	0	2731.8	$[Au_5(CFD)_5]$
	6	2	0	1880.6	$[Au_6(CFD)_2]$
	6	3	7	2454.4	$[Au_6(CFD)_3S_7]$
	6	3	8	2486.5	$[Au_6(CFD)_3S_8]$
	6	4	0	2579.4	$[Au_6(CFD)_4]$
	7	2	0	2077.6	$[Au_7(CFD)_2]$
	7	3	1	2461	$[Au_7(CFD)_3S]$
	7	3	2	2491.1	$[Au_7(CFD)_3S_2]$
	7	4	0	2776.4	$[Au_7(CFD)_4]$
	8	1	0	1925.1	$[Au_8(CFD)\ ]$
	8	**2**	**6**	**2466.9**	$\mathbf{[Au_8(CFD)_2S_6]}$
	8	3	0	2623.9	$[Au_8(CFD)_3]$
	9	1	0	2122.1	$[Au_9(CFD)]$
	9	1	10	2442.7	$[Au_9(CFD)S_{10}]$
	9	1	11	2474.8	$[Au_9(CFD)S_{11}]$
	9	2	0	2471.5	$[Au_9(CFD)_2]$
	10	1	4	2447.3	$[Au_{10}(CFD)S_4]$
	10	2	0	2668.5	$[Au_{10}(CFD)_2]$

2.4.6 Application of CFD labeled Au_8 QCs as fluorescence probe for the detection of Hg^{2+} ions in solution

The supernatant (isolated CFD labeled Au_8 QCs) was directly used as a highly sensitive and selective fluorescent "turn-off" sensor for Hg^{2+} ions without further modification. For this purpose, at first, the effect of the addition of various bivalent, trivalent and tetravalent (Hg^{2+}, Cd^{2+}, Pb^{2+}, Ce^{4+}, Ni^{2+}, Cr^{3+}, Ag^{+}, Li^{+}, Mg^{2+}, Al^{3+}, K^{+}, Ba^{2+}, Zn^{2+}, Cu^{2+}, Na^{+} and Fe^{3+}) metal ions (200 μM) on the fluorescence of CFD labeled Au_8 QCs was studied.

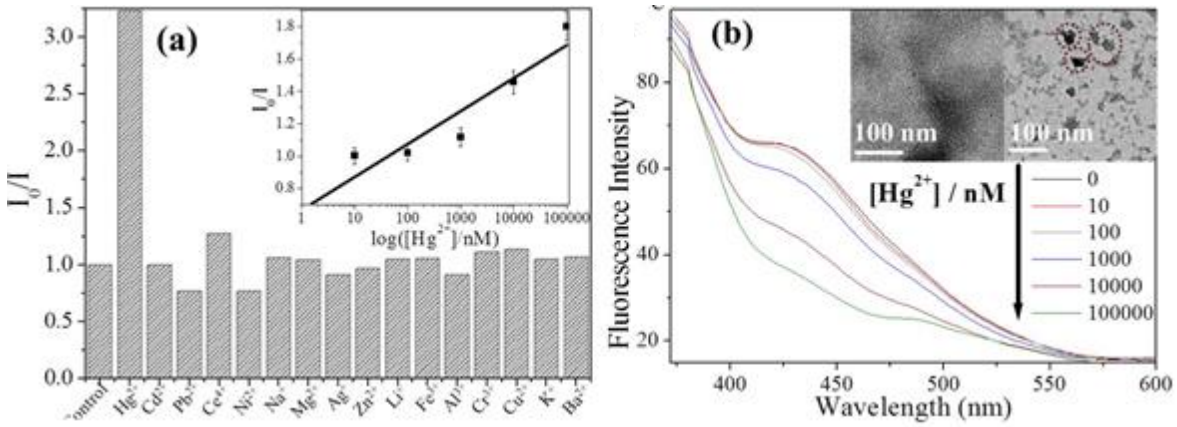

Figure 22. *(a) Relative fluorescence (I_0/I) of CFD labeled Au_8 QCs at an excitation wavelength ca. 337 nm in the presence of various metal ions (Hg^{2+}, Cd^{2+}, Pb^{2+}, Ce^{4+}, Ni^{2+}, Cr^{3+}, Ag^{+}, Li^{+}, Mg^{2+}, Al^{3+}, K^{+}, Ba^{2+}, Zn^{2+}, Cu^{2+}, Na^{+} and Fe^{3+}). The concentration of all the metal ions was 100 μM; I_0 and I correspond to the fluorescence intensity of Au_8 QCs in the absence and presence of metal ions, respectively. Inset shows the sensitivity plot between relative fluorescence intensity (I_0/I) value and the log value of Hg^{2+} ions concentration. (b) Fluorescence spectra of CFD labeled Au_8 QCs at an excitation wavelength ca. 337 nm in the presence of increasing concentration of Hg^{2+} ions. The black arrow shows that fluorescence decreases upon increase in the concentration of Hg^{2+} ions*

(0, 10, 100, 1000, 10000, 100000 nM. Inset shows the TEM images of CFD labeled Au_8 QCs before and after treatment with Hg^{2+} ions. Red circles show the aggregation of Au_8 QCs upon interaction with Hg^{2+} ions.

Figure 22 a shows relative fluorescence (I_0/I) of CFD-labeled Au_8-QCs in the presence of various metal ions. It can be seen from figure 22a that the fluorescence intensity of Au_8-QCs shows a substantial decrease only for the Hg^{2+} ions and was nearly unaffected by other metal ions. The fluorescence intensity of CFD labeled Au-QCs decreased linearly ($R^2 = 0.93$) over the Hg^{2+} ions concentration range of 10–100,000 nM and can be seen from dose response graph plotted in the inset of figure 22a. The fitted linear data could be expressed as

$$I_0/I = 0.67 + 0.2\,[Hg^{2+}]\ (R^2 = 0.93) \quad (1)$$

The limit of detection (LOD) for Hg^{2+} ions was ca. 2 nM; the slope was 0.2 nM^{-1}. The fluorescence of CFD labeled Au-QCs was effectively quenched by Hg^{2+} ions and showed approximately three-fold fluorescence quenching at 100 μM concentration of Hg^{2+} ions (figure 22b). The fluorescence quenching in the presence of Hg^{2+} ions was attributed to the Au_8-QCs aggregation, which might be induced by CFD and Hg^{2+} ion complexation. Figures 22b inset shows the TEM images of Au_8-QCs before and after the Hg^{2+} ions treatment, respectively. The TEM images confirm the aggregation of Au_8-QCs.

2.4.7 Application of Au_8-QCs as a sensing-probe to detect the Hg^{2+}-ions in the bacterial-cells

For this purpose, the overnight-grown *E. coli* cells were washed, diluted in PBS buffer and incubated with Au_8-QCs for 2 h at 37 ^oC over a constant shaking speed of 180 rpm. Thereafter, the cells were washed and spotted on glass slide for fluorescence microscope

examination. The blue fluorescent bacterial cells were visualized under the fluorescence microscope showing the capability of Au_8-QCs to image the bacterial cells (Figure 23a, b). Addition of 10 µM mercury to the bacterial cells leads to a sharp decrease in the fluorescence of the cells which supports the application of the as-synthesized Au_8-QCs for the sensing of Hg^{2+}-ions in biological samples (Figures 23c, d).

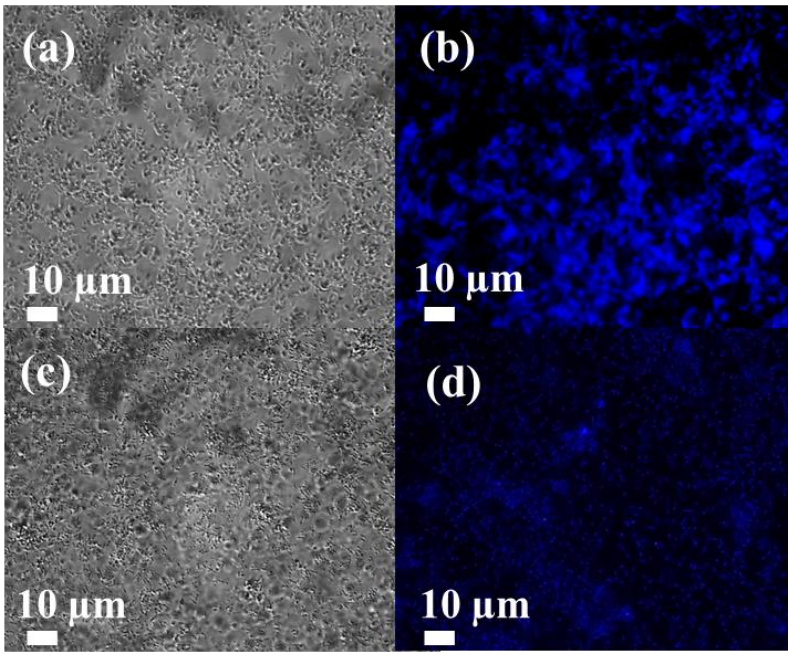

Figure 23. *The DIC images (a, c) and the fluorescence microscopic images (b, d) of bacterial cells incubated with blue luminescent Au_8 QCs for 2 h in absence of mercury ions (a, b) and in presence of 10 µM mercury ions (c, d).*

2.4.8 Study of antibacterial activity of Au-NPs

2.4.8.1 Minimum inhibitory concentration (MIC) determination

In order to investigate the antibacterial properties of Au-NPs (synthesized at pH 4, pH 5 and pH 6) and CFD, the MIC test via the micro-broth dilution method, was performed. The MIC value for CFD was found ca. 8 µg/mL whereas for Au-NPs, it was > 64 µg/mL

(figure 24). The possible reason behind these results may be the negative charge present on the CFD labeled Au-NPs (ca. -30 mV), which hinders the Au-NPs to efficiently interact with negatively charged bacterial cells, especially in LB growth medium.[81]

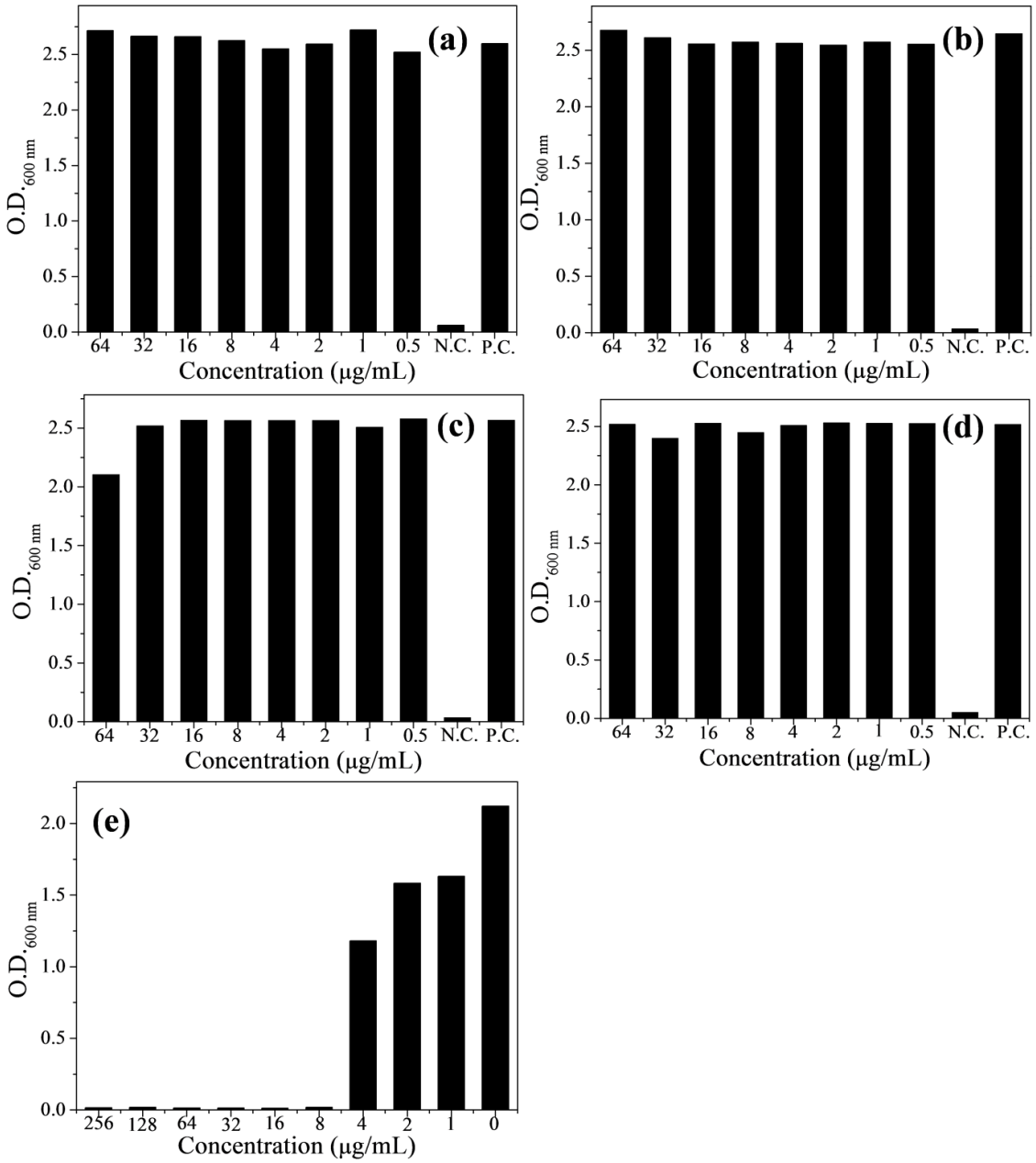

Figure 24. *The effect of concentration of (a) control, (b) pH 4 Au-NPs, (c) pH 5 Au-NPs, (d) pH 6 Au-NPs, and (e) CFD antibiotic on the growth of E. coli.*

2.4.8.2 Reduction in cell-growth

To further investigate the effect of Au-NPs on the growth of bacterial cells, the bacterial cells were treated with 64 μg/mL of Au-NPs and growth of bacterial cells was observed over a period of 18 h (figure 25a). The results show that the growth rate for control, pH 4 NPs, pH 5 NPs and pH 6 NPs was ca. 0.037, 0.034, 0.034, and 0.036 h^{-1}, respectively. It is indicated from the results that the highest growth rate was for control (without Au-NPs) and the lowest and almost equal for pH 4 and 5 Au-NPs (except antibiotic itself). Therefore, the Au-NPs significantly affected the growth rate but it did not show satisfactory antibacterial activity in comparison to the CFD alone which is in consistent with the previous reports in the literature.[35,42,82] The reason behind these results was discussed in the previous section.

2.4.8.3 Reduction in cell survival

To assess the cell survival, the cells after overnight growth were washed, diluted in PBS buffer and incubated with Au-NPs and antibiotics at a concentration ca. 64 μg/mL for a period of 24 h at 180 rpm, 37 ^{o}C. At 0 h and 24 h, the 100 μl aliquots were taken from each sample and plated on LB plates. The plates were incubated for 18 h to visualize the colony formation of cells and their digital photographs are shown in figure 25b. The colonies were counted and the histogram is shown in figure 25c. The results were surprising and did not match with the results from cell-growth. It can be easily seen from the figure 25c that at 0 h, the colonies count were same for all the samples but after 24 h, the colony count was least for pH 4 sample which was followed by pH 6 and pH 5 NPs. On the other hand, the survival of bacterial cells was almost unaffected by antibiotic alone. It may be because the lactam antibiotics can only inhibit the cell-growth by inhibiting the cell-wall synthesis but

cannot affect the cell survival. It was interesting to note that the Au-NPs could reduce the cell survival but not the cell-growth[83] which may be due to the interaction of Au-NPs with the bacterial cells in PBS buffer, which is absent in the LB medium.

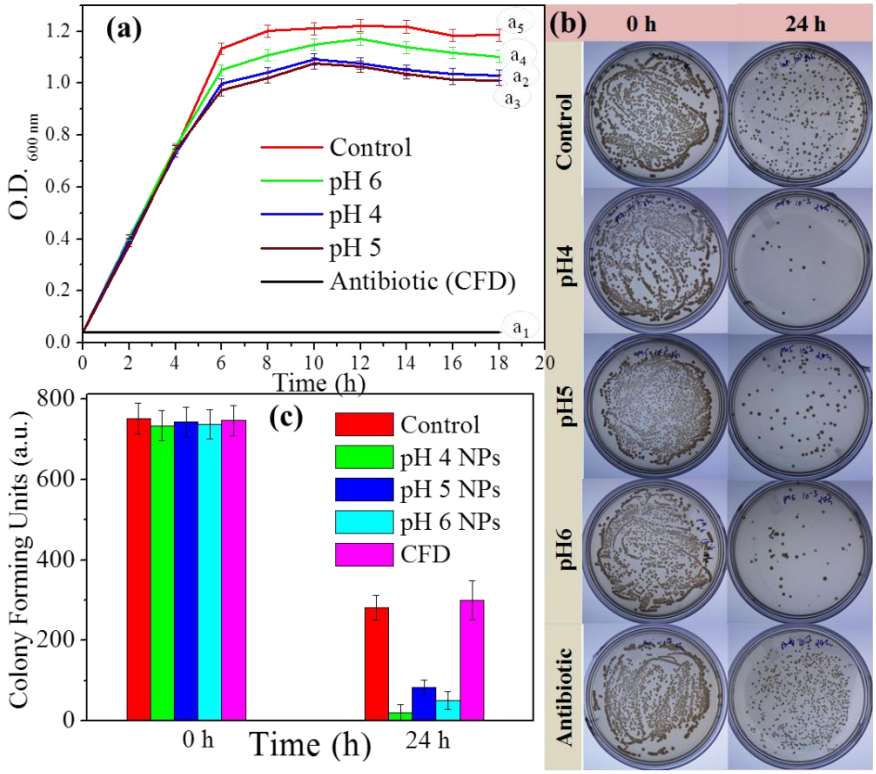

Figure 25. *(a) Growth curves of E. coli cells exposed to (a_1) CFD antibiotic, (a_2) pH 4 Au-NPs, (a_3) pH 5 Au-NPs, (a_4) pH 6 Au-NPs, and (a_5) without Au-NPs at a concentration of 64 μg/mL. All data are the mean ± standard deviation of triplicate determinations. (b) Cell survival assay performed using LB agar petri-dishes inoculated with E. coli, showing the almost same number of colonies at 0 h (in the first row) and decreased number of colonies after 24 h (in second row) upon incubation with different sizes and shapes of Au-NPs synthesized at different pH conditions (pH 4, pH 5, and pH 6). (c) Histogram showing the cell survival before and after 24 h of exposure of antibiotic (CFD) and Au-NPs synthesized at pH 4, pH 5, and pH 6.*

2.4.8.4 Monitoring the changes in bacterial cell membrane upon interaction with Au-NPs

In order to reveal the mechanism behind the damage to the bacterial cells by Au-NPs (the result of cell survival), SEM study was carried out to examine the interaction between bacterial cells and Au-NPs (figure 26). The bacterial cells were incubated with pH 4 Au-NPs, pH 5 Au-NPs, pH 6 Au-NPs and CFD for 4 h at a concentration ca. 64 µg/mL. The bacterial cells suspended in PBS buffer (without Au-NPs incubation) were used as control and as evident in SEM images, these cells did not show any damage. The similar type of bactericidal pattern was found for all types of Au-NPs and these results indicated that the irreversible damage (blabbing) to the cell-walls probably occur by the direct contact of the Au-NPs to the bacterial cells.[84,85] However, it can be observed from the figure 26 that the extent of damage was less in the case of antibiotic in comparison to Au-NPs.

The fluorescence microscopic study has also been performed to monitor the changes in the cell membrane permeability using propidium iodide (PI) dye. The PI molecules can bind with DNA or RNA specifically to acquire enhanced fluorescence, but it cannot cross the membrane and is excluded from the viable cells. Intracellular staining of PI can identify dead cells.[86] It can be noticed from figure 27 that the cells got aggregated when incubated with pH 4 Au-NPs and pH 5 Au-NPs, in particular (as seen in DIC images in figures 27 c and e, respectively). When the cells were treated with pH 4 Au-NPs and pH 5 Au-NPs, the diffused red fluorescent boundaries appeared around the cells (as visualized in the figures 27 d and f). This feature may be due to the combined effect of the damaged cell-walls of the bacterial cells, which allowed the leakage of nucleic acid out of the cells and the aggregation of the cells.[86] These results are also consistent with the findings from

SEM study. However, similar diffused red fluorescent boundaries in cells were not visible for the control cells (figure 27b) and CFD alone (figure 27j).

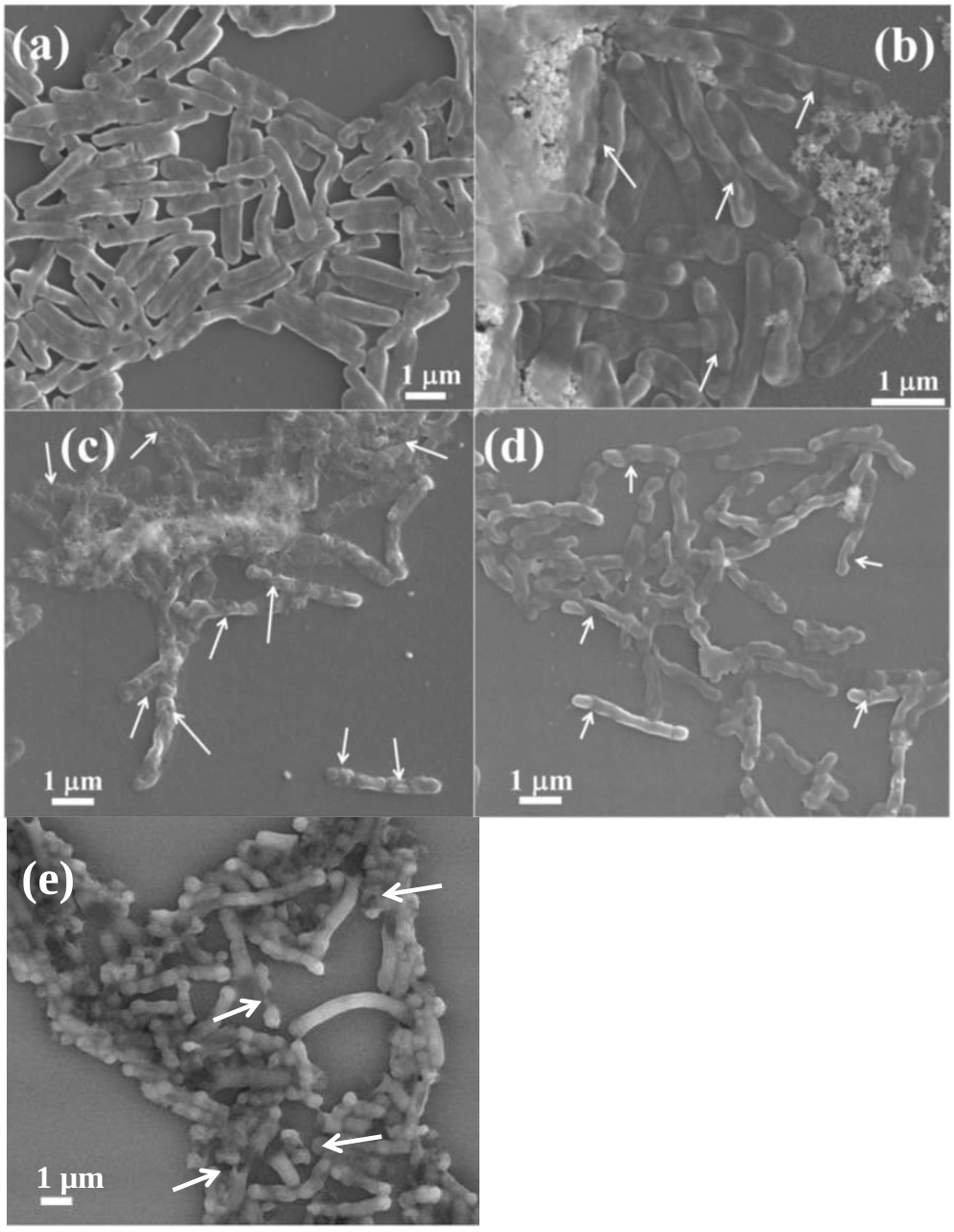

Figure 26. *SEM images of E. coli cells incubated with (a) saline solution, (b) pH 4 Au-NPs, (c) pH 5 Au-NPs, and (d) pH 6 Au-NPs (e) antibiotic (CFD) at a concentration of 64 µg/mL for 4 h. White arrows indicate the degraded cell-walls of bacterial cells.*

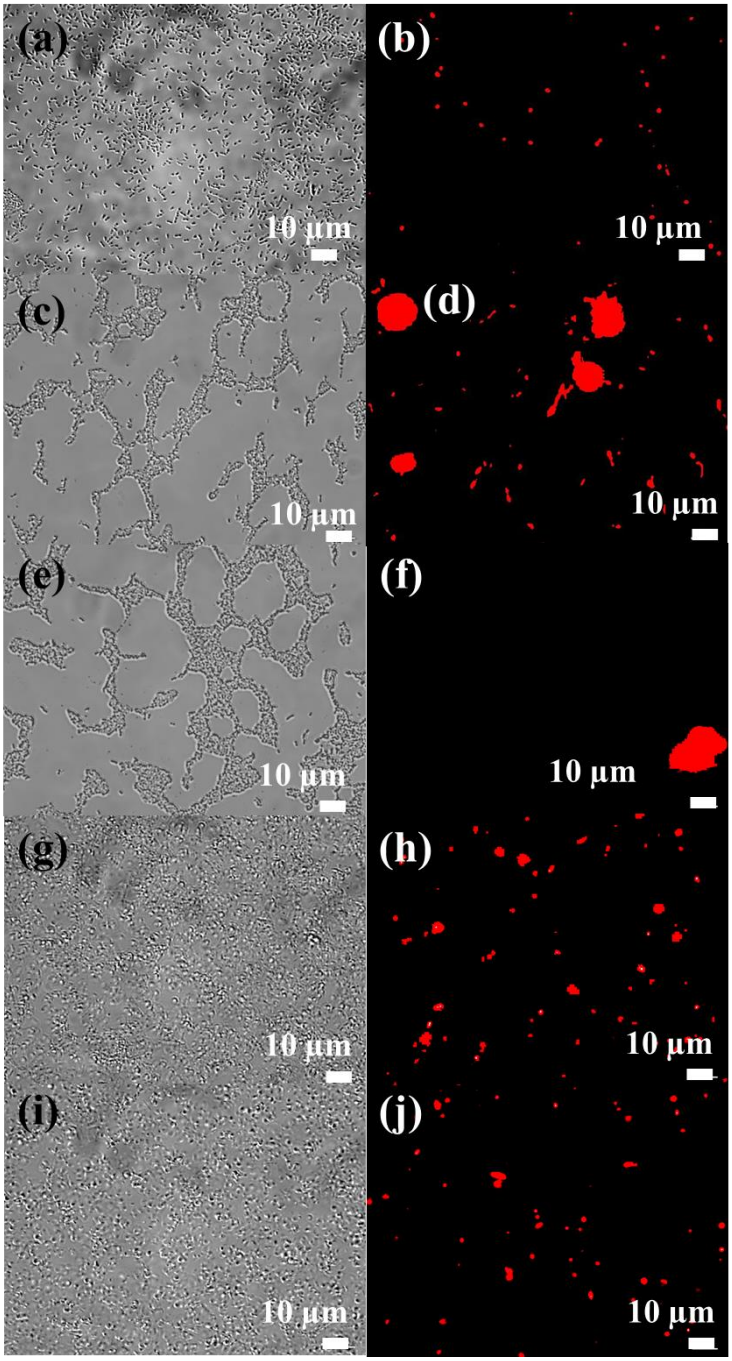

Figure 27. *Fluorescence microscopic images of E. coli cells after incubation with propidium iodide (a, b) and with both propidium iodide as well as pH 4 Au-NPs (c, d), pH 5 Au-NPs (e, f), pH 6 Au-NPs (g, h), CFD (i, j) in DIC mode (a, c, e, g, i) and fluorescence mode (b, d, f, j, h).*

2.4.8.5 Oxidative stress by ROS production

Other than the cell-wall damage mediated by the direct physical contact, a previous study on Au-NPs cytotoxicity showed that the 'oxidative stress by ROS production' might also be one of the toxicity mechanisms.[87] The oxidative-stress is also often suggested as a key mechanism behind the antibacterial properties of several other inorganic nanomaterials, such as Ag-NPs[88–91] and ZnO-NPs.[92,93] We determined cellular ROS by using a DCF probe (originally non fluorescent), which can be easily oxidized to produce the fluorescent DCF by cellular ROS.[94] It can be observed from figure 28 that Au-NPs did not induce an obvious increase of cellular ROS.

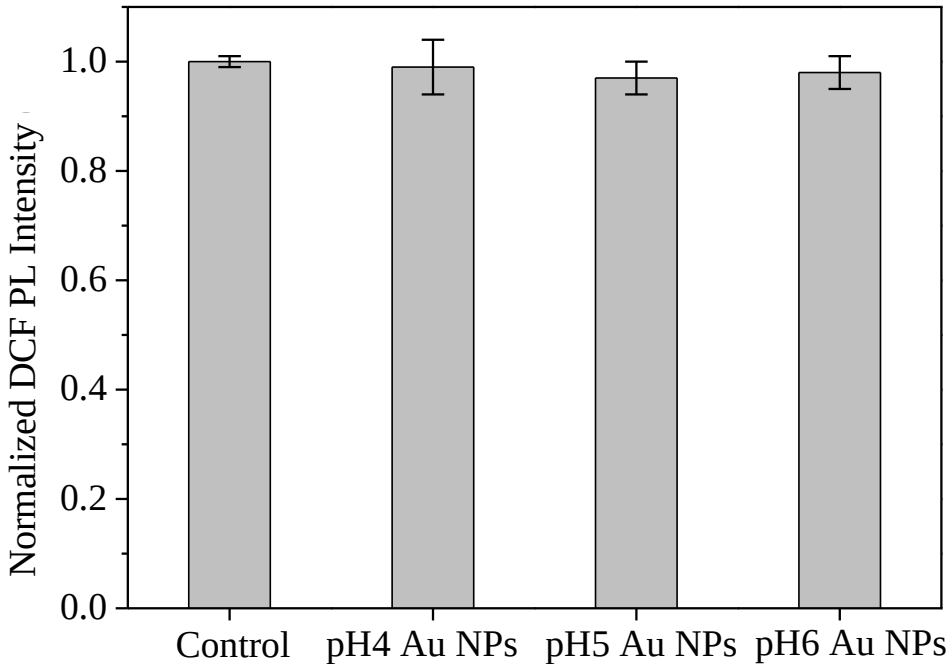

Figure 28. *Determination of ROS in NP-treated or untreated E. coli using DCF dye. All data are the mean ± standard deviation of triplicate determinations. The ROS assay shows that these Au-NPs did not stimulate ROS production and hence, the possibility of ROS to be a mechanism behind loss of cell-viability was ruled out in our study.*

2.5 Conclusion

In summary, we have performed detailed experiments to understand the nucleation and growth of Au-NPs and Au_8 QCs using cefradine molecule as both reducing and capping agent. This study has highlighted the important role of kinetics in the nanocrystals architecture. The $HAuCl_4$/CFD concentration, temperature and pH found to be very crucial factors in modulation of the Au-NPs growth kinetics and hence, guiding the size and morphology of Au-NPs. The growth of anisotropic Au-NPs was shown to be significantly influenced by increase in the concentration, decrease in the temperature and decrease in the pH of the reaction. Experimental and theoretical studies show that oxygen, nitrogen and sulphur moieties are involved in the reduction and/or binding of CFD to Au-NPs. The CV results show that the decrease in the reduction potential of CFD upon increase in the pH of the reaction from 4 to 6 leads to the growth of unstable Au-NPs (ca. 20 nm) suspension to highly stable Au-QCs (< 1 nm) suspension, respectively. MALDI-TOF result shows the synthesis of $[Au_8(CFD)_2S_6]$ QCs and their fluorescence was observed at ca. 432 nm with a Stokes shift of ca. 95 nm. Therefore, this study may be helpful in programmed and controlled nucleation and growth for synthesis anisotropic particles (unstable suspension) to quantum clusters (highly stable suspension).

Further, within a short reaction time, this strategy allows the fabrication of Au_8-QCs, having the capability to sense Hg^{2+} ions. On the basis of an aggregation-induced fluorescence quenching mechanism, these Au_8-QCs offer high selectivity and sensitivity with a limit of detection of ca. 2 nM for the determination of Hg^{2+} ions. This Hg^{2+} ion sensing capability of the Au_8-QCs was also applied to directly detect the presence of 10 μM Hg^{2+} ions in the bacterial samples. We found that although antibiotic labeled Au-NPs

have negative surface charge, they show the decrease in *E. coli* cell-growth rate. The least growth rate was found for pH 5 Au-NPs. The antibiotic reduced Au-NPs have also been shown to cause the significant reduction in the cell survival in comparison to antibiotic alone. The SEM results show that the antibacterial property of Au-NPs is due to the degradation or blabbing of the cell-walls of bacterial cells which was further confirmed by PI based fluorescence imaging of bacterial cells. The ROS assay shows that these Au-NPs did not stimulate ROS production and hence, the possibility of ROS to be a mechanism behind loss of cell-viability, was ruled out in our study. Our studies indicated that the most probable mechanism behind the damage in the bacterial cells is the direct contact to the bacterial cells by NPs.

2.6 References

1 P. Khandelwal, D. K. Singh, S. Sadhu and P. Poddar, *Nanoscale*, 2015, **7**, 19985–20002.

2 Z. Wu, J. Chen and R. Jin, *Adv. Funct. Mater.*, 2011, **21**, 177–183.

3 Z. Wu, M. A. Macdonald, J. Chen, P. Zhang and R. Jin, *J. Am. Chem. Soc.*, 2011, **133**, 9670–9673.

4 Z. Luo, V. Nachammai, B. Zhang, N. Yan, D. T. Leong, D. E. Jiang and J. Xie, *J. Am. Chem. Soc.*, 2014, **136**, 10577–10580.

5 E. E. Connor, J. Mwamuka, A. Gole, C. J. Murphy and M. D. Wyatt, *Small*, 2005, **1**, 325–7.

6 N. Li, P. Zhao and D. Astruc, *Angew. Chemie Int. Ed.*, 2014, **53**, 1756–1789.

7 H. K. Daima, P. R. Selvakannan, R. Shukla, S. K. Bhargava and V. Bansal, *PLoS One*, 2013, **8**, e796761–e7967614.

8 C. J. Murphy, A. M. Gole, J. W. Stone, P. N. Sisco, A. M. Alkilany, E. C. Goldsmith and S. C. Baxter, *Acc. Chem. Res.*, 2008, **41**, 1721–1730.

9 R. Jagannathan, P. Poddar and A. Prabhune, *J. Phys. Chem. C*, 2007, **111**, 6933–6938.

10 P. Khandelwal, D. K. Singh, S. Sadhu and P. Poddar, *Chempluschem*, 2014, **79**, 134–142.

11 R. Jagannathan, A. S. Parmar, S. Adyanthaya, A. Prabhune, M. Muschol and P. Poddar, *J. Phys. Chem. C*, 2009, **113**, 3478–3486.

12 H. Chen, L. Shao, Q. Li and J. Wang, *Chem. Soc. Rev.*, 2013, **42**, 2679–2724.

13 T. A. Major, M. S. Devadas, S. S. Lo and G. V Hartland, *J. Phys. Chem. C*, 2013.

14 X. Huang, P. K. Jain, I. H. El-Sayed, M. A. El-Sayed, H. X, J. PK, E.-S. IH and E.-S. MA, *Nanomedicine*, 2007, **2**, 681–693.

15 Y. Sun and Y. Xia, *Science*, 2002, **298**, 2176–9.

16 O. R. Miranda, X. Li, L. Garcia-gonzalez, Z. Zhu, B. Yan, U. H. F. Bunz and V. M. Rotello, *J. Am. Chem. Soc.*, 2011, **133**, 9650–9653.

17 Y. Xiao, F. Patolsky, E. Katz, J. F. Hainfeld and I. Willner, *Science*, 2003, **299**, 1877–1881.

18 T. K. Sharma, R. Ramanathan, P. Weerathunge, M. Mohammadtaheri, H. K. Daima, R. Shukla and V. Bansal, *Chem. Commun.*, 2014, **50**, 15856–15859.

19 M. Stobiecka and M. Hepel, *Biomaterials*, 2011, **32**, 3312–3321.

20 H. Ding, D. Yang, C. Zhao, Z. Song, P. Liu, Y. Wang, Z. Chen and J. Shen, *ACS Appl. Mater. Interfaces*, 2015, **7**, 4713–4719.

21 G. E. Craig, S. D. Brown, D. a Lamprou, D. Graham and N. J. Wheate, *Inorg.*

Chem., 2012, **51**, 3490–3497.

22 B. Kang, M. M. Afifi, L. A. Austin, M. A. El-sayed, U. States, M. Science, O. Pathology and C. St, *ACS Nano*, 2013, **7**, 7420–7427.

23 Z. Z. W. W. Wang and R. E. Palmer, *Nano Lett.*, 2012, **12**, 5510–5514.

24 P. Maity, S. Xie, M. Yamauchi and T. Tsukuda, *Nanoscale*, 2012, **4**, 4027–4037.

25 H. Häkkinen, *Chem. Soc. Rev.*, 2008, **37**, 1847.

26 J. Zheng, J. T. Petty and R. M. Dickson, *J. Am. Chem. Soc.*, 2003, **125**, 7780–7781.

27 S. Chen, *Science (80-.).*, 1998, **280**, 2098–2101.

28 C. Félix, C. Sieber, W. Harbich and J. Buttet, *Phys. Rev. Lett.*, 2001, **86**, 2992–2995.

29 L. A. Peyser, A. E. Vinson, A. P. Bartko and R. M. Dickson, *Science*, 2001, **291**, 103–106.

30 J. Zheng, P. R. Nicovich and R. M. Dickson, *Annu. Rev. Phys. Chem.*, 2007, **58**, 409–431.

31 H. Yao and A. Sasaki, *Nanoscale*, 2012, **4**, 955–963.

32 R. Fernandes, N. R. Smyth, O. L. Muskens, S. Nitti, A. Heuer-Jungemann, M. R. Ardern-Jones and A. G. Kanaras, *Small*, 2015, **11**, 713–721.

33 E. C. Cho, L. Au, Q. Zhang and Y. Xia, *Small*, 2010, **6**, 517–522.

34 P. Yan, R. Wang, N. Zhao, H. Zhao, D.-F. Chen and F.-J. Xu, *Nanoscale*, 2015, **7**, 5281–5291.

35 A. Rai, A. Prabhune and C. C. Perry, *J. Mater. Chem.*, 2010, **20**, 6789–6798.

36 M. H. Hyun, E. D. Jeong, M. S. Shin and J. S. Jin, *Bull. Korean Chem. Soc.*, 2008, **29**, 1185–1189.

37 O. A. Cephalosporins, *J Infect Dis.*, 1978, **137**, 490–493.

38 L. Shang, L. Yang, F. Stockmar, R. Popescu, V. Trouillet, M. Bruns, D. Gerthsen and G. U. Nienhaus, *Nanoscale*, 2012, **4**, 4155.

39 G. L. Burygin, B. N. Khlebtsov, a N. Shantrokha, L. a Dykman, V. a Bogatyrev and N. G. Khlebtsov, *Nanoscale Res. Lett.*, 2009, **4**, 794–801.

40 Y. Zhao and X. Jiang, *Nanoscale*, 2013, **5**, 8340–50.

41 A. N. Brown, K. Smith, T. a Samuels, J. Lu, S. O. Obare and M. E. Scott, *Appl. Environ. Microbiol.*, 2012, **78**, 2768–74.

42 H. Gu, P. L. Ho, E. Tong, L. Wang, B. Xu, W. Shao, X. Liu, H. Min, G. Dong, Q. Feng and S. Zuo, *Nano Lett.*, 2003, **3**, 1261–1263.

43 G. Chen, Z. Guo, G. Zeng and L. Tang, *Analyst*, 2015, **140**, 5400–5443.

44 *Environmental Health Criteria 101: Methylmercury*, 1990.

45 U. Kumar, A. Shete, A. S. Harle, O. Kasyutich, W. Schwarzacher, A. Pundle and P. Poddar, *Chem. Mater.*, 2008, **20**, 1484–1491.

46 B. Mazumder, I. Uddin, S. Khan, V. Ravi, K. Selvraj, P. Poddar and A. Ahmad, *J. Mater. Chem.*, 2007, **17**, 3910.

47 I. Uddin, A. Jaiswal and P. Poddar, *Int. J. Innov. Biol. Reaserch*, 2013, **2**, 1–5.

48 C. Sharan, P. Khandelwal and P. Poddar, *RSC Adv.*, 2015, **5**, 1883–1889.

49 Y. Zhang, T. P. Shareena Dasari, H. Deng and H. Yu, *J. Environ. Sci. Heal. Part C*, 2015, **33**, 286–327.

50 A. Sengupta and P. Hazra, *Chem. Phys. Lett.*, 2010, **501**, 33–38.

51 M. J. Frisch, G. W. Trucks, H. B. Schlegel and G. E. Scuseria et al., *Off. Gaussian 09 Lit. Cit. Gaussian, Inc., Wallingford CT Gaussian 09.*

52 D. K. Singh, S. K. Srivastava and B. P. Asthana, *Chem. Phys.*, 2011, **380**, 24–33.

53 D. K. Singh, S. K. Srivastava, S. Schlücker, R. K. Singh and B. P. Asthana, *J. Raman Spectrosc.*, 2011, **42**, 851–858.

54 S. Singh, D. K. Singh, S. K. Srivastava and B. P. Asthana, *Vib. Spectrosc.*, 2011, **56**, 26–33.

55 D. K. Singh and B. P. Asthana, *J Mol Model*, 2012, **18**, 3541–3552.

56 P. J. Hay and W. R. Wadt, *J. Chem. Phys.*, 1985, **82**, 299–310.

57 D. K. Singh, E.-O. Ganbold, E.-M. Cho, K.-H. Cho, D. Kim, J. Choo, S. Kim, C. M. Lee, S. I. Yang and S.-W. Joo, *J. Hazard. Mater.*, 2014, **265**, 89–95.

58 A. T. N. Lam, J. Yoon, E. Ganbold, D. K. Singh, D. Kim, K. Cho, S. Y. Lee, J. Choo, K. Lee and S. Joo, *Colloids Surfaces B Biointerfaces*, 2014, **123**, 61–67.

59 A. T. N. Lam, J. Yoon, E.-O. Ganbold, D. K. Singh, D. Kim, K.-H. Cho, S. J. Son, J. Choo, S. Y. Lee, S. Kim and S.-W. Joo, *J. Colloid Interface Sci.*, 2014, **425**, 96–101.

60 B. Mennucci and J. Tomasi, *J. Chem. Phys.*, 1997, **106**, 5151–5158.

61 A. Rai, A. Singh, A. Ahmad and M. Sastry, *Langmuir*, 2006, **22**, 736–741.

62 S. S. Shankar, S. Bhargava and M. Sastry, *J. Nanosci. Nanotech.*, 2005, **5**, 1721–1727.

63 Y. Chiang and J. Turkevich, *J. Colloid Sci.*, 1963, **18**, 772–783.

64 J. A. A. Engelbrecht and H. C. Snyman, *Gold Bull.*, 1983, **16**, 1–4.

65 R. Shukla, V. Bansal, M. Chaudhary, A. Basu, R. R. Bhonde and M. Sastry, *Langmuir*, 2005, **21**, 10644–10654.

66 B. Tzeng and S. Peng, *J. Chem. Soc., Dalt. Trans.*, 1996, 1769–1770.

67 S. Shieh, D. Li, S. Peng and C. Che, *J. Chem. Soc., Dalt. Trans.*, 1993, 195–196.

68 *Sargent-Welch Table Period. Prop. Elem. Sargent-Welch Sci. Company, Skokie, 1980.*, 1980.

69 B. Höffling, F. Ortmann, K. Hannewald and F. Bechstedt, *Phys. Rev. B - Condens. Matter Mater. Phys.*, 2010, **81**, 1–12.

70 E. M. Cho, D. K. Singh, E. O. Ganbold, U. Dembereldorj, S. W. Jang, D. Kim, J. Choo, S. Kim, C. M. Lee, S. I. Yang and S. W. Joo, *Appl. Spectrosc.*, 2014, **68**, 307–314.

71 D. K. Singh, R. Jagannathan, P. Khandelwal, P. M. Abraham and P. Poddar, *Nanoscale*, 2013, **5**, 1882–93.

72 D. K. Singh, E.-O. Ganbold, E.-M. Cho, C. M. Lee, S. I. Yang and S.-W. Joo, *J. Mol. Struct.*, 2013, **1049**, 464–472.

73 J. Zheng, C. Zhang and R. M. Dickson, *Phys. Rev. Lett.*, 2004, **93**, 0774021–0774024.

74 H. Kawasaki, K. Hamaguchi, I. Osaka and R. Arakawa, *Adv. Funct. Mater.*, 2011, **21**, 3508–3515.

75 X. Le Guével, B. Hötzer, G. Jung, K. Hollemeyer, V. Trouillet, M. Schneider, X. Le Guével, B. Hötzer, G. Jung, K. Hollemeyer, V. Trouillet and M. Schneider, *J. Phys. Chem. C*, 2011, **115**, 10955–10963.

76 T.-H. Chen and W.-L. Tseng, *Small*, 2012, **8**, 1–8.

77 M. A. Habeeb Muhammed, S. Ramesh, S. S. Sinha, S. K. Pal and T. Pradeep, *Nano Res.*, 2008, **1**, 333–340.

78 P. L. Xavier, K. Chaudhari, P. K. Verma, S. K. Pal and T. Pradeep, *Nanoscale*, 2010, **2**, 2769–2776.

79 W. Guo, J. Yuan, E. Wang, J. Yuanab and E. Wang, *Chem. Commun.*, 2012, **48**, 3076–8.

80 X. Yang, Y. Su, M. C. Paau and M. M. F. Choi, *Anal. Chem.*, 2012, **84**, 1765–1771.

81 Z. V. Feng, I. L. Gunsolus, T. A. Qiu, K. R. Hurley, L. H. Nyberg, H. Frew, K. P. Johnson, A. M. Vartanian, L. M. Jacob, S. E. Lohse, M. D. Torelli, R. J. Hamers, C. J. Murphy and C. L. Haynes, *Chem. Sci.*, 2015, **6**, 5186–5196.

82 M. Demurtas and C. C. Perry, *Gold Bull.*, 2013, **47**, 103–107.

83 M. R. Smith, M. G. Boenzli, V. Hindagolla, J. Ding, J. M. Miller, J. E. Hutchison, J. a Greenwood, H. Abeliovich and A. T. Bakalinsky, *Appl. Environ. Microbiol.*, 2013, **79**, 728–733.

84 F. Perreault, A. F. de Faria, S. Nejati and M. Elimelech, *ACS Nano*, 2015, **9**, 7226–7236.

85 A. Regiel-Futyra, M. Kus-Liśkiewicz, V. Sebastian, S. Irusta, M. Arruebo, G. G. Stochel, A. Kyzioł, M. Kus-Liśkiewicz, V. Sebastian, S. Irusta, M. Arruebo, G. G. Stochel and A. Kyzioł, *ACS Appl. Mater. Interfaces*, 2015, **7**, 1087–1099.

86 Y. Zhao, Y. Tian, Y. Cui, W. Liu, W. Ma and X. Jiang, *J. Am. Chem. Soc.*, 2010, **132**, 12349–12356.

87 Y. Pan, A. Leifert, D. Ruau, S. Neuss, J. Bornemann, G. Schmid, W. Brandau, U. Simon and W. Jahnen-Dechent, *Small*, 2009, **5**, 2067–2076.

88 S. Kim, J. E. Choi, J. Choi, K.-H. Chung, K. Park, J. Yi and D.-Y. Ryu, *Toxicol. Vitr.*, 2009, **23**, 1076–1084.

89 S. Kim and D.-Y. Ryu, *J. Appl. Toxicol.*, 2013, **33**, 78–89.

90 J. Eun, S. Kim, J. Hee, P. Youn, J. Seok, K. Park, J. Yi and D. Ryu, *Aquat. Toxicol.*,

2010, **100**, 151–159.

91 W. Zhang, Y. Li, J. Niu and Y. Chen, *Langmuir*, 2013, **29**, 4647–4651.

92 V. Sharma, D. Anderson and A. Dhawan, *Apoptosis*, 2012, **17**, 852–870.

93 J. Wang, X. Deng, F. Zhang, D. Chen and W. Ding, *Nanoscale Res. Lett.*, 2014, **9**, 1–12.

94 Y. Cui, Y. Zhao, Y. Tian, W. Zhang, X. Lü and X. Jiang, *Biomaterials*, 2012, **33**, 2327–2333.

Chapter III

Curcumin-conjugated gold quantum clusters for anticancer application

Gold nanoparticles (Au-NPs) have been thoroughly investigated for cancer theranostics purposes. However, their undesired high gold content remains a problem when injected in the body for drug delivery. In this chapter, we made a successful effort to conjugate the curcumin molecules on the surface of gold quantum clusters (Au-QCs) in situ which provide an alternate to reduce the metallic content, as well as increase the loading efficiency. Here, curcumin, itself, acts as reducing and capping agent for the synthesis of Au-QCs. The UV-vis, TEM, and ESI-MS results confirmed the synthesis of Au-QCs. The curcumin-conjugated Au-NPs and GSH conjugated Au-QCs were synthesized as a control. The MTT assay showed that the curcumin-conjugated Au-QCs were less cytotoxic to normal cells while preserving the anticancer property of curcumin. It was also observed that curcumin-conjugated Au-QCs were more effective than curcumin-conjugated Au-NPs and GSH-conjugated Au-QCs.

3.1 Introduction

Curcumin (1,7-bis(4-hydroxy-3-methoxyphenyl)-1,6-heptadiene-3,5-dione) is a polyphenol and main functional component of turmeric derived from the rhizome of a medicinal plant "*Curcuma longa*".[1] Curcumin has been used as the main ingredient of Indian spices and traditional Ayurvedic medicines since an ancient time in the Asian countries.[2] Curcumin has attracted a huge attention due to its wide range of pharmacological applications such as antioxidant, antiangiogenic, antimicrobial, anti-inflammatory, anticancer, anti-Alzheimer, anti-parasitic, and antiviral etc.[1,3–27] Earlier studies show that curcumin has chemo-preventive activity against several types of cancers such as prostate, breast and colorectal cancer.[15,28,29] The molecular basis of chemo-preventive activity of curcumin is its effect on several targets such as transcription factors (NF-κB), growth targets, apoptotic genes (p53, Bcl-2), angiogenesis regulators and cell signaling genes (TNF-α).[6,15]

Despite numerous biological activities, curcumin could not be used efficiently for therapeutic applications due to its poor systemic bioavailability originating from low water solubility and instability.[2] In order to overcome from the problem of water solubility of curcumin, researchers have tried to make various formulations such as encapsulation in polymeric nanoparticles, silica nanoparticles, lipid micelles, metal nanoparticles, microemulsions, and the preparation of curcumin analogue.[17,29–32]

Although the complexation of curcumin with metal nanoparticles, especially gold nanoparticles (Au-NPs), has been used in many reports due to their less toxic and biocompatible nature, gold quantum cluster (Au-QCs) made up of few to few tens of atoms may also be used as an alternate due to their small size, interesting optical and electronic

properties.[33–35] Au-QCs show the discrete energy of states resulting in the emission of light from UV to NIR region.[36–38] In last decade, Au-QCs acquired extremely high attention due to their numerous advantages such as: (1) non-toxic to cells, (2) smaller than the biomolecules of interest, so that normal biological functions such as biomolecular interactions will not disturbed, (3) optimal photo-physical properties including low photo-bleaching, absence of blinking, large Stokes shift, high water dispersibility and high quantum yield; (4) NIR fluorescence; (5) can act as effective radio-sensitizer; and, finally, (6) easy to synthesize and use for labeling biomolecules. Au-QCs have been used extensively for *in vitro* and *in vivo* bio-imaging, sensing, drug delivery, photodynamic therapy, catalysis etc.[39–48]

Au-QCs have been used for cancer therapy in many studies by several groups. Huang et al., in 2013, reported the use of photosensitizer conjugated silica coated Au-QCs for fluorescence imaging guided photodynamic therapy.[49] Nair et al. developed a biocompatible Au-QCs based multifunctional system for fluorescence imaging directed photodynamic therapy application which is useful for effective destruction and monitoring of tumor cells.[41] In 2015, Zhang et al. used the epidermal growth factor receptor conjugated Au-QCs for targeted cancer radiation treatment.[50] Khandelia et al. used the Au-QCs embedded albumin nanoparticles as doxorubicin drug delivery vehicle for anticancer applications.[51] Recently, in 2016, Zhou et al. demonstrated the synthesis of cisplatin conjugated Au-QCs for fluorescence imaging and targeted therapy of the breast cancer.[52] Chen et al. developed the RGD and aptamer conjugated dual targeting Au-QCs bounded with doxorubicin for tumor imaging and deep tissue therapy.[53]

There are several reports in which the biologically active protein molecules have been used for synthesis of Au-QCs where they act as reducing as well as capping agent, and also able of retain their biological activity. For example, Chen et al. synthesized the lysozyme protected Au-QCs which exhibited the potential superior antimicrobial activity.[54] Liu et al. reported the insulin directed synthesis of Au-QCs which were shown to retain the insulin bioactivity.[55] Nair et al. developed the NIR emitting urease conjugated Au-QCs for the highly selective sensing of urea in the whole blood samples.[56] However, there is a lack of reports where the small molecules used to synthesize the Au-QCs and those molecules able to retain their biological activity as well. In this chapter, curcumin molecules used for the synthesis of Au-QCs as reducing and capping agent, and shown to preserve their anticancer activity with less cytotoxicity to normal mammalian cells in comparison to curcumin alone.

3.2 Experimental Section

3.2.1 Materials

All chemicals were of analytical grade and used as-received without any further purification, unless otherwise mentioned. Benzoylated dialysis tube, curcumin (≥ 65%) and $HAuCl_4.3H_2O$ (≥ 49.0% Au basis), DMSO were purchased from Sigma-Aldrich. NaOH was purchased from Thomas Baker. All glassware's were washed with aquaregia (HCl: HNO_3 = 3:1) carefully and rinsed with Millipore™ water (18.2 MΩ resistance) before using them for synthesis.

3.2.2 Synthesis of curcumin-conjugated Au-QCs

Briefly, 14.8 mg of curcumin was taken in a vial. Two mL of NaOH (0.1 M) was added in the vial and vigorously shaken for proper mixing. Just after the addition of NaOH, the

color of suspension changed to dark red color. Immediately, the 36 mL of MQ water and 2 mL of $HAuCl_4$ (10^{-2} M) was added simultaneously, and the solution was stirred vigorously. The reaction suspension was allowed to incubate at 27 ^{o}C for 24 h under constant stirring at 150 rpm.

3.2.3 Purification of curcumin-conjugated Au-QCs

The as-obtained suspension was centrifuged at 20,000 g for 15 min at 0 ^{o}C temperature for the separation of Au-QCs from Au-NPs. The as-obtained supernatant was collected and dialyzed for almost 2 days while continuously washing by changing the water at fixed time intervals of 6 h. The pore-size cutoff of the dialysis tube was 2000 MW which was able to separate the compounds with a molecular weight of ≤1,200 from compounds with a molecular weight >2,000. The dialysis was done for the separation of unreacted molecules and ions from the Au-QCs suspension. After each washing, the samples were collected for the quantification of unbound curcumin molecules as well as to confirm the complete absence of curcumin molecules in the Au-QCs suspension.

3.2.4 Quantification of curcumin molecules in the Au-QCs suspension

The quantification of curcumin molecules in the Au-QCs suspension was done by following two different methods to validate the accuracy in the quantification. First, the UV-vis spectroscopic studies were carried out on the dialysates collected at various intervals. The characteristic UV peak for curcumin was observed ~265 nm and supposed not to change on the binding of curcumin to the nanoparticle surface as well as in alkaline medium. The different dilutions of curcumin molecules in alkaline medium were analyzed by UV-vis spectroscopy and then, the plot were made in between the absorbance and the

concentration. By this linear plot, we have analyzed the curcumin in the Au-QCs suspension as well as in dialysate.

3.2.5 Synthesis of curcumin-conjugated Au-NPs

For the synthesis of curcumin-conjugated Au-NPs, the procedure mentioned by Yang et al[25] has been used with slight modifications. Five hundred µL of 20 mM curcumin was dissolved in DMSO and then, 45 mL of water was added under continuous stirring. The pH of the solution was adjusted to alkaline by addition of 100 µL NaOH. The temperature of the solution was raised to 100 ^{o}C and 2.5 mL of 10 mM $HAuCl_4$ was added under vigorous stirring for 1 h. After that, the mixture was cooled down to room temperature. The dialysis of as-obtained nanoparticle suspension was performed using a dialysis bag with the pore size of 12 kDa to remove all the unreacted impurities and small quantum clusters. The UV-vis spectroscopic analysis (using Jasco UV-vis-NIR dual beam spectrometer (Model V570) operated at a resolution of 2 nm) was done to make sure the complete removal of unbound curcumin molecules.

3.2.6 Synthesis of GSH-conjugated Au-QCs

Thirty mL of water was poured in a round bottom flask. Thereafter, 5 mL of 10^{-2} M $HAuCl_4$ and 10 mL of 10^{-2} M GSH were added in it with vigorous stirring. Hundred µL of NaOH and 5 mL of 50 mM of $NaBH_4$ were added serially. The entire solution was heated at ~70 ^{o}C for 12 h under vigorous stirring. The dialysis of as-obtained suspension was performed in a benzoylated dialysis bag to remove the unreacted molecules, ions and impurities.

3.2.7 *In vitro* studies

3.2.7.1`Cell culture

The breast cancer cell line (MCF-7) and mouse embryo fibroblast cell (NIH3T3) were cultured in Dulbeccòs modified Eagles medium (DMEM) supplemented with 10 % heat inactivated fetal bovine serum, penicillin (100 U/mL) and streptomycin (100 μg/mL) (Invitrogen Corporation, CA, USA) and incubated at 37 °C in 5 % CO_2 incubator (Thermo Scientific, NC).

3.2.7.2 Proliferation assay

The *in vitro* cell viability was assessed using 3-(4, 5-dimethylthiazol-2-yl)-2,5-diphenyltetrazolium bromide (MTT) proliferation assay in NIH3T3 and MCF-7 cells. The MCF-7 and NIH3T3 cells in monolayer culture were cultivated in DMEM media supplemented with 10 % heat inactivated fetal bovine serum, penicillin (100 U/mL) and streptomycin (100 μg/mL) (Invitrogen Corporation, CA, USA). Cells were trypsinized and plated at a density of ~ 20, 000 cells / well in 96-well plate. After ~ 24 h, cells were treated with varying concentration of curcumin, curcumin-conjugated Au-QCs, GSH-conjugated Au-QCs Au-QCs , and curcumin-conjugated Au-NPs, then cells were incubated in 5% CO_2 at 37 °C for 24 h. After the treatment, medium was removed and 10 μL of MTT (methylthiazole tetrazolium, 10 mg/mL) and 90 μl of DMEM was added in each well and further incubated for 4 h at 37°C. Formazan crystals thus formed were solubilized in 100 μL iso-propanol and the absorbance of the MTT was measured at 570 nm with microplate reader (Theromo Multiskan go).

3.2.7.3 Flow cytometry

Quantitatively measure of MCF-7 cells apoptosis was detected by phosphatidylserine exposure on cell-membrane with annexin V. After either unstimulated or stimulated with Curcumin and subsequently treated with Au QCs was studied after 24 h, cells were

trypsinized, washed twice with pre-cooled PBS and incubated with a binding buffer containing annexin V-fluorescein isothiocyanate (FITC) and propidium iodide (PI) (BD Biosciences). Flow cytometry analysis was performed using FACS calibur (Becton Dickinson). Apoptotic cells were defined as both PI-Positive and annexin V-FITC positive.

3.2.7.4 Western blot analysis

Protein extract from MCF-7 cells was obtained in RIPA lysis buffer containing 0.1% PMSF. Same amount of samples were separated by SDS-PAGE gel, transferred and immobilized on a polyvinylidene difluoride membrane. The membrane was blocked with 5% nonfat dry milk in Tris-buffered saline containing 0.05% Tween 20 (TBS-T) for 1 h at room temperature. Appropriate primary antibody was followed by incubation of the membranes in overnight at 4 °C. Horseradish peroxidase-conjugated goat anti-mouse IgG secondary antibody (1:5000) (Santa Cruz Biotechnology) was incubated at room temperature for 1 h at room temperature. After the final wash, the immunoreactive bands were detected on X-ray films by enhanced chemiluminescence (Thermo scientific). Data was obtained from three independent experiments.

3.3 Results and Discussion

The synthesis of Au-QCs using curcumin as both reducing as well as capping agent is very crucial regarding the solubility of curcumin. Curcumin is soluble in water only at alkaline condition but at the same time, it also shows the degradation. According to Price et al, the degradation rate constant rapidly increases from pH ~7.4 to a maximum at about pH ~10.2 and then decline at higher pH values.[26] Therefore, instead of low pH where the curcumin molecules have also low solubility, a high pH ~13.5 was selected for reaction where curcumin molecule was completely soluble and the degradation rate constant was also low.

Moreover, in order to minimize the chances of alkaline degradation of curcumin, the reaction time was also minimized.

The UV-vis spectroscopic study of curcumin in DMSO and alkaline medium shows two distinct absorption bands of curcumin molecules at ~262 nm and ~425 nm, which is related to the n-π* and π-π* transitions (Figure 1).[1,27] It can be seen from the figure 1 that the transition at ~262 nm was least affected when conjugated with Au-NPs and Au-QCs. The UV-vis spectra of curcumin-conjugated Au-NPs show a sharp peak in deep UV at ~262 nm due to n-π* transition of curcumin molecules and a broad peak in visible region at ~528 nm due to the surface plasmon resonance. Interestingly, in the case of curcumin-conjugated Au-QCs, the SPR peak was diminished which shows the absence of Au-NPs in the sample. The GSH-conjugated Au-QCs also did not show any absorption in visible region which again confirmed the absence of Au-NPs in the suspension (Figure 1).

The photoluminescence study (using Cary Eclipse photoluminescence spectrophotometer from Varian equipped with Xenon flash lamp) of curcumin-conjugated gold clusters shows the maximum intensity emission peak ~ 470 nm when excited with the ~ 360 nm wavelength (Figure 2). However, curcumin-conjugated gold nanoparticles did not show fluorescence at any excitation wavelength.

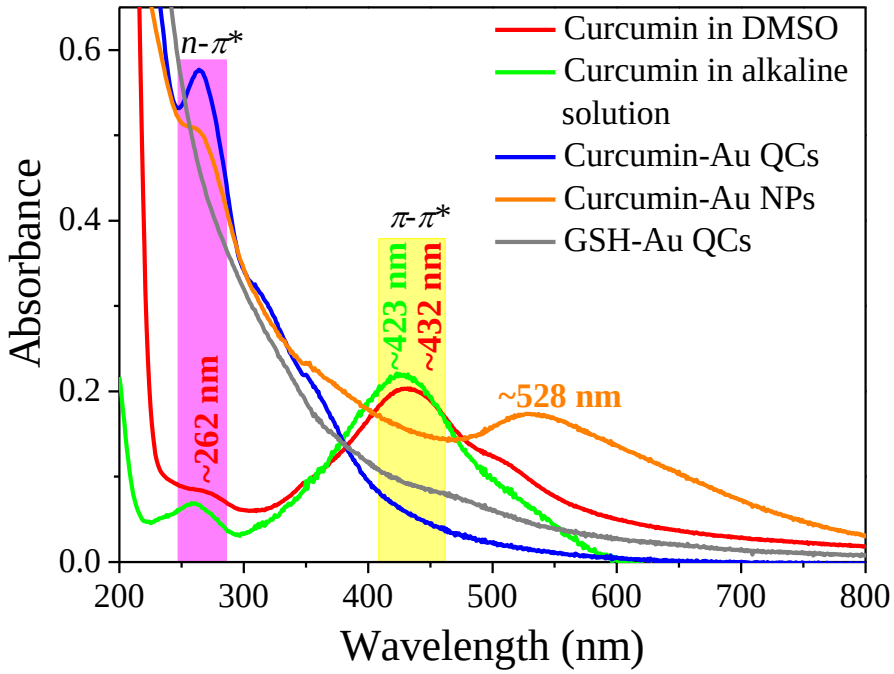

Figure 1. *UV-vis spectroscopic study of curcumin in DMSO and alkaline condition, curcumin-conjugated Au-QCs, curcumin-conjugated Au-NPs, and GSH-conjugated Au-QCs.*

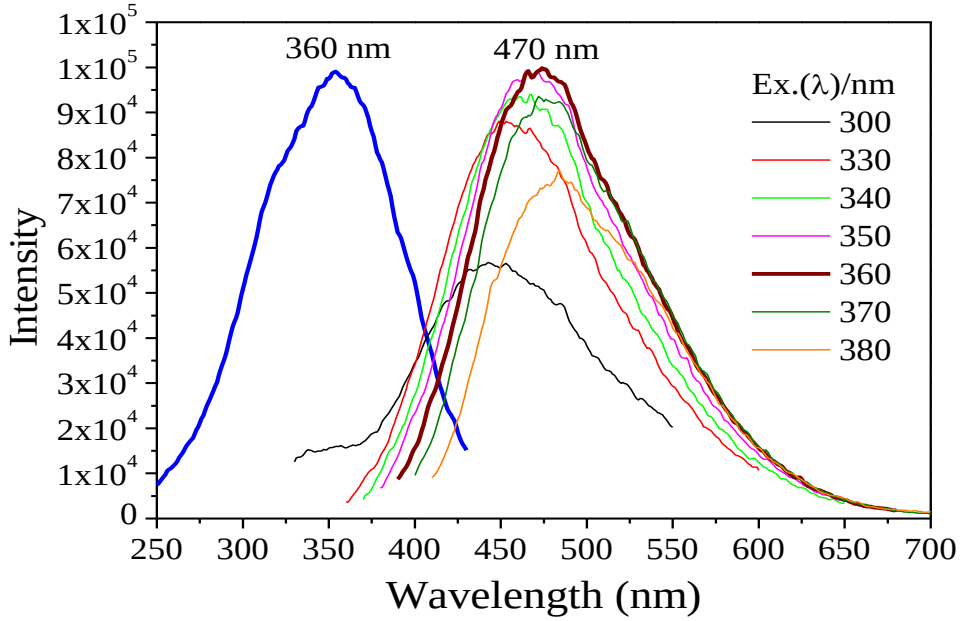

Figure 2. *The photoluminescence spectra of curcumin-conjugated Au-QCs upon excitation with different wavelengths of light.*

TEM images (collected using Tecnai G-2 T20 TEM working at accelerating voltage of 200 kV) of curcumin-conjugated Au-QCs and GSH-conjugated Au-QCs show the presence of very small particles with an average size ~2 nm (Figure 3). The particles were well dispersed and uniform in the size. The curcumin-conjugated Au-NPs were also well dispersed with an average size ~18 nm. DLS results (Brookhaven Instrument Corps.) were well correlated with the particle size observed in TEM results. The mean diameter of curcumin-conjugated Au-QCs, GSH-conjugated Au-QCs and curcumin-conjugated nanoparticles was found around 4 nm, 2 nm, and 20 nm, respectively (Figures 4, 5, and 6).

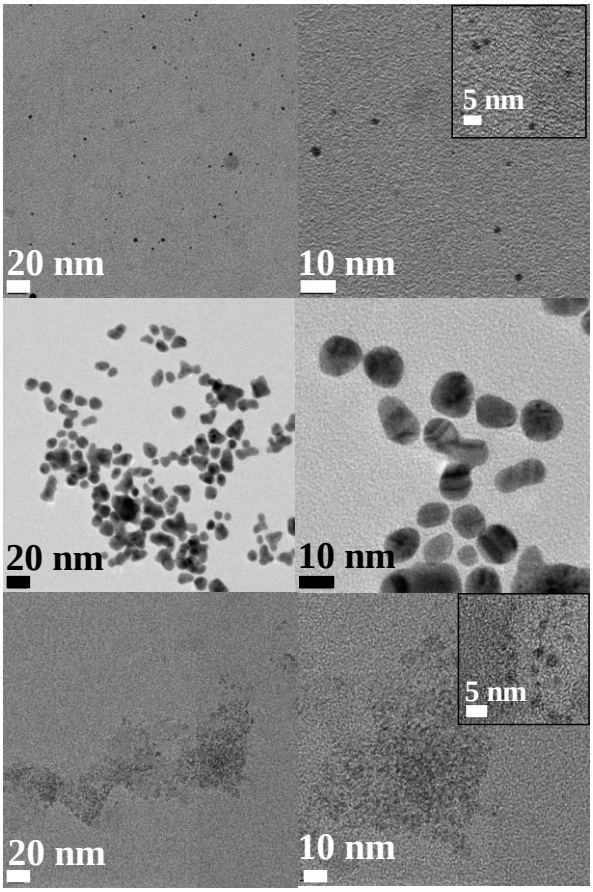

Figure 3. *The TEM images of curcumin-conjugated Au-QCs (top layer), curcumin-capped Au-NPs (medium layer), and GSH-conjugated Au-QCs (bottom layer). The inset in the second row images are corresponding magnified images.*

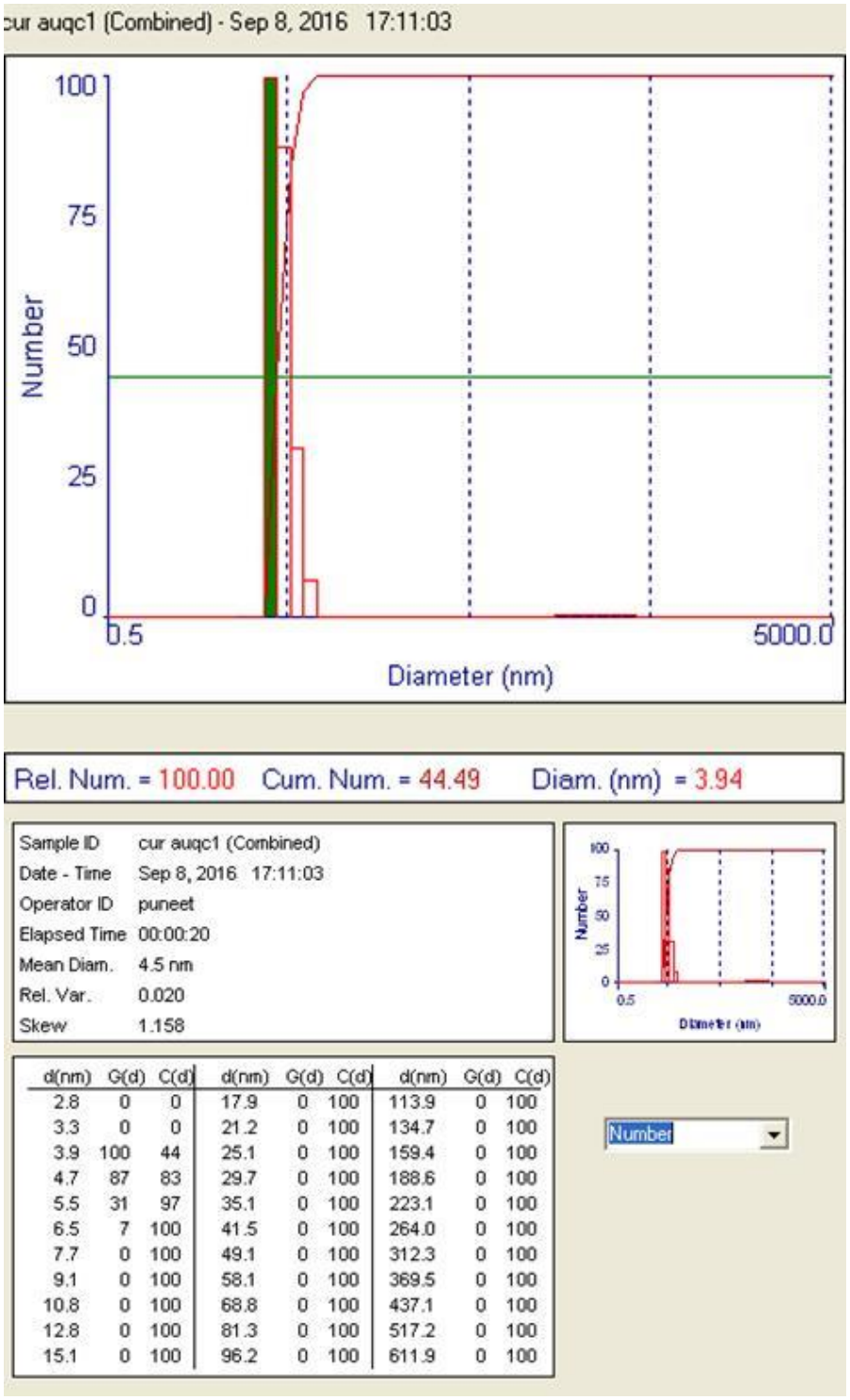

Figure 4. *DLS results of curcumin-conjugated Au-QCs showing the presence of particles with mean diameter around 4 nm.*

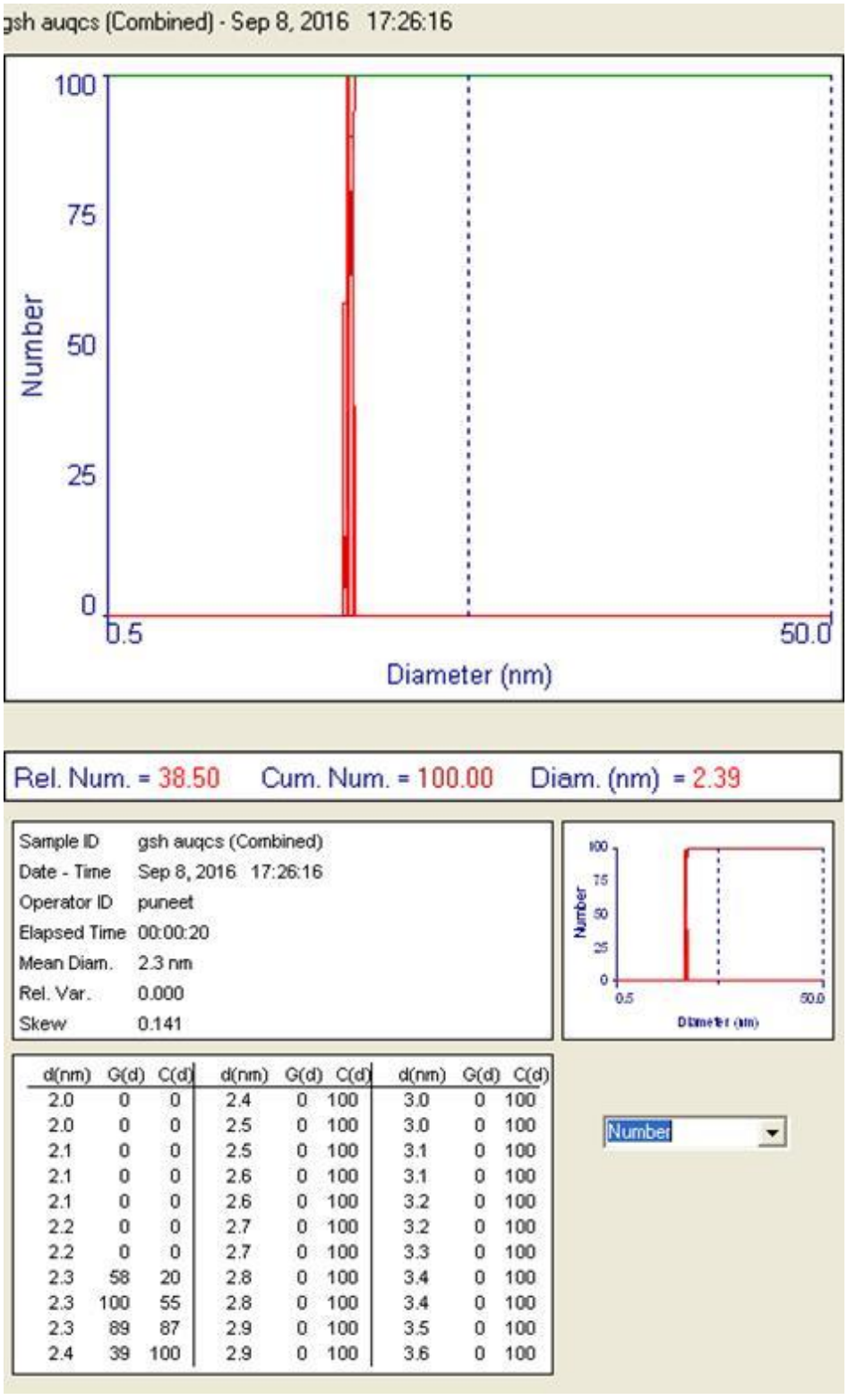

d(nm)	G(d)	C(d)	d(nm)	G(d)	C(d)	d(nm)	G(d)	C(d)
2.0	0	0	2.4	0	100	3.0	0	100
2.0	0	0	2.5	0	100	3.0	0	100
2.1	0	0	2.5	0	100	3.1	0	100
2.1	0	0	2.6	0	100	3.1	0	100
2.1	0	0	2.6	0	100	3.2	0	100
2.2	0	0	2.7	0	100	3.2	0	100
2.2	0	0	2.7	0	100	3.3	0	100
2.3	58	20	2.8	0	100	3.4	0	100
2.3	100	55	2.8	0	100	3.4	0	100
2.3	89	87	2.9	0	100	3.5	0	100
2.4	39	100	2.9	0	100	3.6	0	100

Figure 5. *DLS results of GSH-conjugated Au-QCs showing the presence of particles with mean diameter around 2 nm.*

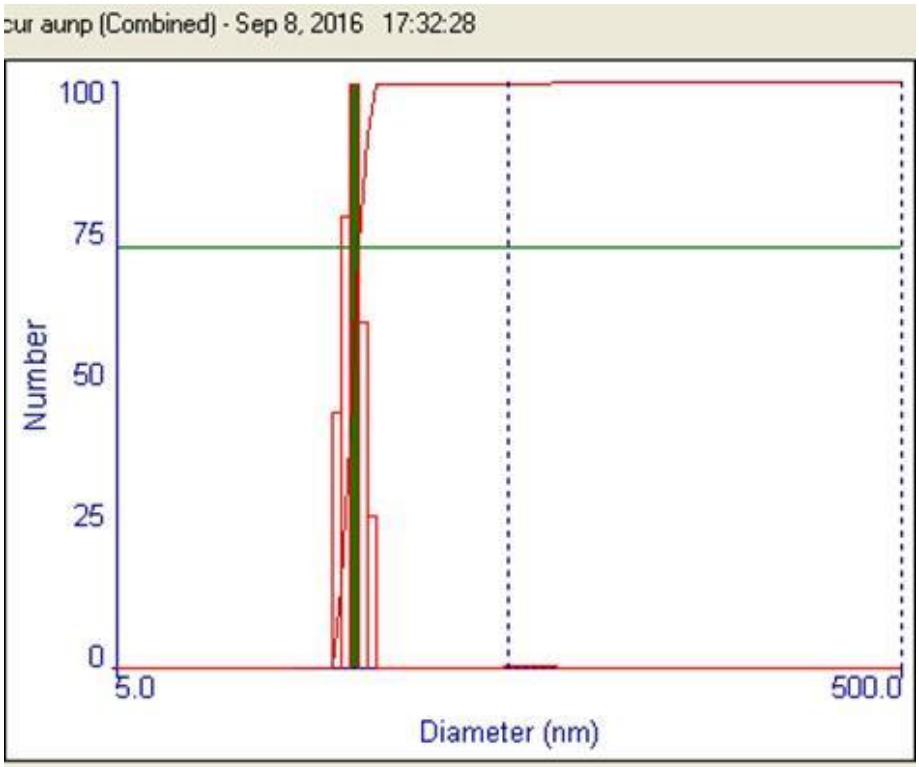

Rel. Num. = 100.00 Cum. Num. = 72.02 Diam. (nm) = 20.19

Sample ID	cur aunp (Combined)
Date - Time	Sep 8, 2016 17:32:28
Operator ID	puneet
Elapsed Time	00:01:00
Mean Diam.	20.1 nm
Rel. Var.	0.011
Skew	10.957

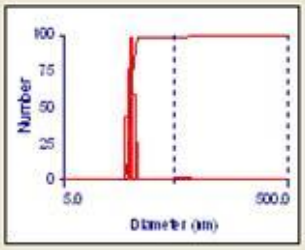

d(nm)	G(d)	C(d)	d(nm)	G(d)	C(d)	d(nm)	G(d)	C(d)
14.7	0	0	26.3	0	100	47.0	0	100
15.5	0	0	27.7	0	100	49.6	0	100
16.3	0	0	29.2	0	100	52.3	0	100
17.2	0	0	30.8	0	100	55.1	0	100
18.2	44	14	32.5	0	100	58.1	0	100
19.1	77	39	34.2	0	100	61.3	0	100
20.2	100	72	36.1	0	100	64.6	0	100
21.3	59	91	38.1	0	100	68.1	0	100
22.4	26	100	40.1	0	100	71.8	0	100
23.7	0	100	42.3	0	100	75.7	0	100
24.9	0	100	44.6	0	100	79.8	0	100

Number

Figure 6. *DLS results of curcumin-conjugated Au-NPs showing the presence of particles with mean diameter around 20 nm.*

The deconvoluted ESI-MS spectrum (collected using Q Exactive Orbitrap Mass Spectrometer from Thermo Scientific) of curcumin-conjugated Au-QCs shows the synthesis of mixed population of gold cluster species (Figure 7).

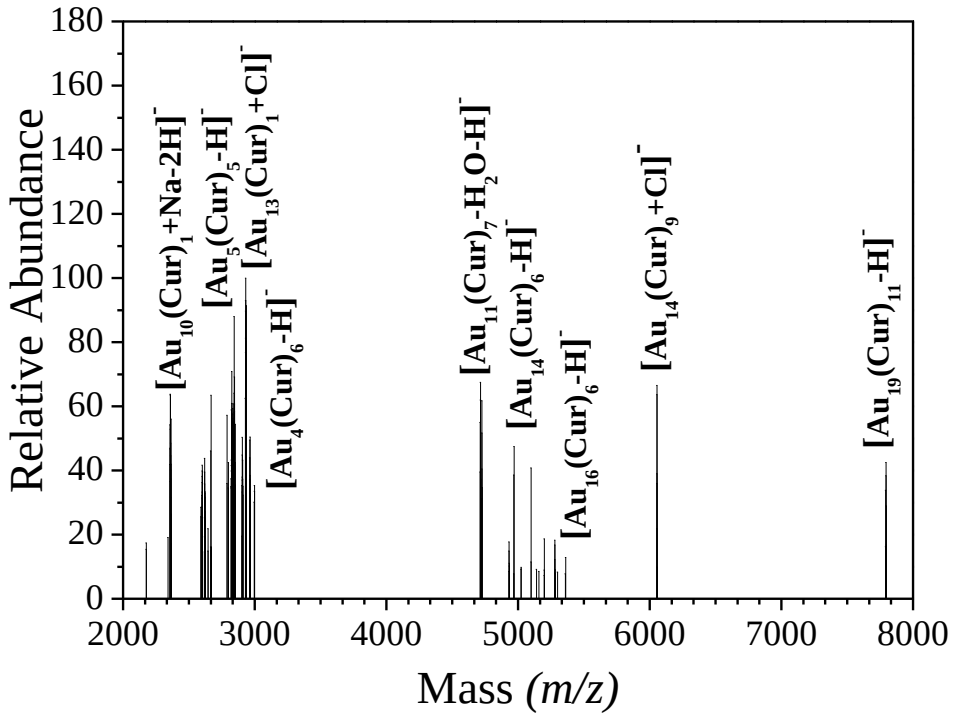

Figure 7. *The deconvoluted ESI-MS spectrum of curcumin-conjugated Au-QCs shows the synthesis of various species.*

In order to determine the cytotoxic effect of curcumin, curcumin-conjugated Au-QCs, GSH conjugated Au-QCs, and curcumin-conjugated Au-NPs, the *in vitro* analysis against the normal (NIH 3T3) and cancer (MCF-7) cell-lines were done using, the MTT assay. Figure 8 shows the cell viabilities against curcumin, curcumin-conjugated Au-QCs, GSH conjugated Au-QCs, and curcumin-conjugated Au-NPs. Curcumin was considered as positive control to compare the cytotoxicity of curcumin-conjugated Au-QCs, GSH conjugated Au-QCs, and curcumin-conjugated Au-NPs (Figure 8). The concentration of

curcumin was set same as the curcumin-conjugated Au-QCs, GSH-conjugated Au-QCs, and curcumin-conjugated Au-NPs.

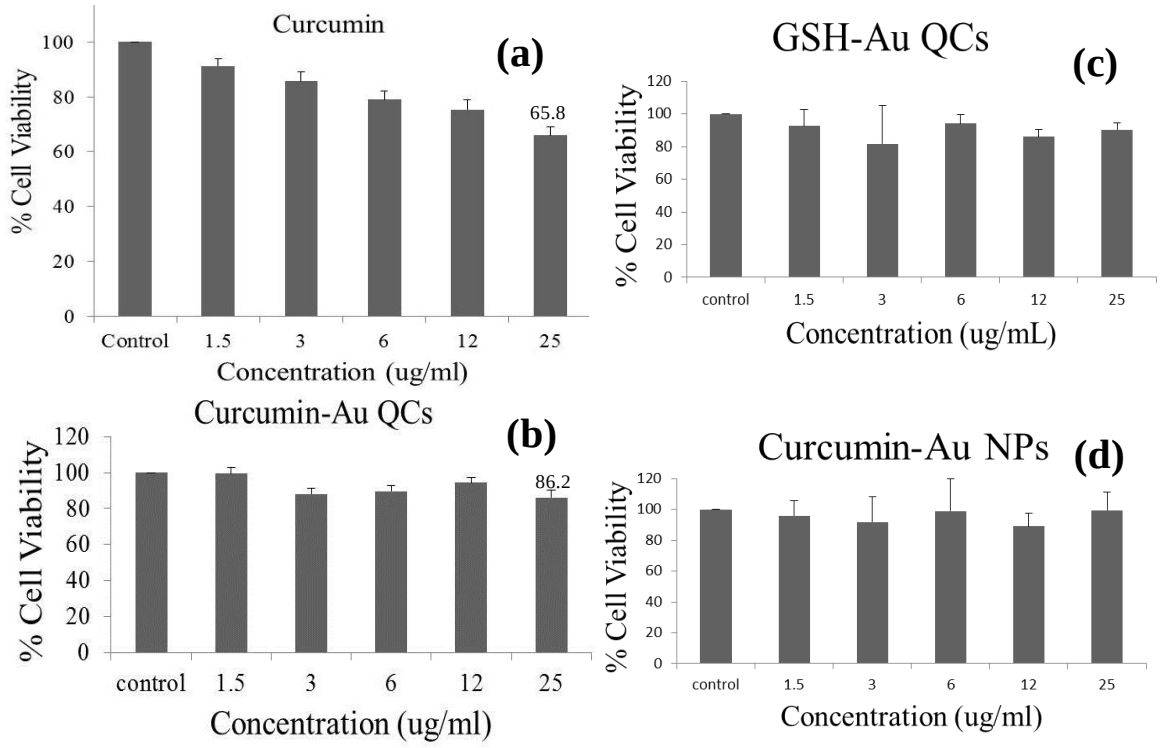

Figure 8. *In vitro* normal cell viabilities after incubation of 24 h with (a) curcumin, (b) curcumin-conjugated Au-QCs, (c) GSH-conjugated Au-QCs, and (d) curcumin-conjugated Au-NPs.

The samples were incubated with MCF-7 cancer cells for 24 h at 37 °C at different concentrations. The curcumin alone was found to be more cytotoxic to normal cells than curcumin-conjugated Au-QCs, GSH-conjugated Au-QCs and curcumin-conjugated Au-NPs at concentrations 25 μg/mL (Figure 8).

Importantly, the cytotoxicity of curcumin-conjugated Au-QCs to MCF-7 cells was almost the same as curcumin up to the concentration of 25 μg/mL. It shows that curcumin was able to retain its anti-cancer property even upon conjugation with Au-QCs (Figure 9).

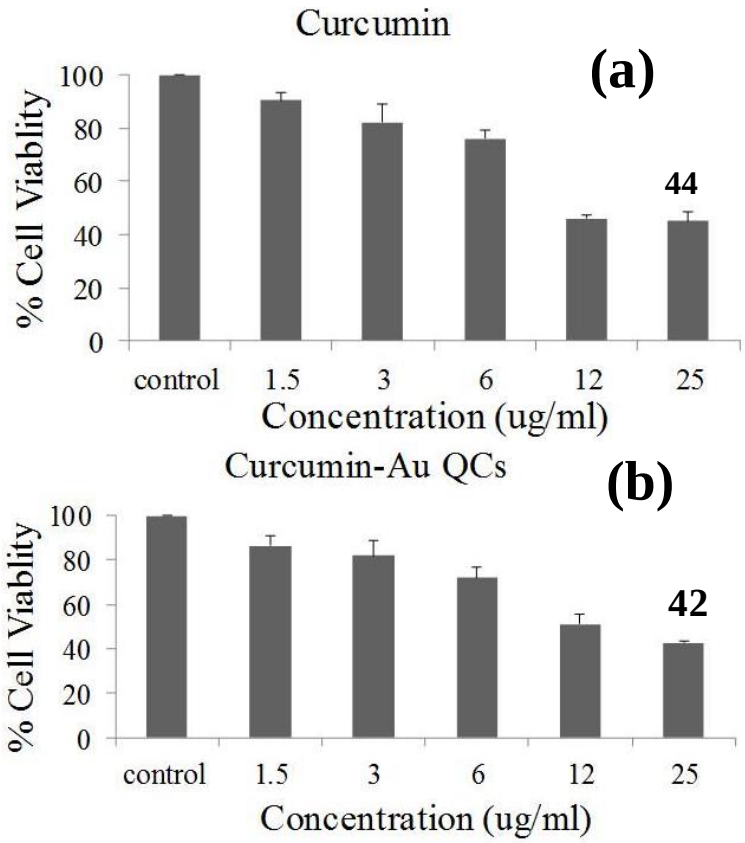

Figure 9. *In vitro MCF-7 cancer cell viabilities after incubation of 24 h with (a) curcumin, and (b) curcumin-conjugated Au-QCs.*

Furthermore, annexin-V and PI staining were applied to confirm apoptotic changes in curcumin-conjugated Au-QCs treated MCF-7 cells. Double stained cells were analyzed by flow cytometer. The results revealed that MCF-7 cells treated with curcumin-conjugated Au-QCs exhibited higher apoptosis in annexin-V (+)/PI (+) staining (apoptotic cells) than control cells without treatment (Figure 10).

To study and compare the effect of curcumin-conjugated Au-QCs over curcumin alone, on apoptotic and inflammatory proteins expression such as AKT, STAT3, Bcl-xL were measured by western blot analysis. It was found that their expressions got decreased upon the treatment of curcumin-conjugated Au-QCs (Figure 11).

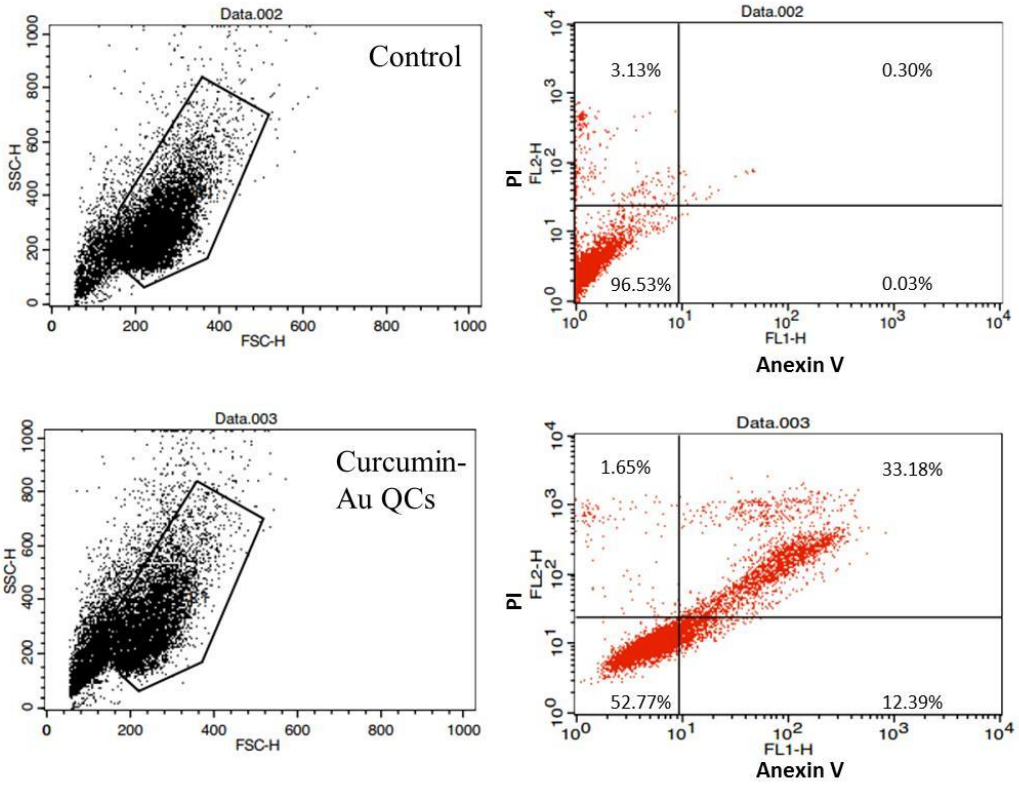

Figure 10. *Flow cytometric analysis of without treated (upper row) and treated with curcumin-conjugated Au-QCs MCF-7 cells.*

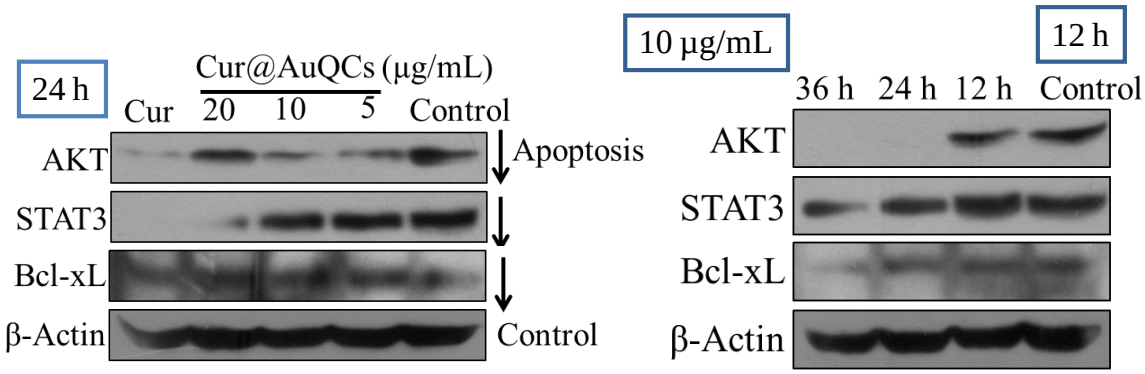

Figure 11. *Western Blot analysis for apoptosis and inflammation related proteins in MCF-7 cells.*

3.4 Conclusion

In summary, we synthesized curcumin-conjugated Au-QCs which have high curcumin loading capacity than their counterparts *ie.* curcumin-conjugated Au-NPs for the same amount of gold content. Curcumin-conjugated Au-QCs were observed to retain their cytotoxicity to cancer cells while show less cytotoxic to the normal cells in comparison to curcumin alone. Flow cytometry and western blot assay confirm that curcumin-conjugated Au-QCs induce the apoptosis in cancer cells. We believe that curcumin-conjugated Au-QCs will be applicable for drug delivery due to their small size, high drug loading capacity, low gold content, and low cytotoxicity.

3.5 References

1 D. K. Singh, R. Jagannathan, P. Khandelwal, P. M. Abraham and P. Poddar, *Nanoscale*, 2013, **5**, 1882–93.

2 L. Shen, C.-C. Liu, C.-Y. An and H.-F. Ji, *Sci. Rep.*, 2016, **6**, 20872.

3 J. S. Wright, *J. Mol. Struct.*, 2002, **591**, 207–217.

4 D. Bagchi, S. Chaudhuri, S. Sardar, S. Choudhury, N. Polley, P. Lemmens and S. K. Pal, *RSC Adv.*, 2015, **5**, 102516–102524.

5 M. Panchatcharam, S. Miriyala, V. S. Gayathri and L. Suguna, *Mol. Cell. Biochem.*, 2006, **290**, 87–96.

6 R. K. Maheshwari, A. K. Singh, J. Gaddipati and R. C. Srimal, *Life Sci.*, 2006, **78**, 2081–2087.

7 C. Y. Loo, R. Rohanizadeh, P. M. Young, D. Traini, R. Cavaliere, C. B. Whitchurch and W. H. Lee, *J. Agric. Food Chem.*, 2016, **64**, 2513–2522.

8 E. El Khoury, M. Abiad, Z. G. Kassaify and D. Patra, *Colloids Surfaces B Biointerfaces*, 2015, **127**, 274–280.

9 S. Z. Moghadamtousi, H. A. Kadir, P. Hassandarvish, H. Tajik, S. Abubakar and K. Zandi, *Biomed Res. Int.*, 2014, **2014**, 186864.

10 P. Tyagi, M. Singh, H. Kumari, A. Kumari and K. Mukhopadhyay, *PLoS One*, 2015, **10**, 1–15.

11 X. Gao, F. Zheng, G. Guo, X. Liu, R. Fan, Z. Qian, N. Huang and Y. Wei, *J. Mater. Chem. B*, 2013, **1**, 5778.

12 A. Valentini, F. Conforti, A. Crispini, A. De Martino, R. Condello, C. Stellitano, G. Rotilio, M. Ghedini, G. Federici, S. Bernardini and D. Pucci, *J. Med. Chem.*, 2009, **52**, 484–491.

13 S. F. Peng, C. Y. Lee, M. J. Hour, S. C. Tsai, D. H. Kuo, F. A. Chen, P. C. Shieh and J. S. Yang, *Int. J. Oncol.*, 2014, **44**, 238–246.

14 S. Hatamie, O. Akhavan, S. K. Sadrnezhaad, M. M. Ahadian, M. M. Shirolkar and H. Q. Wang, *Mater. Sci. Eng. C*, 2015, **55**, 482–489.

15 C.-C. Chen, M. Sureshbabul, H.-W. Chen, Y.-S. Lin, J.-Y. Lee, Q.-S. Hong, Y.-C. Yang and S.-L. Yu, *Evidence-Based Complement. Altern. Med.*, 2013, **2013**, 1–17.

16 A. N. Begum, M. R. Jones, G. P. Lim, T. Morihara, P. Kim, D. D. Heath, C. L. Rock, M. A. Pruitt, F. Yang, B. Hudspeth, S. Hu, K. F. Faull, B. Teter, G. M. Cole and S. A. Frautschy, *J. Pharmacol. Exp. Ther.*, 2008, **326**, 196–208.

17 A. Mathew, T. Fukuda, Y. Nagaoka, T. Hasumura, H. Morimoto, Y. Yoshida, T.

Maekawa, K. Venugopal and D. S. Kumar, *PLoS One*, 2012, **7**, 1–10.

18 S. K. Tiwari, S. Agarwal, B. Seth, A. Yadav, S. Nair, P. Bhatnagar, M. Karmakar, M. Kumari, L. K. Chauhan, D. K. Patel, V. Srivastava, D. Singh, S. K. Gupta, A. Tripathi, R. K. Chaturvedi and K. C. Gupta, *ACS Nano*, 2014, **8**, 76–103.

19 S. Palmal, A. R. Maity, B. K. Singh, S. Basu, N. R. Jana and N. R. Jana, *Chem. - A Eur. J.*, 2014, **20**, 6184–6191.

20 F. Yang, G. P. Lim, A. N. Begum, O. J. Ubeda, M. R. Simmons, S. S. Ambegaokar, P. P. Chen, R. Kayed, C. G. Glabe, S. A. Frautschy and G. M. Cole, *J. Biol. Chem.*, 2005, **280**, 5892–5901.

21 C. Ramassamy, *Eur. J. Pharmacol.*, 2006, **545**, 51–64.

22 L. Cui, J. Miao and L. Cui, *Antimicrob. Agents Chemother.*, 2007, **51**, 488–494.

23 R. Chakrabarti, P. S. Rawat, B. M. Cooke, R. L. Coppel and S. Patankar, *PLoS One*, 2013, **8**, 1–14.

24 N. Mathuria and R. J. Verma, *Acta Pol. Pharm. - Drug Res.*, 2008, **65**, 339–343.

25 X. X. Yang, C. M. Li and C. Z. Huang, *Nanoscale*, 2016, **8**, 3040–3048.

26 L. C. Price and R. W. Buescher, *J. Food Sci.*, 1997, **62**, 267–269.

27 R. Jagannathan, P. M. Abraham and P. Poddar, *J. Phys. Chem. B*, 2012, **116**, 14533–40.

28 M. M. Yallapu, S. Khan, D. M. Maher, M. C. Ebeling, V. Sundram, N. Chauhan, A. Ganju, S. Balakrishna, B. K. Gupta, N. Zafar, M. Jaggi and S. C. Chauhan, *Biomaterials*, 2014, **35**, 8635–8648.

29 P. Verderio, P. Bonetti, M. Colombo, L. Pandolfi and D. Prosperi, *Biomacromolecules*, 2013, **14**, 672–682.

30 R. Kotcherlakota, A. K. Barui, S. Prashar, M. Fajardo, D. Briones, A. Rodríguez-Diéguez, C. R. Patra and S. Gómez-Ruiz, *Biomater. Sci.*, 2016, **4**, 448–459.

31 S. Jambhrunkar, S. Karmakar, A. Popat, M. Yu and C. Yu, *RSC Adv.*, 2014, **4**, 709–712.

32 A. Mathew, A. Aravind, D. Brahatheeswaran, T. Fukuda, Y. Nagaoka, T. Hasumura, S. Iwai, H. Morimoto, Y. Yoshida, T. Maekawa, K. Venugopal and D. Sakthi Kumar, *Bionanoscience*, 2012, **2**, 83–93.

33 R. Jin, *Nanoscale*, 2010, **2**, 343–362.

34 R. C. Price and R. L. Whetten, *J. Am. Chem. Soc.*, 2005, **127**, 13750–13751.

35 L. Zhang and E. Wang, *Nano Today*, 2014, **9**, 132–157.

36 T. Chen, Y. Hu, Y. Cen, X. Chu and Y. Lu, *J. Am. Chem. Soc.*, 2013, **135**, 11595–11602.

37 S. Link, A. Beeby, S. FitzGerald, M. A. El-Sayed, T. G. Schaaff and R. L. Whetten, *J. Phys. Chem. B*, 2002, **106**, 3410–3415.

38 A. Baksi, P. L. Xavier, K. Chaudhari, N. Goswami, S. K. Pal and T. Pradeep, *Nanoscale*, 2013, **5**, 2009.

39 Y. Wang, J. Chen and X. Yan, *Anal. Chem.*, 2013, **85**, 2529–2535.

40 P. L. Xavier, K. Chaudhari, P. K. Verma, S. K. Pal and T. Pradeep, *Nanoscale*, 2010, **2**, 2769–2776.

41 L. V. Nair, S. S. Nazeer, R. S. Jayasree and A. Ajayaghosh, *ACS Nano*, 2015, **9**, 5825–5832.

42 A. M. P. Hussain, S. N. Sarangi, J. A. Kesarwani and S. N. Sahu, *Biosens. Bioelectron.*, 2011, **29**, 60–65.

43 P. Khandelwal, D. K. Singh, S. Sadhu and P. Poddar, *Chempluschem*, 2014, **79**, 134–142.

44 P. Khandelwal, D. K. Singh, S. Sadhu and P. Poddar, *Nanoscale*, 2015, **7**, 19985–20002.

45 A. Samanta, B. B. Dhar and R. N. Devi, *J. Phys. Chem. C*, 2012, **116**, 1748–1754.

46 Y. Gao, N. Shao, Y. Pei and X. C. Zeng, *Nano Lett.*, 2010, **10**, 1055–1062.

47 Z. Z. W. W. Wang and R. E. Palmer, *Nano Lett.*, 2012, **12**, 5510–5514.

48 H. H. Wang, C.-A. J. A. J. Lin, C. H. Lee, Y. C. Lin, Y. M. Tseng, C.-L. L. C. T. Hsieh, C. H. Chen, C. H. Tsai, C.-L. L. C. T. Hsieh, J. L. Shen, W. H. Chan, W. H. Chang and H.-I. I. Yeh, *ACS Nano*, 2011, **5**, 4337–4344.

49 P. Huang, J. Lin, S. Wang, Z. Zhou, Z. Li, Z. Wang, C. Zhang, X. Yue, G. Niu, M. Yang, D. Cui and X. Chen, *Biomaterials*, 2013, **34**, 4643–4654.

50 X. D. Zhang, J. Chen, J. Yang, J. Y. Wang, X. Shen, S. S. Song, H. Wang, H. He, X. J. Wang, S. J. Fan, Y. M. Sun and M. L. Guo, *J. Mater. Chem. B*, 2015, **3**, 4735–4741.

51 R. Khandelia, S. Bhandari, U. N. Pan, S. S. Ghosh and A. Chattopadhyay, *Small*, 2015, **11**, 4075–4081.

52 F. Zhou, B. Feng, H. Yu, D. Wang, T. Wang, J. Liu, Q. Meng, S. Wang, P. Zhang, Z. Zhang and Y. Li, *Theranostics*, 2016, **6**, 679–687.

53 D. Chen, B. Li, S. Cai, P. Wang, S. Peng, Y. Sheng, Y. He, Y. Gu and H. Chen, *Biomaterials*, 2016, **100**, 1–16.

54 W.-Y. W.-J. Chen, J. Lin, W.-Y. W.-J. Chen, L. Luo, E. Wei-Guang Diau and Y. Chen, *Nanomedicine*, 2010, **5**, 755–764.

55 C. Liu, H. Wu, Y. Hsiao, C. Lai, C. Shih, Y.-K. Peng, K.-C. Tang, H.-W. Chang, Y.-C. Chien, J.-K. Hsiao, J.-T. Cheng and P.-T. Chou, *Angew. Chemie Int. Ed.*, 2011, **50**, 7056–7060.

56 L. V Nair, D. S. Philips, R. S. Jayasree and A. Ajayaghosh, *Small*, 2013, **9**, 2673–7.

Chapter IV

Interaction of hTau protein with curcumin-conjugated silver quantum clusters

Amyloid fibrillation is a major reason behind the development of Alzheimer's disease (AD). Nanomaterials have been very well studied for their interaction with amyloid proteins and shown to promote as well as inhibit the amyloid fibrillation process. Amyloid fibrillation process gets affected by the shape, size, surface charge, surface functionalization as well as the nature of nanomaterials. In view of this, metal quantum clusters can be considered as a potential alternate because of their very small size (less than or comparable to protein molecules), which would be favorable for their binding and intercalation with amyloid proteins, resulting in the inhibition of amyloid fibrillation process. In this chapter, the curcumin molecule, which is a well-known therapeutic agent, is used for synthesis of silver quantum clusters where curcumin molecule itself, acts as reducing as well as capping agent. The curcumin-conjugated silver clusters were able to effectively inhibit the amyloid fibrillation process than curcumin itself. Surprisingly, curcumin-conjugated silver nanoparticles and GSH-conjugated silver quantum clusters were found to promote the fibrillation process.

4.1 Introduction

Alzheimer's disease (AD) is a most common type of dementia in all over the world affecting mainly the elderly population. The progressive accumulation of aggregates of β-amyloid proteins (Aβ) induces the neurotoxicity, oxidative damage, and inflammation that result in to the development of AD. The Aβ proteins are required for normal synaptic functioning in the brain but at the time of AD, the Aβ proteins may get self-aggregate and forms oligomers of various sizes and finally, neurotic plaques around the neurons. These plaques are reported to induce the phosphorylation of microtubule-associated proteins called as Tau protein. The hyper-phosphorylation of Tau protein hinders the normal functioning of regulating axonal transport and leads to the accumulation of neurofibrillary tangles and toxic species of soluble Tau inside the neuronal cells, which is considered as second major change in the AD pathology. In contrast, according to the recent reports, this is the Tau protein, not Aβ proteins, which is the key driver for AD's symptoms.[1–3]

Nanomaterials have been studied thoroughly to understand their interaction with Aβ monomers in the fibrillation process.[4] Linse et al. showed that nanoparticles such as copolymer particles, cerium oxide particles, quantum-dots, and carbon nanotubes promotes the fibrillation process by enhancing the probability of appearance of a critical nucleus for nucleation process results in the shortening of lag (nucleation) phase which actually depends on the amount and nature of particle surface.[5] The TiO_2-NPs are also shown to promote the amyloid fibrillation process by shortening the nucleation process which is the key 'rate-determining' step.[6] In contrast, nanomaterials such as CdSe/ZnS QDs, CdTe NPs, protein microspheres, polymer nanoparticles, gold nanoparticles, graphene, graphene oxide, graphene quantum dots are reported to inhibit the fibrillation process.[7–26] In some of

the recent reports, photothermal therapies and megnetothermal therapies using graphene oxide and magnetic nanoparticles, respectively are also used for disruption of amyloid fibrils.[27,28] Altogether, these reports suggest that nanomaterials may become a potential candidate to combat with AD.

The relative concentration of nanoparticles to the amyloid proteins as well as the chemical structure of capping agents found to affect the fibrillation process.[13,29,30] Therefore, the selection of capping agent is a very crucial step while using the nanomaterials for inhibition of the fibrillation process. There are several capping agents used for these studies such as dihydrolipoic acid, polyethylenimine, polyoxometalates with Wells–Dawson structure and LPFFD peptide, amyloid binding aptamer, citrate, N-acetyl-L-cysteine, LVFFARK peptide, KLVFFC-NH_2 peptides, thioglycolic acid, capsaicin, curcumin etc.[7–10,14,20,22,26,31–34]

Among these, curcumin has gained enormous attention as a potential anti-Alzheimer's agent.[35–37] Curcumin is a natural polyphenolic non-flavonoidic product derived from the rhizome of Indian spice turmeric (*curcuma longa*) shows diverse medicinal applications due to its anti-inflammatory and anti-oxidant activities.[38–40] However, due to its poor oral absorption, rapid metabolism, systemic elimination and limited blood brain barrier (BBB) permeability may limit its clinical impacts.[41,42] Several approaches have been explored to improve its bioavailability including solid lipid nanoparticles, PLGA nanoparticles, gold nanoparticles, polymeric micelles, cellulose acetate-solid dispersion, silica coated liposomes, organogel-based nano-emulsions, sugar-curcumin conjugates, nano-liposomes.[19,43–54]

There is a lack of reports on the use of metal nanoclusters to improve the water dispersibility of curcumin as well as curcumin-conjugated metal nanoclusters for anti-AD. In contrast to metal nanoparticles, metal quantum clusters are <2 nm in size and made up of few atoms to few tens of atoms which provide a huge surface area to volume ratio for loading high amount of drugs on the surface.[55,56] Among metal quantum clusters, gold and silver quantum clusters are extensively studied and found to be non-toxic to mammalian cells at the concentration used.[57–60] Silver nanoparticles are reported to cross the BBB and found to be safe for the use.[61,62] Therefore, in the present chapter, I showed the use of silver quantum clusters to improve the water solubility of curcumin as well as to study the effect of curcumin-conjugated silver quantum clusters on the fibrillation process of Tau protein.

4.2 Experimental Section

4.2.1 Materials

All chemicals were of analytical grade and used as received without any further purification, unless otherwise mentioned. Benzoylated dialysis tube, curcumin, $AgNO_3$, and DMSO were purchased from Sigma Aldrich. NaOH was purchased from Thomas Baker. All glassware's were washed with aquaregia (HCl: HNO_3 = 3:1) carefully and rinsed with Millipore water (18.2 MΩ resistance) before using them for synthesis.

4.2.2 Synthesis and purification of curcumin-conjugated silver quantum clusters

For the synthesis of curcumin-conjugated Ag-QCs, 14.8 mg of curcumin was added in to the 2 mL of 0.1 M NaOH and mixed vigorously for proper solubility. The alkaline solution of curcumin was immediately diluted with 36 mL of double distilled water followed by vigorous stirring. Then, 2 mL of 10^{-2} M of $AgNO_3$ was added in above solution without

any delay. Just after the addition of $AgNO_3$, a drastic change in the color of solution from reddish to brownish was observed. The solution was allowed to continuously stir for another 24 h at 180 rpm at 27 °C.

The above suspension was centrifuged at 25,000 g for 15 min at 4 °C to ensure the complete removal of the nanoparticles, if present. The as-obtained supernatant was dialyzed using benzoylated dialysis bag with pore size cutoff ~2,000 Da which can separate the compounds with MW ≤1,200 from compounds with MW >2,000. The dialysis was performed for 2 days while continuously changing the dialysate after every 6 h in order to remove unreacted metal ions and curcumin molecules as well as to neutralize the pH of the suspension. After 2 days, the suspension was stored in a capped bottle at 4 °C.

4.2.3 Quantification of curcumin molecules in the quantum cluster suspension

For the quantification of curcumin molecules, first of all, the UV-vis measurements (Jasco UV-vis-NIR dual beam spectrometer (Model V570) operated at a resolution of 2 nm) were performed for the serially diluted curcumin solutions and the plot was made in between the intensity of ~262 nm peak and the concentration of curcumin molecules. Then, this plot was used to measure the concentration of curcumin present in the nanocluster suspension as well as the dialysates by measuring the intensity of ~262 nm peak.

4.2.4 Synthesis of curcumin-conjugated Ag-NPs

For the synthesis of curcumin-conjugated Ag-NPs, the procedure mentioned by Yang et al[63] was used with slight modifications. Briefly, a solution of 500 µL of 20 mM curcumin was prepared in DMSO and diluted by 45 mL of double distilled water followed by vigorous stirring. The pH of the solution was adjusted to alkaline by the addition of 100 µL of 1M NaOH and the temperature was set to ~100 °C while continuous stirring. Then, 2.5

mL of 10^{-2} M $AgNO_3$ was added in the above solution, which leads to the change in the color of the solution from reddish to brownish, immediately. The mixture was cooled down and dialyzed using dialysis bag with pore size ~12 kDa for 2 days after continuous change of dialysate at every 6 h of period which is able to separate the nanoparticles from unreacted metal ions and curcumin molecules impurities.

4.2.5 Synthesis and purification of GSH-conjugated Ag-QCs

Briefly, 10 mL of 10^{-2} M GSH was added to 30 mL of double distilled water and the pH was maintained to alkaline by the addition of 200 µL of 1 M NaOH with vigorous stirring ~70 °C. Then, 5 mL of 10^{-2} M $AgNO_3$ was added followed by the addition of 5 mL of 50 mM $NaBH_4$. After 12 h of continuous stirring ~70 °C, the mixture was cooled down and dialyzed using the benzoylated dialysis bag with pore size ~2 kDa for 2 days with continuous change of dialysate after every 6 h.

4.2.6 Tau interaction study

4.2.6.1 Expression and Purification of Tau

The four repeat Tau (*ie.* K18Wt) domain cloned in pT7 vector were transformed successfully in BL21* and expressed at 37 °C. Cells were induced with 0.5 mM IPTG after the OD at A_{600} reached to 0.5 to 0.6. The cells were allowed to grow at 37 °C post-induction and were harvested by pelleting at 4000 rpm at 4 °C for 10 min. The pellets were resuspended in cell lysis buffer containing 1 mM EGTA, 2 mM $MgCl_2$, 5 mM DTT, 1 mM PMSF, protease inhibitor cocktail in 50 mM MES. The purification was done as described previously with minor changes. Cells were homogenized at 15,000 psi pressure and the lysate was collected at the end of 15 min. After adding NaCl and DTT to make their final concentration as 0.5 M and 5 mM, respectively to the lysate it was cooked for 20 min at 90

°C. This was further cooled and centrifuged at 40,000 rpm for 45 min. The supernatant was then dialyzed against Buffer A (20 mM MES, 50 mM NaCl, 1 mM EGTA, 1 mM $MgCl_2$, 2 mM DTT and 0.1 mM PMSF) over night. This was again centrifuged at 40,000 rpm for 45 min and loaded onto cation exchange column pre-equilibrated with buffer A. The protein was eluted with linear NaCl concentration of 1 M. Fractions were confirmed by SDS-PAGE and concentrated by 3 kDa centricons. Thus, concentrated Tau was loaded on gel filtration column pre-equilibrated with 1 M PBS containing 2 mM DTT. The eluted fractions were analyzed by SDS-PAGE. The confirmed fractions were pooled and concentrated by using 3 kDa centricons. The concentrated protein was aliquoted, snap freezed and stored in -80°C until further used. The concentration was estimated using bichinchoninic acid method.

4.2.6.2 Tau aggregation inhibition assay

Tau was induced to aggregate in presence of 4:1 ratio of Tau and heparin (17,500 Da) in assembly buffer containing 20 mM BES, pH 7.4, 25 mM NaCl, 1 mM DTT, 0.01 % NaN_3 and protease inhibitor. The reaction mixture was incubated at 37 °C and the aggregates formation was monitored by ThS (Thioflavin S) fluorescence at certain time intervals. The aggregation was performed in presence and absence of compounds in increasing concentrations with constant Tau concentrations of 0.28 mg/mL for repeat domain. The effect of compounds on aggregates formation was monitored by ThS fluorescence assay at different time points of incubation. The changes in the conformation of Tau protein were monitored by CD spectroscopy.

4.2.6.3 Thioflavin S fluorescence assay

Five µl of reaction mixture was diluted with 8 µM ThS in 50 mM ammonium acetate, pH 7.4 and added to 384 well-plates in triplicates. Subsequently blank was also prepared for subtracting background fluorescence. ThS fluorescence was measured after 20 min of incubation of the plate in the dark at an emission wavelength of 521 nm by exciting it at 440 nm in Tecan spectrofluorometer.

4.2.6.4 Conformational changes of Tau measured by CD spectroscopy

CD spectroscopy was performed in far UV region to study the conformational changes in the protein. Tau is a random coiled protein and upon aggregation it acquires β-sheet conformation. The impact of the compounds on preventing the formation of β-sheet structure was studied by CD spectroscopy. It was performed on a Jasco J-815 spectrometer, using cuvette with 1 mm path length. The measurements were performed in the source wavelength ranging from 250 nm to 190 nm, with a data pitch of 1.0 nm, scanning speed of 100 nm/min. All the spectra were obtained at 25 °C. The reaction mixture was diluted to 3 µM in 50 mM phosphate buffer, pH 6.8. The effect of compound on soluble Tau was also studied by incubating Tau along with compounds alone at 37 °C and the spectra was read at 25 °C.

4.3 Results and Discussion

4.3.1 Optical properties

The UV-vis absorption spectroscopic study of curcumin in DMSO shows two absorption peaks ~262 nm and ~432 nm due to the n-π* and π-π* transition in curcumin molecule (Figure 1).[42] In alkaline medium also, curcumin shows the same absorption features with slight shift which may be due to the change in the polarity of solvent.[42] In the case of curcumin-conjugated Ag-QCs, a single well defined peak was observed ~262 nm and

another broad peak also observed ~350 nm which may be due to the ligand-metal complex. The disappearance of ~432 nm peak shows the involvement of the functional group by which the π-π* transition observed. The absence of SPR peak in curcumin-conjugated as well as GSH conjugated Ag-QCs shows the absence of nanoparticles in the suspension (Figure 1).

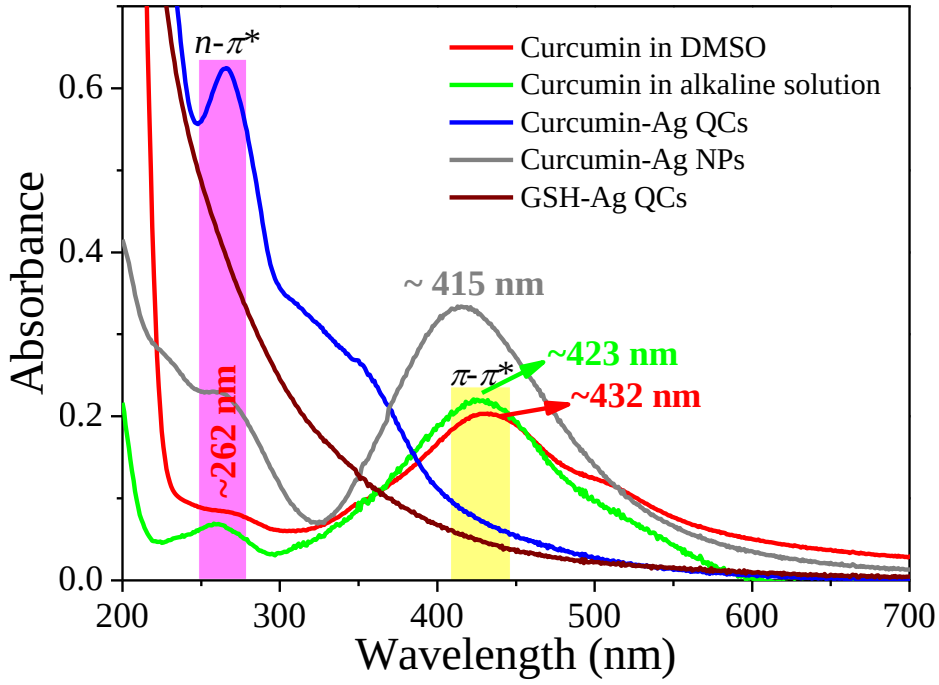

Figure 1. *UV-vis spectra of curcumin in DMSO (red color) and alkaline medium (green color) showing two main absorption peaks related to n-π* and π-π* transitions. Curcumin-conjugated Ag-NPs (grey color) show the two main absorptions related to n-π* transition of curcumin and SPR while curcumin-conjugated Ag-QCs and GSH-conjugated Ag-QCs did not show any SPR absorption.*

The photoluminescence study (using Cary Eclipse photoluminescence spectrophotometer from Varian equipped with Xenon flash lamp) of curcumin-conjugated Ag-QCs shows the fluorescence ~470 nm with a shoulder ~550 nm at an excitation wavelength ~360 nm (Figure 2).

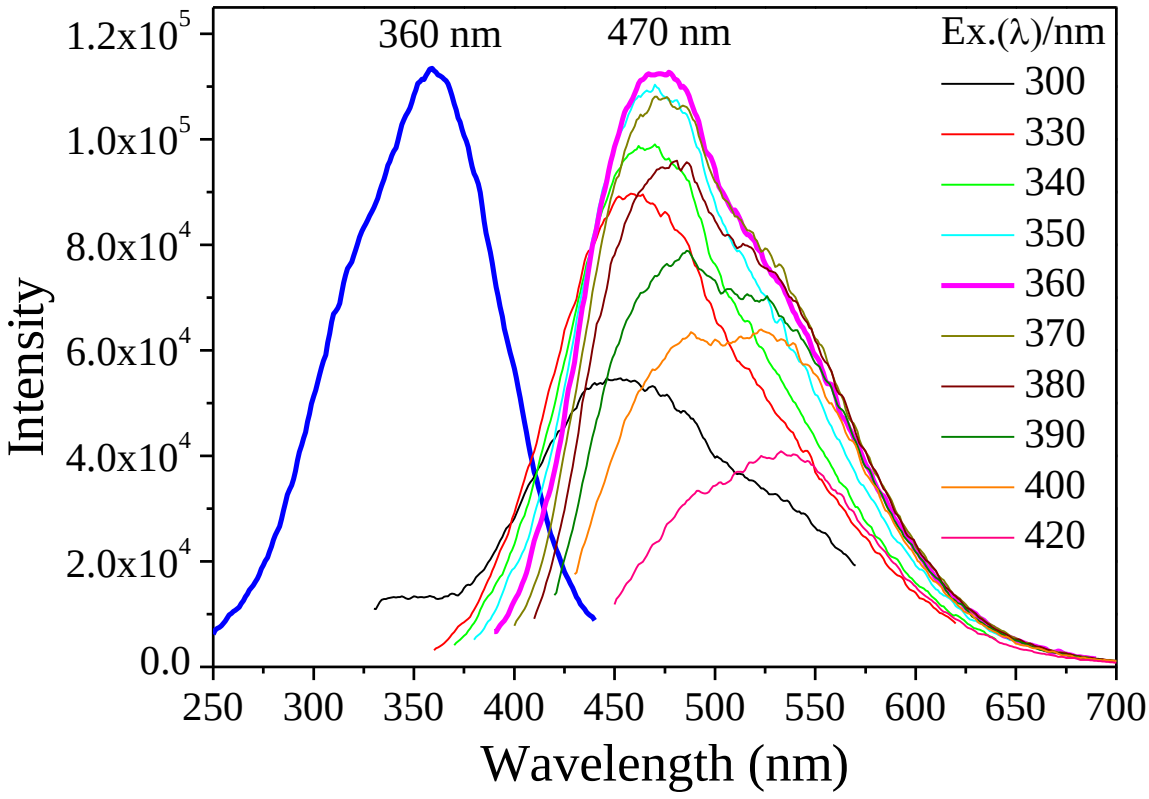

Figure 2. *Photoluminescence spectra of curcumin-conjugated Ag-QCs show the maximum fluorescence ~470 nm upon excitation with ~360 nm while the shoulder may be due to the bound curcumin molecules.*

4.3.2 Morphological and structural properties

TEM study (using Tecnai G-2 T20 TEM working at accelerating voltage of 200 kV) of curcumin-conjugated silver clusters shows the presence of very small population with the size ~2 nm (Figure 3). On the other hand, the curcumin-conjugated Ag-NPs were monodispersed, quasi-spherical particles with the size ~10 nm. The TEM images of GSH-conjugated Ag-QCs shows a well-dispersed population with size ~2 nm.

The deconvoluted ESI-MS spectrum (collected using Q Exactive Orbitrap Mass Spectrometer from Thermo Scientific) of curcumin-conjugated Ag-QCs shows the presence of mixed population of silver clusters (Figure 4).

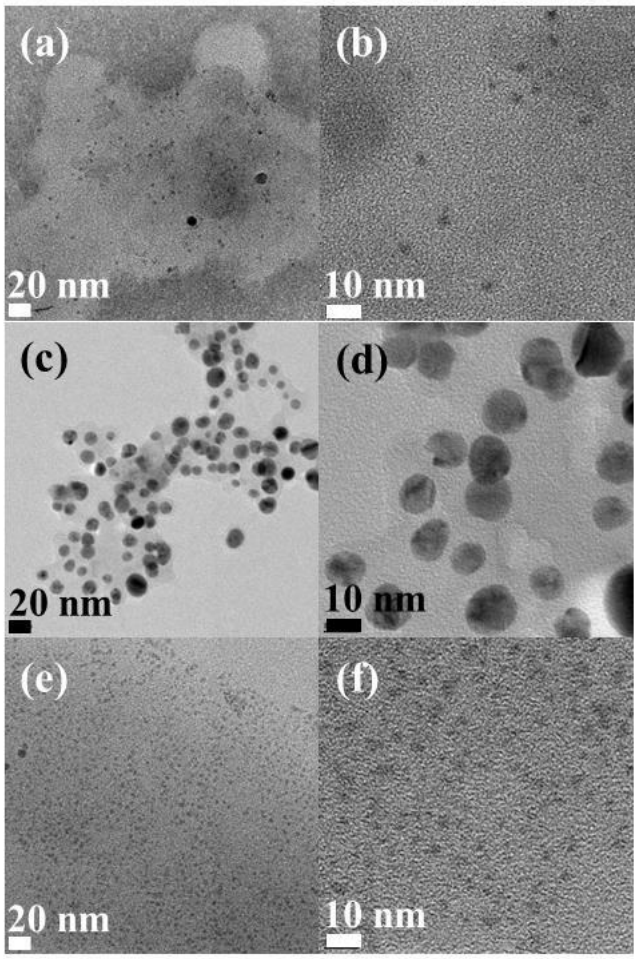

Figure 3. *TEM images of (a,b) curcumin-conjugated Ag-QCs, (c,d) curcumin-conjugated Ag-NPs, and (e,f) GSH conjugated Ag-QCs at two different resolutions (Scale bar: 20 nm and 10 nm).*

4.3.3 Tau aggregation inhibition by curcumin-conjugated Ag-QCs

Tau protein is a highly water-soluble protein and adopts a natively unfolded structure in solution. It is one of the major microtubule-associated proteins in neuronal axons that mainly functions to stabilize and assemble microtubules. In AD, Tau protein comes out from microtubules and destabilizes them as well as forms highly toxic aggregates known as "neurofibrillary tangles".

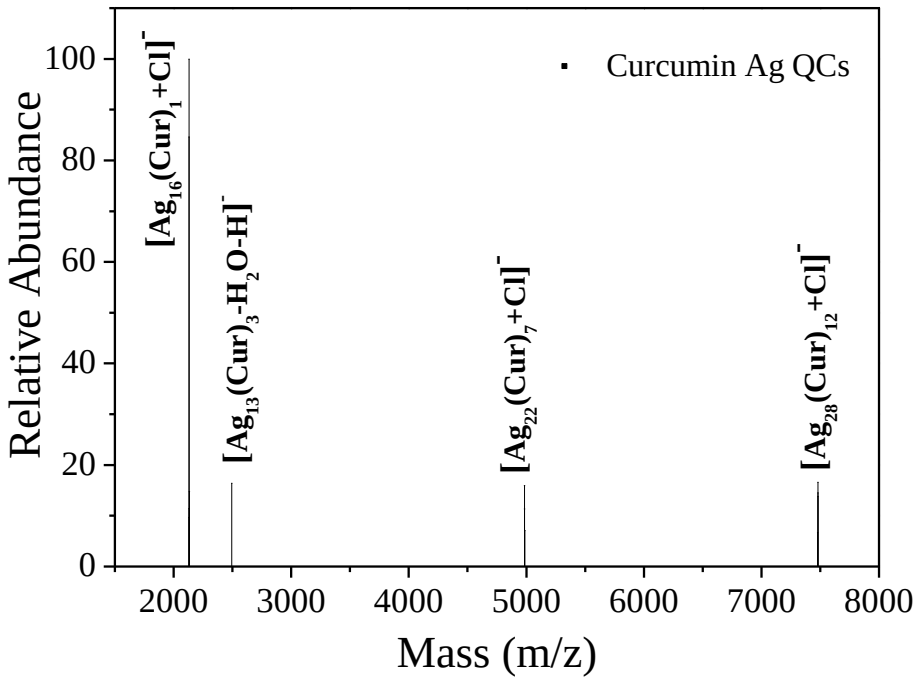

Figure 4. *ESI-MS spectrum of curcumin-conjugated Ag-QCs shows the presence of mixture of different populations of Ag-QCs.*

In *in vitro* conditions, heparin is used as an inducer to enhance aggregation/fibrillation. Heparin binds to the positively charged residues flanking repeat 2 and 3, thus leading to charge neutralization. Binding of heparin also leads to β-sheet conformation, which serves as nucleation center for aggregation/fibrillation. Tau is incubated at 37 °C in presence of compounds and assembly buffer. The extent of aggregation is then probed by ThS fluorescence at different time intervals.

The curcumin, curcumin-conjugated Ag-QCs, curcumin-conjugated Ag-NPs, and GSH-conjugated Ag-QCs were examined for their ability to inhibit four repeat Tau (*ie.* K18Wt) aggregation. All of these compounds were incubated with the K18Wt Tau (0.28 mg/mL protein concentration), with curcumin (~50 μg/mL), curcumin-conjugated Ag-QCs (curcumin content ~50 and 100 μg/mL, Ag content ~0.8 μg/mL), curcumin-conjugated Ag-NPs (curcumin content ~2 μg/mL, Ag content ~0.8 μg/mL), and GSH conjugated Ag-QCs

(Ag content ~0.8 μg/mL). The comparison between curcumin and curcumin-conjugated Ag-QCs were done on the basis of curcumin concentration *ie.* same curcumin concentration was used for both samples in order to check the effect of Ag-QCs. In order to know the effect of size, we compared the effect from curcumin-conjugated Ag-QCs and curcumin-conjugated Ag-NPs while keeping the same amount of silver content (~0.8 μg/mL). In order to isolate the effect of capping agent, we compared the effect from curcumin-conjugated Ag-QCs and GSH-conjugated Ag-QCs while keeping the same amount of silver content (~0.8 μg/mL).

Thioflavin S (ThS) assay was performed to study aggregation of Tau as a function of interaction-time required to form β-sheets during aggregation. ThS is a non-fluorescent dye which binds to only the amyloid fibrils and after binding, it gives the fluorescence. The aggregation propensity was monitored by ThS fluorescence. Surprisingly, curcumin-conjugated Ag-QCs were found to be more effective in inhibiting aggregates formation by K18Wt than curcumin itself. In contrast, curcumin-conjugated Au NPs and GSH-conjugated Ag-QCs were found to promote the aggregates formation of K18Wt (Figure 5).

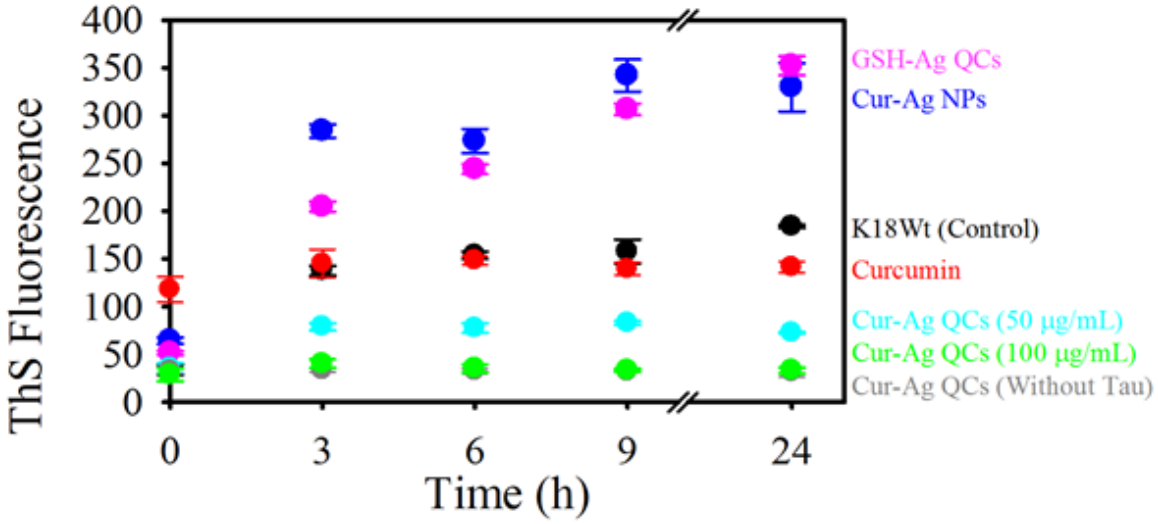

Figure 5. Inhibition of aggregates formation of K18Wt Tau. *Fluorescence assay was performed to monitor the aggregates formation in absence and presence of curcumin, curcumin-conjugated Ag-QCs, curcumin-conjugated Ag-NPs, and GSH-conjugated Ag-QCs.*

4.3.4 Conformational changes in K18Wt Tau structure

The conformational change in K18Wt Tau was studied by CD spectroscopy for aggregation after its interaction with curcumin, curcumin-conjugated Ag-QCs, curcumin-conjugated Ag-NPs, and GSH-conjugated Ag-QCs. The Tau protein is highly water-soluble protein with no secondary structure and exists as a random coil structure, which absorbs ~200 nm. When Tau aggregates, there is a typical shift in its absorption spectrum towards higher wavelength, which signifies the formation of β-sheet conformation in aggregated-Tau. We observed that after interaction with curcumin-conjugated Ag-QCs, the change in the conformation of Tau is much less in comparison to the change in its conformation after interaction with curcumin itself, curcumin-conjugated Ag-NPs, and GSH-conjugated Ag-QCs respectively; and the Tau protein maintains its random coil conformation. This again signifies the effect of curcumin-conjugated Ag-QCs in preventing aggregates formation (Figure 6). The four repeat Tau also has random coil conformation and shows absorption ~200 nm. But, upon aggregation it attains β-sheet and strongly absorbs ~220 nm. Nonetheless, in presence of curcumin-conjugated Ag-QCs, the change in conformation was prevented (Figure 6).

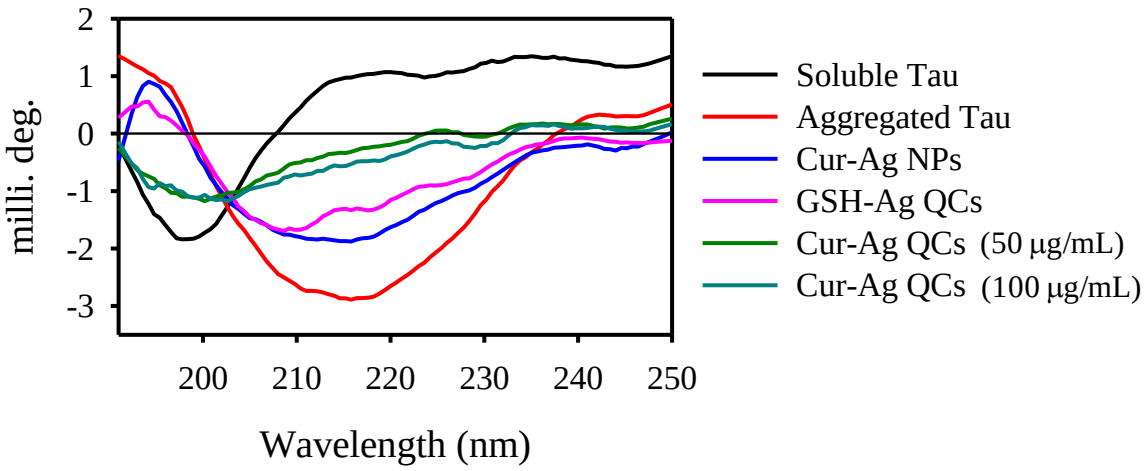

Figure 6. Curcumin-conjugated Ag-QCs induces Tau into random coil structure in solution. *In presence of inducer alone the repeat domain of Tau aggregates to give a dip in the negative axis in far UV region ~220 nm, which signifies β-sheet conformation (red). But, in presence of curcumin-conjugated Ag-QCs, the random coil conformation of Tau is maintained.*

4.4 Conclusion

We have synthesized curcumin-conjugated Ag-QCs and studied their interaction with Tau protein monomers in the fibrillation process. It was observed that curcumin-conjugated Ag-QCs effectively inhibit the fibrillation process while curcumin-conjugated Ag-NPs as well as GSH-conjugated Ag-QCs promote the fibrillation process. The circular dichroism study also supports these observations. We believe that curcumin-conjugated Ag-QCs may be applicable as a potential candidate in AD treatment.

4.5 References

1 D. L. Castillo-Carranza, M. J. Guerrero-Muñoz, U. Sengupta, C. Hernandez, A. D. T. Barrett, K. Dineley and R. Kayed, *J. Neurosci.*, 2015, **35**, 4857–68.

2 M. L. Cohen, C. Kim, T. Haldiman, M. ElHag, P. Mehndiratta, T. Pichet, F.

Lissemore, M. Shea, Y. Cohen, W. Chen, J. Blevins, B. S. Appleby, K. Surewicz, W. K. Surewicz, M. Sajatovic, C. Tatsuoka, S. Zhang, P. Mayo, M. Butkiewicz, J. L. Haines, A. J. Lerner and J. G. Safar, *Brain*, 2015, **138**, 1009–1022.

3 E. Underwood, *Science (80-.).*, 2016.

4 D. Brambilla, B. Le Droumaguet, J. Nicolas, S. H. Hashemi, L.-P. Wu, S. M. Moghimi, P. Couvreur and K. Andrieux, *Nanomedicine Nanotechnology, Biol. Med.*, 2011, **7**, 521–540.

5 S. Linse, C. Cabaleiro-Lago, W.-F. Xue, I. Lynch, S. Lindman, E. Thulin, S. E. Radford and K. a Dawson, *Proc. Natl. Acad. Sci. U. S. A.*, 2007, **104**, 8691–8696.

6 W. hui Wu, X. Sun, Y. ping Yu, J. Hu, L. Zhao, Q. Liu, Y. fen Zhao and Y. mei Li, *Biochem. Biophys. Res. Commun.*, 2008, **373**, 315–318.

7 G. Thakur, M. Micic, Y. Yang, W. Li, D. Movia, S. Giordani, H. Zhang and R. M. Leblanc, *Int. J. Alzheimers. Dis.*, 2011, **2011**, 1–15.

8 A. Mathew, A. Aravind, D. Brahatheeswaran, T. Fukuda, Y. Nagaoka, T. Hasumura, S. Iwai, H. Morimoto, Y. Yoshida, T. Maekawa, K. Venugopal and D. Sakthi Kumar, *Bionanoscience*, 2012, **2**, 83–93.

9 N. Xiong, X. Dong, J. Zheng, F. Liu and Y. Sun, *ACS Appl. Mater. Interfaces*, 2015, **7**, 5650–5662.

10 S. Il Yoo, M. Yang, J. R. Brender, V. Subramanian, K. Sun, N. E. Joo, S. H. Jeong, A. Ramamoorthy and N. A. Kotov, *Angew. Chemie - Int. Ed.*, 2011, **50**, 5110–5115.

11 C. Cabaleiro-Lago, F. Quinlan-Pluck, I. Lynch, S. Lindman, A. M. Minogue, E. Thulin, D. M. Walsh, K. a Dawson and S. Linse, *J. Am. Chem. Soc.*, 2008, **130**,

15437–15443.

12 L. Xiao, D. Zhao, W. Chan, M. M. F. Choi and H. Li, *Biomaterials*, 2010, **31**, 91–98.

13 S. Mirsadeghi, R. Dinarvand, M. H. Ghahremani, M. R. Hormozi-Nezhad, Z. Mahmoudi, M. J. Hajipour, F. Atyabi, M. Ghavami and M. Mahmoudi, *Nanoscale*, 2015, **7**, 5004–5013.

14 G. Brancolini, A. Corazza, M. Vuano, F. Fogolari, M. C. Mimmi, V. Bellotti, M. Stoppini, S. Corni and G. Esposito, *ACS Nano*, 2015, **9**, 2600–2613.

15 S. Sardar, S. Pal, S. Maity, J. Chakraborty and U. C. Halder, *Int. J. Biol. Macromol.*, 2014, **69**, 137–145.

16 D. Ghosh, P. Dutta, C. Chakraborty, P. K. Singh, A. Anoop, N. N. Jha, R. S. Jacob, M. Mondal, S. Mankar, S. Das, S. Malik and S. K. Maji, *Langmuir*, 2014, **30**, 3775–3786.

17 L. Bellucci, A. Ardèvol, M. Parrinello, H. Lutz, H. Lu, T. Weidner and S. Corni, *Nanoscale*, 2016, **8**, 8737–8748.

18 Y. Liu, L.-P. Xu, W. Dai, H. Dong, Y. Wen and X. Zhang, *Nanoscale*, 2015, **7**, 19060–19065.

19 A. Mathew, T. Fukuda, Y. Nagaoka, T. Hasumura, H. Morimoto, Y. Yoshida, T. Maekawa, K. Venugopal and D. S. Kumar, *PLoS One*, 2012, **7**, 1–10.

20 M. Richman, S. Wilk, N. Skirtenko, A. Perelman and S. Rahimipour, *Chem. - A Eur. J.*, 2011, **17**, 11171–11177.

21 Z. Yang, C. Ge, J. Liu, Y. Chong, Z. Gu, C. A. Jimenez-Cruz, Z. Chai and R. Zhou,

Nanoscale, 2015, **7**, 18725–18737.

22 C. H. Vannoy and R. M. Leblanc, *J. Phys. Chem. B*, 2010, **114**, 10881–10888.

23 M. Mahmoudi, O. Akhavan, M. Ghavami, F. Rezaee and S. M. A. Ghiasi, *Nanoscale*, 2012, **4**, 7322.

24 Y.-H. Liao, Y.-J. Chang, Y. Yoshiike, Y.-C. Chang and Y.-R. Chen, *Small*, 2012, **8**, 3631–3639.

25 H. Skaat, R. Chen, I. Grinberg and S. Margel, *Biomacromolecules*, 2012, **13**, 2662–2670.

26 L. Xiao, D. Zhao, W. H. Chan, M. M. F. Choi and H. W. Li, *Biomaterials*, 2010, **31**, 91–98.

27 M. Li, X. Yang, J. Ren, K. Qu and X. Qu, *Adv. Mater.*, 2012, **24**, 1722–1728.

28 C. N. Loynachan, G. Romero, M. G. Christiansen, R. Chen, R. Ellison, T. T. O'Malley, U. P. Froriep, D. M. Walsh and P. Anikeeva, *Adv. Healthc. Mater.*, 2015, **4**, 2100–2109.

29 C. Cabaleiro-Lago, F. Quinlan-Pluck, I. Lynch, K. A. Dawson and S. Linse, *ACS Chem. Neurosci.*, 2010, **1**, 279–287.

30 H. Skaat, G. Shafir and S. Margel, *J. Nanoparticle Res.*, 2011, **13**, 3521–3534.

31 H. Mohammad-Beigi, seyed A. Shojaosadati, A. T. Marvian, J. N. Pedersen, L. H. Klausen, G. Christiansen, J. S. Pedersen, M. Dong, D. Morshedi and D. E. Otzen, *Nanoscale*, 2015, **7**, 19627–19640.

32 N. Gao, H. Sun, K. Dong, J. Ren and X. Qu, *Chem. - A Eur. J.*, 2015, **21**, 829–835.

33 B. G. Anand, K. Dubey, D. S. Shekhawat and K. Kar, *Biochemistry*, 2016, **55**, 3345–3348.

34 S. Palmal, A. R. Maity, B. K. Singh, S. Basu, N. R. Jana and N. R. Jana, *Chem. - A Eur. J.*, 2014, **20**, 6184–6191.

35 F. Yang, G. P. Lim, A. N. Begum, O. J. Ubeda, M. R. Simmons, S. S. Ambegaokar, P. P. Chen, R. Kayed, C. G. Glabe, S. A. Frautschy and G. M. Cole, *J. Biol. Chem.*, 2005, **280**, 5892–5901.

36 G. K. Jayaprakasha, L. Jagan Mohan Rao and K. K. Sakariah, *Trends Food Sci. Technol.*, 2005, **16**, 533–548.

37 R. K. Maheshwari, A. K. Singh, J. Gaddipati and R. C. Srimal, *Life Sci.*, 2006, **78**, 2081–2087.

38 M. Salem, S. Rohani and E. R. Gillies, *RSC Adv.*, 2014, **4**, 10815.

39 S. K. Tiwari, S. Agarwal, B. Seth, A. Yadav, S. Nair, P. Bhatnagar, M. Karmakar, M. Kumari, L. K. Chauhan, D. K. Patel, V. Srivastava, D. Singh, S. K. Gupta, A. Tripathi, R. K. Chaturvedi and K. C. Gupta, *ACS Nano*, 2014, **8**, 76–103.

40 G. K. Jayaprakasha, L. Jaganmohan Rao and K. K. Sakariah, *Food Chem.*, 2006, **98**, 720–724.

41 A. N. Begum, M. R. Jones, G. P. Lim, T. Morihara, P. Kim, D. D. Heath, C. L. Rock, M. A. Pruitt, F. Yang, B. Hudspeth, S. Hu, K. F. Faull, B. Teter, G. M. Cole and S. A. Frautschy, *J. Pharmacol. Exp. Ther.*, 2008, **326**, 196–208.

42 R. Jagannathan, P. M. Abraham and P. Poddar, *J. Phys. Chem. B*, 2012, **116**, 14533–40.

43 D. K. Singh, R. Jagannathan, P. Khandelwal, P. M. Abraham and P. Poddar, *Nanoscale*, 2013, **5**, 1882–93.

44 J. Shaikh, D. D. Ankola, V. Beniwal, D. Singh and M. N. V. R. Kumar, *Eur. J. Pharm. Sci.*, 2009, **37**, 223–230.

45 V. Kakkar, S. Singh, D. Singla and I. P. Kaur, *Mol. Nutr. Food Res.*, 2011, **55**, 495–503.

46 X. Xie, Q. Tao, Y. Zou, F. Zhang, M. Guo, Y. Wang, H. Wang, Q. Zhou and S. Yu, *J. Agric. Food Chem.*, 2011, **59**, 9280–9289.

47 X. Gao, F. Zheng, G. Guo, X. Liu, R. Fan, Z. Qian, N. Huang and Y. Wei, *J. Mater. Chem. B*, 2013, **1**, 5778.

48 R. K. Gangwar, V. A. Dhumale, D. Kumari, U. T. Nakate, S. W. Gosavi, R. B. Sharma, S. N. Kale and S. Datar, *Mater. Sci. Eng. C*, 2012, **32**, 2659–2663.

49 S. Wan, Y. Sun, X. Qi and F. Tan, *AAPS PharmSciTech*, 2012, **13**, 159–66.

50 C. Li, Zhang, Su, Feng, Long and Chen, *Int. J. Nanomedicine*, 2012, **7**, 5995.

51 J. Sun, C. Bi, H. M. Chan, S. Sun, Q. Zhang and Y. Zheng, *Colloids Surfaces B Biointerfaces*, 2013, **111**, 367–375.

52 H. Yu and Q. Huang, *J. Agric. Food Chem.*, 2012, **60**, 5373–5379.

53 S. Dolai, W. Shi, C. Corbo, C. Sun, S. Averick, D. Obeysekera, M. Farid, A. Alonso, P. Banerjee and K. Raja, *ACS Chem. Neurosci.*, 2011, **2**, 694–699.

54 M. Taylor, S. Moore, S. Mourtas, A. Niarakis, F. Re, C. Zona, B. La Ferla, F. Nicotra, M. Masserini, S. G. Antimisiaris, M. Gregori and D. Allsop, *Nanomedicine*

Nanotechnology, Biol. Med., 2011, **7**, 541–550.

55 P. Khandelwal, D. K. Singh, S. Sadhu and P. Poddar, *Chempluschem*, 2014, **79**, 134–142.

56 P. Khandelwal, D. K. Singh, S. Sadhu and P. Poddar, *Nanoscale*, 2015, **7**, 19985–20002.

57 Y. Antoku, J. Hotta, H. Mizuno, R. M. Dickson, J. Hofkens and T. Vosch, *Photochem. Photobiol. Sci.*, 2010, **9**, 716–721.

58 S. Chandirasekar, C. Chandrasekaran, T. Muthukumarasamyvel, G. Sudhandiran and N. Rajendiran, *ACS Appl. Mater. Interfaces*, 2015, **7**, 1422–1430.

59 Y. Wang, C. Dai and X.-P. Yan, *Chem. Commun.*, 2014, **50**, 14341–14344.

60 A. K. Sahoo, U. Goswami, D. Dutta, S. Banerjee, A. Chattopadhyay and S. S. Ghosh, *ACS Biomater. Sci. Eng.*, 2016, **2**, 1395–1402.

61 G. Aliev, J. Daza, A. Herrera, M. Carmen Arias Esparza, L. Morales, V. Echeverria, S. Bachurin and G. Barreto, *CNS Neurol. Disord. - Drug Targets*, 2015, **14**, 1235–1242.

62 Y. Morishita, Y. Yoshioka, Y. Takimura, Y. Shimizu, Y. Namba, N. Nojiri, T. Ishizaka, K. Takao, F. Yamashita, K. Takuma, Y. Ago, K. Nagano, Y. Mukai, H. Kamada, S. Tsunoda, S. Saito, T. Matsuda, M. Hashida, T. Miyakawa, K. Higashisaka and Y. Tsutsumi, *ACS Nano*, 2016, **10**, 8180–8191.

63 X. X. Yang, C. M. Li and C. Z. Huang, *Nanoscale*, 2016, **8**, 3040–3048.

Chapter V

Conclusion and future perspective

This chapter deals with the salient features and the future perspectives of the research work presented in this thesis.

5.1 Conclusion

In summary, we have concluded that metal clusters are more effective than nanoparticles among all the applications related to sensing, imaging and therapy mainly due to their very small size (less than or comparable to the protein/nucleic acid molecules) which provides huge surface area for the binding of high concentration of drug molecules. The large surface area of QCs also facilitates their interaction with biomolecules, and biological cells. We have mentioned chapter-wise conclusion as follows.

From chapter 2, we have concluded that antibiotic-conjugated gold nanoparticles, as well as gold quantum cluster, can be synthesized using the reducing as well as capping ability of antibiotic molecules and altering the molar ratio of reactants, temperature and most importantly, the pH of the reaction.[1–4] The importance of various groups such as amino, carboxyl, and sulfur groups of antibiotic in binding with gold nanoparticle surface was also observed by combined experimental as well as theoretical studies. We could also able to synthesize blue luminescent gold clusters and applied them for sensing and imaging of mercury ions in aqueous and bacterial samples, respectively. Finally, we also observed the antibacterial property of antibiotic capped gold nanoparticles as well as gold clusters in buffers. The reason behind the killing of bacterial cells using gold particles was proposed to be due to direct contact of these particles with bacterial cells as analyzed by SEM and confocal studies.

In chapter 3, we could able to synthesize the curcumin-conjugated gold clusters for the first time using reducing as well as capping ability of curcumin molecules in alkaline conditions.[5] It was also observed that the loading amount of curcumin on the gold clusters was very high which also increased the water dispersibility of curcumin to great extent.[6]

Curcumin was observed to retain its anticancer property upon conjugation with gold clusters. Surprisingly, the cytotoxic property of curcumin got decreased upon conjugation with gold clusters. The anticancer mechanism of curcumin and curcumin-conjugated gold clusters were found to be same.

In chapter 4 of this thesis, we have presented our results on the synthesis of curcumin-conjugated silver clusters using the reducing as well as binding property of curcumin molecules. We observed that curcumin-conjugated silver clusters were able to more effectively reduce the tau fibril formation than curcumin and curcumin conjugated silver nanoparticles upon considering the same concentration of curcumin molecules. It was also observed that curcumin-conjugated silver clusters were more effective in the reduction of tau fibrillation than glutathione-conjugated silver clusters. In fact, glutathione-conjugated silver clusters and curcumin-conjugated silver nanoparticles enhanced the tau fibrillation.

5.2 Future Perspective

In this thesis, we made the efforts to understand the nucleation and growth of metal nanoparticles starting from monomers and their applicability in various fields. However, there are few points which have to be addressed and after applying some of them, it would be possible to enhance their applicability in various fields. We have summarized these points chapter-wise as follows:

Chapter 2. The methods for one-step synthesis of antibiotic-conjugated gold quantum clusters are needed to be developed which will be able to synthesize atomically precise gold clusters in one pot and these methods should be scalable in order to produce gold clusters in larger amounts. The quantification of nanoparticles should be done based on the

number of antibiotic molecules attached to the surface, not on the basis of gold or antibiotic content used at the time of reaction. It would be better to use bulky antibiotic molecules for the synthesis rather than small ones because there are chances that capping on the top of QCs might block the active sites of smaller antibiotic molecules. The experiments should be performed to analyze the effectivity of these gold quantum clusters on multi-drug resistant bacterial strains. The *in-vivo* study should also be done in order to check the effectivity of these gold quantum clusters for antibacterial activity in the body.

Chapter 3. The method for one-step synthesis of curcumin-conjugated water dispersible gold quantum clusters has to be developed in order to synthesize gold clusters in bulk amount with lesser efforts. The studies should be performed to determine the curcumin bioavailability *in-vivo* before and after conjugation with gold quantum clusters. *In-vivo* antitumor activity using a combination of radio and chemotherapy, and imaging of tumor destruction using CT scan should be performed in order to analyze the effectivity of these clusters.

Chapter 4. One-step synthesis methods of curcumin-conjugated water dispersible silver quantum clusters have to be developed for the bulk synthesis with lesser efforts. In order to analyze the effectivity of curcumin-conjugated silver clusters, *in vitro* neurotoxicity study and *in vivo* anti-Alzheimer's studies should be performed.

5.3 References

1 R. Jagannathan, P. Poddar and A. Prabhune, *J. Phys. Chem. C*, 2007, **111**, 6933–6938.

2 R. Jagannathan, A. S. Parmar, S. Adyanthaya, A. Prabhune, M. Muschol and P. Poddar, *J. Phys. Chem. C*, 2009, **113**, 3478–3486.

3 P. Khandelwal, D. K. Singh, S. Sadhu and P. Poddar, *Chempluschem*, 2014, **79**, 134–142.

4 P. Khandelwal, D. K. Singh, S. Sadhu and P. Poddar, *Nanoscale*, 2015, **7**, 19985–20002.

5 D. K. Singh, R. Jagannathan, P. Khandelwal, P. M. Abraham and P. Poddar, *Nanoscale*, 2013, **5**, 1882–93.

6 R. Jagannathan, P. M. Abraham and P. Poddar, *J. Phys. Chem. B*, 2012, **116**, 14533–40.

List of publications:

(1) Singh, D. K.; Jagannathan, R.; **Khandelwal, P.**; Abraham, P. M.; Poddar, P. In Situ Synthesis and Surface Functionalization of Gold Nanoparticles with Curcumin and Their Antioxidant Properties: An Experimental and Density Functional Theory Investigation. *Nanoscale* **2013**, *5*, 1882–1893.

(2) **Khandelwal, P.**; Singh, D. K.; Sadhu, S.; Poddar, P. Modulation of Reaction Kinetics for the Tuneable Synthesis of Gold Nanoparticles and Quantum Clusters: Application of Gold Quantum Clusters as "Turn-Off" Sensing Probe for Sn 4+ Ions. *Chempluschem* **2014**, *79*, 134–142.

(3) Sharan, C.; **Khandelwal, P.**; Poddar, P. The Mechanistic Insight into the Biomilling of Goethite (α-FeO(OH)) Nanorods Using the Yeast Saccharomyces Cerevisiae. *RSC Adv.* **2015**, *5*, 91785–91794.

(4) Sharan, C.; **Khandelwal, P.**; Poddar, P. Biomilling of Rod-Shaped ZnO Nanoparticles: A Potential Role of Saccharomyces Cerevisiae Extracellular Proteins. *RSC Adv.* **2015**, *5*, 1883–1889.

(5) **Khandelwal, P.**; Singh, D. K.; Sadhu, S.; Poddar, P. Study of the Nucleation and Growth of Antibiotic Labeled Au NPs and Blue Luminescent Au 8 Quantum Clusters for Hg 2+ Ion Sensing, Cellular Imaging and Antibacterial Applications. *Nanoscale* **2015**, *7*, 19985–20002.

(6) Sharma, N.; Sivalingam, V.; Maurya, S.; Prasad, A.; **Khandelwal, P.**; Yadav, S. C.; Patel, B. K. New Insights into in Vitro Amyloidogenic Properties of Human Serum Albumin Suggest Considerations for Therapeutic Precautions. *FEBS Lett.* **2015**, *589*, 4033–4038.

(7) Gade, M.; **Khandelwal, P.**; Sangabathuni, S.; Bavireddi, H.; Murthy, R. V.; Poddar, P.; Kikkeri, R. Immobilization of Multivalent Glycoprobes on Gold Surfaces for

Sensing Proteins and Macrophages. *Analyst* **2016**, *141*, 2250–2258.

(8) Batkulwar, K. B.; Jana, A. K.; Godbole, R. K.; **Khandelwal, P.**; Sengupta, N.; Kulkarni, M. J. Hydralazine Inhibits Amyloid Beta (Aβ) Aggregation and Glycation and Ameliorates Aβ 1–42 Induced Neurotoxicity. *RSC Adv.* **2016**, *6*, 108768–108776.

(9) Biswas, A.; **Khandelwal, P.**; Das, R.; Salunke, G.; Alam, A.; Ghorai, S.; Chattopadhyay, S.; Poddar, P. Oxidant Mediated One-Step Complete Conversion of Multi-Walled Carbon Nanotubes to Graphene Quantum Dots and Their Bioactivity against Mammalian and Bacterial Cells. *J. Mater. Chem. B* **2017**, *5*, 785–796.

(10) Gorantla, N. V.; **Khandelwal, P.**; Poddar, P.; Chinnathambi, S. Global Conformation of Tau Protein Mapped by Raman Spectroscopy. In *Tau Protein: Methods and Protocols*; Smet-Nocca, C., Ed.; Springer New York, 2017; pp. 21–31.

(11) Biswas, A.; Salunke, G.; **Khandelwal**, **P.;** Das, R.; Poddar. P. Surface Disordered Rutile TiO_2-Graphene Quantum Dots (TiO_2-GQDs) Hybrid: A New Multifunctional Material with Superior Photocatalytic and Antibacterial Properties. *New J. Chem.* **2017**, *41*, 2642-2657.

(12) **Khandelwal**, **P.;** Gorantla, N. V.; Chinnathambi, S.; Poddar, P. The Interaction of Curcumin-Capped Ag-QCs with Tau Protein (Manuscript under preperation).

(13) **Khandelwal**, **P.;** Alam, A.; Chattopadhyay, S., Poddar, P. Curcumin-Conjugated Au-QCs as a Theranostics Probes for Anticancer Application (Manuscript under preperation).

(14) **Khandelwal**, **P.;** Singh, D. K.; Poddar, P. One Pot Process for the Preparation of Gold Quantum Clusters. US Patent App. 14/779,197, Year: 02/2016.